JAEA-Conf
2009-004

Proceedings of the 2008 Annual Symposium on Nuclear Data (NDS 2008)

November 20-21, 2008, Ricotti, Tokai, Japan

(Ed.) Satoshi CHIBA

Advanced Science Research Center

October 2009

Japan Atomic Energy Agency

日本原子力研究開発機構

JAEA-Conf

本レポートは独立行政法人日本原子力研究開発機構が不定期に発行する成果報告書です。
本レポートの入手並びに著作権利用に関するお問い合わせは、下記あてにお問い合わせ下さい。
なお、本レポートの全文は日本原子力研究開発機構ホームページ（http://www.jaea.go.jp）
より発信されています。

独立行政法人日本原子力研究開発機構　研究技術情報部　研究技術情報課
〒319-1195　茨城県那珂郡東海村白方白根 2 番地 4
電話 029-282-6387, Fax 029-282-5920, E-mail:ird-support@jaea.go.jp

This report is issued irregularly by Japan Atomic Energy Agency
Inquiries about availability and/or copyright of this report should be addressed to
Intellectual Resources Section, Intellectual Resources Department,
Japan Atomic Energy Agency
2-4 Shirakata Shirane, Tokai-mura, Naka-gun, Ibaraki-ken 319-1195 Japan
Tel +81-29-282-6387, Fax +81-29-282-5920, E-mail:ird-support@jaea.go.jp

Proceedings of the 2008 Annual Symposium on Nuclear Data (NDS2008)

November 20-21, 2008, Ricotti, Tokai, Japan

(Ed.) Satoshi CHIBA

Advanced Science Research Center
Japan Atomic Energy Agency
Tokai-mura, Naka-gun, Ibaraki-ken

(Received July 22, 2009)

The annual nuclear data symposium, organized by the Nuclear Data Division of Atomic Energy Society of Japan (AESJ) was held at Ricotti, Tokai, on Nov. 20 and 21, 2008 in cooperation with Advanced Science Research Center of JAEA and under final support from North-Kanto Branch of AESJ. The symposium was devoted for discussions and presentations of research results in wide variety of fields related to nuclear data, including 2 tutorial talks. Talks as well as posters presented at the symposium aroused lively discussions among approximately 80 participants. This report contains 36 papers submitted from the talkers and poster presenters.

Keywords: Proceedings, Annual Nuclear Data Symposium 2008, Nuclear Data, JENDL-4, Radiation Behaviour, Recent Topics

---

Organizers: M. Ishikawa (JAEA, Chair), S. Chiba (JAEA, Vice-Chair), K. Kato (Hokkaido Univ.), Y. Watanabe (Kyushu Univ.), S. Matsufuji (NIRS), G. Hirano (TEPCO systems), K. Konno (JAEA), H. Harada (JAEA), H. Koura (JAEA), O. Iwamoto (JAEA)

2008年度核データ研究会(NDS2008)報告集

2008年11月20日～11月21日、テクノ交流館リコッティー、東海村

日本原子力研究開発機構 先端基礎研究センター

(編) 千葉　敏

(2009 年 7 月 22 日受理)

2008年度核データ研究会は、2008年11月20日から21日にかけて、東海村のテクノ交流館リコッティーにて開催された。当研究会は日本原子力学会核データ部会の主催、日本原子力研究開発機構先端基礎研究センターの共催、及び日本原子力学会北関東支部の後援の下、核データ分野におけるJENDLを含む幅広い分野についての最新の情報交換と議論の場として多くの研究者の参加を得て行われた。初日には2件のチュートリアルも行われた。参加総数は約80名で、盛況のうちに全日程を終えた。本レポートは、同研究会における講演、ポスター発表の報告集である。

原子力科学研究所（駐在）:〒319-1195 茨城県那珂郡東海村白方白根2-4

2008年核データ研究会実行委員会：石川　眞（委員長、原子力機構）、千葉　敏（副委員長、原子力機構）、加藤　幾芳（北大）、渡辺　幸信（九大）、松藤　成弘（放医研）、平野　豪（テプコシステムズ）今野　力（原子力機構）、原田　秀郎（原子力機構）、小浦　寛之（原子力機構）、岩本　修 (原子力機構）

Contents

目 次

This is a blank page.

1. Program of 2008 Symposium on Nuclear Data

Nov. 20-21, 2008
RICOTTI Convention Center, Tokai, Ibaraki, Japan

Nov. 20 (Thu.)
10:20-10:25
1. Opening Address M. Ishikawa (JAEA)

10:25-12: 00
2. Towards the Completion of JENDL-4 Chaired by M. Igashira (TIT)
 2.1 Present Status of JENDL-4 [15+5] K. Shibata (JAEA)
 2.2 JENDL Actinoid File 2008 [20+5] O. Iwamoto (JAEA)
 2.3 Systematic Coupled-channel Optical Model Analysis
 for Nuclear Data Evaluation [20+5] K. Kunieda (JAEA)
 2.4 Current Status of Integral Test [20+5] G. Chiba (JAEA)

12:00-13:00 Lunch

13:00-14:45
3. Nuclear Data Tutorial (1)
 Present Status and Prospects on Nuclear Data and Neutron Spectrum Adjustment Methods
 for Reactor Dosimetry
 T. Iguchi (Nagoya U.)

14:45-15:00 Coffee Break

15:00-16:45
4. Nuclear Data Tutorial (2)
 Tutorial of Nuclear Reaction Theoretical Calculation Code CCONE O. Iwamoto (JAEA)

16:45-17:00
5. Q&A and Enquête Chaired by S. Chiba (JAEA)

Nov. 21 (Fri.)
10:20-12:00
6. Poster Presentation

12:00-13:00 Lunch

13:00-14:45
7. Progress of Researches in Nuclear Data and Radiation Behavior in Japan
 Chaired by Y. Watanabe (Kyushu U.)
 7.1 Thirty Years along with Neutron Nuclear Data [25+5] M. Baba (Tohoku U.)
 7.2 Fusion Neutronics and the Nuclear Data [20+5] T. Nishitani (JAEA)
 7.3 Development of Radiation Design Methods for Radiological Safety of J-PARC [20+5]
 H. Nakashima (JAEA)
 7.4 Accelerator-based BNCT with Medium- to High-Energy Proton Beams [20+5]
 S. Yonai (NIRS)

14:45-14:50 Photo

14:50-15:05 Coffee Break

15:05-16: 45

8. Latest Topics around Nuclear Data from the World — Chaired by N. Yamano (TIT)

8.1 A Dispersive Lane-consistent Optical Potential, Coupled-channel Optical Model Code OPTMAN and Its Application [20+5] — E. Soukhovitkij (Belarus)

8.2 Neutrino Physics and Nuclear Data [20+5] — T. Yoshida (NAOJ)

8.3 KUCA Experiments and Criticality Safety Analyses in R & D of Er-SHB Fuel [20+5] — T. Kuroishi (NFI, Ltd.)

8.4 Recent Activities of OECD/NEA/NSC/WPEC [20+5] — J. Katakura (JAEA)

16:45-17:00

9. Poster Award and Closing Address — M. Igashira (TIT)

Poster Presentation

1. Nuclear Reaction DataBase : NRDF/A — K. Kato (Hokkaido U.)
2. Evaluation of Neutron Cross Sections on Silver Isotopes for JENDL-4 — N. Iwamoto (JAEA)
3. Measurement of Neutron-Production Double-Differential Cross Section for Continuous-Energy Neutron-Incidence on Al — Y. Nakamura (Kyushu U.)
4. A Global Dispersive Coupled-Channel Optical Model Potential for A=24-122 Mass Range up to 200 MeV — HAO LIJUAN (Kyushu U.)
5. Nuclear data-induced uncertainty calculation for fast reactor eigenvalue separation — G. Chiba (JAEA)
6. Criticality calculations with fission spectrum — G. Chiba (JAEA)
7. Recent progress of fragment measurement from tens of MeV proton induced reaction using Bragg Curve Counter — T. Sanami (KEK)
8. Gamma strength function for La-139 below the neutron separation energy — A. Makinaga (Konan U.)
9. Neutron capture cross section measurements on Am-243 with a 4π Ge spectrometer — J. Hori (KURRI)
10. Calculation of beta-delayed fission and neutron emission probabilities with the use of gross theory and KTUY mass formula — T. Tachibana (Waseda U.)
11. Global properties of nuclear decay modes — H. Koura (JAEA)
12. Sensitivity Analysis of beryllium benchmark experiment at JAEA/FNS — C. Konno (JAEA)
13. Measurement of keV-neutron capture cross sections and gamma-ray spectra of ^{88}Sr — T. Katabuchi (TIT)
14. Benchmarking of Effective Delayed Neutron Fraction — Dwi IRWANTO (TIT)
15. Effect of spectrum shifter for nuclear data benchmark in MeV energy region on $LiAlO_2$ with D-T neutrons — M. Ohta (Osaka U.)
16. A Theoretical Model Analysis of Li(d,xn) Reactions Up To 51 MeV — Ye Tao (Kyushu U.)
17. Preliminary Measurement of The Neutron Emission Spectra for Beryllium at 21.65 MeV Neutrons — Lan Chang-lin (Kyushu U.)
18. Measurement of the thermal-neutron capture cross-section and the resonance integral of the ^{112}Cd(n, gamma)^{113m}Cd reaction — S. Nakamura (JAEA)
19. Measurement of keV-neutron capture cross sections and capture gamma-ray spectra of ^{80,82}Se — S. Kamada (TIT)
20. Analysis of the ^{7}Li (d, p) ^{8}Li reaction in the incident energy — T. Murata
21. Measurement of Light Charged Particle Production Double-differential Cross Sections for 360- and 500-MeV Proton Induced Reactions — H. Iwamoto (Kyushu U.)
22. Neutron flux measurement by means of multi-foil activation method in Be and Be/Li2TiO_3 experiments with DT neutrons — Y. Tatebe (JAEA)
23. Pandemonium Problem in FP Decay Heat Calculations and its Solution — N. Hagura (Musashi I.T.)

2. Present Status of JENDL-4

Keiichi SHIBATA
Nuclear Data Center
Japan Atomic Energy Agency
Tokai-mura, Naka-gun, Ibaraki-ken 319-1195
e-mail: shibata.keiichi@jaea.go.jp

The fourth version of Japanese Evaluated Nuclear Data Library is being developed at the JAEA Nuclear Data Center in cooperation with the Japanese Nuclear Data Committee. As for actinides, we already released JENDL Actinoid File 2008, which contains the evaluated data for 79 nuclei. The high-energy cross sections of FP nuclei have been evaluated by using the CCONE and POD statistical model codes. The nuclear data for structural materials and light nuclei are being revised. The fission product yields were updated on the basis of ENDF/B-VII.0. Ternary fission was included in the yield data.

1. Introduction

As a mid-term project for FY2005-2009, the JAEA Nuclear Data Center is developing the fourth version of Japanese Evaluated Nuclear Data Library (JENDL-4) in cooperation with the Japanese Nuclear Data Committee. The time schedule is illustrated in Fig. 1. The statistical model codes CCONE[1)] and POD[2)] were developed and they have been used to evaluate FP and MA data. As for actinide data, we already released JENDL Actinoid File 2008 (JENDL/AC-2008)[3)], which contains the evaluated data for 79 nuclei. This file reveals a good performance for reactor benchmarks. Evaluation of medium and light nuclei is in progress. Fission product yields have been evaluated on the basis of ENDF/B-VII.0 with some modifications. This paper deals with the activities on JENDL-4, but excludes those on the actinide data that are presented by Iwamoto *et al.* in this symposium.

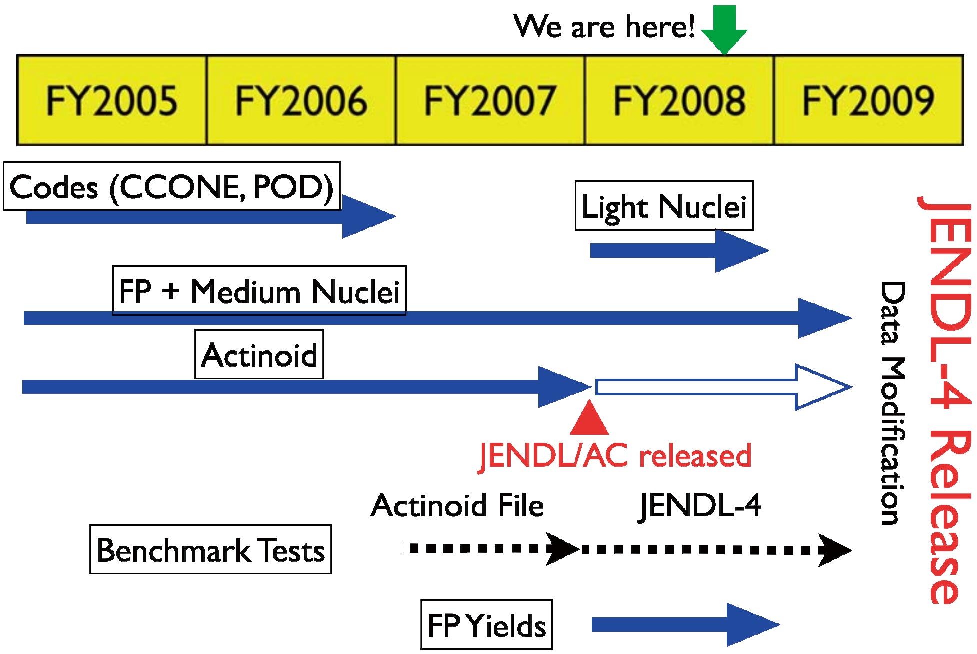

Fig. 1 Time schedule of JENDL-4

2. Fission Product Data

A total of 214 nuclei are categorized as fission products. The resolved resonance parameters were updated or newly evaluated for 121 nuclei by considering the measurements that were made available after JENDL-3.3 had been released.

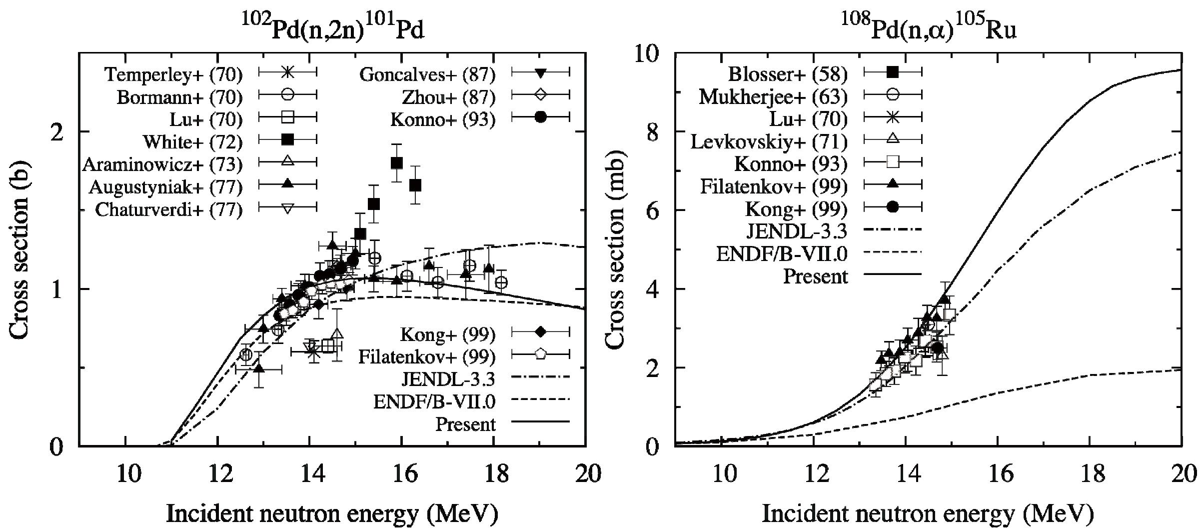

Fig.2 ^{102}Pd(n,2n) and ^{108}Pd(n,α) cross sections

The smooth cross sections were evaluated using the CCONE and POD statistical model codes for 73 nuclei as of Nov. 6, 2008. We used the spherical optical model parameters obtained by Koning and Delaroche[4] or the coupled-channel ones obtained by Kunieda *et al.*[5] for neutrons. As an example, Fig. 2 shows the evaluated[6] (n,2n) cross section of ^{102}Pd and (n,α) cross section of ^{108}Pd.

3. Structural Material Data

Considering the results of various benchmarks, the data on structural materials were partly revised. The inelastic scattering cross sections for the first three low-lying levels of ^{56}Fe were evaluated with the POD code. Moreover, the elastic angular distributions of ^{56}Fe were modified by using the fine-resolution experimental data[7,8] and the POD calculations. The first-order Legendre coefficient for the angular distribution is illustrated in Fig. 3. It is found from the figure that the present evaluation exhibits large fluctuations below 2.5 MeV. On the other hand, the coefficients in JENDL-3.3, which are completely based on the optical and statistical model calculation, are smooth in the entire energy region. The inelastic scattering cross section for the first excited state of ^{57}Fe

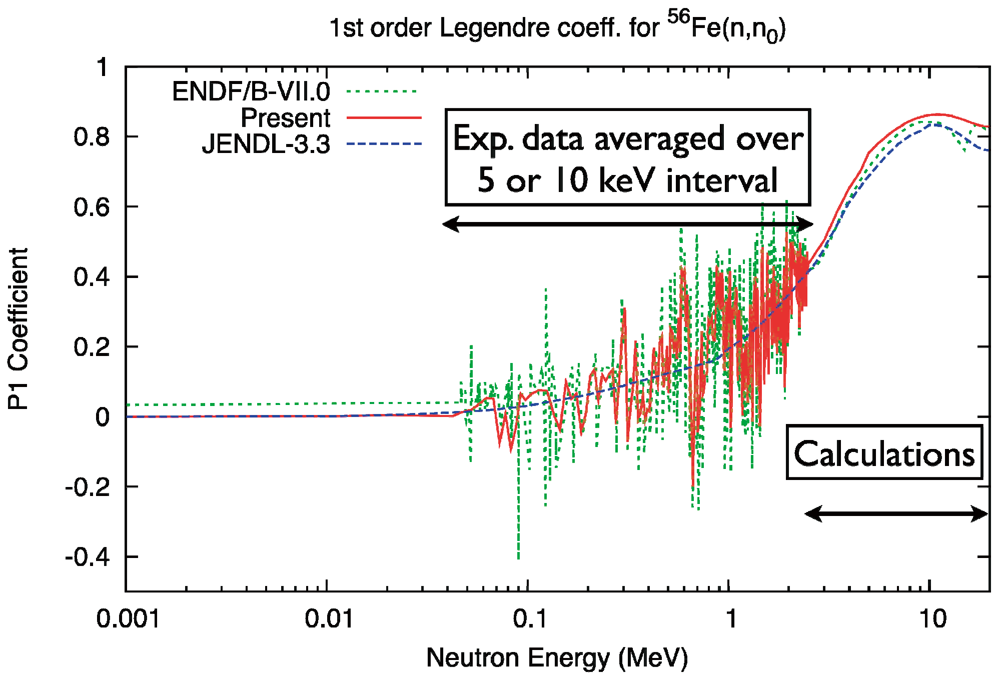

Fig. 3 1st order Legendre coefficient of elastic angular distributions for ^{56}Fe was modified below 200 keV, since the shielding benchmark results indicated[9] the problem of the cross section.

The total cross sections of ^{63,65}Cu in JENDL-3.3 were replaced with the measurements by Pandey *et al.*[10] in the energy region from 50 keV to 1.1 MeV. The experimental data contains more resonances than JENDL-3.3. The angular distributions of neutrons elastically scattered from ^{63,65}Cu were calculated using the coupled-channel optical model parameters obtained by Kunieda *et al.* [5] The newly calculated distributions reproduce available experimental data better than JENDL-3.3.

The ^{52}Cr data of JENDL-3.3 has a problem: big background cross sections were placed so that the total cross sections reconstructed from the resolved resonance parameters could reproduce the measured total cross section of elemental Cr. To solve the problem, the resonance parameters of ^{52}Cr were taken from JEFF-3.1 up to 855 keV. Concerning the elastic angular distribution, the Legendre coefficients were taken from JEFF-3.1 in the energy region from 1 keV to 855 keV. Above 855 keV, the distributions were calculated with the POD code using the coupled-channel optical model parameters of Kunieda *et al.*

4. Light Nuclei Data

We decided to adopt the ^{1}H data of ENDF/B-VII.0 for JENDL-4, since they were evaluated under the IAEA coordinated research program and regarded as reliable. Frankly speaking, the difference in the elastic scattering cross section between ENDF/B-VII.0 and JENDL-3.3 is so small that it is almost impossible to judge which one is better by comparing with experimental data. However, the ^{1}H cross section of ENDF/B-VII.0 is a standard, and this most important standard should be common to major libraries. The ^{2}H cross sections were calculated[11] with the Faddeev theory using the phenomenological nucleon-nucleon potentials. It was pointed out that the angular distributions of neutrons elastically scattered from ^{2}H might affect the criticality of the reactors with heavy-water soluble fuel.

Total and elastic scattering cross sections and elastic angular distributions for ^{16}O were re-evaluated with the R-matrix theory below 3 MeV. Figure 4 shows the total cross section of ^{16}O in the energy region from 1 to 100 keV. The present evaluation reproduces the experimental data better than JENDL-3.3.

In the present work, the thermal scattering cross section increased to 3.841 b from 3.780 b in JENDL-3.3.

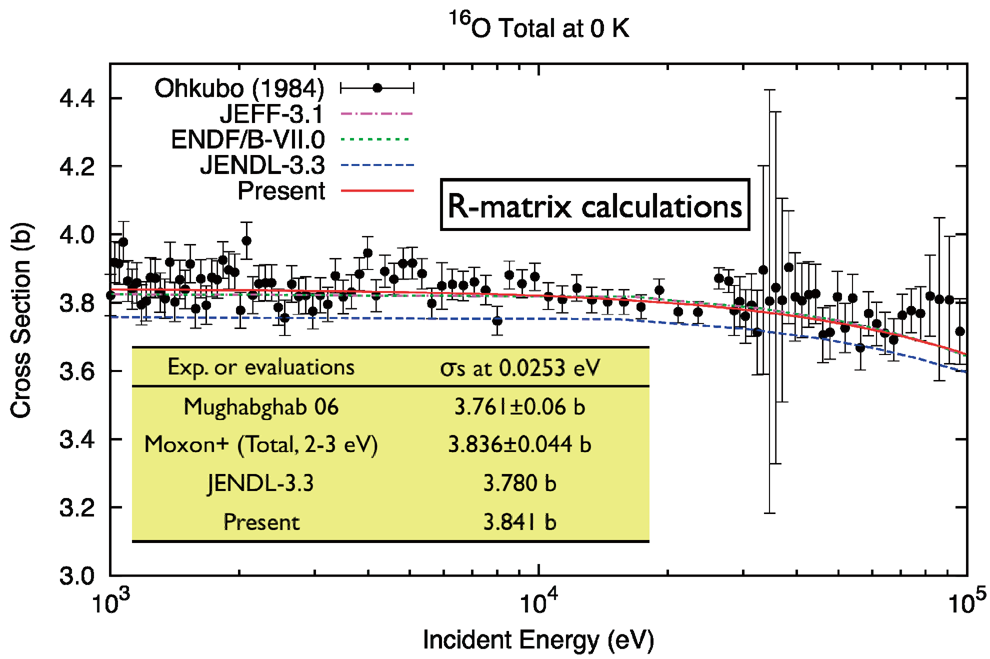

Fig.4 Total cross section of ^{16}O

The total cross section of ^{9}Be was modified below 900 keV in order to improve the predicted criticality of the fast reactors with a beryllium moderator or reflector. The $^{10}B(n,t)2\alpha$ cross section is being examined[11)], since the reaction plays a significant role of estimating tritium production in PWR.

5. Fission Product Yield Data

Fission product yields were taken from ENDF/B-VII.0 with some modifications[12)]. We considered ternary fission producing light nuclei from H to Li. Moreover, the number of FP nuclides coincides with that of JENDL FP Decay Data File 2000[13)].

6. Concluding Remarks

JENDL-4 is being developed. As for actinide data, JENDL/AC-2008 was released on schedule. Covariances of actinide data are being estimated, and further re-evaluation is going on. Smooth cross sections for FP have been calculated with the statistical model codes. The data for light nuclei and structural materials were partly re-evaluated. Fission product yield data were replaced by the ENDF/B-VII.0 data with some modifications.

References

1) O. Iwamoto: *J. Nucl. Sci. Technol.*, **44**, 687 (2007).
2) A. Ichihara *et al.*: JAEA-Data/Code 2007-012 (2007).
3) O. Iwamoto *et al.*: Submitted to *J. Nucl. Sci. Technol.*
4) A.J. Koning and J.P. Delaroche: *Nucl. Phys.*, **A713**, 231 (2003).
5) S. Kunieda *et al.*: *J. Nucl. Sci. Technol.*, **44**, 838 (2007).
6) N. Iwamoto: Private communication (2008).
7) C.M. Perey *et al.*: Proc. Int. Conf. Nuclear Data for Science and Technology, Jülich 1991, p. 41 (1992).
8) W.E. Kinney and J.W. McConnell: Proc. Int. Conf. Interactions of Neutrons with Nuclei, Lowell 1976, p.1319 (1976).
9) C. Konno *et al.*: Proc. 2007 Symposium on Nuclear Data, Tokai, Nov. 29-30, 2007, JAEA-Conf 2008-008, p.103 (2008).
10) M.S. Pandey *et al.*: *Phys. Rev.*, **C15**, 600 (1977).
11) S. Chiba: Private communication (2008).
12) J. Katakura: Private communication (2008).
13) J. Katakura *et al.*: JAERI 1343 (2001).

3. JENDL Actinoid File 2008

O. Iwamoto,[1,*], T. Nakagawa[1], N. Otuka[1,2], S. Chiba[1], K. Okumura[1], G. Chiba[1]
[1] Japan Atomic Energy Agency, Tokai-mura, Ibaraki 319-1195, Japan
[2] International Atomic Energy Agency, Wagramer Straße 5, A-1400 Wien, Austria
[*] iwamoto.osamu@jaea.go.jp

Abstract

The JENDL Actinoid File 2008 (JENDL/AC-2008) was released in March 2008. The file includes neutron reaction data for 79 actinoids from Ac to Fm. The data for 62 actinoids in JENDL-3.3 were revised. Data of 17 nuclides whose half-lives are longer than 1 day were newly evaluated. The neutron energy range is from 10^{-5} eV to 20 MeV. Covariances for the JENDL/AC-2008 are under evaluation. The covariance data for the fission and capture cross sections and the number of neutrons per fission are planned to be prepared for important nuclides in JENDL/AC-2008. In this paper the evaluation methods and results are presented with preliminary results of covariances.

1 Introduction

The actinoid nuclear data in JENDL-3.3[1] were re-evaluated taking account of new experimental data and using a new theoretical model calculation code. In addition to those nuclides, new 17 nuclides whose half-lives are longer than 1 day have been newly evaluated. The evaluated data were compiled to ENDF-6 formatted files and released as the JENDL Actinoid File 2008 (JENDL/AC-2008) in March 2008. JENDL/AC-2008 is intended to improve qualities of nuclear data for minor actinoids (MA) as well as major ones. The nuclides in JENDL/AC-2008 are listed in Table 1 indicating their priorities for evaluation.

It is planned that the JENDL/AC-2008 covariance files will include covariance data at least for the fission and capture cross sections, and the number of neutrons per fission. The covariances will be evaluated basically using the same methods as the JENDL-3.3 covariance evaluation. An overview of evaluation methods and results are presented with preliminary results of covariance evaluation for JENDL/AC-2008 in the following sections.

Table 1: Nuclides in JENDL/AC-2008.

	A	B	C	D	E(new)
Ac				225, 226, 227	
Th	232		228, 229, 230	227, 233, 234	231
Pa			231, 232, 233		229, 230
U	233, 235, 238	232, 234, 236	237		230, 231
Np		237	236, 238, 239	235	234
Pu	239, 240, 241	242	238, 244	236, 237, 246	
Am	241, 243	242m	242	244, 244m	240
Cm		242, 244, 245	243, 246, 247,248, 250	240,241,249	
Bk			247	249, 250	245, 246, 248
Cf			249, 250	251, 252, 254	246, 248, 253
Es				254, 255	251, 252, 253,254m
Fm				255	

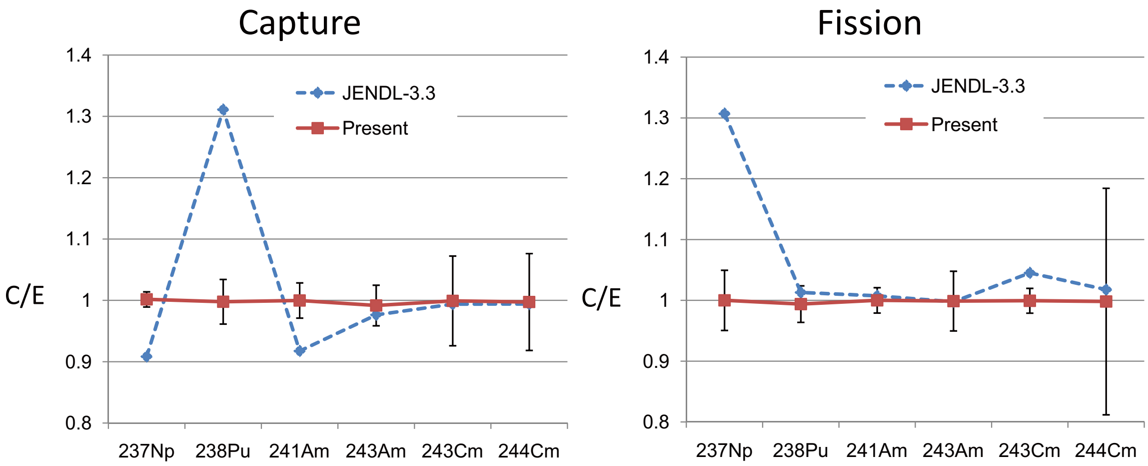

Figure 1: C/E values of thermal capture and fission cross sections. The C/E values represent the ratio of averaged experimental data and calculated values from resonance parameters. The error bars around C/E=1 indicate experimental errors estimated by averaging.

2 Resonance parameters

Prior to the evaluation of resonance parameters, thermal cross sections for fission and capture reactions were estimated by averaging over experimental data with suitable weights depending on their measured years.

The negative and low-lying resonance parameters in JENDL-3.3 were adjusted to reproduce those thermal cross sections. JENDL-3.3 resonance parameters were checked for reproducibility of experimental data and revised to agree with them. Thermal capture and fission cross sections of JENDL/AC-2008 and JENDL-3.3 were compared in Fig. 1. The cross sections calculated from the resonance parameters (C) in JENDL/AC-2008 agree with experimental data (E). The thermal cross sections are largely changed from JENDL-3.3 for ^{237}Np, ^{238}Pu, ^{241}Am capture and ^{237}Np fission reactions.

Newly analyzed resonance parameters[2, 3, 4, 5] were taken from ENDF/B-VII[6] for major nuclides of ^{232}Th, ^{233}U, ^{238}U and ^{241}Pu. For ^{239}Pu, recently revised resonance parameters by Derrien[7] were adopted.

3 Fission cross section evaluation with GMA code

Fission cross sections for 25 nuclides, whose experimental data were available, were evaluated with GMA code[8, 9]. The experimental data were mainly adopted from the EXFOR database[10]. Ratio data to the ^{235}U or ^{239}Pu fission cross sections were normalized by data of JENDL-3.3. Statistical and systematic errors were carefully checked, and suitable errors were assumed if necessary.

Fission cross section for ^{243}Cm are shown in Fig. 2. The present result and JENDL-3.3 evaluation are indicated by solid and dashed lines, respectively. Experimental data are plotted using various symbols. Errors (standard deviation) of the cross section deduced by GMA calculation are shown by doted line. The present results agree with JENDL-3.3 within one standard deviation except 40 keV to 1 MeV, where JENDL takes intermediate values of the inconsistent experimental data. The errors and correlation matrix of the ^{243}Cm fission cross section are shown in Fig. 3. The errors were estimated to be 2 to 5 % below 7 MeV. Above 10 MeV the errors were increased to 10 % because of insufficient experimental data. The rather strong

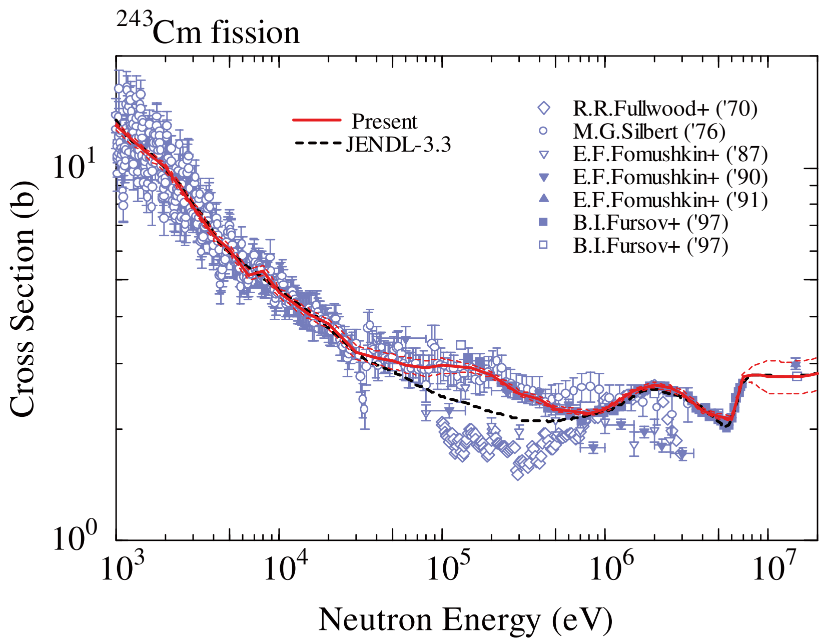

Figure 2: Fission cross section for ^{243}Cm

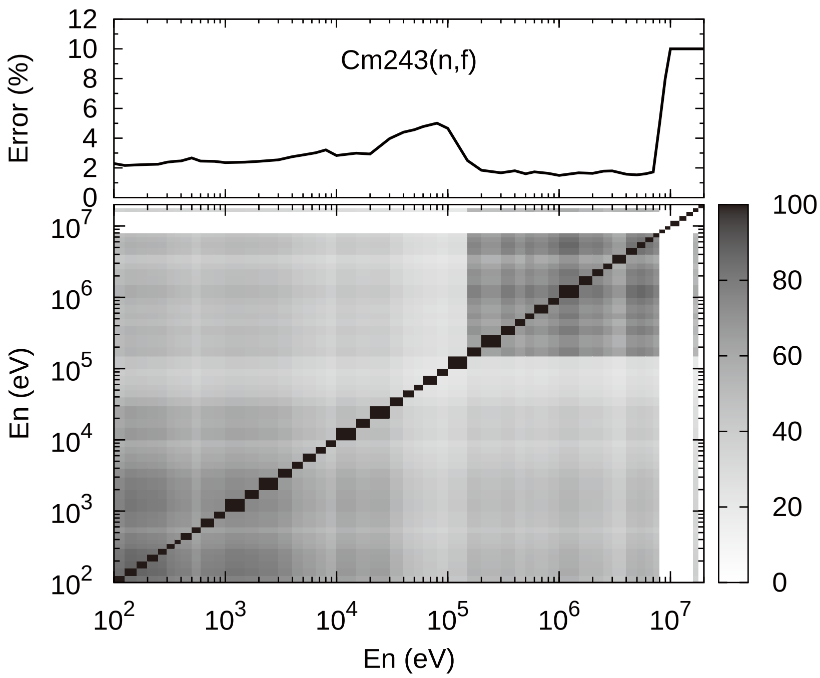

Figure 3: Errors and correlation matrices for fission cross sections of ^{243}Cm.

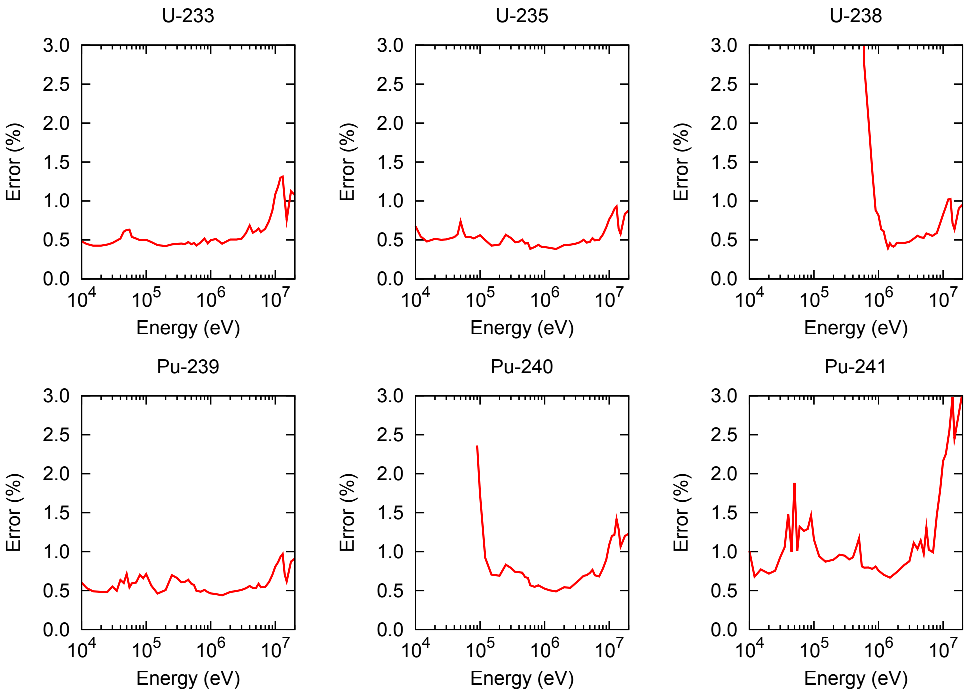

Figure 4: Errors (standared deviations) of fission cross section by the simultaneous evaluation.

correlations are seen from 200 keV to 7 MeV and weak correlations exist in all energies where experimental data exist.

4 Simultaneous evaluation of fission cross sections

In the simultaneous evaluation, cross sections are estimated taking account of both of absolute and ratio data simultaneously. For JENDL-3.3, fission cross sections of 6 isotopes (^{233}U, ^{235}U, ^{238}U, ^{239}Pu, ^{240}Pu and ^{241}Pu) were evaluated by this method using the SOK code (Simultaneous evaluation on KALMAN)[11, 12].

In the JENDL/AC, fission cross sections of these nuclides were evaluated for the same nuclides but extending their energy range. The data in the EXFOR database were mainly used and the data sets were carefully selected. In the present evaluation, totally 124 data sets were used.

Figure 4 shows errors (standard deviation) of the evaluated cross sections. The errors are below 1 % at most energies for all isotopes except at sub-threshold region of fission for ^{238}U and ^{240}Pu. Correlation matrices obtained by the SOK are shown in Fig. 5 for ^{233}U and ^{235}U. Rather strong positive correlations are seen for the same energy points between of the different nuclides. Weak correlations are distributed in wide energy regions for all nuclides.

5 Calculations with CCONE code

A new theoretical model calculation code CCONE[13] was widely adopted to calculate cross sections and emission spectra for JENDL/AC-2008. In the CCONE calculation, direct (couped-channel optical model), pre-equilibrium (exciton model) and compound (Hauser-Feshbach statistical model) reaction processes were taken into account. CC Optical potentials of Soukhovitskii *et al.*[14] and Kunieda *et al.*[15] were used with small modifications. The CC calculations estimate total, shape-elastic scattering and direct inelastic scattering cross sections. Transmission

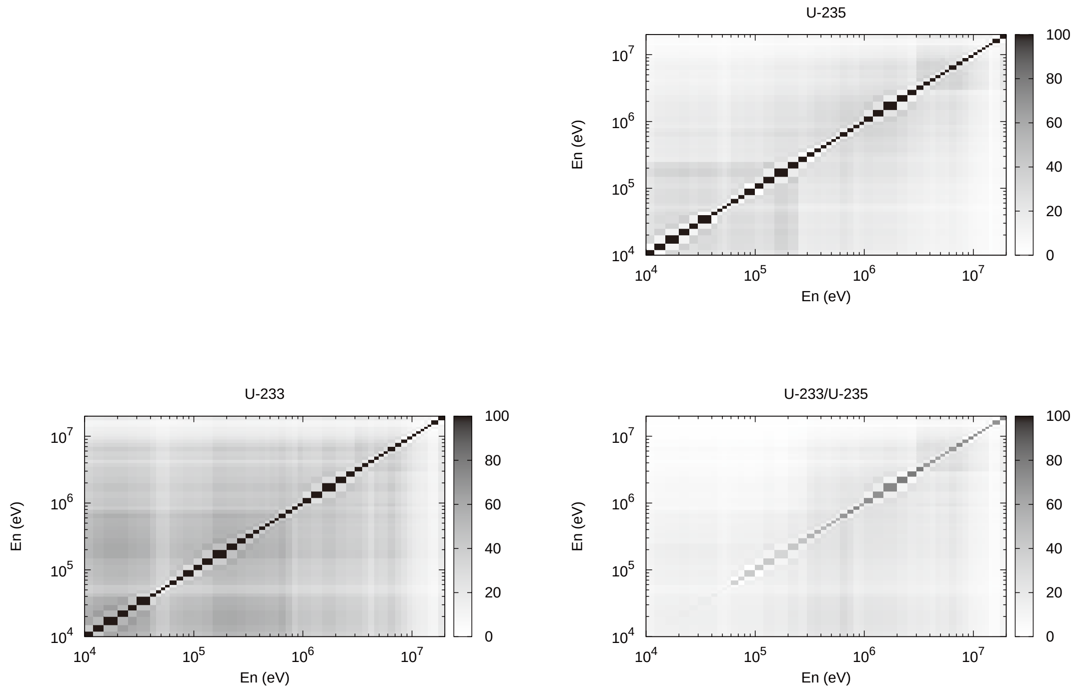

Figure 5: Correlation matrices (positive elements only) of fission cross section obtained by simultaneous evaluation. The left panel shows the correlations for ^{233}U and the right upper panel for ^{235}U. The right lower panel show correlation matrix between ^{233}U and ^{235}U.

coefficients for statistical model calculation were also obtained from the same CC calculations. Double-humped fission barriers were assumed for fission channels in the statistical model. The barrier parameters were adjusted so as to reproduce experimental fission cross sections. In JENDL/AC-2008, the calculated values with CCONE were adopted for various cross sections, angular distributions and double differential cross sections.

KALMAN code[16] will be used for evaluations of covariance data for the cross sections which were calculated by CCONE incorporating with CCONE sensitivity calculations.

6 Conclusion

Nuclear data of neutron induced reactions were evaluated for 79 actinoid nuclides from Ac to Fm in the neutron energy range of 10^{-5} eV to 20 MeV. The evaluated data were released as JENDL/AC-2008 in March 2008. Actinoid nuclear data in JENDL-3.3 were widely revised and 17 new actinoid nuclear data were added. Covariance data for JENDL/AC-2008 are planed to be evaluated in 2009.

Acknowledgments

We are grateful to Dr. Ohsawa for the contributions of the fission neutron spectra of importand nuclides and to Dr. Furutaka for the resonance parameters of ^{236}Np and ^{238}Np.

References

[1] K. Shibata *et al.*: J. Nucl. Sci. Technol vol. 39, p. 1125, 2002.

[2] H. Derrien *et al.*: Proc. PHYSOR-2006, ANS Topical Meeting on Reactor Physics, Sep. 10–14, 2006, Vancouver, BC, Canada, B071, 2006.

[3] L.C. Leal *et al.*: "R-Matrix Resonance Analysis and Statistical Properties of the Resonance Parameters of ^{233}U in the Neutron Energy Range from Thermal to 600 eV", ORNL/TM-2000/372, 2001.

[4] H. Derrien *et al.*: Proc. International Conference on Nuclear Data for Science and Technology, Sep. 26 – Oct. 1, 2004, Santa Fe, New Mexico, USA, p. 276, 2004.

[5] H. Derrien *et al.*: Nucl. Sci. Eng., vol. 150, p. 109, 2005.

[6] M.B. Chadwick *et al.*: Nucl. Data Sheet, vol. 107, p. 2931, 2006.

[7] H. Derrien, L.C. Leal, N.M. Larson: Proc. International Conference on Nuclear Data for Science and Technology, Nice, France, Apr. 22–27, pp. 667-670, 2007.

[8] W.P. Poenitz: Proc. Conference on Nuclear Data Evaluation Methods and Procedures, Sep. 22–25, 1980, BNL, New York, USA, BNL-NCS-51363 vol. I, pp. 249–285, 1980.

[9] S. Chiba, D.L. Smith: "A Suggested Procedure for Resolving an Anomaly in Least-Squares Data Analysis Known as Peelle's Pertinent Puzzle and the General Implications for Nuclear Data Evaluation", ANL/NDM-121, 1991.

[10] O. Schwerer *et al.*: "Nuclear Reaction Data Centre Network: A success story", Proceedings of International Conf. Nucl. Data for Science and Technology, Santa Fe, USA, Sep. 26 – Oct. 4, 2004 (AIP-769), pp. 83-86, 2005.

[11] T. Kawano *et al.*: "Evaluation of fission cross sections and covariances for ^{233}U, ^{235}U, ^{238}U, ^{239}Pu, ^{240}Pu, and ^{241}Pu", JAERI-Research 2000-004, 2000.

[12] T. Kawano *et al.*, J. Nucl. Sci. Technol. vol. 37, p. 327, 2000.

[13] O. Iwamoto: J. Nucl. Sci. Technol., vol. 44, p. 687, 2007.

[14] E. Sh. Soukhovitskii, R. Capote, J. M. Quesada *et al.*: Phys. Rev. vol. C72, p. 024604, 2005.

[15] S. Kunieda *et al.*: J. Nucl. Sci. Technol. vol. 44, p. 838, 2007.

[16] T. Kawano, K. Shibata: "Covariance Evaluation System", JAERI-Data/Code 97-037, 1997 (in Japanese).

4. Systematic Coupled-channel Optical Model Analysis for Nuclear Data Evaluation

S. Kunieda, S. Chiba, K. Shibata, A. Ichihara O. Iwamoto,
N. Iwamoto, T. Fukahori and E. Sh. Sukhovitskii†

Japan Atomic Energy Agency, Tokai-mura, Naka-gun, Ibaragi-ken 319-1195, Japan
†Joint Institute for Energy and Nuclear Research, 220109, Minsk-Sosny, Belarus

e-mail : kunieda.satoshi@jaea.go.jp

Abstract

A global nucleon optical model potential was estimated for medium- and heavy-nuclei up to 200 MeV. The coupled-channel method based on the rigid-rotator model was employed to deduce optical model potential parameters. The soft-rotator model analysis was also carried out for various even-even nuclei in order to obtain more realistic coupling strengths. The obtained findings will provide a basis for the nuclear data evaluation toward JENDL-4.

1 Introduction

Nuclear data evaluations are now in progress toward the completion of JENDL-4. For incident neutron energies above resolved resonances, the optical model plays an important role since it calculates not only the basic quantities such as the total, total reaction, elastic- and inelastic-scattering cross sections but also transmission coefficients which will be required in the statistical model computations. The key parameter in this model calculations is the optical potential which varies with particles, target nuclei, and collision energies. However, it is difficult to optimize the model parameters for each nucleus because experimental data are scarce or sparse in general except for some major nuclei. Therefore, it is required to derive a global optical potential in order to predict cross sections for various nuclei over a wide energy range. Before now, a lot of studies have been devoted in order to obtain such potential. The most useful one was estimated by Koning and Delaroche [1] which covered $24 \leq A \leq 209$ up to 200 MeV. However, the spherical shape was assumed in their analyses, where a consideration of deformed shapes and the coupled-channel (CC) calculation should give more actual answers. Furthermore, they did the analysis for incident neutrons and protons, separately.

We review our recent CC optical model studies [2, 3] in this presentation. A systematic optical model analysis was carried out for medium- and heavy-nuclei ($26 \leq \quad \leq 92$) over a wide energy range (1 keV - 200 MeV) with CC method based on the rigid-rotator (RRM) model. The functional form of Sukhovitskii and Chiba [4] was employed to obtain the optical potential for neutrons and protons, simultaneously. Global calculations were done with obtained systematic optical potential in order to survey the prediction power for cross sections. The soft-rotator model (SRM) analyses were also performed for various even-even medium- and heavy-nuclei to estimate more realistic coupling strengths. Obtained findings were/will be applied to the nuclear data evaluation for actinoid, bulk of fission product and structural material nuclei toward JENDL-4.

2 Systematic Optical Model Analysis

The collective motions of a target nucleus are ascribed to rotation and/or vibration in general. At first, the coupled-channels method based on RRM was uniformly adopted as an initial approach to simplify the problem. The functional forms of Sukhovitskiĩ-Chiba [4] were used to express the energy-dependent optical potential depths. They are written as follows for real volume, imaginary surface and imaginary volume terms, respectively.

$$
\begin{aligned}
{}_{R}(\;{}^{\dagger}) &= \left(\sum_{n=0}^{3} {}_{R}^{(n)}\;{}^{\dagger n} + {}_{R}^{DISP}\;{}^{-\lambda_R E^{\dagger}}\right)\left[1 + \frac{1}{{}_{R}^{0} + {}_{R}^{DISP}}(-1)^{Z'+1}\;{}_{viso}\frac{\acute{}\;\;-}{A}\right] \\
&\quad + {}_{coul}\frac{\prime}{A^{1/3}}\;{}_{coul}(\;{}^{\dagger})\;, \qquad (1)\\
{}_{D}(\;{}^{\dagger}) &= \left[\;{}_{D}^{DISP} + (-1)^{Z'+1}\;{}_{wiso}\frac{\acute{}\;\;-}{A}\right]\;{}^{-\lambda_D E^{\dagger}}\frac{{}^{\dagger 2}}{{}^{\dagger 2} + {}_{D}^{2}}\;, \qquad (2)\\
{}_{V}(\;{}^{\dagger}) &= {}_{V}^{DISP}\frac{{}^{\dagger 2}}{{}^{\dagger 2} + {}_{V}^{2}}\;. \qquad (3)
\end{aligned}
$$

The most essential feature of these forms are the considerations of isospin dependence. So they allow us to carry out optical model analyses for incident neutrons and protons simultaneously. Also, the symmetric terms describe major parts of the isotopic variation of potential depths. The symbols † and $'$ denote projectile energy relative to the Fermi energy and the charge number of projectile, respectively. The Coulomb term $_{coul}$ was treated as a minus derivative of the other terms of real volume strength $_R$ with respect to . The values of $_R^{(0-3)}$, $_R^{DISP}$, $_D^{DISP}$, $_V^{DISP}$, $_R$, $_D$, $_{viso}$, $_{wiso}$ and $_{coul}$ were adjustable parameters to be optimized.

Those parameters were searched for together with deformation parameters so as to reproduce experimental data of total, total-reaction, elastic and inelastic scattering cross sections concentrating on some specific nuclei: ^{54,56,58,nat}Fe, ^{58,60,62,64,nat}Ni, ^{63,65,nat}Cu, ^{89}Y, ^{90,92,94,nat}Zr, ^{93}Nb, ^{92,94,96,98,100,nat}Mo, ^{116,118,120,122,124,nat}Sn, ^{182,184,nat}W, ^{197}Au, ^{208,nat}Pb, ^{209}Bi, ^{232}Th and ^{238}U. Note that the spin-orbit terms were taken from those of Koning and Delaroche [1]. The CC computations and parameter searches were done with the OPTMAN code [5] which considered the relativistic kinematics and the relativistic generation of optical potential. The program POD [6] was supplementarily adopted in order to calculate compound elastic scattering cross sections. We obtained a systematic nucleon optical potential which was formulated by simple forms over ranges 1 keV$\leq$ E $\leq$200 MeV and 26 $\leq$ $\leq$ 92. Its validity was surveyed by some global calculations. For example, the calculated s-wave neutron strength functions are shown in **Fig.1** together with experimental data recommended by Mughabghab [7]. The CC calculations reproduce measured data better than the spherical model results.

3 SRM-CC Analysis

It is very important to consider the collective natures of a target nucleus in CC optical model calculation. The natures were expressed just by the rotation of the axial deformed shape in RRM-CC. However, it might be an extreme approach except for typical deformed nuclei, because it confuses with vibrational property. We employed SRM-CC which was expected to treat collective properties of nuclei more precisely. Before now, the model had been applied to nucleon-nucleus interaction studies for some of the major nuclei, and its applicability has been confirmed step by step (see e.g., refs [8, 4, 9, 10]). Now, we are trying to apply the model to various nuclei.

The SRM Hamiltonian parameters were deduced for 63 even-even medium and heavy nuclei. We obtained those values by the low-lying level structure analysis. The level data were taken from the latest versions of the Nuclear Data Sheets. The ground state (G.S.) band, the $_{2}$-vibrational (n_{β_2}=1), -vibrational (= 2) and the octupole negative parity (n_{β_3}=0) bands were considered. The softness and non-axial deformation parameters (and some parameters) can be obtained in this analysis. However, major equilibrium deformation parameters such as $_{20}$ and $_{30}$ can not be deduced just by the level structure analysis. Therefore, the coupled-channels proton scattering analyses were also carried out simultaneously in order to obtain a complete parameter set for each nucleus. **Figure 2** presents the SRM-CC result for ^{152}Sm together with experimental level and proton-scattering data at 65 MeV [11] as an example. Some systematic trends were also seen among the parameters (see Ref [3]). The effective deformations $\langle 0_1^+ | \;_2 | 2_1^+ \rangle$ and $\langle 0_1^+ | \;_3 | 3_1^- \rangle$ were compared with data deduced from the measured electric-quadrupole and -octupole transition probabilities [12, 13] for various even-even isotopes. As for the quadrupole deformation, present results almost correspond with those data except for some anomalous cases as shown in **Fig.3**. According to our preliminary research, SRM-CC can predicts low-energy neutron cross sections better than RRM-CC especially for non-axially deformed ($\sim 30^\circ$) nuclei [3].

4 Sample Applications to Nuclear Data Evaluation

The CC calculations were adopted together with the obtained optical potential to the nuclear data evaluation for JENDL-4. If experimental cross section data were available at least for some energy points, the parameters are slightly modified so as to obtain more complete agreements. **Figure 4** presents the evaluated results of total cross section for ^{159,160}Tb. In this case, some differences are seen among the evaluated data because measured data are scarce. Preset evaluation is expected to be valid since it is predicted with the systematic CC optical model potential. So, it may be useful in the evaluation for bulk of fission product nuclei. Present findings also applied to the evaluation for some of the actinoid nuclei and structural material nuclei for which extremely high accuracy is required. The evaluated neutron scattering differential cross sections are shown in **Fig.5** for ^{238}U together with experimental data [14] as an example. Furthermore, our results will be applicable to high-energy data evaluation up to 200 MeV both for incident neutron and proton reactions.

5 Summary

A systematic CC optical model analyses were carried out for medium and heavy nuclei over an energy range from 1 keV to 200 MeV. The RRM-CC analysis enabled us to describe global tendencies of optical potential by simple functional forms and the systematical parameters. We also adopted SRM-CC for various even-even nuclei in order to obtain more realistic nuclear shape and coupling strengths. The obtained effective deformations almost corresponded with those derived from experimental electric-quadrupole (octupole) transition probabilities except for some anomalous cases. The findings obtained in this work were (will be) useful for the nuclear data evaluation toward JENDL-4.

References

[1] A. J. Koning, J. P. Delaroche, , **A713**, 231 (2003).

[2] S. Kunieda, S. Chiba, K. Shibata, , , **44**, 838 (2007).

[3] S. Kunieda, S. Chiba, K. Shibata, , , EDP Sciences, 2008, pp 227-230.

[4] E. Sh. Sukhovitskii , , **39**(8), 816 (2002).

[5] E. Sh. Sukhovitskii , JAERI-Data/Code 2005-002 (2005).

[6] A. Ichihara , JAEA-Data/Code 2006-025 (2007).

[7] S. F. Mughabghab, M. Divadeenam, N. E. Holden, , Vol.1, Part A, Academic Press, New York (1981); S. F. Mughabghab, , Vol.1, Part B, Academic Press, New York (1984).

[8] E. Sh. Sukhovitskii , , **C62**, 044605 (2000).

[9] E. Sh. Sukhovitskii , , (AIP, Melville, New York, 2005), pp. 1058-1061.

[10] S. Chiba , , **37**(6), 498 (2000).

[11] T. Ichihara, H. Sakaguchi, M. Nakamura, , , **C36**, 1754 (1987).

[12] S. Raman, C. W. Nestor Jr., P. Tikkanen, , **78**, 1 (2001).

[13] T. Kibedi, R. H. Spear, , **80**, 35 (2002).

[14] A. B. Smith and S. Chiba, , **23**, 459 (1996).

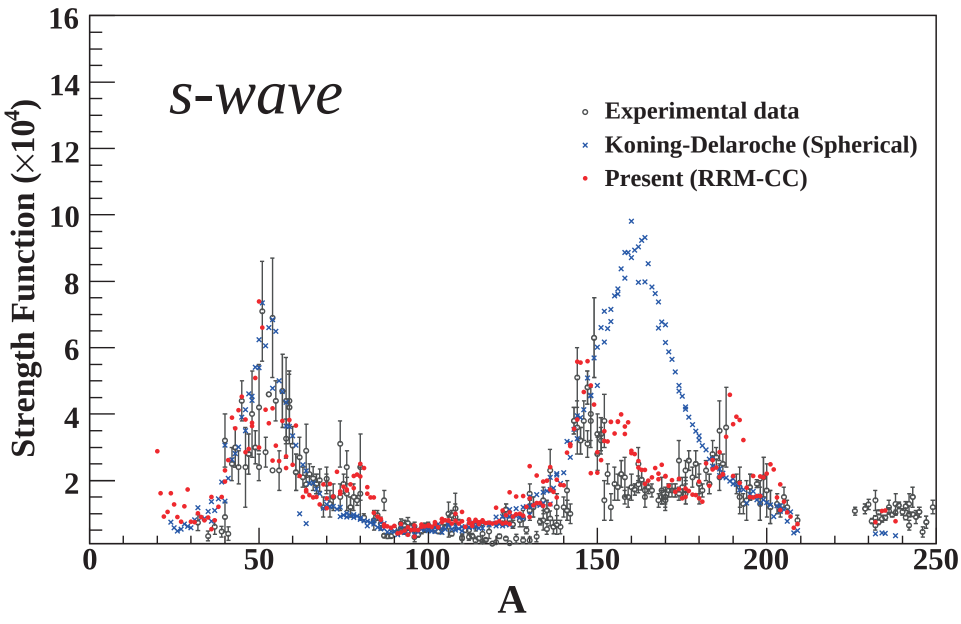

Figure 1: Calculated s-wave strength functions at neutron energy 10 keV, together with experimental data recommended by Mughabghab [7]

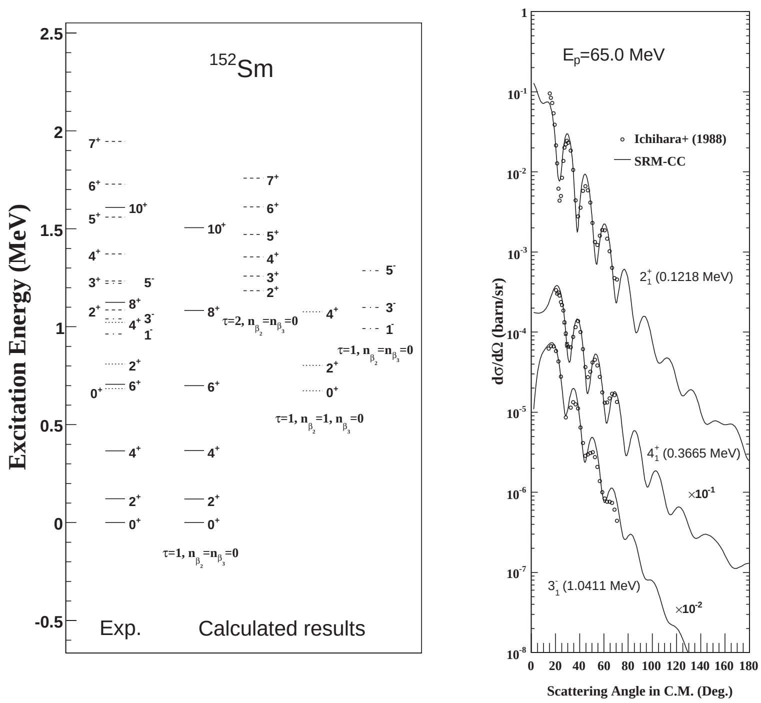

Figure 2: The SRM(-CC) calculations obtained with the present Hamiltonian parameters which are compared to the experimental data for ^{152}Sm: The SRM low-lying level structure together with the experimental one (left) and the SRM-CC differential cross sections of inelastically-scattered protons at 65.0 MeV together with measured ones[11] (right)

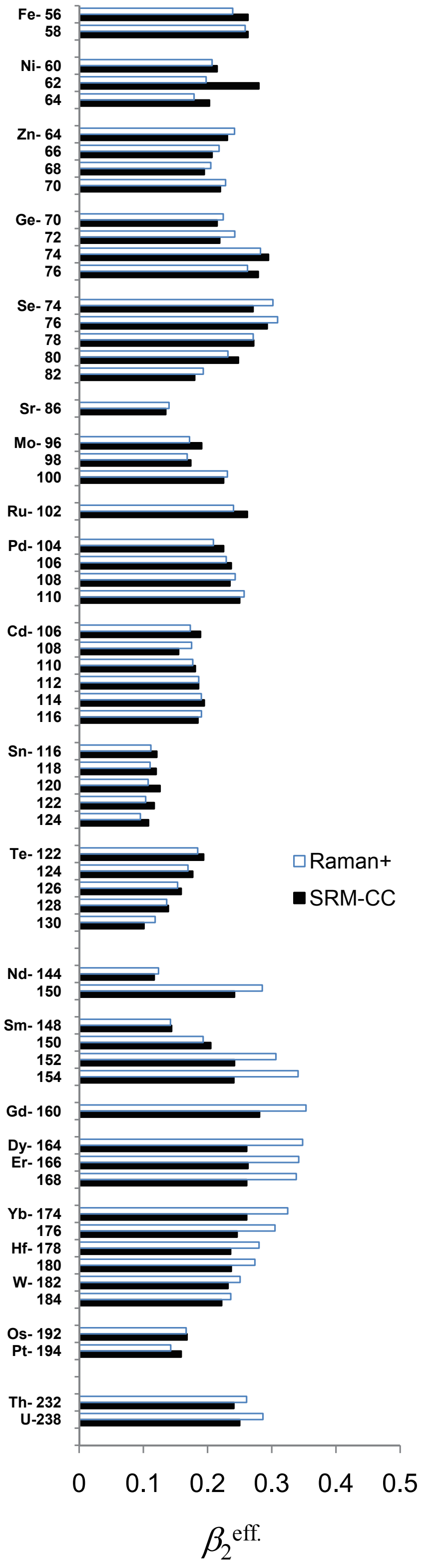

Figure 3: The effective quadrupole deformation parmeter is compared with experimental data compiled by Raman [12].

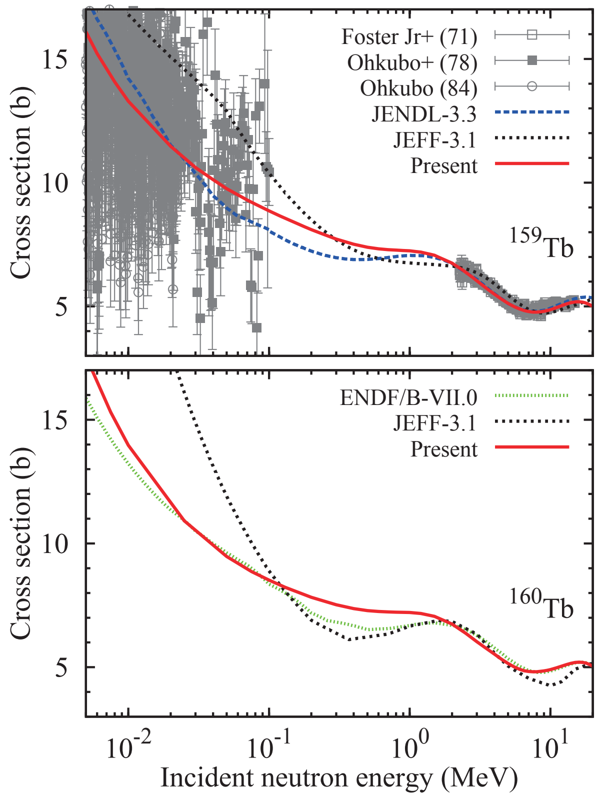

Figure 4: Total cross sections for ^{159,160}Tb.

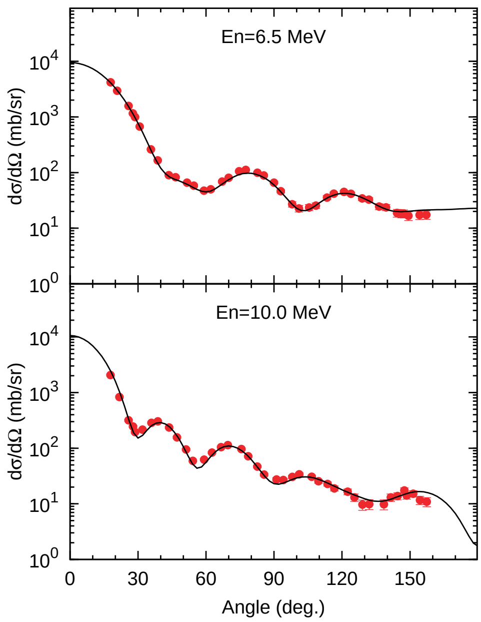

Figure 5: Evaluated neutron scattering differential cross sections (from 0_1^+, 2_1^+, 4_1^+, 6_1^+) for ^{238}U together with measured data [14]

5. Towards the Completion of JENDL-4: Current Status of Integral Test

Go CHIBA and Keisuke OKUMURA
Reactor Physics Group, Japan Atomic Energy Agency
Tokai-mura, Naka-gun, Ibaraki-ken 319-1195
e-mail: chiba.go@jaea.go.jp

We performed benchmark calculations with a test library for JENDL-4 for thermal and fast neutron systems. This test library showed a good performance on neutronic calculations for both the thermal and fast neutron systems. In addition, we estimated an impact of Am-241 capture cross section in a thermal energy range on characteristics of thermal neutron systems, and concluded that the large Am-241 capture cross section in the thermal range is desirable from a view point of an integral testing.

1. Introduction

Currently, a new version of Japanese evaluated nuclear data library, JENDL-4, is under development. Nuclear data for major nuclides have been being re-evaluated with the sophisticated evaluation codes and experimental database. In this development, integral data, such as criticalities of neutron multiplication systems measured through experiments, have been effectively utilized to assess the qualities of the evaluated nuclear data.

In the present paper, we show results of benchmark calculations of a test library for JENDL-4 for thermal and fast neutron systems.

2. Results for thermal neutron systems

For thermal neutron systems, we carry out an integral test with two nuclear data libraries. One is named "JENDL/AC", in which the JENDL actinoid file 2008 [1] is adopted for actinoids and JENDL-3.3 is adopted for other nuclides. The thermal scattering law of the latest ENDF/B-VI file is used for chemically-bound nuclides. The other is "Test 1". This library is almost the same as JENDL/AC except for H-1, O-16 and the thermal scattering law data. In this library, the newly evaluated data for H-1 and O-16 [2] and the thermal scattering law of ENDF/B-VII.0 are adopted. In addition, we also carry out benchmark calculations with the latest released libraries, JENDL-3.3, JEFF-3.1 and ENDF/B-VII.0.

Neutron transport calculations are performed with a continuous-energy Monte Carlo code MVP-II. Utilized integral data are mainly extracted from the ICSBEP handbook.

Figure 1 shows C/E values of criticalities of low-enriched uranium-fueled systems. Underestimations by JENDL-3.3 observed in the integral data, whose enrichments are less than 4wt%, are improved by both JENDL/AC and Test 1. The Test 1 library results in larger C/E values than ENDF/B-VII.0, but these differences are negligible.

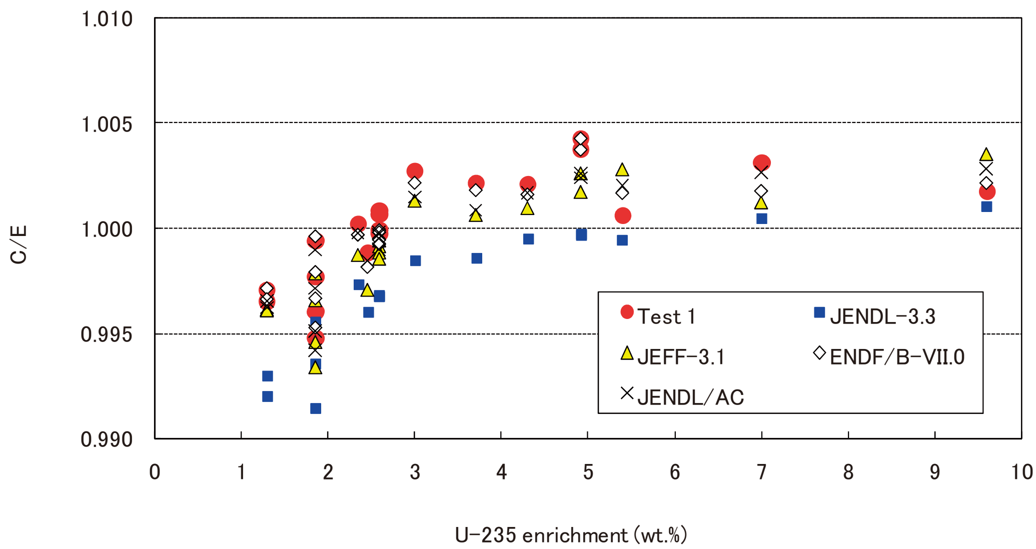

Fig.1 Results of criticality of low-enriched uranium-fueled thermal systems

Figure 2 shows C/E values of criticalities of MOX-fueled systems. For the three integral data, which are the MISTRAL and BASALA data, large C/E values are observed in the ENDF/B-VII.0 results. The reason of this trend is described later. Except for these data, the Test 1 library results in larger C/E values than ENDF/B-VII.0. It is found through a sensitivity analysis that this difference between the two libraries comes from differences in O-16 (P1 coefficient of elastic scattering cross section), Pu-239 and Pu-240 cross sections.

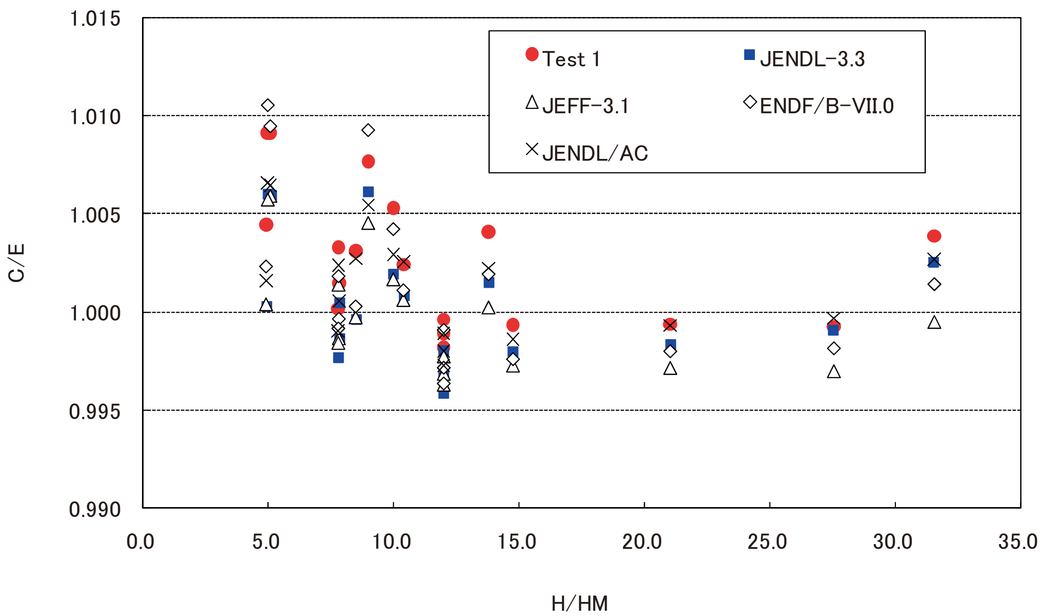

Fig.2 Results of criticality of MOX-fueled thermal systems

There have been several indications on Am-241 capture cross section from other integral tests [3], i.e. Am-241 capture cross sections of the latest released libraries are small in the thermal energy range. Figure 3 compares the Am-241 capture cross sections among the several libraries. Below 0.1eV, JENDL/AC takes larger value than the others. On the other hand, JEFF-3.1 takes larger value than the others in the first and second resonances.

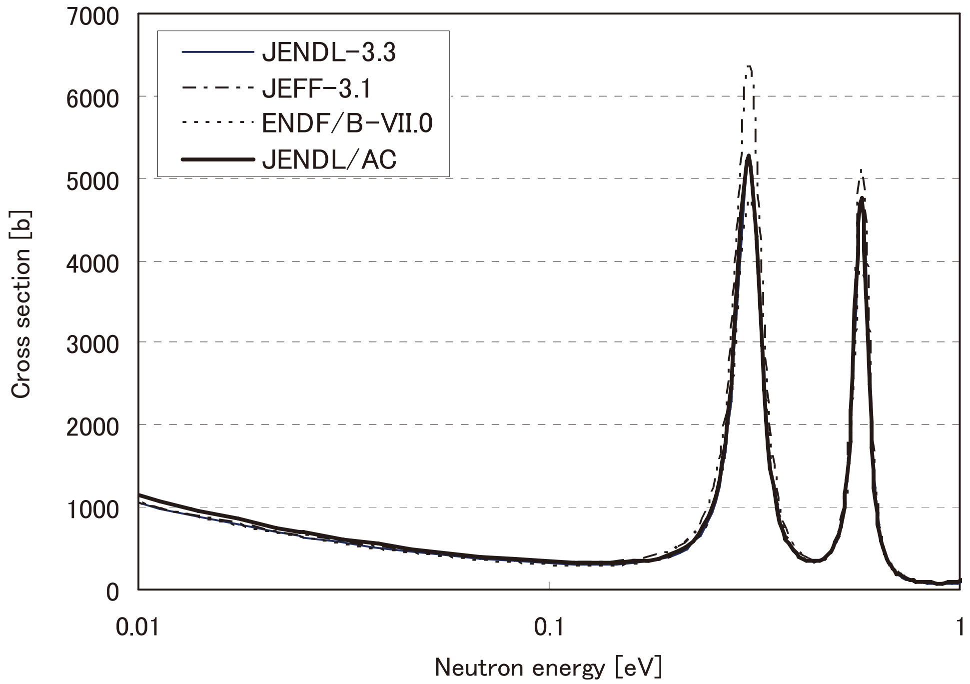

Fig.3 A comparison of Am-241 capture cross sections

In order to estimate an impact of Am-241 capture cross section on thermal system characteristics, we produce an Am-241 test file, in which JENDL/AC is adopted below 0.2 eV and JEFF-3.1 is adopted above 0.2 eV for capture cross section. Figure 4 shows results of the Test 1 library with the Am-241 test file ("Test 2") for the MOX-fueled systems. It is found that the large C/E values observed in the Test 1 results for the MISTRAL and BASALA data become smaller in the Test 2 results because of the large Am-241 capture cross section. It should be noted that JENDL/AC seems to give better C/E values than Test 2. This difference between these two libraries mainly comes from differences in H-1 and O-16 cross sections and the thermal scattering law data. Towards the JENDL-4 completion, we should discuss on this matter.

Figure 5 shows results for a TCA plutonium aging problem. This problem consists of two critical data which have a difference in the dates when experiments were performed. Since Pu-241 has a short half-life (14.4y), compositions of Pu-241 and Am-241 are different between the two critical systems. Differences in C/E values between the two critical systems are 0.22%dk/kk' for JENDL-3.3 and 0.27%dk/kk' for ENDF/B-VII.0. It can be said that these libraries have a bias on prediction accuracy for the plutonium aging effect. On the other hand, the Test 2 library results in a bias of 0.07%dk/kk', which are smaller than the others. The above result supports the large Am-241 capture cross section in the thermal energy range.

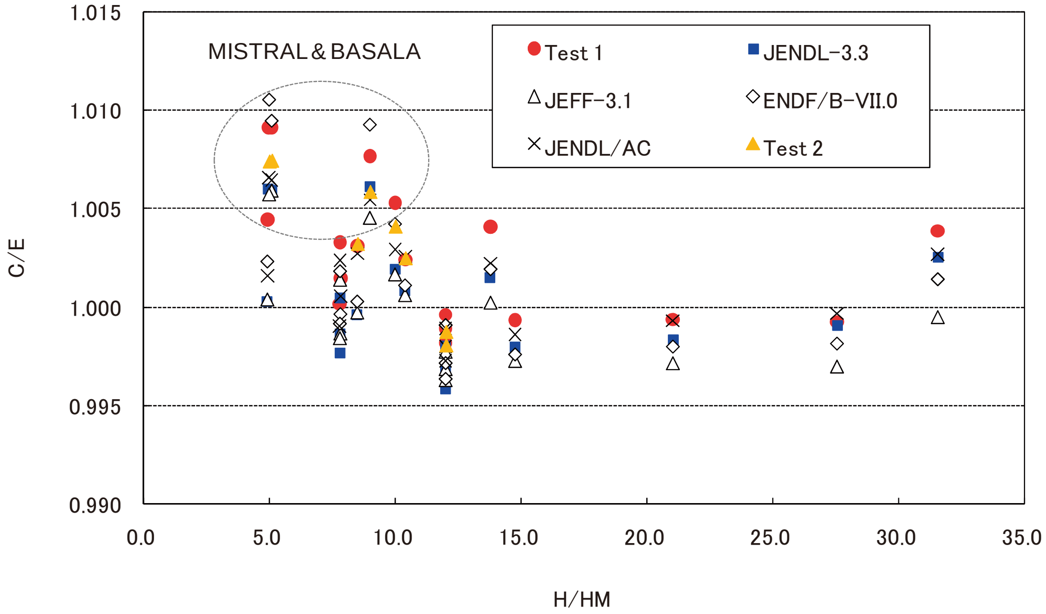

Fig.4 Results of criticality of MOX-fueled thermal systems obtained with Am-241 test file

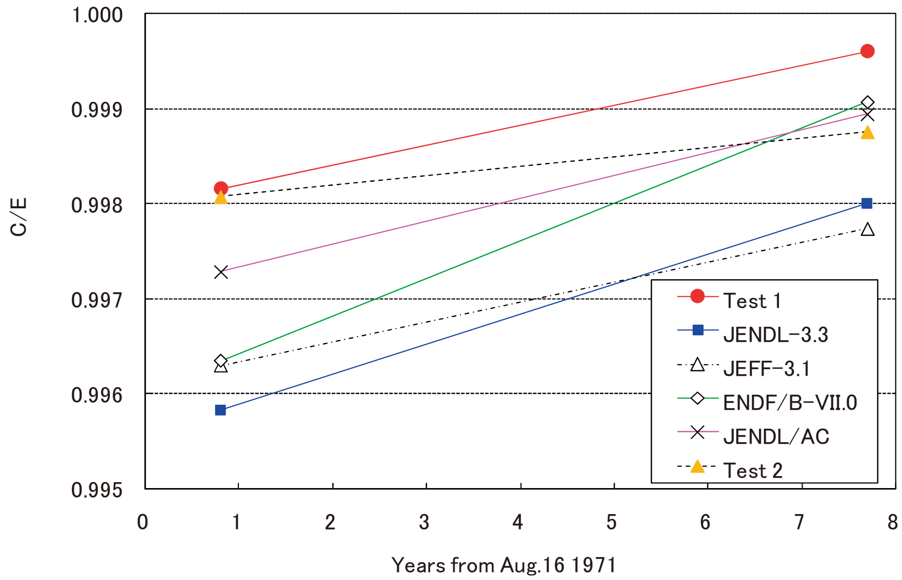

Fig.5 Results of TCA-MOX criticality data

Finally, we show results of a post-irradiation examination analysis for PWR in Fig.6. This analysis is performed with the MVP-BURN code [4]. This figure shows C/E values on nuclide number densities after burn-up. Error bars in this figure indicate the experimental uncertainties. JENDL/AC and Test 2 predict the number densities for Am-241, Cm-243, -244 and -245 much better than the other libraries.

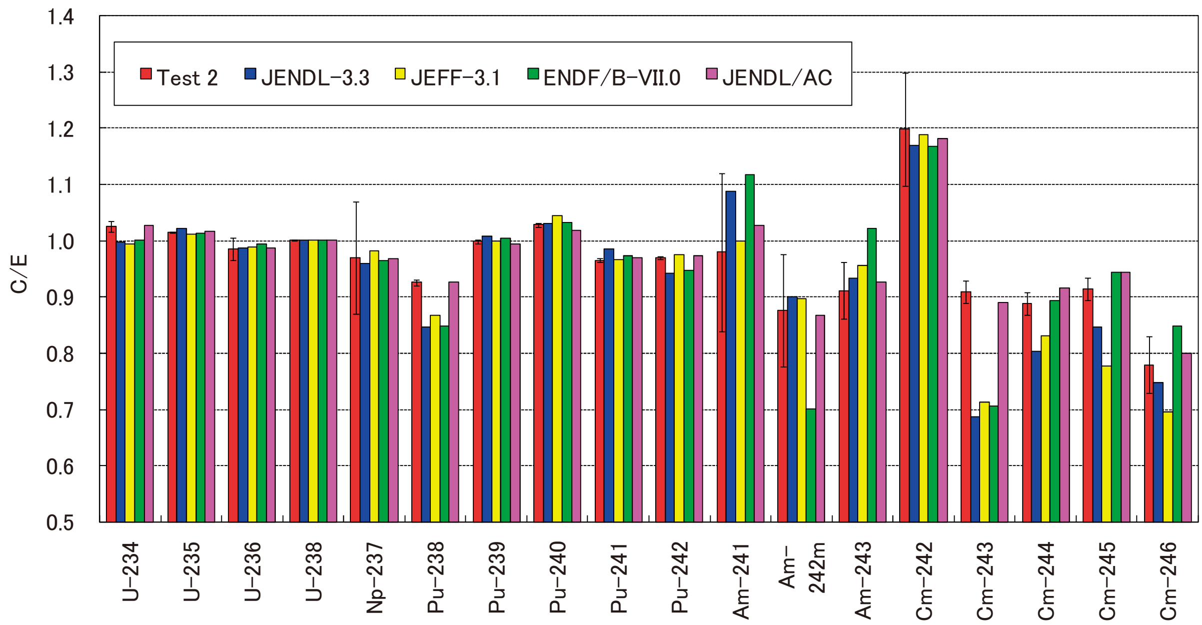

Fig.6 Results of PIE analysis for PWR

3. Results for fast neutron systems

For fast neutron systems, we carry out an integral test with JENDL/AC, together with JENDL-3.3, JEFF-3.1 and ENDF/B-VII.0.

Neutron transport calculations are performed as follows. A unit lattice is simplified into a one-dimensional slab or cylinder. Lattice calculations are performed with a SLAROM-UF code and its library UFLIB, which is composed of a 70-group base library and an ultra-fine energy group library. The resonance self-shielding is treated with the table-look-up method above 50keV. Below 50keV, resonances are treated explicitly with the ultra-fine energy group library. After obtaining 70-group homogenized cross sections, whole-core calculations are performed. For the cores which can be treated by Cartesian mesh, we adopt a neutron transport solver SNT based on the discrete ordinates method. In this calculation, the scattering anisotropy is treated by the transport approximation. In addition, a neutron anisotropic streaming effect is considered. For the BFS-2 cores, a neutron diffusion solver DHEX is utilized. A transport effect, which was evaluated in the previous study [5], is considered.

Figure 7 shows C/E values of criticalities of fast neutron systems. Cores which have a large U-235 contribution to total fission reactions are located in the left side of this figure. A significant U-235 contribution dependence of the C/E values is observed in the JENDL-3.3 result. On the other hand, JENDL/AC predicts the criticalities of the fast neutron systems well regardless of fuel compositions. Since JENDL/AC will be adopted into JENDL-4, JENDL-4 will have the same quality as JENDL/AC in fast neutron system applications. Other integral testing of JENDL/AC has been performed for fast neutron systems and it has provided beneficial information to nuclear data evaluators. Those are described in a reference in detail [6].

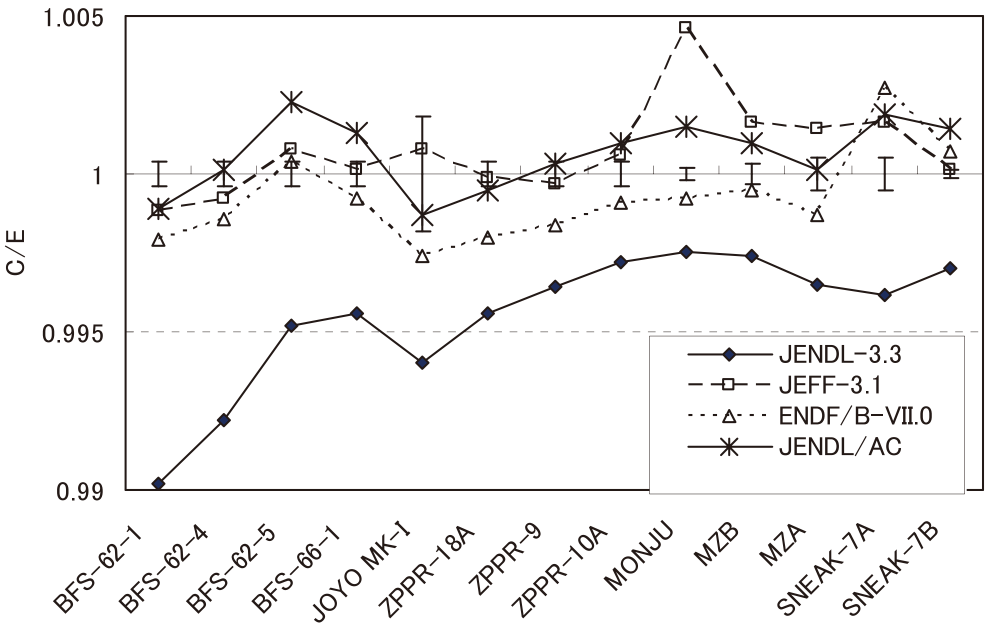

Fig.7 Results of criticality of fast neutron systems

4. Conclusion

We have performed benchmark calculations with a test library for JENDL-4 for thermal and fast neutron systems. This test library has shown a good performance on neutronic calculations for both the thermal and fast neutron systems. In addition, we have estimated an impact of Am-241 capture cross section in the thermal energy range on characteristics of thermal neutron systems, and concluded that the large Am-241 capture cross section in the thermal energy range is desirable from a view point of an integral testing.

Acknowledgment

The authors wish to express their deep gratitude to T. Kugo of Japan Atomic Energy Agency for providing useful comments on this manuscript.

References

[1] O. Iwamoto, et al.: "Development of JENDL Actinoid File," Proc. of Physor2008, Interlaken, (2008).
[2] K. Shibata, private communication (2008).
[3] (For example) T. Yamamoto: "Analysis of Core Physics Experiments of High Moderation Full MOX LWR," Proc. of the 2005 symposium on nuclear data, Tokai, Japan, p.7-13, JAEA Conf 2006-009 (2006).
[4] K.Okumura, et al.: "Verification of a Continuous Energy Monte Carlo Burn-up Code MVP-BURN," J. Nucl. Sci. Technol., 37, p.128 (2000).
[5] M. Ishikawa, et al.: "Development of a standard data base for FBR core nuclear design (VIII)," PNC TN9410 97-099, Power Reactor and Nuclear Fuel Development Corporation, (1997). [in Japanese]
[6] G. Chiba and K.Okumura: "Benchmark Test of Evaluated Nuclear Data Files for Development of JENDL-4," JAEA-Research 2008-089 (2008) .[in Japanese]

6. Thirty Years along with Neutron Nuclear Data

Mamoru BABA
Cyclotron & Radioisotope Center, Tohoku University
Aramaki, Aoba-ku, Sendai 980-8578, Japan
e-mail: babam@cyric.tohoku.ac.jp

A brief review is given on the experimental neutron nuclear data works carried out by author's group during around thirty years. Studies on neutron emission reactions, light- and heavy-charged particle emission reactions will be described as well as development of experimental techniques and neutron source.

1. Introduction

Neutron nuclear data are one of the major data base for development of nuclear energy, i.e., nuclear reactors, fusion reactors and accelerator based systems. In recent days, the data requirement is expanding to a variety of fields from basic to applied science, like, nuclear astrophysics, radiation effect in semiconductors (soft/ hard errors), and medical fields and so on.

Nuclear data are evaluated and established based on the experimental data and nuclear theories. Generally, experimental data play a crucial role because the required accuracy is beyond the prediction of the theory.

From the point of view, the author has been involved in the measurement of nuclear data like double-differential cross sections of neutron emission, light- and heavy-charged particle emission reactions which play an essential role in transport of radiation and energies. We have also paid attention on the development of advanced neutron source, detector and experimental systems which are essential to produce high quality and highly reliable data.

These experiment were mainly carried out in three facilities, Tohoku University (TU) Fast Neutron Laboratory (FNL), JAEA TIARA, and Tohoku University Cyclotron & Radioisotope Center (CYRIC) . The outlines of the facilities are summarized in Table1.

In the following sections, experimental equipment and experiments carried out using them are described for each laboratory together with references.

Table 1 Out line of laboratories used for experiments

Facility	TU Dynamitron	JAEA TIARA	TU CYRIC
Major apparatus	4.5MV Dynamitron	K=110 MeV cyclotron	K=110MeV cyclotron
Beam energy	Ep, Ed < 4.5 MeV	Ep< 90, Ed< 65 MeV, HI	Ep< 90, Ed< 65 MeV, HI
Neutron source Neutron energy	^{7}Li,T(p,n), D,T(d,n) 8keV- 18 MeV	^{7}Li(p,n) 30- 80 MeV	^{7}Li(p,n) 30- 80 MeV
Major apparatus	TOF spectrometer Grid ion chamber Neutron flux monitor	TOF spectrometer Charged particle spectrometer	Beam swinger TOF spectrometer Intense ^{7}Li(p,n) source Automated irradiator

2 Experiments at Tohoku University Fast Neutron Laboratory

2.1 Experimental Equipments and neutron source [1]

TU FNL is equipped with a pulsed electrostatic accelerator, 4.5 MV Dynamitron, a neutron shield-collimator, neutron detectors, γ-ray spectrometers, charged particle spectrometers and various neutron flux monitor for neutron experiments [1].

To carry out neutron works over a wide incident energy range, mono-energy neutron sources were established from 7.8 keV to 18 MeV using various monoenergetic source reactions. Special attention was given to obtain mono-energy neutrons with low backgrounds and low energy spreads. In particular, for 14 MeV neutrons, a special arrangement was developed to use neutrons emitted to ~95-deg as primary neutrons for neutron emission reactions and α-emission reactions. In addition, quasi-monoenergetic neutron source using the ^{14}N(d,n) and ^{15}N(d,n) reactions was newly adopted to obtain mono-energy neutrons for 8-13 MeV region where mono-energy neutrons were missing. Using these neutrons sources, experiments on double-differential cross section (DDX) were carried out for neutron emission and α-production reactions between 0.5 MeV to 18 MeV.

2.2 Neutron emission DDX [2-5]

Neutron emission DDXs were measured for about thirty nuclides from ^{6}Li, ^{7}Li to ^{238}U, in incident energies from 0.5 MeV to 18 MeV. Measurements allover the spectrum with good energy resolution and signal-to-background ratio was intended to clarify the spectrum shape and its angle dependence. For the purpose, the neutron spectrometer was designed to cover an energy range from ~0.3 MeV to ~20 MeV using a two-bias technique. This technique could be applied to the measurement of fission spectrum [3].

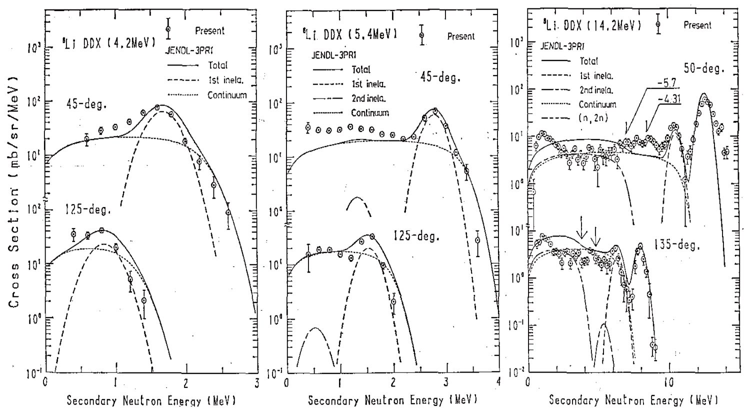

Fig.1(a): DDX data of ^{6}Li together with modeling [2]

Typical example of neutron emission DDX is shown in Fig.1(a)(^{6}Li) and 1(b) (^{238}U). These data proved to be very useful too to verify the spectrum shape of continuum inelastic scattering as shown in Fig.1. The data in FNL contributed significantly to improve the neutron scattering and emission data in JENDL.

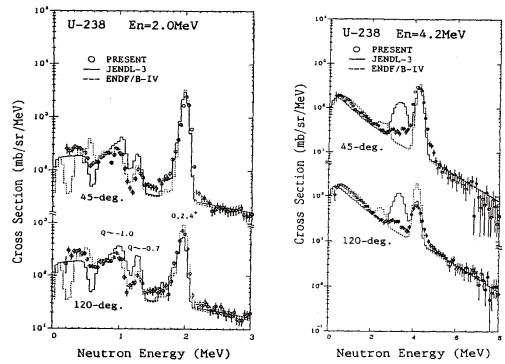

(b) 2.0 MeV (c) 4.2 MeV

Fig.1 (b) DDX of ^{238}U [3]

2.3 α-production DDX [6-8]

The data of α–production cross section and its energy-angular differential cross sections are required with high priority for estimation of radiation effects by helium accumulation and recoil effects. However, in early 1990s, there were large discrepancies among current evaluated data because of lacks of experimental data and ambiguity in the theoretical calculation. To improve the situation, reliable experimental data are highly required.

For charged particle detection, usually, a conventional counter-telescope had been used. However, in the case of α–production reactions, another technique with large geometrical efficiency and low energy loss looked desirable because of large stopping power and smaller production cross sections of α–particles.

Figure 2 illustrates a schematic view of the gridded-ionization chamber (GIC) developed for α–production reactions for the purpose. In this detector, a thin sample placed on the cathode is bombarded by neutrons and α-particles emitted are detected by twin gridded chamber with very large solid angle close to 4π. Furthermore, the signals from the anode and the cathodes are proportional to the energy and the product of energy and function of emission angle, respectively. Therefore, if the α-particles are stopped before grid, the energy and angle can be known from these data. The α-particles can be identified by using the difference in stopping power. The structural elements and counting gas consisted of high-Z elements to suppress charged particle background from the chamber.

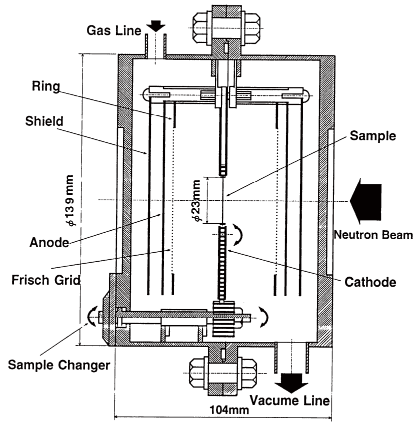

Fig.2: Schematic view of GIC [6]

GIC was employed very effectively for the (n,xα) cross section measurement of Cr, Fe, Ni, Cu, C, and O for 4 – 14 MeV [6,7], and the ^{14}N(n,p) reaction for 23 keV neutrons [8]. The measurement for C and O were done with gas samples taking advantage of the signal property of GIC. These data also contributed to the improvement of α-production data.

3. Experiments in JAERI TIARA [9-12]

The experiment in TIARA was conducted under the framework of the JAERI(JAEA)-universities joint collaboration program on the neutron shielding using a quasi-monoenergetic neutron beam produced by a newly installed ^{7}Li(p,n) source. Under the program, 1)source characterization, 2)calibration and characterization of neutron detectors, 3)shielding benchmark experiment, 4)cross section measurement relevant to the shielding, were carried out. Here, items 1) and 4) are described.

3.1 Characterization of the ^{7}Li(p,n) source [9]

The ^{7}Li(p,n) reaction is the most prominent mono-energy neutron source above ~30 MeV although it is not purely mono-energetic due to continuum neutrons. This source were used extensively in various laboratories, but its intensity and spectrum were not known satisfactorily. Therefore, we first intended to determine the neutron intensity and the spectrum of continuum neutrons using a proton-recoil telescope (PRT) which was most reliable device above 20 MeV. Then we developed PRT with annular geometry to achieve high efficiency and low background. Using the PRT, the intensity of peak neutrons, neutron production cross section and the shape of the continuum neutrons were determined. Besides, the detector efficiency of liquid scintillation counter and others were also determined [9] for shielding experiments.

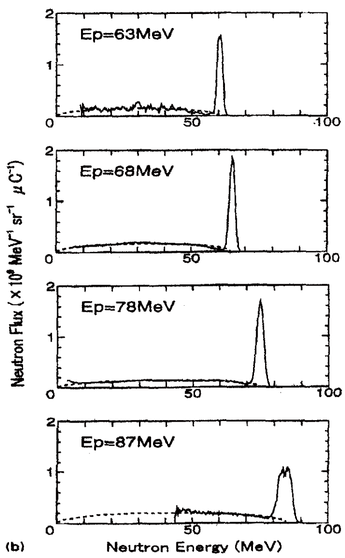

Fig.3(a): ^{7}Li(p,n) spectra

3.2 Cross section studies [10-12]

Using the source, (n,α) cross section measurement in FNL was extended to higher energy region and to p, d, t, α production reactions in 50 to 75 MeV regions [10,11]. To compensate limited neutron flux in TIARA (< 5 x 10^4 ncm^{-2}s^{-1}), a charged particle detector system consisting of three sets of large-solid angle three-elements-telescope (proportional counter, Si SSD, BaF_2 scintillator) was developed. Using these detectors, DDXs data were obtained for C, Al, Fe, Ni (n,xp,d,t,α) reactions [10,11].

Besides, neutron elastic scattering cross sections were also studied using the conventional TOF technique in the energy region from 55 to 75 MeV for C, Si, Fe, Zr and Pb [12]. Taking advantage of a well collimated neutron beam, the measurement was extended to an extremely forward angle of 2.5. The experiments provided new high quality data in the energy region where only very few data with limited precision were available and contributed to examine the optical model potentials and scattering models. They pointed out the problem of the systematics in the neutron angular distribution used in the neutron transport codes [12].

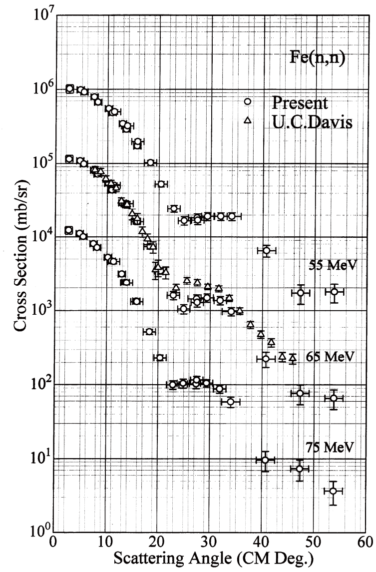

Fig.3(b): Neutron elastic scattering cross sections [12]

4. Experiments at TU CYRIC [13]

4.1 Experimental apparatus and neutron source development

The AVF cyclotron in CYRIC is the same type with that in TIARA, but equipped with a beam swinger system and a well collimated neutron flight path, which enables angular distribution measurements with a fixed neutron detector system [13]. This system can be used as a ^{7}Li(p,n) neutron source for neutron induced reaction, but the neutron intensity was limited in the order of 10^4 n cm^{-2} s^{-1} because of relatively long distance (~3 m) between the target and experimental position. To obtain higher neutron flux, a new ^{7}Li(p,n) source was installed by adopting a different configuration to shorten the collimator thickness and achieved a neutron flux up to 10^7 n cm^{-2} s^{-1} which is the highest over the world at present [14]. This source proved to enables measurements of nuclear data with small cross sections and irradiation test of DRAM-type semiconductors which is relatively insensitive to the radiation effect [14].

In addition, activation by proton and deuteron can be studied by use of an automated irradiation system and stacked target technique. This system produced a plenty of activation data for production of radio isotopes useful for engineering and medical purposes with proton and deuteron beams.

4.2 Neutron emission spectra for (p,xn), (d,xn) reactios

Energy-angular neutron emission spectra for proton and deuteron induced reactions are basic nuclear data for the design of accelerator shielding and accelerator-based neutron sources. For these purposes, neutron emission spectrum data are required over the emission spectrum but past data were limited in both energy angular range. In the present study, neutron spectra for thick targets (TTY) were measured from the maximum neutron energy (~ 80 MeV) down to around 1 MeV employing a two-bias and two-flight path technique [15]. TTY data were obtained for Li, Be, C, Al, Fe, Cu, Zr, Ta, W(p,n)

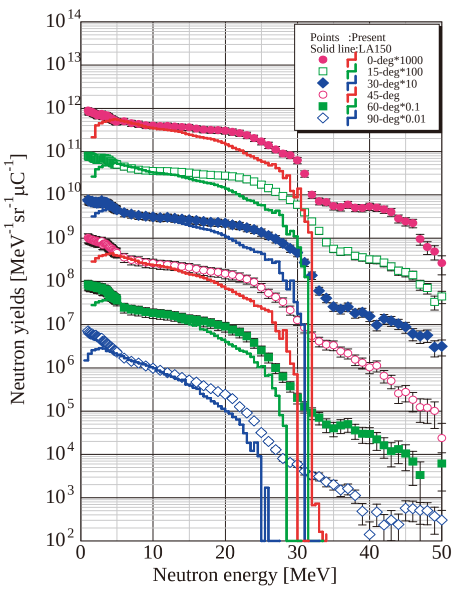

Fig.4(a): TTY of C(p,n) reaction [15]

reactions [15], and Li, Be, C, Fe, Cu(d,n) reactions [16,17]. Figure 4(a) illustrates an example of TTY. Data for thin target were also obtained for some cases to study the reaction mechanism. The data for (d,n) reaction provided a unique data base for IFMIF (International Fusion Materials Irradiation test Facility) which utilizes Li(d,n) reactions for neutron production. The present data clarified the spectrum shapes up to the high energy end which is important to estimate neutrons irradiation effects in IFMIF.

4.3 Fragment production cross section

Until the end of 1990s, a fair amount of data was accumulated for production of light charged-particle up to α-particles, but only very few data were available for heavier charged-particles like Li, Be, B,C, etc (fragments). These data are required for the analysis of radiation effect of microelectronics devices (soft errors) and dosimetry in space or high energy accelerators. For these studies, we adopted a Bragg Curve Counter (BCC): BCC is a gridded ionization-chamber with a large cathode-grid separation to stop particles before grid. BCC provides all the information on the particle, i.e., atomic number Z, mass M, energy E [18,19]. In the present study, BCC was improved for wider dynamic range and applicability to neutron induced reactions [20]. Owing to these improvements, new data have been obtained for fragment spectrum in proton-induced and neutron-induced reactions in ten’s of MeV region, while further improvement is required.

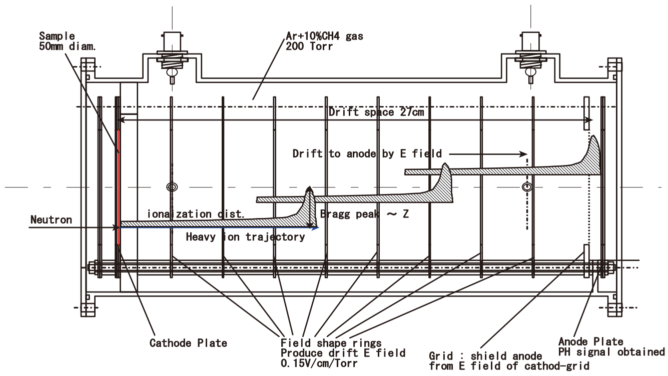

Fig.4(b): Schematic of Bragg curve counter [18,19]

5. Summary and Expectation for the future

A review was given for author’s experimental activities on nuclear data studies. It was stated that the experimental data are crucial in the nuclear data activity and that the availability of appropriate neutron source and powerful detection system are essential to obtain high quality and reliable data.

As mentioned in introduction, requirement for nuclear dada is extending from traditional energy fields to various fields like medical, engineering area, basic sciences and so on. Besides, even in the energy fields, the required physical quantities seem to be getting difficult to study, e.g., minor actinides with high activity, unstable nuclei, and small amount of samples, higher energy and so on.

To reply such challenging requirement, technical development to enable measurement for such objects and/or quantities will be crucial in both neutron or particle source and detection system. For the aim, employment of advanced neutron/particle source and equipment seems essential as well as collaboration with scientists in the physics area. New experiments at J-PARC which will be starting soon, and RCNP (Research Center for Nuclear Physics, Osaka University), RIBF in RIKEN are expected to open new possibilities. Of course, upgrading of existing facilities is also indispensable to promote basic tasks for detector development and education of young scientists.

Acknowledgement

The author wishes to express his hearty thanks to the organizing committee of the 08 Nuclear Data Symposium for providing him an opportunity to present the review. The works introduced above were done in collaboration with many colleagues in Tohoku University, JAERI(JAEA) and other institutions. He wishes to express his thanks to all of them, in particular, to Prof. T.Momota, K.Sugiyama, and N.Hirakawa of Tohoku University for their kind supports.

References:

[1] M.Baba et al., “Development of Monoenergetic Neutron Calibration Fields between 8 KeV and 15 MeV”, *Nucl. Instrum. Methods*, A376, (1996), 115

[2] S. Chiba et al., “Double-Differential Neutron Emission Cross Sections of ^{6}Li and ^{7}Li at incident Neutron Energies of 4.2,5.4,6.0 and 14.2 MeV.” *J.Nucl Sci.Technol.*,22 (1985) 771

[3] M.Baba, H.Wakabayashi, et al., “Double-differential Neutron Emission Spectra from Uranium- 238.”, *J. Nucl. Sci. Technol.*, 27 (7), (1990), 601

[4] M.Ibaraki et al. “Measurement of Double-differential Neutron Emission Cross Section of ^{6}Li, ^{7}Li and ^{9}Be for 11.5 MeV and 18.0 MeV Neutrons”, *J. Nucl. Sci. Technol.*, 35 (12), (1998) 843

[5] M.Baba et al., “Measurements of Double-differential Neutron Emission Cross Sections of Nb, Mo, Ta, W and Bi for 14 and 18 MeV Neutrons”, *J.Nucl.Sci.Technol.*, 31 (8), (1994) 757

[6] N.Ito, M.Baba et al., “Large Solid Angle Spectrometer for the Measurements of Differential (n,charged-particle) Cross Sections”, *Nucl. Instrum. Methods*, A337, (1994) 474

[7] M.Baba, N.Ito, et al., “Differential α-Production Cross Sections of Iron and Nickel for 4.3 to 14.1 MeV Neutrons”, *J. Nucl. Sci. Technol.*, 31 (7), (1994) 745

[8] T.Sanami, M.Baba, et al., “Measurement of ^{14}N(n,p)^{14}C Cross Section for KT=25.3 KeV Maxwellian Neutrons Using Gridded Ionization Chamber”, *Nucl. Instrum. Methods*, A394, (1997) 368-

[9] M.Baba, Y.Nauchi et al., “Characterization of 40-90 MeV ^{7}Li(p,n) Neutron Source at TIARA using a Proton Recoil Telescope and a TOF Method.”, *Nucl. Instrum. Methods*, A428, (1999) 454

[10] Y.Nauchi, M.Baba et al., “Measurement of (n,xp), (n,xd) Double Differential Cross Sections of Carbon and Aluminum for 65 and 75 MeV”, *J. Nucl. Sci. Technol.*, 36 (2), (1999), 143

[11] M.Baba et al., “Measurement of Differential Neutron-Induced Charged-Particle Emission Cross Sections for 5-75 MeV Neutrons”, ASTM STP 1398 (2001)447

[12] M. Ibaraki et al., “Measurement of Elastic Scattering Cross Sections for Carbon, Silocon, Iron, Zirconium and Lead for 75 MeV Neutrons” *J.Nucl.Sci.Technool.*, supl.1 (2000) 683

[13] M. Baba, “Experimental Studies on Particle and Radionuclide Production Cross Sections for Tens of MeV Neutrons and Protons”, *AIP Conf. Proc.Volume 769, Proceedings of ND2004* (September 2004, Santa Fe) (2005) 884

[14] M.Baba, H.Okamura et al., “Installation and Application of Intense ^{7}Li(p,n) Neutron Source” *Radiation Protection and Dosimetry*, doi:10.1093/rpd/ncm005

[15] T. Aoki, M. Baba, “Measurement of differential thick-target neutron yields of C, Al, Ta, W(p,xn) reactions for 50-MeV protons”, *Nucl. Sci. Eng.*, 146, (2004) 200 .

[16] M. Hagiwara et al., “Experimental studies on the neutron emission spectrum and activation cross-section for 40 MeV deuterons in IFMIF accelerator structural elements,” *J. Nuclear Materials*, 329-333, Part 1 (August 2004) 218

[17] M. Hagiwara et al., “Measurement of neutron emission spectra in Li(d,n) reaction with thick and thin Targets for 40 MeV deuterons”, *Fusion Sci. Technol.*, 48 (2005) 1320

[18] T. Sanami, et al., “A Bragg curve counter with an active cathode to improve the energy threshold in fragment measurements”, *Nucl. Instrum. Methods* A 589, (2008) 193

[19] M.Hagiwara, T.Sanami, T.Oishi, M.Baba, M.Takada, “Extension of energy acceptance of Bragg curve counter at the high energy end”, *Nucl. Instrum. Methods* A 592, (2008) 73

[20] M. Hagiwara et al., “Differential cross section on neutron-induced fragment emission reaction for microdosimetry study” *Radiation Protection and Dosimetry*, doi:10.1093/rpd/ncm022

7. Fusion Neutronics and the Nuclear Data

Takeo NISHITANI
Fusion Research and Development Directorate, Japan Atomic Energy Agency
801-1 Mukoyama, Naka-shi, Ibaraki-ken, 311-0193
e-mail: nishitani.takeo@jaea.go.jp

For the International Thermonuclear fusion Experimental Reactor (ITER), shielding calculations with the extremely complicated geometry have been carried out by MCNP, where FENDL-2.1 is adopted as a reference nuclear library. In the ITER Test Blanket Module (TBM) program, prototypes of breeding blanket will be tested at ITER. The Integral test of the TBM mock-up has been carried out at FNS. For the International Fusion Materials Irradiation Facility (IFMIF), D-induced activation cross sections of the IFMIF accelerator materials have been measured at the TIARA AVF cyclotron.

1. Introductions

Aiming at scientific and technical feasibility demonstration of the fusion energy, the construction of the International Thermonuclear fusion Experimental Reactor (ITER) just started by the international collaboration. The nuclear issue becomes much more important in ITER compared with the present fusion machines. Several nuclear related issues on fusion reactors are shown in Fig.1. In ITER, neutron shielding for the surrounding components such as the superconducting magnets is one of the most important issues. In the fusion power plant, a breeding blanket converts neutron energy to the heat and reproduces tritium. Prototypes of breeding blanket will be tested at ITER as the ITER TBM program. On the other hand, neutrons and gamma-rays from the plasma bring us useful information about the plasma such as fusion power, ion temperature, energetic ion behaviors.

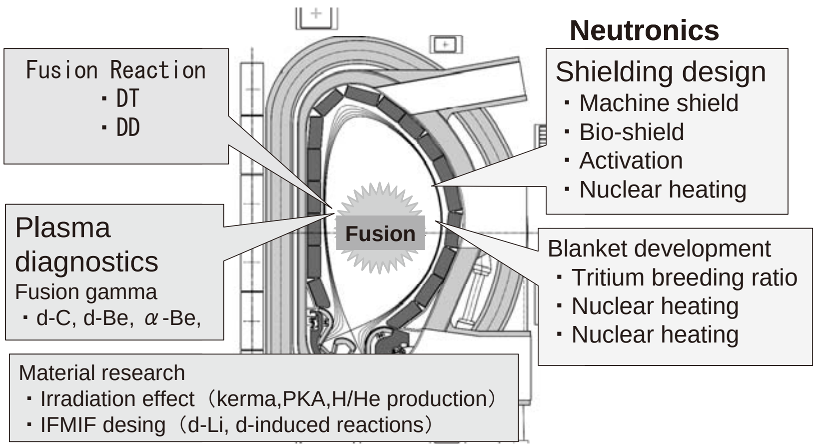

Figure1 Nuclear related issues on fusion reactors.

In the fusion material development, nuclear data for the KERMA factor, dpa evaluation etc. are necessary. For the International Fusion Materials Irradiation Facility (IFMIF), neutron and D induced cross section data are newly required in the energy range 20-50 MeV.

2. Shielding Design for ITER

In ITER and other magnetic confinement fusion devices, the plasma which is a neutron source, is surrounded by the radiation sensitive components such as superconducting coils. The total construction cost of the fusion device strongly depends on the amount of the superconducting coils, therefore the radiation shield between the plasma and the superconducting coils should be minimized to save the construction cost. So the machine shielding is the most important in the shielding design of the fusion device. Fusion devices have complicated structures containing many kinds of ducts. The duct streaming of neutrons and gamma-rays is the major issue in the shielding design, where a Monte Carlo code MCNP is the most popular tool.

Figure 2 shows the 80 deg. sector model of ITER including NB ports for the nuclear heat estimation of the superconducting Toroidal Field Coils (TFCs). The model consists of about 6000 cells. We calculated the total nuclear heating power in TFCs to be 12.7 kW at the 500 MW ITER operations, which is only 7 % margin against the design target of 13.7 kW determined by the cryogenics capacity [1].

In the case of the ITER model shown in Fig. 2, it took more than one person•year to complete the modeling. So automatic conversion program from the CAD file to the MCNP input file is strongly desired for the efficient design work.

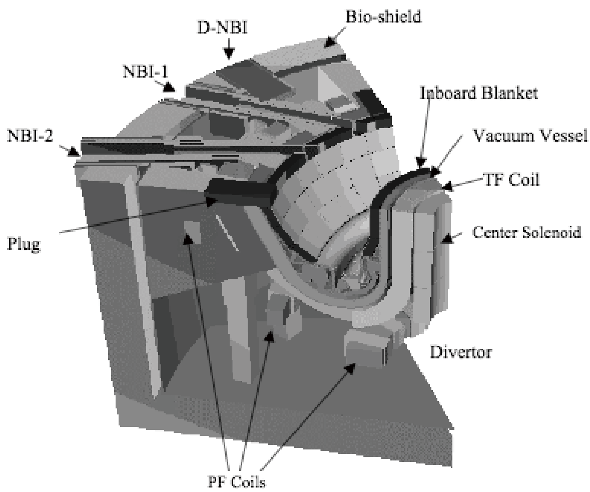

Figure 2 ITER 80° sector model for the MCNP calculation including NB ports.

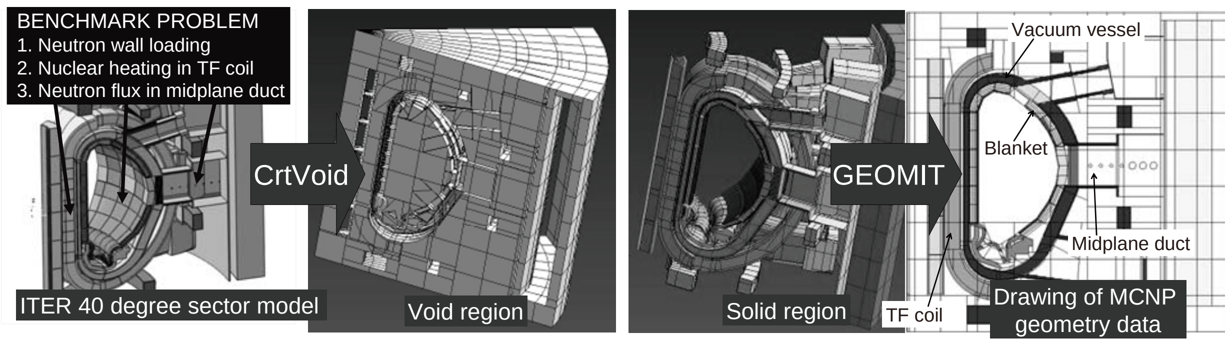

Figure 3 Flow of the automatic conversion program from the CAD file to the MCNP input file developed by JAEA.

Figure 3 shows the flow of the automatic conversion program developed by JAEA. This system consists of a void creation program (CrtVoid) and a conversion program (GEOMIT) from CAD drawing data to geometry input data of MCNP. First CrtVoid creates void region data. The void region data is very large and complicated geometry. CrtVoid automatically divides the overall region to many small cubes, and the void region data can be created in each cube. Next GEOMIT generates surface data from CAD data including the void data generated with CrtVoid. These surface data are connected, and cell data are generated [2, 3].

3. Integral Test at FNS

In order to benchmark nuclear libraries to be used for fusion, many integral experiments and the analyses have been carried out in FNS. Slab assemblies of fusion related materials, with geometry several times thicker than the mean free pass of 14 MeV neutrons, have been installed in front of the tritium target for the neutron generation. We analyzed the integral benchmark experiments (Iron, SS316, Copper, Beryllium, Li_2O, etc.) with FENDL-2.1, JENDL-3.3, JEFF-3.1 and ENDF/B-VII.0 and compared the results each other. Figure 4 shows the example of the results for ion and beryllium. For ion, JENDL-3.3 overestimated the neutron spectrum in the energy range from thermal to keV [4], which discrepancy will be improved in JENDL-4. For beryllium, all libraries except JEFF-3.1 overestimated the neutron spectrum in the energy range of 2-10 MeV [4].

(a)

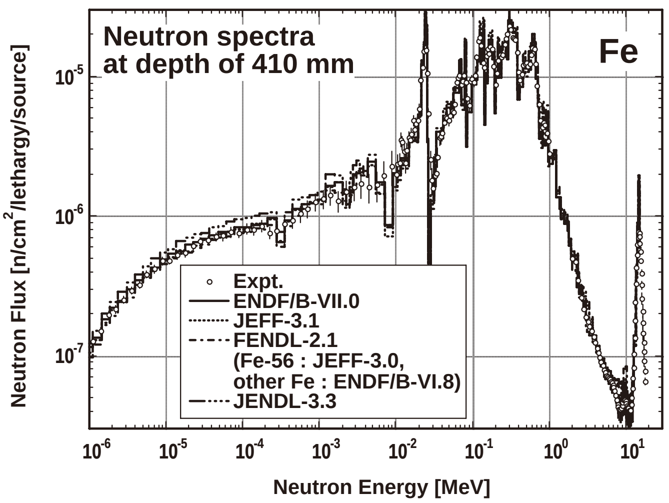

(b)

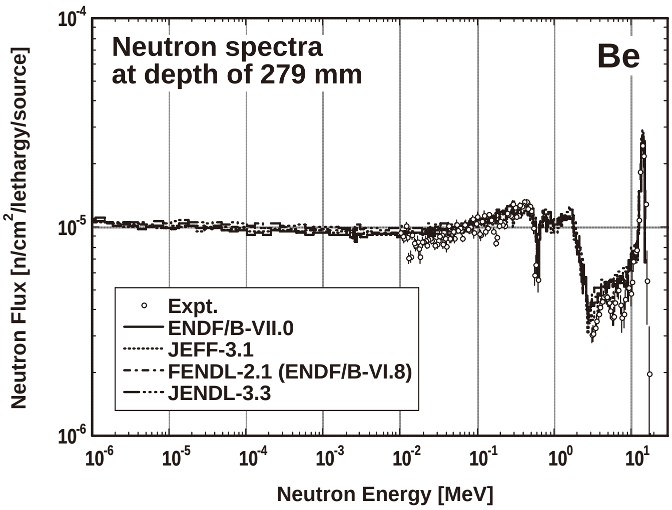

Figure 4 Neutron spectra in the (a) ion and (b) beryllium slabs for the 14 MeV neutron injection.

In ITER, prototypes of breeding blanket (TBM) will be tested aiming at the development of fusion DEMO reactor blankets. Japan is developing the water cooled solid breeder blanket with reduced activation ferritic/martensitic steel as a structural material as one of the most promising blanket concepts for DEMO reactors. Integral experiment for the mock-up of the water-cooled pebble bed type TBM has been carried out at FNS. Slab mockup assembly shown in Fig.5 (a) consists of the first wall with water, water panels, Be neutron multiplier and a breeder layers. After the irradiation, the amount of tritium produced in the diagnostic Li_2CO_3 pellets is measured by liquid scintillation counting method. Figure 5 (b) shows the measured and calculated tritium production rate distributions in the first and second breeder layers. The C/E ratios for the tritium production rate in those experiments are within 1 ± 0.05, which gave us a good prospect to the neutronics test of the TBM on ITER [5].

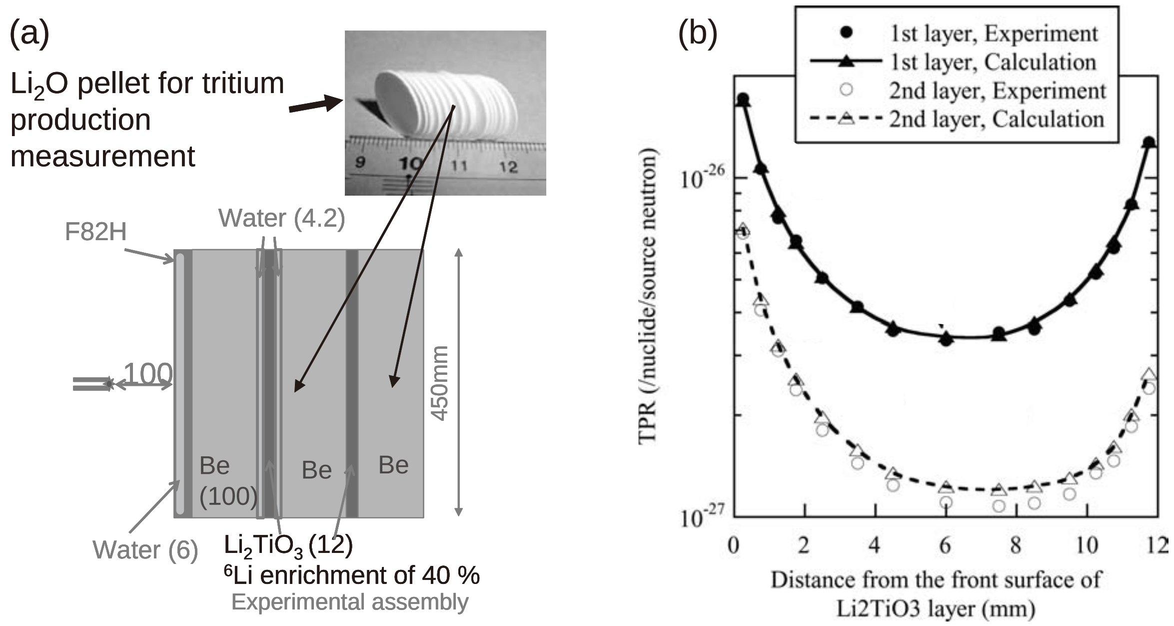

Figure 5 (a) Mock-up assembly of the water-cooled pebble bed type TBM, and (b) the measured and calculated tritium production rate distributions in the first and second breeder layers.

4. Nuclear Data for IFMIF

IFMIF is an accelerator-based neutron source for fusion material irradiation tests. D ions accelerated by RFQ and DTL, are injected to the flowing liquid lithium target, which produces neutrons with fusion like spectrum by d-Li reactions. The neutron spectra have a peak around 14 MeV and continuum tail up to about 50 MeV as shown in Fig.6 [6]. So the neutron cross sections in the energy range of 20-50 MEV are required not only for the shielding design of the IFMIF facility but also for the estimation of the higher energy tail effect on the irradiation characteristics of the samples in the IFMIF irradiation rig such as the dpa value and the H/He production.

In the design of IFMIF, long-term operation with more than 70 % total facility availability is required. However, the activation of structural materials composing the IFMIF accelerator due to the bombardment by deuteron beam limits the maintenance time and makes the long-term operation difficult. Therefore, the accurate estimation of deuteron-induced radioactivity and the selection of low activation structural materials are important. Thus, measurements of deuteron-induced activation cross sections for main structural materials (aluminum, copper and tungsten) were performed on the basis of a stacked-foil technique at TIARA AVF cyclotron. We have obtained the activation cross sections for the reactions ^{27}Al(d,x)^{27}Mg or ^{24}Na, ^{nat}Cu(d,x)^{62,63}Zn or ^{61,64}Cu, and ^{nat}W(d,x)^{187}W or $^{181\text{-}184,186}$Re in 22-40 MeV range. These results were compared with other experimental cross sections and estimated data in the ACSELAM library and calculated ones by TALYS and PHITS [7]. Figure 7 shows the cross sections of ^{27}Al(d,x)^{24}Na reaction. Calculated values with TALYS are better agreement with the measured ones.

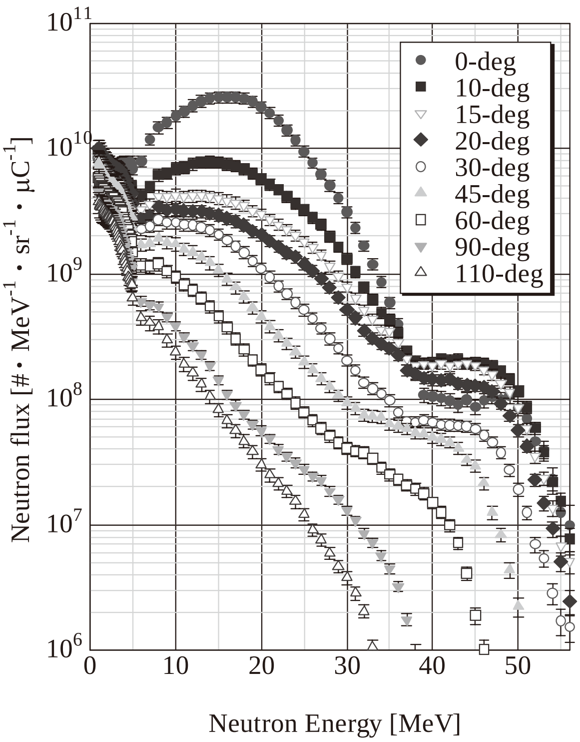

Figure 6 Neutron spectra from the lithium thick target bombarded with 40 MeV deuterium.[6]

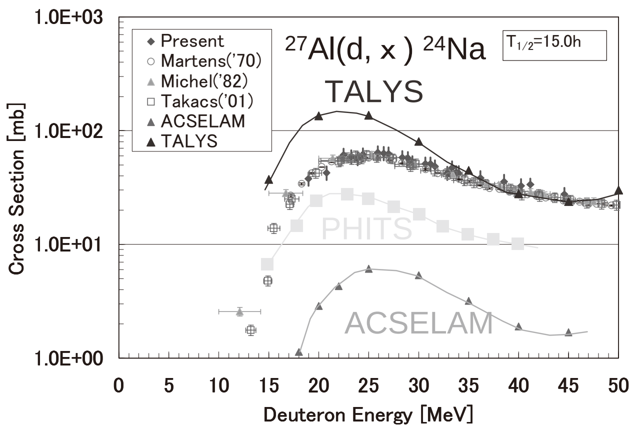

Figure 7 Measured cross sections of ^{27}Al(d,x)^{24}Na reaction compared with compared with other experimental cross sections and estimated data in the ACSELAM library and calculated ones by TALYS and PHITS.

5. Burning Plasma Diagnostics using Nuclear Reaction

In D-D and D-T plasma experiment, neutron measurement is one of the most important diagnostics for the fusion output and the ion temperature. Many neutron measurement techniques such as fission chambers, neutron spectrometers and activation foils are employed, which are reviewed in Ref. 8. In the fusion power measurement, the calibration between the total neutron yield and the neutron detector count rate is the most important issue, where very precise neutronics calculation with whole tokamak geometry and the neutron detector is necessary.

In the D-T burning plasma, alpha particles produced by the D-T reactions will be confined and heat the plasma during showing down. So the information on the confined alpha particles is important for the burning plasma physics. However, the diagnostics technique is not established. Recently, measurement of gamma-rays from the nuclear reaction between alpha particle and impurity ions such as ^{9}Be(α, n)^{12}C is proposed and demonstrated for the diagnostics of alpha particle density and energy distribution [9]. Similar nuclear reactions between energetic ions and impurity or bulk ions such as $^{9}Be(p, \alpha)^{6}Li$, $^{9}Be(p, n)^{10}B$, etc. are used for the diagnostics for the energetic ion behaviors. Some nuclear data of those reactions are required to be more precise for the diagnostics purpose.

6. Summary

Neutronics and the nuclear data become more important in the fusion energy development. In ITER, very complicated neutronics calculations are carried out. New technique of the MCNP input generation code from CAD data is under development. Basically, fusion neutronics design uses general purpose nuclear libraries. Integral experiments have pointed out that some discrepancy still exists among those libraries. For the IFMIF design and the material irradiation experiment by IFMIF, D-induced cross-sections and neutron induce cross-sections are needed. But those are not sufficient so far. For the fusion plasma diagnostics, several charged particle induce reaction cross-section are required.

Acknowledgement

The author would like to appreciate Drs. Konno, Sato and Ochiai of FNS and Prof. Baba for their supporting for this paper.

References

[1] S. Sato, et al., “Monte Carlo Analyses for ITER NBI Duct by 1/4 Tokamak Model”, J. Nucl. Sci. Technol, Supplement 1, 258 (2000).
[2] S. Sato, et al., “Development of CAD/MCNP interface program prototype for fusion reactor nuclear analysis”, Fusion Eng. Des., 81, 2767 (2006).
[3] K. Ochiai, et al., “Advancement of Nuclear Analysis Method for ITER”, 22nd IAEA Fusion Energy Conf., Geneva, October 2008.
[4] C. Konno, et al., “Analyses of fusion integral benchmark experiments at JAEA/FNS with FENDL-2.1 and other recent nuclear data libraries”, Fusion Eng. Des., 83,1774 (2008).
[5] S. Sato, et al., “Measurement of tritium production rate in water cooled pebble bed multi-layered blanket mockup by DT neutron irradiation experiment”, Nucl. Fusion., 47, 517 (2007).
[6] H. HAGIWARA, et al., “Measurement of neutron emission spectra in Li(d,xn) reaction with thick and thin targets for 40-MeV Deuterons,” Fusion Sci. Technol., 48, 1320 (2005).
[7] K. Ochiai, et al., “Measurements of Deuteron-induced Activation Cross Sections for IFMIF Accelerator Structural Materials in the Energy Range of 22-40 MeV”, Fusion Eng. Des., 81, 1459 (2006).
[8] M. Sasao, et al., “chapter 9, fusion product diagnostics”, Fusion Sci. Technol., 53, 604 (2008).
[9] V.G. Kiptily, et al, “Gamma-ray imaging of D and ^{4}He ions accelerated by ion-cyclotron-resonance heating in JET plasmas”, Nucl. Fusion 45, L21 (May 2005).

8. Development of Radiation Shielding Design Methods for Radiological Safety of J-PARC

Hiroshi NAKASHIMA
Japan Atomic Energy Agency
Tokai-mura, Naka-gun, Ibaraki-ken 319-1195
nakashima.hiroshi@jaea.go.jp

Abstract

J-PARC (Japan Proton Accelerator Research Complex) is a high-energy proton accelerator complex of the world's highest beam power. The characteristics of high beam intensity and energy cause many difficulties on radiological safety. In order to overcome the problems, some radiation shielding methods were developed by benchmarking based on experimental data. This paper reviews the development of the radiation shielding design methods for radiological safety of J-PARC.

1. Introduction

Aiming at studies on basic and applied sciences and the advancing nuclear technologies, the J-PARC project is being conducted under collaboration between High Energy Accelerator Research Organization and Japan Atomic Energy Agency. J-PARC is composed of three accelerator facilities: linac, and 3 GeV rapid cycle synchrotron and 50 GeV synchrotron, and four experimental facilities: Material & Life Science Facility, Hadron Experimental Facility, Neutrino Experimental Facility and Nuclear Transmutation Experiment Facility, as shown in Fig. 1. The high-energy proton accelerator complex with the world highest intensity of 1 MW maximum beam power is under construction. [1]

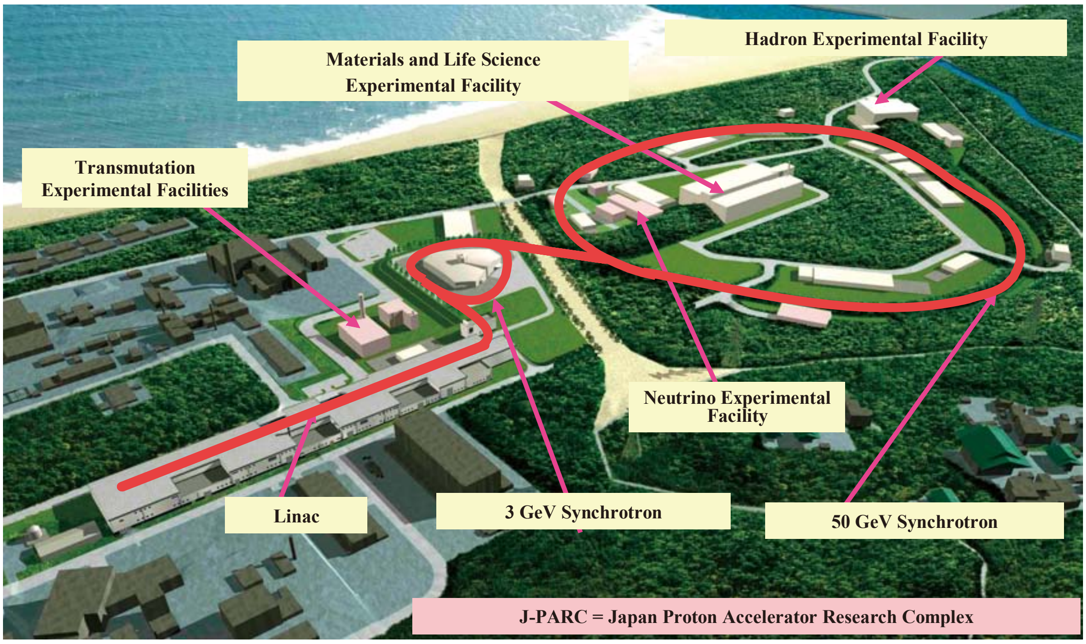

Fig.1 Bird's eye view of planned J-PARC facilities [1]

From the viewpoint of radiological safety, the large-scale accelerator complex with high beam intensity and energy causes many difficulties. Characteristics of J-PARC are high beam power, high beam energy and large-scale accelerator complex. Radiation problems come from widely distributed radiation source, thick shield, many ducts and so on, while shielding design methods with high accuracy were strongly required for the detailed shielding design of the facilities. In order to overcome the radiation problems, a calculation system with both simplified and detailed methods are applied for shielding design and safety analyses.[2] The accuracy of the methods was estimated by using experimental benchmark analyses.[3] This paper reviews the development of the radiation shielding design methods for radiological safety of J-PARC.

2. Shielding design methods

A calculation system with both simplified and detailed methods is used for the shielding design of J-PARC.[2] In detailed methods, a calculation system combined with various codes is used, as shown in Fig. 2. In this system, several Monte-Carlo codes PHITS [3], MARS14 [5] and MCNPX [6], are used for high-energy particle transport calculation, making full use of the characteristics of each code. The PHITS code is a multi-purpose particle and heavy ion transport Monte-Carlo code based on the NMTC/JAM code [7]. The MCNPX code is widely used for the designs, because the code has various kinds of estimators and valiance reduction techniques. The MARS code can calculate the radiation flux and dose in a rather short time, compared with other Monte-Carlo codes. The MCNP-4 code [8] with a nuclear data set, JENDL-3.3 [9], is applied for low-energy neutrons up to 20 MeV and photons. The DCHAIN-SP 2001 code [10] with mainly the FENDL-Dosimetry file [10] is used for induced radioactivity and dose estimations due to residual nuclei of machine components and the wall of the accelerator room. The JENDL-HE file[10] is also used to estimate the residual activity of light nuclei in air in accelerator room and cooling water for accelerator devices and beam dumps.

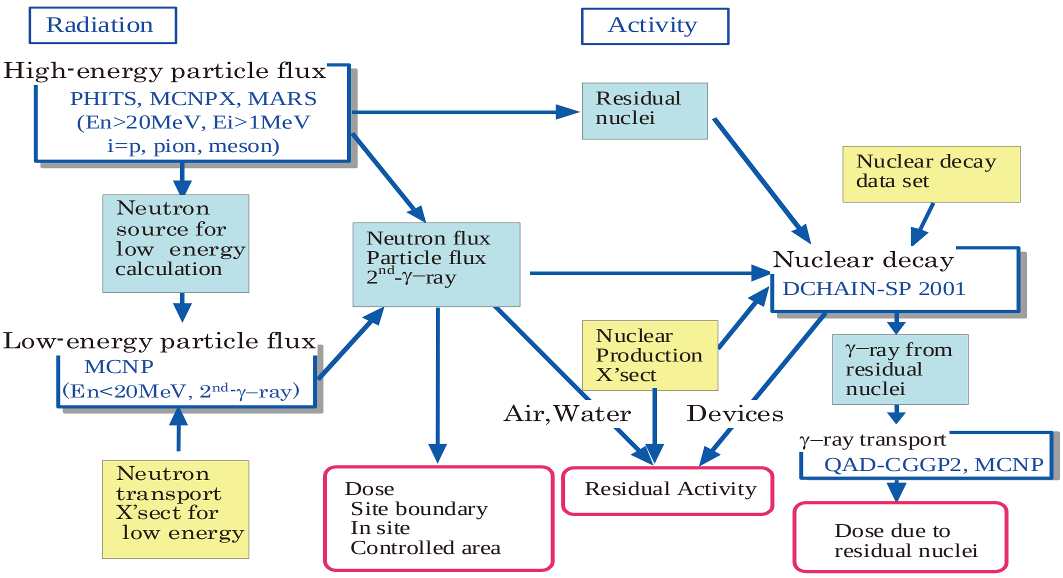

Fig.2 Calculation flow of radiation and activity used in the J-PARC shielding design [2]

3. Benchmarking

In order to develop the methods and study the accuracy of the methods, some benchmark analyses on thick target neutron yield, beam dump, bulk shielding, and streaming were carried out and compiled in ref. [3]. In this paper, benchmarking based on AGS (the Alternating Gradient Synchrotron) and TIARA (Takasaki Ion Accelerators for Advanced Radiation Application) experiments are presented as examples.

3.1 AGS experiments [13]

A series of experiments using a mercury spallation target with high-peak-power GeV proton-beam from (AGS) of Brookhaven National Laboratory (BNL) was carried out [13] and analyzed on beam dump and deep penetration.

In the beam dump experiment, a mercury target was bombarded with 1.6-, 12- and 24-GeV-protons, and spatial distributions of neutron reaction rates along the target were measured. The cross sectional view of the mercury target is shown in Fig. 3. In the experiments, various kinds of activation detectors such as In and Bi were used to measure wide neutron energy region.

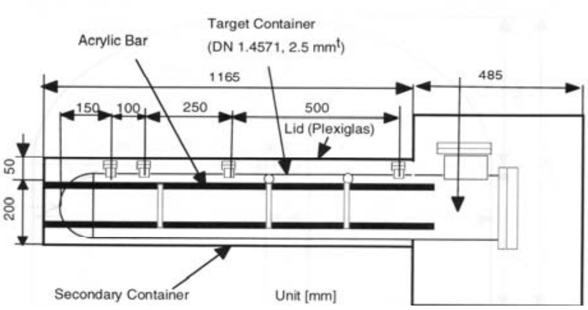

Fig.3 Cross-sectional view of the mercury target irradiated by proton beams at BNL/AGS [13]

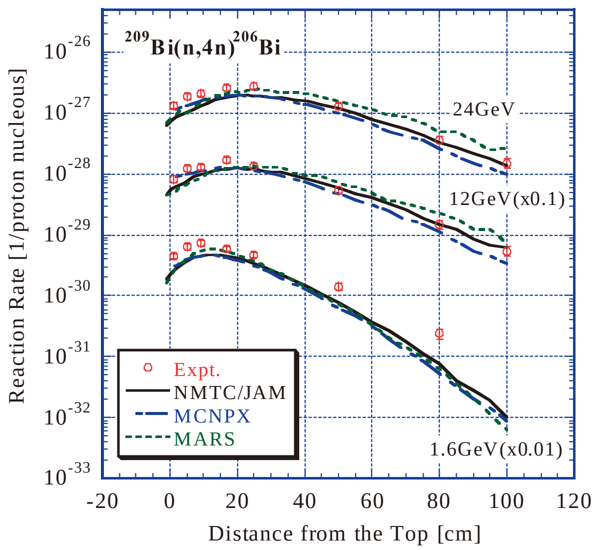

Fig.4 Comparisons on distributions of ^{209}Bi(n, 4n)^{206}Bi reaction rates parallel to the axis of the mercury target among calculations and measurement at BNL/AGS [13]

Figure 4 shows measured spatial distributions of the rate of the ^{209}Bi(n, 4n)^{206}Bi reaction (threshold energy: E_{th} 22.6 MeV) due to neutrons generated in the mercury target by incident protons of 1.6, 12 and 24 GeV, compared with calculations by the NMTC/JAM code with free and in-medium cross section options and by the MCNPX code as an example. In the NMTC/JAM code, the parametrized in-medium NN cross sections similar to those of Cugnon[14] are used instead of the free cross sections to calculate the mean free path and collision probability of nucleon in a target nucleus divided some regions as an alternative option for the intranuclear cascade calculation. All calculations are in good agreement with the measurements as a whole. The calculations of NMTC/JAM with the in-medium cross section (In medium) underestimate the measurement at 1.6 GeV and at positions less than 40 cm from the front of the target at 12 and 24 GeV by a factor of 2. The NMTC/JAM calculations with the free cross section (Free) underestimate all measurements. The NMTC/JAM (In medium) calculation is larger and closer to the measurements than the NMTC/JAM (Free) calculations within a factor of 2. The MCNPX calculation at 1.6 GeV gives almost the same result as the NMTC/JAM (In medium) calculation, while the shape of the distributions at 12 and 24 GeV given by

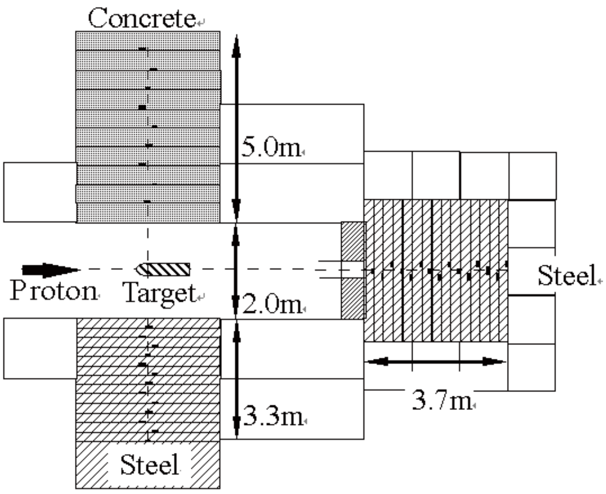

Fig.5 Horizontal cross sectional view of shield arrangement for shielding experiment at BNL/AGS [13]

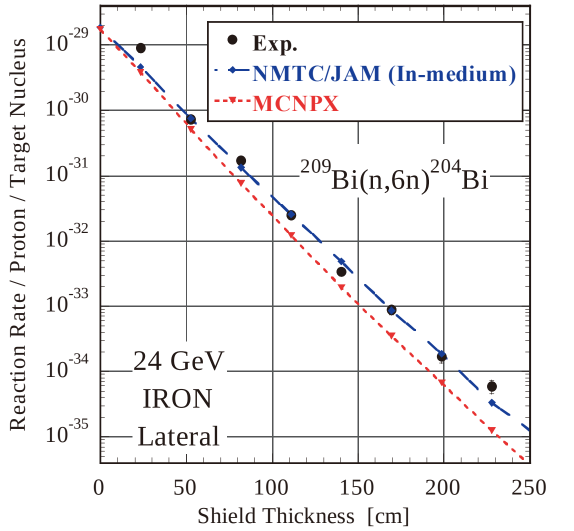

Fig.6 Comparisons on distributions of ^{209}Bi(n, 6n)^{204}Bi reaction rates in iron shield among calculations and measurement at BNL/AGS [13]

the MCNPX code are different from those by the NMTC/JAM code within a factor of 2.

Figure 5 shows an arrangement of shields made of iron 3.3 m thick and ordinary concrete 5.0 m thick for the deep penetration experiment. As example, spatial distribution of neutron reaction rates of the ^{209}Bi(n, 6n)^{204}Bi reaction (E_{th} 38.0 MeV) measured inside the lateral iron shield is compared with the NMTC/JAM (In-medium) calculations and the MCNPX calculations at 24 GeV protons in Fig. 6. The NMTC/JAM (In-medium) calculation agrees very well with the measurements almost at all positions. The MCNPX calculation shows the same tendency of neutron attenuation and agrees with the measurement within a factor of 2, although the calculations yield slightly lower values than the measurement.

3.2 TIARA experiment [15]

The cross-sectional view of the TIARA deep penetration experiment is shown in Fig. 7. [15] Quasi-monoenergetic source neutrons were generated by 43- and 68-MeV protons bombarding ^{7}Li targets. Neutrons above about 5 MeV were measured just behind the concrete and iron shields along the neutron beam axis and at the positions of 20 and 40 cm from the beam axis using an unfolding method with the BC501A liquid scintillation detector. [16], [17]

The measured neutron energy spectra were compared with the calculations using the old version of the NMTC/JAM code firstly. In Fig 8, the measured neutron energy spectrum

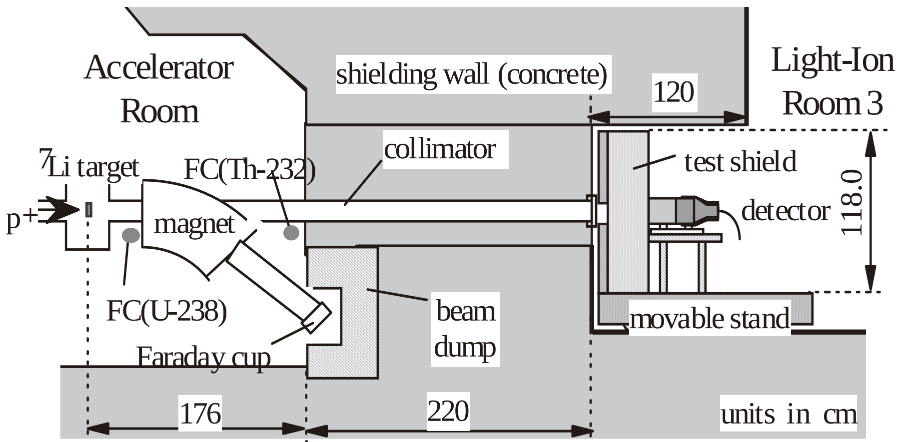

Fig.7 Cross-sectional view of the TIARA neutron facility with the experimental arrangement [15]

behind the steel shield of 70 cm thick is compared with the calculation for 68-MeV p-Li neutron sources. It was found that the calculation overestimated the measurement more than an order of magnitude. The overestimation was due to the fact that the geometrical cross section of a target nucleus was used as the total cross section in transport calculation. After the comparison, the NMTC/JAM code was modified using the energy–dependent total and elastic scattering cross sections obtained from the data due to the Pearlstein's systematics [18]. It is shown in Fig. 8 that the calculation with the modified version of the NMTC/JAM code agrees well with the measurement.

The measured neutron energy spectra at the off-center positions were used to modify the angular distribution of elastic scattering reaction in the NMTC/JAM code. It is shown in Fig. 9 that the measured neutron energy spectrum behind the steel shield is compared with the calculation using the old version at the position of 10 cm thick and 40 cm off center position for 68-MeV p-Li neutron source. The calculation with the old version of the NMTC/JAM code failed to reproduce the energy spectrum. Although in the old version of the NMTC/JAM code, the angular distribution was calculated by an optical model code and approximated by the Bessel function, the calculation underestimated the measurement. Then a series of measurements on angular distribution of elastic scattering cross section was carried out at TIARA.[19] Angular distributions of elastic scattering reaction cross section with the JLM potential parameters[20] were used to modify the NMTC/JAM code.[21] It is shown in Fig. 9 that the calculation of the modified version of the NMTC/JAM code succeed to reproduce the measurement.

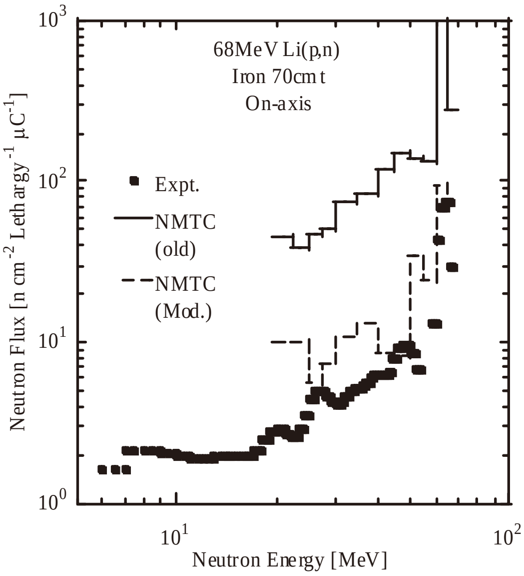

Fig.8 Comparison on transmitted spectra through 70-cm-thick iron shield for the 68-MeV p-Li neutron source among experiment and calculations by the old and modified NMTC codes [15]

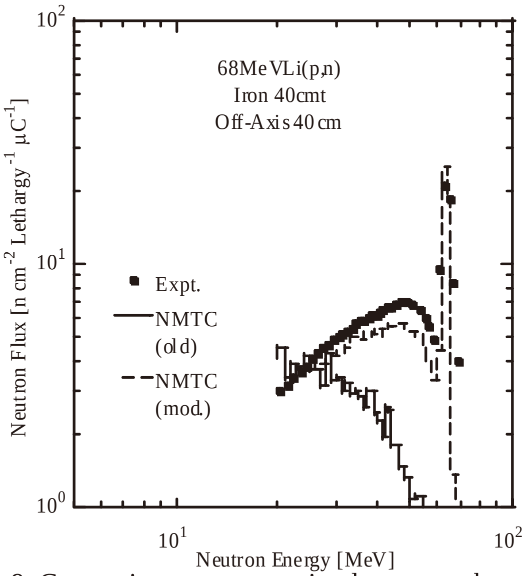

Fig.9 Comparison on transmitted spectra through 40-cm-thick iron shield at 40-cm off center position for the 68-MeV p-Li neutron source among experiment and calculations by the old and modified NMTC codes [15]

4. Summary

J-PARC is a high-energy proton accelerator complex of the world's highest beam power, and its characteristics caused many difficulties on radiological safety. In order to overcome the difficulties and secure safety, various experiments such as AGS and TIARA experiments were carried out, the accuracy of the methods was estimated, and the shielding design methods were developed. And, based on benchmarking with experitental data, a safety factor was applied for the shielding design. By using the methods, the J-PARC shielding design was performed and the facilities are under construction. In near future the first phase of the J-PARC project is scheduled in completion and J-PARC will move to the next phase.

References

[1] S. Nagamiya: *J. of Nucl. Materials*, 343, 1-6 (2005).

[2] H. Nakashima, et al.: “Radiation Shielding Design for the J-PARC Project,” to be published at Proc. of shielding aspects of accelerators, targets and irradiation facilities - SATIF 8, 22-24 May 2006 (2006).

[3] N. Matsuda, et al.: “Analyses of Shielding Benchmark Problems for the Shielding Design of the High Intensity Proton Accelerator Facilities,” JAEA-Technology 2008-030, JAEA (2008).

[4] H. Iwase, et al.: *J. Nucl. Sci. Technol.*, 39, 1142 (2002).

[5] N. V. Mokhov: “The Mars Code System User's Guide,” Fermilab-FN-628 (1995); N. V. Mokhov and O. E. Krivosheev, “MARS Code Status,” Fermilab-Conf-00/181 (2000).

[6] L. S. Waters, (Ed.): “MCNPX Users Manual – Version 2.1.5,” TPO-E83-G-UG-X-00001, LANL (1999).

[7] K. Niita, et al.: “High Energy Particle Transport Code NMTC/JAM,” JAERI-Data/Code 2001-007, JAERI (2001).

[8] J. F. Briesmeister, (Ed.): “MCNP – A General Monte Carlo N-Particle Transport Code,” Version 4A, LA-12625, LANL (1993).

[9] K. Shibata, et al.: *J. Nucl. Sci. Technol.*, 39, 1125 (2002).

[10] A. B. Pashchenko: “IAEA Consultants' Meeting on Selection of Evaluations for the FENDL/A-2 Activation Cross Section Library, Summary Report,” INDC(NDS)-341, IAEA (1996).

[11] T. Kai, et al.: “DCHAIN-SP 2001: High Energy Particle Induced Radioactivity Calculation Code,” JAERI-Data/Code 2001-016, JAERI (2001) (in Japanese).

[12] Y. Watanabe, et al.: “Nuclear Data Evaluation for JENDL High-Energy File,” Proc. of Int. Conf. on Nuclear Data for Science and Technology, Santa Fe, New Mexico, USA, Sep. 26 - Oct. 1, 2004, Vol. 1, 326 (2004).

[13] H. Nakashima, et al.: Proc. of OECD/NEA Workshop on Shielding Aspects on Accelerator, Target and Irradiation Facilities, SATIF 6, NEA No. 3828, 27-36 (2004).

[14] J. Cugnon, et al: *Nucl. Phys.*, A352, 505 (1981).

[15] H. Nakashima, et al.: Proc. on the 6th Int. Mtg. on Nucl. App. of Acc. Technol., San Diego, California U.S.A., Jun. 1-5, 2003, 959-968 (2004).

[16] N. Nakao, et al.: *Nucl. Sci. Eng.*, 124, 228-242 (1996).

[17] H. Nakashima, et al.: *Nucl. Sci. Eng.*, 124, 243-257 (1996).

[18] S. Pearlstein: *J. Astrophys.*, 346, 1049 (1989).

[19] M. Ibaraki, et al.: *Nucl. Instrum. Methods*, A446, 536-544 (2000).

[20] J. P. Jeukenne, et al.: *Phys. Rev.*, C16, 80 (1977).

[21] H. Takada, et al.: *J. Nucl., Sci. Technol.*, 37, 307-315 (2000).

9. Accelerator-based BNCT with medium- to high-energy proton beams

Shunsuke Yonai
National Institute of Radiological Sciences
4-9-1 Anagawa, Inage-ku, Chiba 263-8555, Japan
e-mail: yonai@nirs.go.jp

The realization of the accelerator-based boron neutron capture therapy (BNCT) will greatly contribute to the development of BNCT. To solve some difficulties in realizing the accelerator-based BNCT in clinical use, we have proposed the accelerator-based BNCT using medium- to high-energy proton beams. Here, our systematic study of accelerator-based BNCT using medium- to high-energy proton beams was introduced.

I. Introduction

Boron neutron capture therapy (BNCT) is a radiotherapy modality in which cancer cells are killed by α particles and ^{7}Li nuclei produced through the $^{10}B(n, \alpha)^{7}Li$ reaction between a boron compound selectively absorbed in tumor cells and a neutron beam provided by a neutron source. BNCT is an effective and promising treatment for nonlocalized and radio-resistant malignancies that are presently considered to be inoperable, especially for brain tumors such as glioblastoma multiforme. Neutron sources used for BNCT must deliver a sufficiently high dose to tumor tissues while keeping the dose to normal tissues within a tolerable level. Due to poor penetration, thermal neutrons, which was mainly used for BNCT in Japan, cannot kill deep seated malignancies such as gliobastoma multiforme, which often is located near the center of the brain and surrounded by healthy tissues. Besides, it is not possible to kill a cell selectively using high-energy neutrons because of the large kerma coefficient of the $^{1}H(n,n)^{1}H$ reaction in a tissue. As a compromise, the use of epithermal neutrons in BNCT has recently been of increasing interest, taking into account the fact that incident neutrons are moderated in the human body. For example, Yanch et al. showed that epithermal neutrons in the energy range from 4 eV to 40 keV are most effective in the treatment of a brain tumor at a depth of 7 cm and 10 keV neutrons are most effective for that at a depth of 10 cm.[1)] In the case of the currently employed reactor-based neutron source for BNCT, however, it is difficult to provide such neutrons because the reflectors and moderators are built in the reactor. Actually, the reactor-based neutron source provides a spectrum that has a wide energy peak between several tens and several hundreds of eV. Therefore, an accelerator-based neutron source is desired for BNCT to provide neutrons suitable for the treatment of deep-seated malignancies. Furthermore, the accelerator-based neutron source is strongly desired for the widespread use of BNCT, because facilities with the accelerator-based neutron source can be constructed more easily in the city areas, together with a hospital, than those with the reactor-based neutron source. For these reasons, many groups have investigated accelerator-based neutron sources for BNCT as summarized in Table 1.[2-8] However, their investigations in which low-energy accelerators of a few MeV are employed, have not yet been applied to the clinical use of BNCT mainly because of the serious difficulties in realizing target cooling and target reliability against very high beam current.

In order to solve these difficulties, we have proposed an accelerator-based BNCT using medium- to high-energy proton beams, and found out that the BNCT system is feasible with currently-available technologies through systematic studies consisted of the conceptual designs by using Monte Carlo simulations[9], their experimental verifications[10),11], engineering design[12] including investigations on the stability of the neutron production target, and its application[13]. In this paper, the concept and the application of our accelerator-based BNCT using medium- to high-energy proton beams are introduced.

Table1. Summary of proposed accelerator-based neutron sources for BNCT

Neutron production reaction	Accelerated energy [MeV]	Beam current [mA]	Heat load [kW]	Reference
$^{7}Li(p,n)^{7}Be$	1.9	10	19	2)
	1.95	≥5	≥10	3)
	2.3	10	23	4)
	2.4	20	48	5)
	2.3-2.5	10	23-25	6)
	2.8	3.3	9.2	7)
$^{2}H(d,n)^{3}He$	0.4	5000	200	8)
$^{3}H(d,n)^{4}He$	0.12	1000	120	8)

II. Concept of accelerator-based BNCT with medium- to high-energy proton beams

Advantages by using higher energy incident particles are the higher neutron production yield and the resultant lower heat load and heat density in the target. However, it results in the contamination of high energy neutrons beyond MeV energies, which increases undesired dose to normal tissue especially to the skin, due to the $^{1}H(n,n)^{1}H$ reaction. In the conceptual design, the selections of a neutron source and moderators and the optimization of the moderator assembly were focused on, assuming the use of the AVF cyclotron at the Cyclotron and Radioisotope Center, Tohoku University, which provides maximum beam intensities of a 50 MeV proton beam of 300 μA and a 25 MeV deuteron beam of 150 μA.

1. Neutron source

Regarding to the neutronics, the neutron source for BNCT is primarily required to provide an intense neutron yield for reducing therapeutic time and, at the same time, only a small fraction of fast neutron components for reducing undesired dose to normal tissues. In the selection of the neutron source, the deuteron-induced reactions were included as well as the proton-induced reactions, because of the intense neutron yield of the (d,n) reaction due to the knock-on reaction. Neutron sources that we considered are as

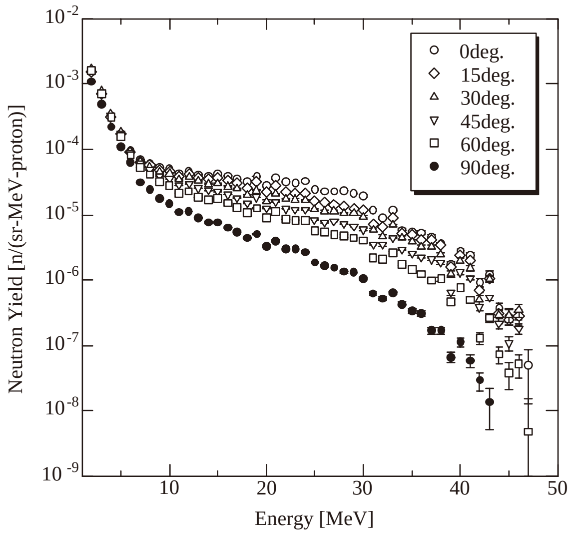

Fig.1. Measured neutron energy spectra for Ta(p,n) reaction. (Ep=50 MeV)

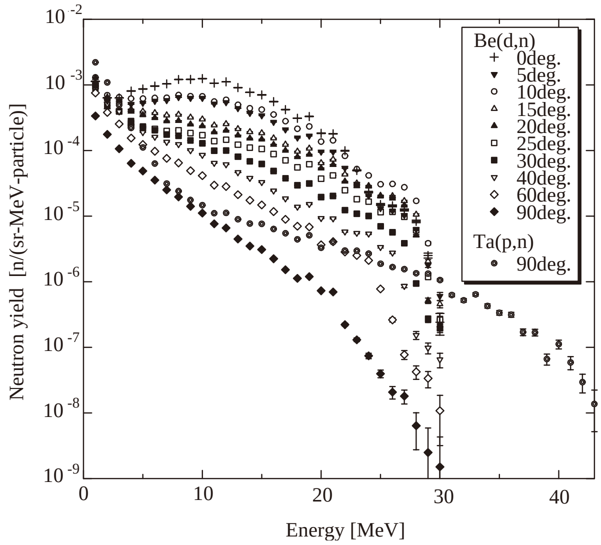

Fig.2. Comparison of measured neutron energy spectra between Be(d,n) (E_d=25 MeV) and Ta(p,n) (Ep=50 MeV) reactions. reactions

follows. For deuteron beams, the Be (d,n) reaction (Q value of 4.4 MeV) is considered to be suitable, because it provides a high neutron yield comparable to the Li(d,n) reaction and a lower fast neutron contamination than the Li(d,n) reaction having the high Q value of 15 MeV of the ^{7}Li (d,n) ^{8}Be reaction. For proton beams, the neutron production reactions with heavy target materials such as W(p,n) and Ta(p,n) reaction are considered, because they exhibit a large fraction of low energy neutrons due to evaporation processes and a relatively low contamination due to the fast neutron component. Finally, we selected the Ta (p,n) reaction for the neutron source of accelerator-based BNCT from the followings;

1) The evaporation peak produced by the reaction between protons and heavy elements in the backward direction is practically identical in magnitude to the one in the forward direction as shown in Fig.1, although the neutron yield in the high energy region is much lower in the backward direction than in the forward direction.
2) The neutron energy spectra and the neutron yields for Ta(p,n) and W(p,n) reactions (E_p=50 MeV) are quite similar neutron yields in the entire energy region at all emission angles according to our measurements.
3) As shown in Fig. 2, the Be(d,n) reaction has a larger fraction of high energy neutron contamination than the Ta(p,n) reaction, without a pronounced evaporation peak.
4) The Ta target has relatively high boiling and melting points, which is very important in respect of target cooling. The W target has better heat properties than the Ta target, whereas W is soluble in water under high irradiation flux and at high temperature. This solubility is of disadvantage to water cooling.

For the above reasons, we selected to use neutrons emitted around 90 degree from the Ta(p,n) reaction.

2. Moderators

The moderators are inevitably required to shape neutrons emitted from the neutron source into epithermal neutrons that are appropriate for BNCT. Generally, moderators are introduced into the accelerator-based BNCT system only for shaping epithermal neutrons. However, we introduced the moderator assembly combined the epithermal neutron filter with an additional material that effectively slows down high-energy neutrons because the neutron production reaction with medium- to high-energy proton beams results in the contamination of high energy neutrons beyond MeV energies, Based on the Monte Caro studies, the combination of iron backed by AlF_3, Al and LiF layers were finally selected for the moderator assembly.

3. Optimization of the moderator assembly

Figure 3 shows the schematic view of the accelerator-based BNCT neutron source assembly optimized for incident protons of 50 MeV.[13)] A lead gamma-ray absorber, a lead reflector and lithium fluoride collimator are additionally introduced into the moderator assembly. Figures 4 and 5 show calculated depth dose distribution and neutron energy spectrum behind the moderators by using moderator assembly shown in Fig. 3. Table 2 shows figure of merits obtained by the moderator assembly. This assembly can provide better dose distribution at deeper positions within a phantom than that of the presently employed reactor-based neutron sources, and adequate epithermal neutron flux for the BNCT clinical application.

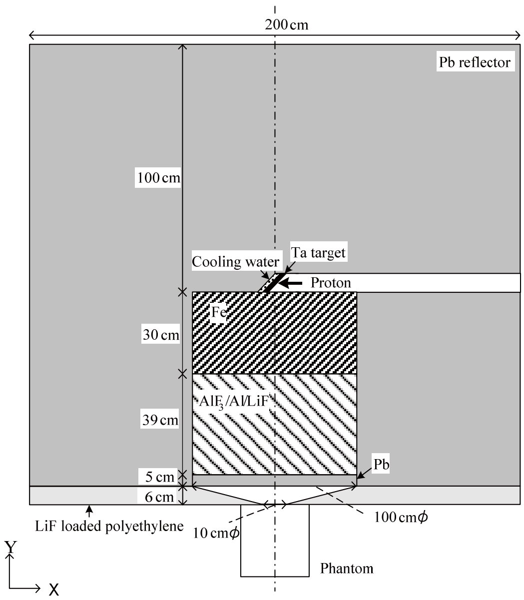

Fig.3. Schematic view of an assembly optimized for incident protons of 50 MeV[13)]

III. Application of accelerator-based BNCT with medium- to high-energy proton beams

We extended our investigation with 50 MeV proton beams to cover medium- to high-energy accelerators with a proton energy range of 30 to 600MeV. As a result, it was found that the acclerator-based BNCT is feasible using 30 to 600MeV protons only by adjusting the iron moderator thickness. This finding leads commercial accelerators routinely used for the production of SPECT and PET radiopharmaceuticals into the accelerator-based BNCT. Also, the 600MeV proton linac at J-PARC will be useful for generating a BNCT neutron field. Currently-employed proton radiotherapy accelerators can not be directly applied for

BNCT due to the low beam current. However, if the accelerator having the high proton beam intensity could be used, the combined radiotherapy between the proton radiotherapy, which is effective for various localized cancers but not for radio-resistant cancers, and BNCT, which is effective for nonlocalized and radio-resistant cancers, can have a very wide applicability.

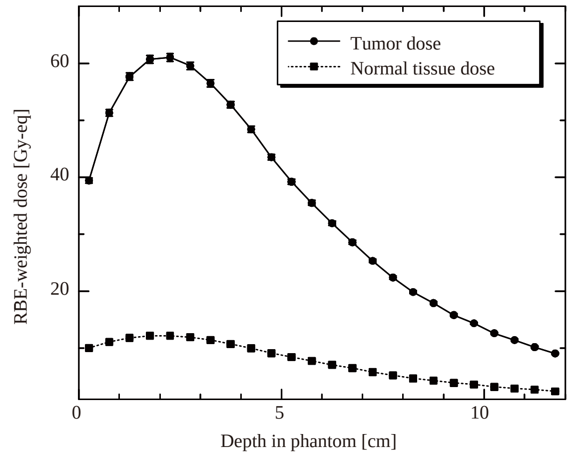

Fig. 4. Calculated depth dose distribution by using moderator assembly shown in Fig. 3.
(^{10}B concentration : 13 ppm for normal tissue, 45.5 ppm for tumor tissue.)

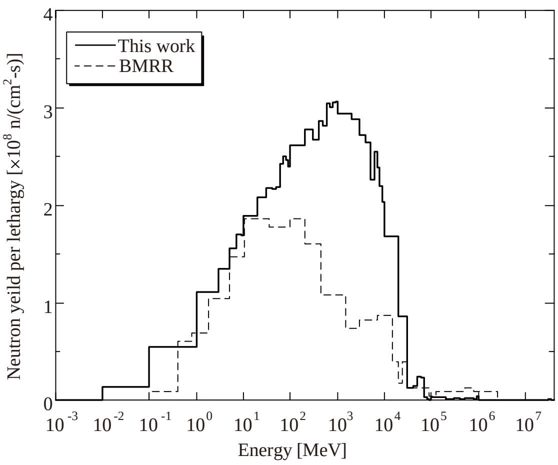

Fig. 5. Calculated neutron energy spectrum behind the moderators

Table 2. Figure of merits obtained by using the moderator assembly shown in Fig. 3

Therapeutic time [min]	D_{max} [Gy-eq]	D_{5cm} [Gy-eq]	$D_{8\ cm}$ [Gy-eq]	Epithermal neutron flux (4eV-40keV) [n/(cm^2-s)]
23.9	61.0	41.4	21.1	2.01×10^9 (±0.02×10^9)

D_{max}: maximum tumor dose, D_{5cm} and D_{8cm}: Tumor dose at a depth of 5 or 8 cm

IV. Conclusion

Our systematic study of accelerator-based BNCT using medium- to high-energy proton beams was introduced in this paper. This concept is currently developing, especially in Japan. An epithermal neutron generator for BNCT based on the Be(p,n) reaction using a 30 MeV proton cyclotron accelerator is under construction to start operation in the spring of 2009.[14)] Also, an epithermal neutron generator using 400MeV Protons from the J-PARC linac is continuously being studied.[15)] Though further verifications of the simulations in more detail in order to realize the neutron field for clinical use are required, the neutron source using medium- to high-energy proton beams is expected to be very promising for the accelerator-based BNCT.

Acknowledgement

These studies were carried out in collaboration of Tohoku University, Mitsubishi Heavy Industries, Ltd., Engineering Development Co., Ltd. and Advanced Reactor Technology Co., Ltd. I would like to thank Prof. Baba (Tohoku University) and Dr. Tahara (Japan Science and Technology Agency) for their comments and suggestions to write this paper.

Reference

1) J. C. Yanch et al., “A Monte Carlo investigation of the dosimetric properties of monoenergetic neutron beams for neutron capture therapy,” Radiat. Res. 126, 1-20 (1991)

2) K.Tanaka et al., “Irradiation characteristics of BNCT using near-threshold ^{7}Li(p,n)^{7}Be direct neutrons: application to intra-operative BNCT for malignant brain tumours,” Phys. Med. Biol. 47, 3011-3032 (2002)

3) C.L. Lee et al. “A Monte Carlo dosimetry-based evaluation of the ^{7}Li(p,n)^{7}Be reaction near threshold for accelerator boron neutron capture therapy,” Med. Phys. 27 (1), 192-202 (2000)

4) O.E. Kononov et al., “Optimization of an accelerator-based epithermal neutron source for neutron capture therapy,” App. Rad. and Iso. 61, 1009-1013 (2004)

5) D. L. Bleuel et al, “Designing accelerator-based epithermal neutron beams for BNCT,” Med. Phys. 25(9), 1725-1734 (1998)

6) J.E. Woollard et al. “A comparison of neutron beams for BNCT based on in-phantom neutron field assessment parameters,” Med. Phys. 28(9), 184-193 (2001)

7) D.A. Allen et al., “Toward a final design for the Birmingham boron neutron capture therapy,” Med. Phys. 26, 77-82 (1999)

8) J.M. Verbeke et al. “Investigation of ^{2}H(d,n)^{3}H and ^{3}H(d,n)^{4}H fusion reactions as alternative neutron sources for BNCT,” 8th Int. Symp. on NCT for Cancer, Sep 13-18 , Ja jolla, CA, USA (1998)

9) S. Yonai et al., “Feasibility study on epithermal neutron field for cyclotron-based boron neutron capture therapy,” Med. Phys., 30 (8), 2021-2030 (2003).

10) S. Yonai et al., “Benchmark Experiment for Cyclotron-Based Neutron Source for BNCT,” Appl. Radiat. Iso., 61, 997-1001 (2004)

11) S. Yonai et al. “Influences of neutron source spectrum and thermal neutron scattering law data on the MCNPX simulation of a cyclotron-based neutron field for boron neutron capture therapy,” J. Nucl. Sci. Technol., 44[11], 1361-1367 (2007)

12) Y. Tahara et al.,“Engineering design of a spallation reaction-based neutron generator for Boron Neutron Capture Therapy, ” J. Nucl. Sci. Technol., 43[1], 9-19(2006).

13) S. Yonai et al., “Extension of spallaition-baesd BNCT concept to medium- to high-energy accelerators,” J. Nucl. Sci. Technol., 45[5], 378-383 (2008)

13) S. Yonai et al., “Optimization of moderator assembly for cyclotron-based BNCT taking account of target structure,” The 4th Japan-Korea Joint Meeting on Medical Physics and the 5th Asia-Oceania Congress of Medical Physics, Kyoto, September, 2005, Japanese Journal of Medical Physics, 25 supplement No. 3-2, 157-160, 2005

14) H. Tanaka et al., “An epithermal neutron generator based on the Be(p,n) reaction using a 30 MeV proton cyclotron accelerator at KURRI,” 13th International Congress on Neutron Capture Therapy Florence, Italy, November 2-7, 2008

15) Y. Tahara et al., “Epithermal Neutron Generator Using J-PARC 400MeV Protons,” 13th International Congress on Neutron Capture Therapy Florence, Italy, November 2-7, 2008

10. A Dispersive, Lane-consistent Optical Potential, Coupled-channel Optical Model Code OPTMAN and its Application

Efrem Sh. Soukhovitski*, Satoshi Chiba†, Roberto Capote** and Jose M. Quesada‡

*Joint Institute of Energy and Nuclear Research-Sosny, Academician A.K. Krasin Str. 99, Minsk 220109, Belarus
†Japan Atomic Energy Agency, Tokai-mura, Nakagun, Ibaraki 319-1195, Japan
**NAPC-Nuclear Data Section, International Atomic Energy Agency, Vienna A-1400, Austria
‡Departamento de Fisica Atomica, Molecular, Univesidad de Sevilla, Ap.1065,E-41080 Sevilla, Spain

Abstract. Coupled-channels optical model code OPTMAN is widely applied to analyze experimental nucleon-nucleus interaction data and evaluation. Recently sophisticated dispersive optical potential forms had been included in the code along with possibility to calculate direct excitations of isobar analog states in (p,n) reactions. The latter along with accounting of the proton "effective" energy decrease due to Coulomb repulsion by nuclei, leads to completely Lane-consistent optical potential. Such approach had been successfully applied to nucleon-nucleus interaction experimental data analyses of different A-mass nuclides up to incident energies 200 MeV.

INTRODUCTION

Coupled-channels optical model is an effective and powerful method for prediction of nucleon-nuclear interaction cross sections, simultaneously providing transmission coefficients to enter statistical models for calculations of various inelastic and reaction cross sections. The functions to be used in calculations of matrix elements in a quantum-mechanical way, e.g., for DWBA and other accurate approuches are also supplied.

Requests on evaluated nuclear data from various applications expanding list of nuclides and interacting nucleon energy can be only satisfied by utilizing optical model codes with a sophisticated optical model potential (OMP). Such OMP must be derived as a result of best-fit description of all available regional experimental data, allowing reliable prediction of the data for isotopes measurements for which are unavailable or not reliable.

OMP accounting dispersive relationships between its imaginary and real part[1, 2], as much more theoretically grounded pretend to give much more reliable results. It is expected, that dispersive potentials should have much less free adjustable parameters, as the letter appear to compensate unaccounted dispersive contributions. It is also expected, that dispersive potentials by the same reasons should allow usage of energy independent nuclear form-factor geometry.

In this work, we propose dispersive Lane-consistent optical potential form and demonstrate its application to analyses of experimental optical data for nuclides from different A-mass regions. This activity is based on using couples-channel optical code OPTMAN, which new version, modernized under ISTC Project B-1319 activity incorporates already these options.

DISPERSIVE LANE-CONSISTENT OPTICAL POTENTIAL FORM

We consider, that dispersive potential depending of energy can be written as:

$$
\begin{aligned}
V(r,R(\theta',\varphi'),E) = & -V_{HF}(E)\times f_{WS}(r,R_R(\theta',\varphi'))+ \\
& -[\Delta V_V(E)+iW_V(E)]\, f_{WS}(r,R_V(\theta',\varphi')) \\
& -[\Delta V_D(E)+iW_D(E)]\, g_{WS}(r,R_D(\theta',\varphi')) \\
& +\left(\frac{\hbar}{m_\pi c}\right)^2 [V_{so}(E)+iW_{so}(E)] \qquad (1)\\
& \times \frac{1}{r}\frac{d}{dr} f_{WS}(r,R_{so})\left(\hat{\sigma}\cdot\hat{L}\right) \\
& +V_{Coul}(r,R_c(\theta',\varphi')),
\end{aligned}
$$

where the first term is the real smooth, so called Hartree-Fock (HF), volume potential. Successive complex-valued terms are the volume, surface and spin-orbit potentials, all containing the corresponding dispersive contributions $\Delta V_V(E), \Delta V_D(E)$ and $\Delta V_{so}(E)$.

It is known that the energy dependence of the depth $V_{HF}(E)$ is due to the replacement of a microscopic nonlocal HF potential by a local equivalent. For a Gaussian non-locality, $V_{HF}(E)$ is a linear function of E for large negative E and is an exponential for large positive E. Following Mahaux and Sartor [3], the energy dependence of the smooth HF part of the nuclear mean field is taken as that found by Lipperheide [1], accounting the isospin dependence [4]: $V_{HF}(E) = V_R^{DISP}\left[1+(-1)^{Z'+1}\frac{C_{viso}}{V_R^{DISP}}\frac{N-Z}{A}\right]\exp(-\lambda_R(E-E_F))$. In case of proton potential Coulomb correction $\Delta V_R^{Coul}(E)$, which in standard approach is proportional to potential derivative $\Delta V_R^{Coul}(E) = -C_{Coul}\frac{ZZ'}{A^{1/3}}\frac{d}{dE}(V_R(E))$. Similar Coulomb correction terms $\Delta V_V^{Coul}(E)$ and $\Delta V_D^{Coul}(E)$ are also calculated for volume $\Delta V_V(E)$ and surface $\Delta V_D(E)$ dispersive contributions to the real potential. For the reasons explained below we do not show Coulomb correction terms in the OMP(1). The geometrical form factors are given as:

$$
\begin{aligned}
f_{WS}(r,R_i(\theta',\varphi')) &= \left[1+\exp\left[\left(r-R_i(\theta',\varphi')\right)/a_i\right]\right]^{-1}, \\
i &= R,V,so
\end{aligned}
$$

$$
g_{WS}(r,R_D(\theta',\varphi')) = -4a_D\frac{d}{dr}f(r,R_D(\theta',\varphi')),
$$

where $R_i(\theta',\varphi')$ denotes the deformed radii with the deformations considered, while spin-orbit potential is considered to be not deformed.

In our formulation of the OMP in in the geometrical parameters of the Hartree-Fock potential R_R and a_R are in general different from the geometrical parameters R_V, a_V, R_D, a_D of the volume and surface absorptive potentials; however the real and imaginary spin-orbit terms share the same R_{so} and a_{so} parameters. Therefore the volume dispersive contribution has different geometry (determined by R_V and a_V) from the real smooth volume potential (determined by R_R and a_R). As a result we have two separate volume contributions to the potential (as can be seen in the first and second line of Eq.(1)), effectively giving us more flexibility for the fitting of the experimental data. The present optical potential includes relativistic corrections as discussed by Elton [5] and explained in our recent paper [6]. It is useful to represent the variation of surface $W_D(E)$ and volume absorption potential $W_V(E)$ depth with energy in functional forms suitable for the dispersive optical model analysis. A commonly used energy dependence for the imaginary-surface term has been suggested by Delaroche *et al.* [7],

$$
W_D(E) = A_D\frac{(E-E_F)^2}{(E-E_F)^2+WID_D^2}\ \exp(-\lambda_D(E-E_F)). \tag{2}
$$

The isospin dependence of the surface and volume potential terms (the Lane term [4]) was considered in imaginary surface $W_D(E)$ and volume $W_V(E)$ potentials as follow,

$$
A_{D,V} = W_{D,V}^{DISP}\left[1+(-1)^{Z'+1}\frac{C_{wiso,wviso}}{W_{D,V}^{DISP}}\frac{N-Z}{A}\right]. \tag{3}
$$

An energy dependence for the imaginary volume term has been suggested in studies of nuclear matter theory by Brown and Rho [8]:

$$
W_V(E) = A_V\ \frac{(E-E_F)^2}{(E-E_F)^2+(WID_V^{DISP})^2}. \tag{4}
$$

The assumption that the imaginary potential $W(E)$ is symmetric about $E' = E_F$ is plausible for small values of $|E'-E_F|$, however as was pointed out by Mahaux and Sartor [3] this approximate symmetry no longer holds for large values of $|E'-E_F|$. In fact the influence of the nonlocality of the imaginary part of the microscopic mean field will produce an increase of the empirical imaginary potential $W(E')$ at large positive E' and approaches zero at large negative E' [9, 10]. The DOM analysis of neutron scattering on ^{232}Th [6] showed the importance of the non-local contribution to describe total cross-section σ_T data for energies above 100 MeV using a non-symmetric version of the volume absorptive potential for large positive and large negative energies. For the details of the implementation of the imaginary potential $W(E)$ symmetry braking due to nonlocality see Ref[6].

LANE CONSISTENCY OF THE OMP AND DIRECT EXCITATIONS OF THE ISOBARIC ANALOG STATES (IAS)

An isospin-dependent coupled channel optical model potential, can be used to predict direct quasi-elastic (p,n) scattering to the isobaric analogue states (IAS) of the target nucleus; being such exercise the best test of the quality of the isovector part of the optical potential. It has been pointed out by Lane [4] that the optical model potential can be written in a charge-independent form. The extent to which we can state that a derived optical model potential is *Lane-consistent* can be established from the basic Lane equations [4]:

$$
\begin{aligned}
V_{pp} &= V_0+\frac{N-Z}{4A}V_1 \\
V_{nn} &= V_0-\frac{N-Z}{4A}V_1 \\
V_{pn} &= \frac{\sqrt{N-Z}}{2A}V_1,
\end{aligned} \tag{5}
$$

where V_0 and V_1 are the isoscalar and isovector components of the potential with the Coulomb interaction switched off. In such way one is able to calculate the charge-exchange channels in a (p,n) reaction (to the *elastic IAS* and excited states of the rotational band of the residual nucleus).

An accurate calculation of the nucleon scattering from deformed nuclei must include the coupling to the low-lying collective states. A very successful computational method to account for the importance of the multistep processes is the coupled-channel (CC) method using Tamura's formalism [11], which permits an exact solution of the Lane CC equations. The Coulomb displacement energy, Δ_C, between the ground state and its corresponding IAS is well approximated by the empirical relation [12], $\Delta_C = 1.444Z/A^{1/3} - 1.13$ MeV, with Z being equal the average charge of the target and residual nuclei in the reaction. As example for actinide targets, the value of Δ_C is about 20 MeV. The coupling formfactors for the charge-exchange calculations are defined as

$$\begin{aligned}
&< \nu;0^+_{IAS}|V(\tau,\vec{r})|\pi;0^+_{gs} > \\
&=< \nu|\mathscr{T}|\pi >< 0^+_{IAS}|V_1^{diag}(r)|0^+_{gs} > \\
&= \frac{\sqrt{(N-Z)}}{2A} < 0^+_{IAS}|V_1^{diag}(r)|0^+_{gs} >, \qquad (6)
\end{aligned}$$

for the "quasi-elastic" $0^+_{gs} \to 0^+_{IAS}$ excitation of the *IAS*, as a particular case of

$$\begin{aligned}
&< \nu;I^+(residual)|V(\tau,\vec{r})|\pi;I^+(target) > \\
&=< \nu|\mathscr{T}|\pi >< I^+(residual)|V_1(\vec{r})(|I^+(target) > \\
&= \frac{\sqrt{(N-Z)}}{2A} < I^+(residual)|V_1(\vec{r})|I^+(target) >, \quad (7)
\end{aligned}$$

for the coupling between analog states of both rotational bands, and

$$\begin{aligned}
&< \nu;I^{+\prime}(residual)|V(\tau,\vec{r})|\pi;I^+(target) > \\
&=< \nu|\mathscr{T}|\pi >< I^{+\prime}(residual)|V_1^{coupl}(\vec{r})(|I^+(target) > \\
&= \frac{\sqrt{(N-Z)}}{2A} < I^{+\prime}(residual)|V_1^{coupl}(\vec{r})|I^+(target) >, \\
&\qquad (8)
\end{aligned}$$

for the coupling between $I' \neq I$ states. In these expressions $\mathscr{T}$ is the isospin operator, ν and π represent the entrance and exit isospin states of projectile and ejectile respectively and $V_1^{diag}(r)$ and $V_1^{coupl}(\vec{r})$ are the usual spherical and deformed components of the isovector potential, as defined in the Tamura's *canonical* work [11]. These expression have been implemented into the OPTMAN code allowing to directly calculate the quasi-elastic scattering cross-section or to consider existing IAS scattering data during the optical potential fitting. In this way the isovector component of the potential is much better constrained, as coupling with IAS states, determined by the third line of Eq.(5) is proportional to pure isovector term. In our recent work [13] we determined global potential for actinides. This potential describes all available optical data for actinides within 1.5 experimental error in average for both incidents neutrons and protons up to 200 MeV energies. Ratio of U Th cross sections, that is measured much more accurately and is not described by any other potential is described with excellent accuracy by our potential. Figs. 1-2 demonstrate the quality of neutron total cross-sections predictions for various actinide isotopes.

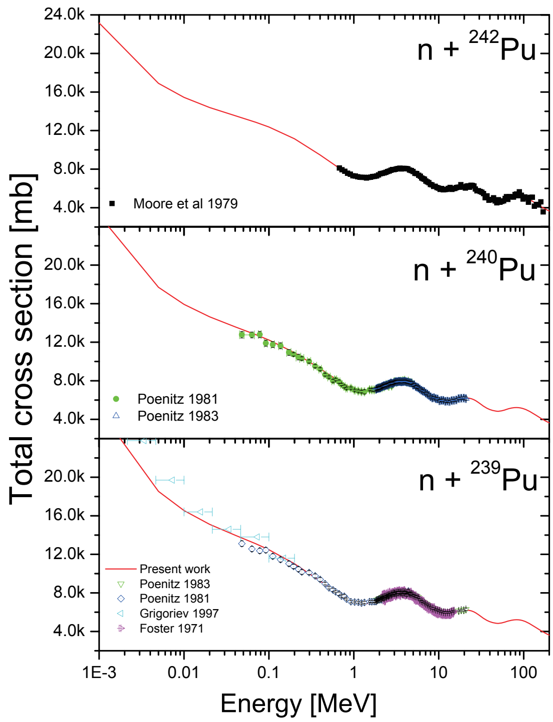

FIGURE 1. Comparison of total cross-sections predictions for Pu isotopes with experimental data.

Low energy observables such as neutrons strength functions S_0, S_1 and scattering radii R' are also reproduced by our calculations. It is significant, that adjusted individual deformation values allowing the best fit of experimental data for different actinides coinside within 10% the theoretically calculated values.

Using new option allowing direct IAS excitation calculations, the determined potential had been use to cal-

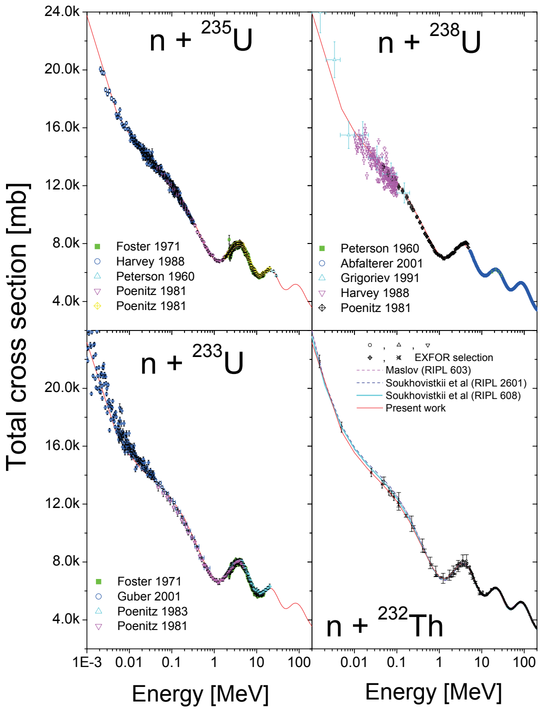

FIGURE 2. Comparison of total cross-sections prediction for U-Th isotopes with experimental data.

culate Angular distributions of IAS for ^{238}U and ^{232}Th. Fig. 3 demonstrates the quality of angular distribution of neutrons emitted in p+ ^{238}U$\longrightarrow$n+^{238}Np reaction predictions. One can see that we describe experimental IAS angular distributions with good accuracy. Fig. 4 shows similar comparison for IAS scattering on ^{232}Th.

So all allows us to state, that we have dispersive *approximate* Lane consistent optical potential for actinides. We say *approximate*, as the potential used is not symmetric for protons and neutrons, having Coulomb correction terms in proton case. Below we explain how the problem can be solved.

EXACT LANE CONSISTENT COULOMB CORRECTION POTENTIAL FORM

The nature of the Coulomb correction used for incident charged particles is well understood. It is applied for incident protons to account for the change of the interacting proton energy due to Coulomb repulsion of it by nucleus. Usually such corrections were assumed either the

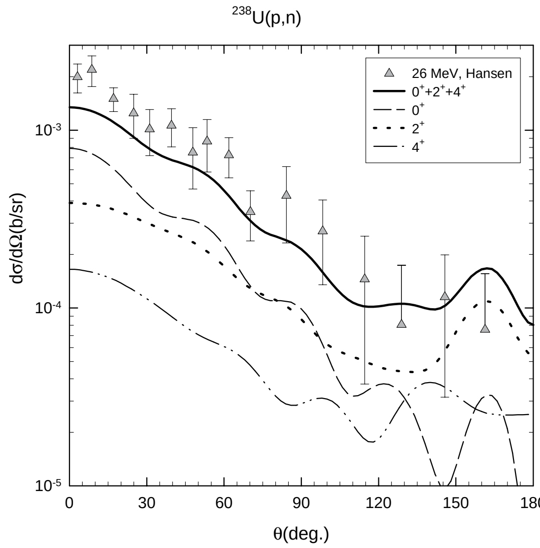

FIGURE 3. Calculated and experimental neutron angular distribution emitted in p+ ^{238}U$\rightarrow$n+^{238}Np reaction.

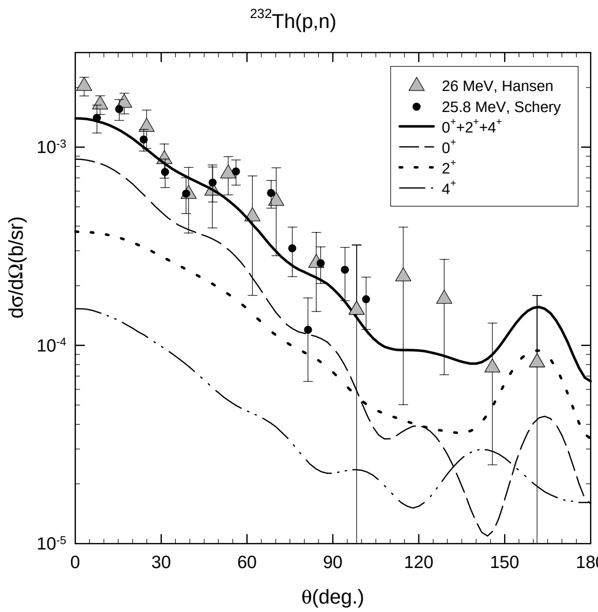

FIGURE 4. Comparison of calculated neutron angular distribution emitted in p+ ^{232}Th$\rightarrow$n+^{232}Pa reaction with experimental data.

value proportional to the derivative of real potential:

$$\Delta V_R^{Coul}(E) = -C_{Coul}\frac{ZZ'}{A^{1/3}}\frac{d}{dE}(V_R(E)), \qquad (9)$$

or as an energy-independent constant to be added to the real potential, that straight comes from Eq.(9) for linear depended real potentials. One can see, that such correction is just the first term of Taylor expansion of the proton potential accounting for the Coulomb repulsion, assuming that the "effective" interacting energy of the proton is $E - C_{Coul}\frac{ZZ'}{A^{1/3}}$. It should be noted that constant e^2 in our definition is included in constant C_{Coul}. In fact, the term $C_{Coul}\frac{ZZ'}{A^{1/3}}$ is an estimation of the kinetic energy loss of the incident proton in the interaction region due to Coulomb repulsion. Indeed, the optical potential at this "effective" energy becomes:

$$V(E - C_{Coul}\frac{ZZ'}{A^{1/3}}) = V(E) - C_{Coul}\frac{ZZ'}{A^{1/3}}\frac{d}{dE}(V_R(E)) + ... \tag{10}$$

Above the left side of formula [10] is a generalization of the previously used Coulomb correction, which considers such corrections in all orders. It has been included in the OPTMAN code by using the "effective" energy $E - C_{Coul}\frac{ZZ'}{A^{1/3}}$ for incident protons instead of the physical incident energy E. The constant C_{Coul} is an adjustable constant meant to account for the "effective" radius of interaction of proton in nucleus. It's value is expected to be near one. It should be noted that full Coulomb correction as defined by [10] is a pre-condition to the exact Lane consistency, as with such Coulomb correction OMP becomes completely symmetric with the respect of nucleon charge.

By the moment we have dispersive Lane consistent potentials for incident nucleon energies up to 200 MeV for the actinides and Hf/Ta/W regions and for a number of individual isotopes: ^{55}Mn, ^{103}Rh, ^{197}Au and ^{90}Zr for a soft-rotator case. The quality of IAS excitation predictions using this approach is demonstrated for ^{55}Mn and

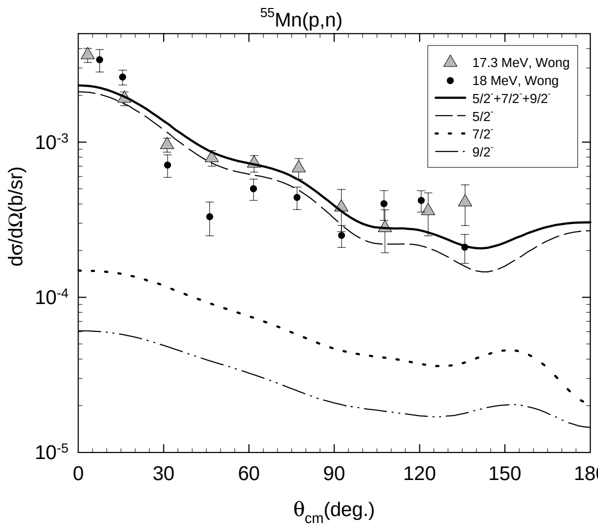

FIGURE 5. Comparison of calculated neutron angular distribution emitted in p+ ^{55}Mn⟶n+^{56}Fe reaction with experimental data.

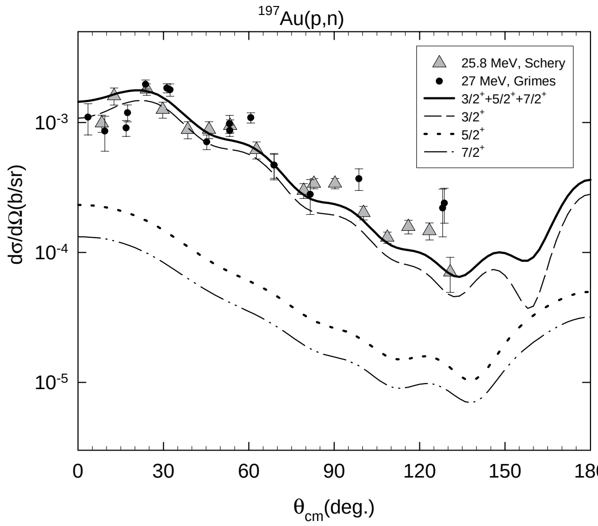

FIGURE 6. Comparison of calculated neutron angular distribution emitted in p+ ^{197}Au⟶n+^{198}Cd reaction with experimental data.

Recently we tried to get the Lane consistent OMP for such light nuclide as ^{9}Be, knowledge of (p,n) reaction cross section is very significant for medical applications in beam therapy. Finally in Figs. 7 - 10 we demonstrate

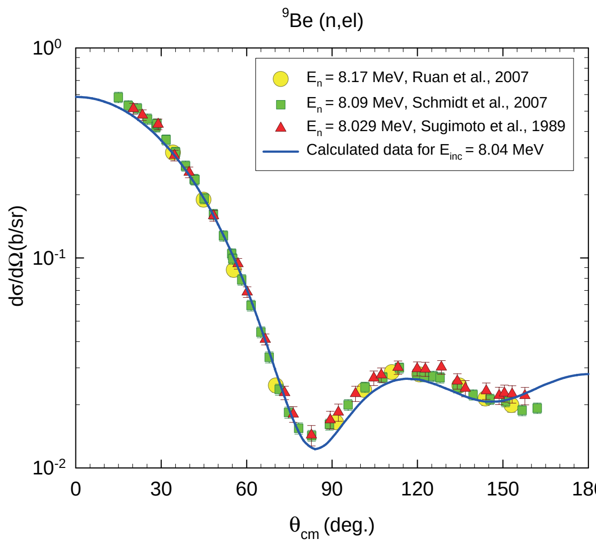

FIGURE 7. Comparison of experimental and predicted angular distributions of neutrons with incident energy 8.08 MeV elastically scattered by ^{9}Be.

CONCLUSION

We had developed dispersive Lane consistent OMP approach, which had been implemented in the new ver-

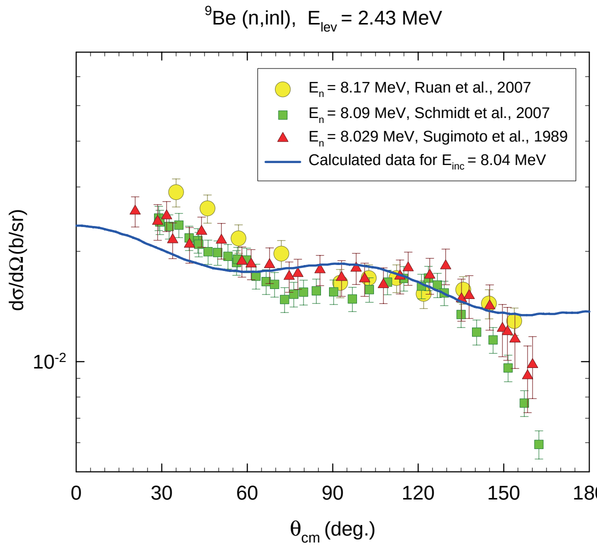

FIGURE 8. Comparison of experimental and predicted angular distributions of neutrons with incident energy 8.08 MeV inelastically scattered by ^{9}Be.

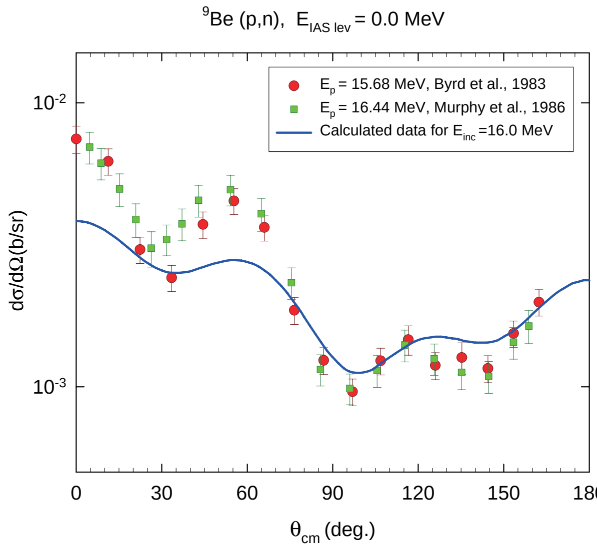

FIGURE 9. Comparison of experimental and predicted angular distributions of neutrons emitted in p+^{9}Be⟶n+^{10}B reaction with excitation of the ground state ^{10}B for incident proton energy 16.0 MeV.

sion of coupled-channel optical model code OPTMAN. Lane consistent OMP's describing available experimental data up to 200 MeV incident nucleon (both protons and neutrons) with high accuracy are suggested for actinides, Hf/Ta/W, ^{55}Mn, ^{103}Rh, ^{197}Au and ^{90}Zr.

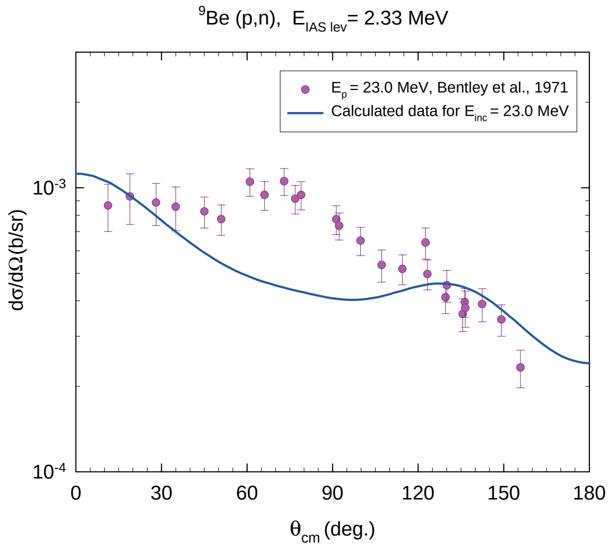

FIGURE 10. Comparison of experimental and predicted angular distributions of neutrons emitted in p+^{9}Be⟶n+^{10}B reaction with excitation of the second level of ^{10}B for incident proton energy 23.0 MeV.

ACKNOWLEDGMENT

This work was carried out as ISTC Project B-1319 with Japan and European Council as Financing Parties. It is also supported by Grant-in-Aid for Science Research (C) 18560805 of Japan Society for Promotion of Science. The authors are grateful to the guidance of later Dr Y. Kikuchi who had initiated the collaboration among authors. They thank the members of JIENR, IAEA Nuclear Data Section and JAEA Nuclear Data Center for helpful comments and supports. One of the authors, E. Soukhovitski, is grateful to Nuclear Data Center and Advanced Science Research Center of JAEA and IAEA Nuclear data Section for there financial support and hospitality during his stays, that made this work possible

REFERENCES

1. Lipperheide, Z., Z. Phys. **202**, 58 (1967).
2. Romain, P. and Delaroche, J.P.,Proc. of Meeting on Nucleon-Nucleus Optical Model up to 200 MeV, Brevers-le-Chatel, p.167 (available online), OECD, Paris, 1997.
3. Mahaux, C. and Sartor,R./*Nucl. Phys.* **A528**, *253*, (1991).
4. Lane ,A.V., Phys. Rev.Lett. **8**, 171 (1962); A.M. Lane, Nucl. Phys. **35**, 676 (1962).
5. Elton, R.L.B., Nuovo Cimento **XLII B**, **277** (1966).
6. Soukhovitskiĩ, E.Sh., Capote, R., Quesada, J.M., S. Chiba, *Phys. Rev. C* **72**, *024604* (2005).
7. Delaroche, J.P., Wang, Yu., and Rapaport, J., *Phys. Rev. C* **39**, *391*, (1989).
8. Brown, G.E. and Rho, M.*Nucl. Phys.* **A372**, *397*, (1981).

9. Mahaux, C, and Ngô, N., *Nucl. Phys.* **A431**, *486*, (1984).
10. Mahaux, C. and Sartor, R.,. *Nucl. Phys.* **A458**, *25*, (1986).A. M. Lane. *Phys. Rev. Lett.* **8**, *171*, (1962).
11. Tamura, T., Rev. Mod. Phys. **37**, 679 (1965).
12. Anderson, A.D., Wong, C., and McClure, J.W., *Phys. Rev.* **138**, *B615*, (1965).
13. Capote, R., Chiba, S., Soukhovitskii, E.Sh., Quesada, J.M. and Bauge E.,*JNST* **45**, *333*, (2008).

This is a blank page.

11. Neutrino Physics and Nuclear Data

Takashi Yoshida

e-mail: tyoshida@astron.s.u-tokyo.ac.jp

Supernovae supply many kinds of elements produced in their evolution. They are also one of the main neutrino sources in the Universe. This strong neutrino emission enables to enhance the abundances of some less abundant elements through neutrino-nucleus reactions. We explain the neutrino nucleosynthesis in supernovae. Cross sections of neutrino-nucleus reactions calculated using new shell-model Hamiltonians for ^{4}He, ^{12}C, and ^{56}Ni are shown. The dependence of the abundances of light elements and odd iron-peak elements in supernovae on the ν-process cross sections are investigated. Astrophysical applications of the ν-process elements are also discussed.

1. Neutrino Emission from Supernovae

Stars with masses of $\sim 12-20M_\odot$ end their lives as supernova (SN) explosions. Many kinds of elements are synthesized in SNe and a huge amount of neutrinos are released. Although SN explosion mechanism has not been clarified completely, recent hydrodynamics studies revealed general features of the time evolution of SNe. Figure 1 shows a schematic diagram of the time evolution of a SN. First, the central Fe core collapses by photo-disintegrations and electron captures (a). The electron captures produce ν_e. When the density of the collapsing core is larger than $\sim 10^{11}$ g cm^{-3}, neutrinos are trapped in the central region, i.e., a neutrino sphere is formed (b). When the core density becomes to $\sim 10^{14}$ g cm^{-3}, accreting materials bounce at the core and the shock wave propagates outward (c). When the shock wave arrives at the neutrino sphere, materials around the neutrino sphere are heated and dissociated into protons and neutrons. As a result, electron captures proceed rapidly and neutronization burst occurs (d). The shock wave is considered to grow up by standing shock accretion shock instability (SASI) (e) . The shock wave passes through the central core and finally explodes the surrounding stellar materials (f).

After the neutronization burst, neutrinos are continuously released by the proto-neutron star cooling in a time scale of several seconds (g). Neutrinos inside the neutrino sphere are thermalized by neutrino-nucleus reactions. Whereas neutral-current reactions affect all flavor neutrinos, charged-current reactions affect ν_e and $\bar{\nu}_e$. The reactions for ν_e are effective more than those of $\bar{\nu}_e$ because of neutronization of the core. Therefore, the neutrino sphere of each neutrinos is smaller in the order of $R_{\nu_{\mu,\tau}}$, $R_{\bar{\nu}_e}$, and R_{ν_e}, and the average energy is larger in the order of $\langle \varepsilon_{\nu_{\mu,\tau}} \rangle$, $\langle \varepsilon_{\bar{\nu}_e} \rangle$, and $\langle \varepsilon_{\nu_e} \rangle$ (h). Typical value of average neutrino energy is $\sim 10-20$ MeV. The total energy carried by neutrinos is almost equal to the gravitational binding energy of a proto-neutron star, $E_{\nu,total} \sim 3 \times 10^{53}$ ergs. The corresponding neutrino number is $\sim 10^{58}$. Typical explosion energy of a SN is evaluated as 1×10^{51} ergs, which is about 0.3 % of the total neutrino energy.

The neutrinos emitted from a proto-neutron star interact with nuclei in the exploding stellar materials. When typical radius of stellar interior is $\sim 10^9$ cm, the total neutrino number flux is $\phi_\nu dt \sim 10^{37}$ cm^{-2}. A typical cross section of neutrino-nucleus reactions is $\sigma_\nu \sim 10^{-42}$ cm^2. Therefore, the production ratio of products to target nuclei by a neutrino-nucleus reaction is $\sigma_\nu \phi_\nu dt \sim 10^{-5}$. This production ratio is not so large for abundant elements. However, this synthesis process is important for less abundant elements. It is called the ν-process. The ν-process is the main production process for light elements ^{7}Li, ^{11}B, ^{15}N, and ^{19}F in SNe [1, 2, 3, 4, 5, 6, 7]. This process affects Mn production in innermost regions [8]. Neutron-deficient nuclei ^{138}La and ^{180}Ta are also produced through the ν-process [3].

Cross section data of neutrino-nucleus reactions are important for evaluating isotopic and elemental yields of the species of nuclei produced through the ν-process. Recently, the cross sections of neutrino-^{12}C and ^{4}He reactions have been calculated using new shell model Hamiltonians. These cross sections

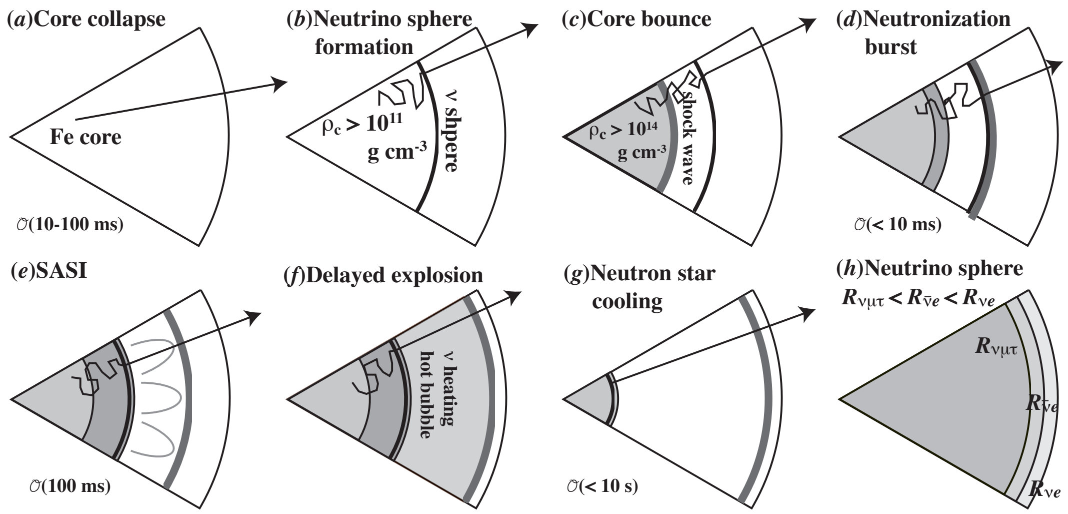

Figure 1: Schematic diagram of SN explosion. (a) core collapse, (b) neutrino sphere formation, (c) core bounce, (d) neutronization burst, (e) SASI, (f) delayed explosion, (g) proto-neutron star cooling, (h) locations of neutrino sphere.

affect the yields of light elements, Li, Be, and B. The cross sections of the ν-process for ^{56}Fe and ^{56}Ni were also evaluated by considering the Gamow-Teller transition with a new pf-shell model Hamiltonian. The ν-process cross sections of ^{56}Ni have important roles for evaluating the Mn yield in SNe. In this proceeding, we show the dependence of the abundances of ^{11}B and Mn produced in SNe on new and conventional ν-process cross sections. We also discuss astrophysical applications of the abundances of ν-process elements.

2. Supernova Light Element Synthesis through the ν-Process

2.1. Cross sections of neutrino-nucleus reactions for ^{12}C and ^{4}He

Cross sections of neutrino-^{12}C reactions are calculated using Suzuki-Fujimoto-Otsuka (SFO) Hamiltonian [9, 10, 7]. Experimental values of the Gamow-Teller (GT) transitions and magnetic moments in most of p-shell nuclei are well reproduced by the SFO Hamiltonian [9]. The shell configuration space is included up to $3\hbar\omega$ and multipolarities up to $J = 4$. The effective axial coupling constant with $g_A^{\rm eff} = 0.95 g_A$, where $g_A = -1.263$ is the bare axial vector coupling constant, is adopted to reproduce the experimental GT strength of the charged-current cross section $^{12}{\rm C}(\nu_e, e^-)^{12}{\rm N}(1^+_{\rm g.s.})$ induced by neutrinos from π^+ and μ^+ decay at rest (DAR). The cross sections for ^{12}C to $^{12}{\rm C}^*(1^+, T = 1,\ 15.1\ {\rm MeV})$ induced by DAR neutrinos evaluated with the SFO Hamiltonian well reproduce the experimental ones. The contribution from spin-dipole transitions is also important for evaluating the cross sections for ^{12}C. The cross sections of $^{12}{\rm C}(\nu_e, e^-)^{12}{\rm N}^*$ induced by DAR neutrinos are evaluated with effective axial-vector coupling constants $g_A^{\rm eff} = 0.70 g_A$. The obtained cross section reproduces the experimental one [10].

The cross sections of neutral- and charged-current cross sections of ^{12}C with the SFO Hamiltonian are evaluated as a function of neutrino energy. Branching ratios for γ transitions and n, p, d, t, ^{3}He, and α knock-out channels are considered using Hauser-Feshbach theory. The cross sections as a function of the neutrino temperature assuming Fermi-Dirac energy distribution with zero-chemical potentials are also evaluated. Figure 2 shows the cross sections of neutral- and charged-current reactions of ^{12}C as a function of the neutrino temperature. The cross sections of the previous study in [11] (HW92) are also shown for comparison. Detailed tables for the cross sections of neutral- and charged-current reactions are listed as a function of neutrino energy in [7].

Cross sections of neutrino-^{4}He reactions are calculated using the Warburton-Brown (WBP) Hamiltonian [12, 10, 7]. Branching ratios of n, p, and d knock-out channels are considered. The d knock-out channels are important for ^{6}Li production [7]. The cross sections as a function of the neutrino temperature are shown in Figs. 2(g) and (h). Detailed tables of the cross sections as a function of the neutrino energy are listed in [7].

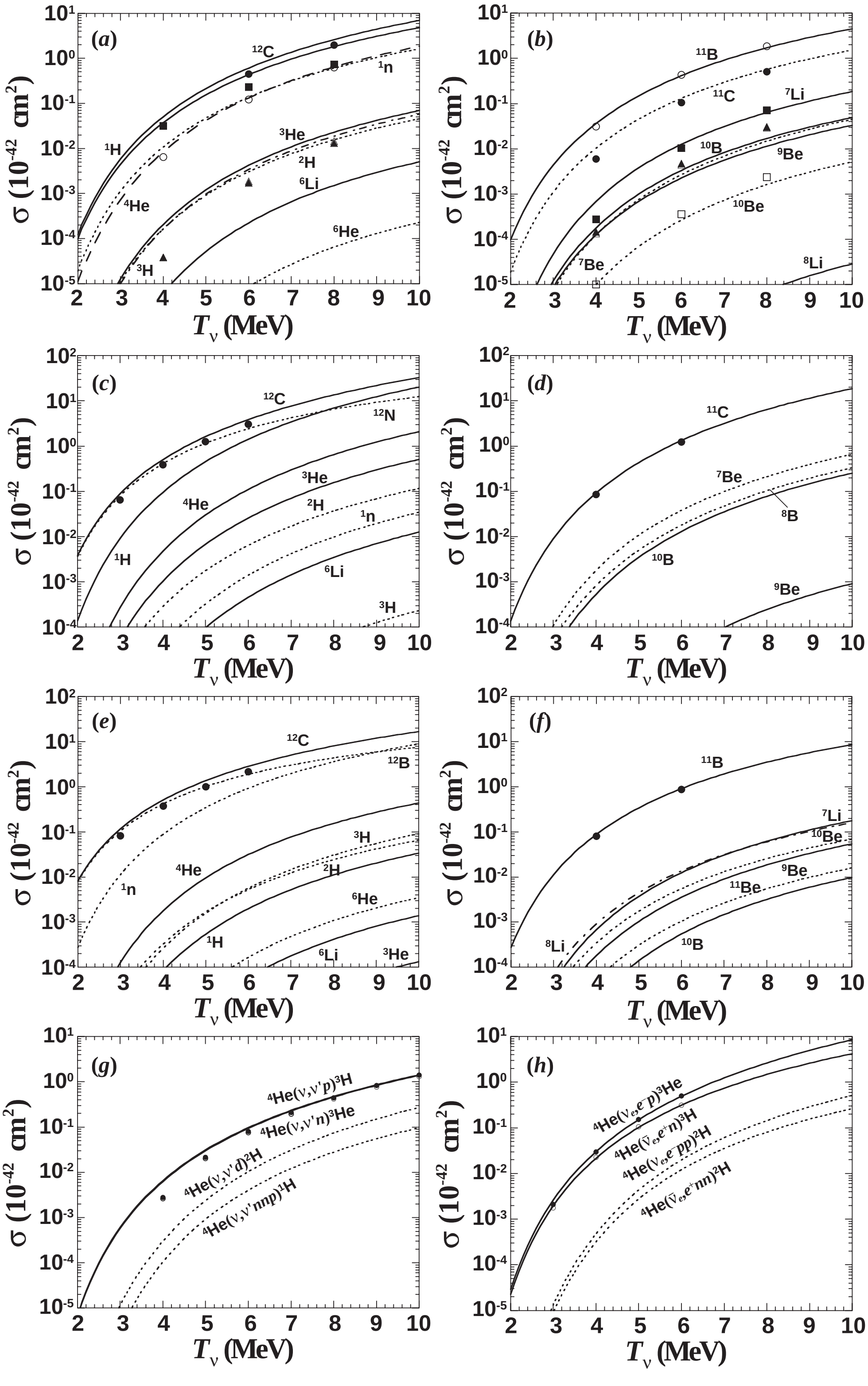

Figure 2: Cross sections of (a) and (b) neutral-current reactions, (c) and (d) charged-current $(\nu_e, e^- x)$ reactions, (e) and (f) charged-current $(\bar{\nu}_e, e^+ x)$ reactions for ^{12}C with the SFO Hamiltonian, and (g) neutral- and (h) charged-current reactions for ^{4}He with the WBP Hamiltonian. Symbols indicate the previous cross sections [11]. In (a), open circles, closed circles, squares, and triangles correspond to ^1n, ^{1}H, ^{3}He, and ^{12}C. In (b), open circles, closed circles, squares, and triangles correspond to ^{11}B, ^{11}C, ^{10}B, and ^{7}Li. In (c), (d), (e), and (f), circles correspond to ^{12}C, ^{11}C, ^{12}C, and ^{11}B, respectively. In (g), cross sections of proton- and neutron-emission are overlapped. In (h), open and closed circles correspond to $\bar{\nu}_e$ and ν_e reactions.

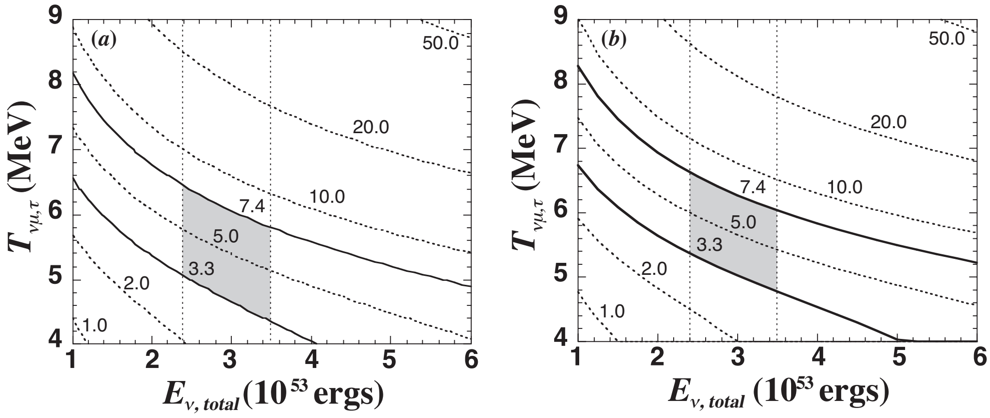

Figure 3: Contours of the ^{11}B yield in units of $10^{-7}M_\odot$ evaluated with (a) new reaction rates and (b) the conventional rates [11] as a function of the total neutrino energy and the neutrino temperature. The shaded regions satisfy the GCE constraint of the ^{11}B yield and the gravitational binding energy of a neutron star.

2.2. SN light element synthesis

Light element nucleosynthesis of a 16.2 $M_\odot$ star SN [13] corresponding to SN 1987A is calculated [2, 5, 6, 7]. The nuclear reaction network consists of 291 species of nuclei from ^1n, ^{1}H, to Ge [2]. In order to calculate the ν-process in the SN, the SN neutrino model is set as follows. The neutrino luminosity decreases exponentially with a time scale of 3 s. The luminosity is equally partitioned among three flavors of neutrinos and antineutrinos. The energy spectra of neutrinos emitted from the neutrino sphere obey Fermi-Dirac distributions with zero chemical potentials. The total neutrino energy $E_{\nu,total}$ is parametrized between 1×10^{53} ergs and 6×10^{53} ergs. The temperature of $\nu_{\mu,\tau}$ and $\bar{\nu}_{\mu,\tau}$, $T_{\nu_{\mu,\tau}}$ is also parametrized. The temperatures of ν_e and $\bar{\nu}_e$ are set to be (T_{ν_e}, $T_{\bar{\nu}_e}$) = (3.2 MeV, 5.0 MeV).

The main products through the ν-process among light elements in the SN are ^{7}Li and ^{11}B. When the total neutrino energy is 3×10^{53} ergs and the neutrino temperature $T_{\nu_{\mu,\tau}}$ is 6 MeV, the yields of ^{7}Li and ^{11}B are 2.7×10^{-7} $M_\odot$ and 7.1×10^{-7} $M_\odot$. The ^{7}Li is mainly produced in the He-rich layer and ^{11}B is produced in the O-rich and He-rich layers. In the He-rich layer, the ν-process reactions ^{4}He$(\nu,\nu'p)^3$H and ^{4}He$(\nu,\nu'n)^3$He mainly occur, and the following α-capture reactions ^{3}H$(\alpha,\gamma)^7$Li and ^{3}He$(\alpha,\gamma)^7$Be induced by the shock arrival produce ^{7}Li and ^{7}Be. An additional α-capture reaction ^{7}Li$(\alpha,\gamma)^{11}$B produces ^{11}B. In the O-rich layer, the ν-process reactions of ^{12}C, ^{12}C$(\nu,\nu'p)^{11}$B and ^{12}C$(\nu,\nu'n)^{11}$C, produce ^{11}B.

Light elements have been continuously produced by the ν-process in SNe and Galactic cosmic rays during Galactic chemical evolution (GCE). The meteoritic abundances and the abundances observed in metal-poor stars indicate traces of light element production in GCE. Since the light element yields depend on the characteristics of SN neutrinos, the observed abundances of the light elements constrain SN neutrinos. We constrain the neutrino temperature $T_{\nu_{\mu,\tau}}$ from the ^{11}B abundance determined from GCE models. We also investigate the dependence of the appropriate $T_{\nu_{\mu,\tau}}$ range on the adopted ν-process cross sections.

Figure 3 shows contours of the ^{11}B yield as a function of the neutrino temperature $T_{\nu_{\mu,\tau}}$ and the total neutrino energy $E_{\nu,total}$. We consider the ν-process cross sections with the SFO Hamiltonian for ^{12}C and the WBP Hamiltonian for ^{4}He (Fig. 3a) and with the previous HW92 rates [11] for ^{12}C and ^{4}He (Fig. 3b). Roughly speaking, the ^{11}B yield is in the range of $1 \times 10^{-7}M_\odot \sim 5 \times 10^{-6}M_\odot$ and the yield increases with $T_{\nu_{\mu,\tau}}$ and $E_{\nu,total}$. For a given $T_{\nu_{\mu,\tau}}$ and $E_{\nu,total}$, the yield evaluated using the cross sections with the SFO and WBP Hamiltonians is larger than that in the previous rates.

We evaluate from GCE models that the appropriate range of the ^{11}B yield produced in a $\sim 20M_\odot$ SN is between $3.3 \times 10^{-7}M_\odot$ and $7.4 \times 10^{-7}M_\odot$ [4]. This range is presented as a region between two thick solid curves in Fig. 3. The total neutrino energy is constrained from the gravitational binding energy of a $\sim 1.4M_\odot$ neutron star [14]. The appropriate range is between 2.4×10^{53} ergs and 3.5×10^{53} ergs. These energies are written as vertical dotted lines. Hence, the appropriate range of the neutrino

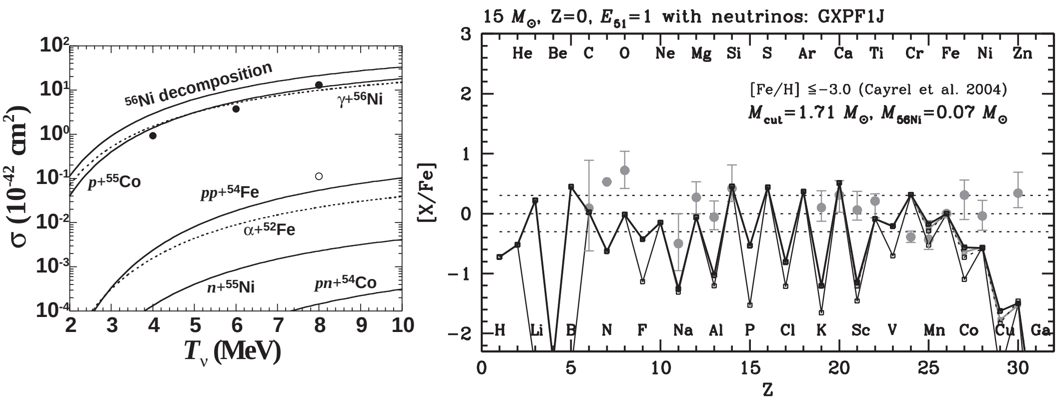

Figure 4: Left panel: Neutral-current cross sections of ^{56}Ni calculated using the GXPF1J Hamiltonian. Closed and open circles correspond to p and n knock-out channels in [11]. Right panel: Abundance distribution of a 15 $M_\odot$ Pop III star SN. Grey and dashed lines correspond to the abundances with the cross sections of the GXPF1J and HW92. Solid line corresponds to the abundances with twice as the GXPF1J cross sections. Thin solid line corresponds to the abundances without the ν-process. Circles are the observed abundances averaged in 22 EMP stars (see [8]).

temperature for the SFO and WBP Hamiltonians case is

$$4.3 \text{ MeV} < T_{\nu_{\mu,\tau}} < 6.5 \text{ MeV}. \tag{1}$$

In the case of HW92 rates, this range becomes between 4.8 MeV and 6.6 MeV. Therefore, the neutrino temperature range appropriate for the ^{11}B abundance in GCE evaluated using the new cross sections with the SFO and WBP Hamiltonians is slightly smaller than the case of the previous rates.

3. ν-Process for Odd Iron-Peak Elements

Recent progress of high resolution observations with large telescopes enables to measure the abundance distributions of extremely metal-poor (EMP) stars, of which metallicities are [Fe/H] < -3, where [X/Y] $\equiv \log_{10}(N_X/N_Y) - \log_{10}(N_X/N_Y)_\odot$, N_X and N_Y are the abundances of elements X and Y, $\odot$ means the solar value. These stars are considered to have suffered pollution from only several SNe and/or hyprenovae evolved from Population III (Pop III, i.e., first generation) stars. However, the abundances of some odd iron-peak nuclei evaluated with SN models are smaller than the observed abundances. The ν-process in Pop III SNe well reproduces the Mn abundance in EMP stars [8]. The evaluation of neutrino-^{56}Ni cross sections using a new shell model is in progress [15]. We investigate the ν-process in Pop III SNe and the dependence on neutrino-^{56}Ni reaction cross sections.

Neutrino-^{56}Ni reaction cross sections are investigated using a new shell model, GXPF1J [16], Hamiltonian [15]. This Hamiltonian well reproduces the GT strength distribution in ^{58}Ni and magnetic dipole moments for most of pf-nuclei. Neutral-current reaction cross sections of ^{56}Ni are calculated taking into account the GT transitions. Branching ratios for n, p, and α knock-out channels are considered. The cross sections as a function of the neutrino temperature are shown in Fig. 4 (left panel). The conventional cross sections [11] are also shown for comparison. For ^{56}Ni$(\nu, \nu' p)^{55}$Co which decays to ^{55}Mn, the new cross section is larger than the previous one in the neutrino temperature range appropriate for SNe.

We show the dependence of the abundance distribution in a 15 $M_\odot$ Pop III SN on the neutrino-^{56}Ni cross sections in Fig. 4 (right panel). We consider odd iron-peak nuclei. The abundances of odd iron-peak nuclei such as Sc, V, Mn, and Co with the ν-process are larger than those without the ν-process. In the innermost region of the SN ejecta where complete Si burning proceeds, the ν-process reactions of ^{56}Ni enhance the abundances of odd iron-peak nuclei. The abundance of ^{55}Mn is enhanced through ^{56}Ni$(\nu, \nu' p)^{55}$Co$(\beta^+)^{55}$Fe$(\beta^+)^{55}$Mn. Protons produced through this process increase the abundances of other odd iron-peak elements through p-captures. The Mn abundance calculated with the new cross sections is larger than the one with the previous rates. This enhancement is preferable to reproduce the Mn abundance observed in EMP stars. We also show the abundance distribution assuming that the neutrino-^{56}Ni reaction cross sections are twice as those of the GXPF1J owing to the consideration of other transitions (see solid line). The Mn abundance is slightly larger.

4. Summary and Outlook

We have explained neutrino nucleosynthesis in SNe. The nucleosynthesis of light elements and odd iron-peak elements were demonstrated. Neutrino-induced reaction cross sections evaluated using new shell model Hamiltonians were taken to the nuclear reaction network. Among light elements, ^{7}Li and ^{11}B are mainly produced through the ν-process. Neutral-current reactions of ^{4}He and ^{12}C mainly contribute to produce these nuclei. SN contribution to the ^{11}B abundance in GCE constrains the SN neutrino temperature. The appropriate range of the SN neutrino temperature with new ν-process cross sections is between 4.3 MeV and 6.5 MeV, which is slightly smaller than the range evaluated using the conventional rates. The ν-process also affects Mn production in SNe. The Mn abundance evaluated using the ν-process cross sections of ^{56}Ni with the GXPF1J Hamiltonian is more favorable to the observational abundance in EMP stars than that with the previous cross sections.

It is becoming possible to calculate multi-dimensional hydrodynamics with neutrino transport in SN explosions owing to progress of high-performance computing. Long time ($\sim$ 10 s) evolution from core collapse to proto-neutron star cooling will be evaluated. These calculations will show the time evolution of neutrino energy spectra different from Fermi-Dirac distributions. Neutrino oscillations also change neutrino spectra, which affect neutrino nucleosynthesis [5, 6, 7]. In these cases the ν-process reaction rates should be evaluated with non-thermal neutrino energy spectra. However, most of the ν-process rates except ^{1}H, ^{4}He, ^{12}C, and ^{56}Ni are tabulated as a function of neutrino temperature assuming Fermi-Dirac distribution [11]. In order to calculate the ν-process with non-thermal neutrino energy spectra, cross sections as a function of the neutrino energy (not neutrino temperature) should be adopted. These cross section data will bring about more precise evaluation of SN yields of the ν-process elements.

The works shown in this proceeding have been carried out by collaboration with Toshitaka Kajino (NAOJ), Toshio Suzuki (Nihon Univ.), Satoshi Chiba (JAEA), Hidekazu Yokomakura (Nagoya Univ.), Keiichi Kumura (Nagoya Univ.), Akira Takamura (Toyota National Col. of Tech.), Hideyuki Umeda (Univ. of Tokyo), Ken'ichi Nomoto (Univ. of Tokyo), Dieter H. Hartmann (Clemson Univ.), Michio Honma (Aizu Univ.), Koji Higashiyama (Chiba Inst. of Tech.), and Takaharu Otsuka (Univ. of Tokyo).

References

[1] S. E. Woosley and T. A. Weaver: [illegible], **101**, 181 (1995).

[2] T. Yoshida, M. Terasawa, T. Kajino, and K. Sumiyoshi: [illegible], **600**, 204 (2004).

[3] A. Heger, et al.: [illegible], **606**, 258 (2005).

[4] T. Yoshida, T. Kajino, and D. H. Hartmann: [illegible], **94**, 231101 (2005).

[5] T. Yoshida, et al.: [illegible], **96**, 091101 (2006).

[6] T. Yoshida, et al.: [illegible], **649**, 319 (2006).

[7] T. Yoshida, et al.: [illegible], **686**, 448 (2008).

[8] T. Yoshida, H. Umeda, and K. Nomoto: [illegible], **672**, 1043 (2008).

[9] T. Suzuki, R. Fujimoto, and T. Otsuka: [illegible], **67**, 044302 (2003).

[10] T. Suzuki, S. Chiba, T. Yoshida, T. Kajino, and T. Otsuka: [illegible], **74**, 034307 (2006).

[11] R. D. Hoffman and S. E. Woosley: unpublished (1992).
URL `http://www-phys.llnl.gov/Research/RRSN/nu_csbr/neut_rate.html`

[12] E. K. Warburton and B. A. Brown: [illegible], **46**, 923 (1992).

[13] T. Shigeyama and K. Nomoto: [illegible], **360**, 242 (1990).

[14] J. M. Lattimer and M. Prakash: [illegible], **550**, 424 (2001).

[15] T. Suzuki, et al.: [illegible], AIP Conf. Proc. 1016, 321 (2008).

[16] M. Honma, T. Otsuka, B. A. Brown, and T. Mizusaki: [illegible], **65**, 061301 (2002).

12. KUCA experiments & Criticality Safety Analyses in R&D of Erbia-bearing Super High Burnup Fuel

Masatoshi Yamasaki, Takeshi Kuroishi
Nuclear Fuel Industries, Ltd.
950-1, Asashironishi Kumatori-cho Sennan-gun Osaka 590-0481. Japan
yamasaki@nfi.co.jp

Toshikazu Takeda
Osaka University
2-1 Yamada-oka, Suita-shi, Osaka, Japan, 565-0871
takeda@see.eng.osaka-u.ac.jp

Akio Yamamoto
Nagoya University
Furo-cho, Chikusa-ku, Nagoya, Japan, 464-8603
a-yamamoto@nucl.nagoya-u.ac.jp

Hironobu Unesaki
Kyoto University
2-1010 Asashiro-Nishi, Kumatori-cho, Sennan-gun, Osaka, Japan, 590-0494
unesaki@kuca.rri.kyoto-u.ac.jp

Masaaki Mori
Nuclear Engineering, Ltd.
1-3-7 Tosabori Nishi-ku. Osaka 550-0001. Japan
mmori@neltd.co.jp

In order to reduce the number of spent fuel assemblies and then to improve fuel economics, the development project on Erbia bearing super high-burnup fuel with high uranium enrichment is under going. The development program covers wide aspect of the development of LWR fuel such as critical experiments of Erbia core whose ^{235}U enrichment is 5 to 10wt%, criticality safety analysis using Erbia credit, fabrication test and physicochemical properties measurement of Erbia-bearing fuel pellet, and so on. Consequently of these studies, the fiesibility of Er-SHB is confirmed.

I. INTRODUCTION

Utilization of high burnup fuels with higher uranium enrichment is effective for reducing the number of spent fuel assemblies. However, the upper limitation of enrichment for LWR fuels is commonly 5wt% and current advanced fuel assemblies for LWR are already reaching this limit (e.g. maximum ^{235}U enrichment used in the current LWR fuels is 4.95wt%). Though various efforts to overcome the 5wt% enrichment limit have been undergoing[1], it would require considerable cost that could offset the economic benefit of high burnup fuels.

We are proposing another pathway by the Er-SHB fuel.[2] By adding low content (>0.2wt%) of erbia in all UO_2 powder, reactivity of high enrichment (>5wt%) fuel is suppressed under that of current fuel assemblies, i.e. we can take the advantage of negative reactivity credit of erbia. Since erbia is mixed into UO_2 powder just after the re-conversion process, we can avoid most of the criticality safety issues appearing in the front-end stream. Namely, major improvements and re-licensing for equipments in transportation, storage and fabrication process would not be necessary. Besides, the Er-SHB fuel could have affinity with the back-end stream in consideration of burnup behavior of not only erbia but also UO_2. Therefore, the Er-SHB fuel will significantly contribute to reduction of fuel cycle cost.

Erbia is one of the major burnable absorber used in LWRs and has rich experience. However, concept of the Er-SHB fuel is completely different from the current LWR fuel loaded with erbia. Erbia is used to control in-core power distribution and moderator temperature coefficient, and loaded in the part of fuel rods in an assembly. Contrary to this, erbia is added in all fuel rods to meet the criticality safety requirements in the Er-SHB fuels.

We have launched four years development program of the Er-SHB fuel in 2005 under the support project of Ministry of Economy, Trade and Industry (METI) for Innovative and Viable Nuclear Energy Technologies (IVNET). The development program for the Er-SHB fuel covers wide aspect of the development of LWR fuel as follows:

(1) Critical experiments
(2) Development of an uncertainty reduction technique for neutronics parameters
(3) Criticality safety analysis
(4) Fabrication test and physicochemical properties measurement of erbia-bearing fuel pellet
(5) Core design using the Er-SHB fuel assemblies
(6) Source term estimation for heat load / shielding analysis
(7) Applicability of burnup credit for the Er-SHB fuels
(8) Effect on the back-end stream such as disposal of high-level radioactive waste (HLW), etc.

So far, we have almost completed rough feasibility evaluation of reload core design using the Er-SHB fuel, development of the uncertainty reduction technique of neutronics parameters, preliminary critical experiments using erbia and sintering test of the Er-bearing fuel pellet. The present paper summarizes status of experiments and analyses carried out in this project.

Concept of the Er-SHB fuel is an attractive candidate to make a breakthrough in the 5wt% enrichment limit. The above program will prompt the development of the Er-SHB fuel as a production assembly.

II. Concept of Er-SHB Fuel

Criticality safety is one of the major concerns of an extended high burnup fuel whose ^{235}U enrichment is higher than 5wt%. Actually, limitations of 5wt% enrichment are used throughout the front-end stream of LWR fuels. In the Er-SHB fuel, the above issue will be addressed by the erbia; erbia is mixed into UO_2 powder just after the re-conversion process. Since erbia is a neutron absorber, reactivity of UO_2 can be suppressed. By adjusting content of erbia, reactivity of the erbia-mixed fuel can be lower than that of current fuels whose enrichment is lower than 5wt%. Such erbia-mixed fuel would be handled in similar way with the current fuels. In other words, by adding erbia as burnable absorber, higher enrichment fuel (>5wt%) would be handled by conventional equipments in the front-end stream. Such simplification of fabrication process will contribute to reduce fuel costs.

There are various neutron absorbers used in LWR fuels other than erbia, e.g., boron and gadolinia. Actually, boron and gadolinia are more familiar in PWR and BWR fuels thus have rich experiences as LWR fuels. Unfortunately, these materials cannot be used in the present concept because:

- Absorption cross section of Gd is much larger than that of Er, as shown in Fig. 1. Therefore, when the Gd is mixed into all fuels as burnable absorber, reactivity hold-down of Gd at BOL becomes very large as shown in Fig. 2. Cores loaded with such fuels would be difficult to reach critical. (Remember that the poison is mixed into all UO_2 powder in the fuel) Furthermore, Gd burns out very rapidly due to its "blackness" hence reactivity variation during burnup becomes very quick and large. Such rapid variation of reactivity makes in-core design very difficult.
- Moderator temperature coefficient of erbia loaded fuel tends to be negative due to the large resonance absorption cross section in the epi-thermal energy range of Er. Actually, erbia is used as an effective burnable absorber for longer cycle operation of PWR, in which critical boron concentration at BOC becomes higher thus the moderator temperature coefficient tends to be positive.

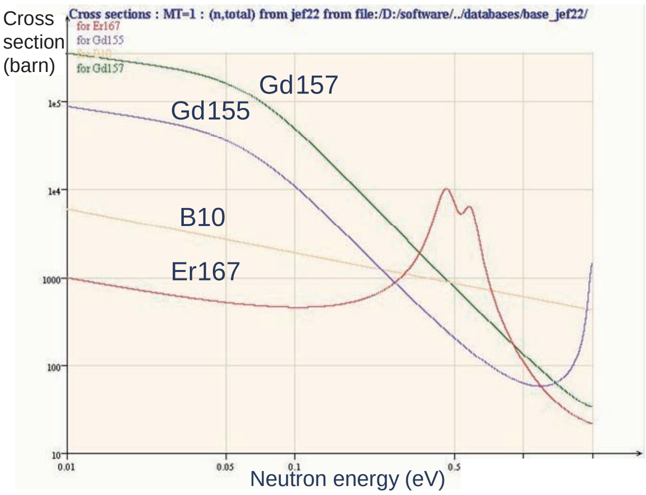

Fig. 1. Cross sections of various burnable absorbers

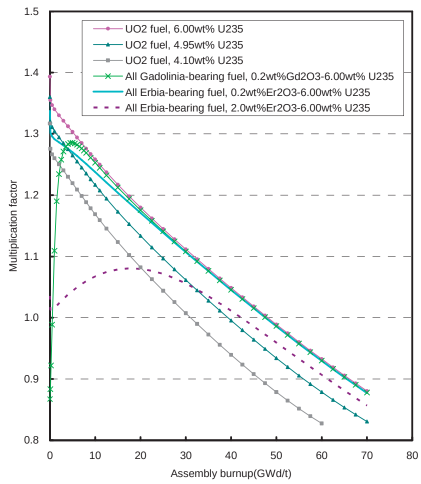

Fig.2. Multiplication factor versus burnup

III. Critical Experiments in KUCA

Kyoto University Critical Assembly (KUCA) has a solid moderated plate type fuel cores[3]. A schematic view of the core is shown in Fig. 3.

As the fuel plate, 1/16-inch thickness high enriched (93 wt%) U-Al alloy (EU) and 1mm thickness natural uranium metal (NU) is used. Both of them have 2 inches square shape in radial direction. For moderator material, polyethylene and graphite plate of various thicknesses are used. Adjusting a combination of fuel and moderator plates, various fuel enrichments and moderation ratio can be simulated.

In order to perform critical experiments with massive loading of Erbia, one thousand pieces of thin Erbia coated (~30μ) graphite plates (1.5mm) are prepared.

The first fully Erbia-loaded core has achieved critical in December 2006. Following the first experiment, another two criticality experiments have performed from December 2007 to January 2008. Those core parameters are summarized in Table I. The neutron spectram of cell calculation for these cores are shown in Fig. 4 in comparison with a tipical PWR geometry with ^{235}U 6wt% and Er 0.4wt%.

The measurement results of criticality and Erbia reactivity worth are compared with calculation. Fig. 5 shows the comparison result of core criticality, which was calculated by continuous energy Monte-Carlo code named MVP using several cross-section libraries. In Fig.5, although constant biases for each library can be observed, no apparent dependence on uranium enrichment and moderation ratio seems to exist.

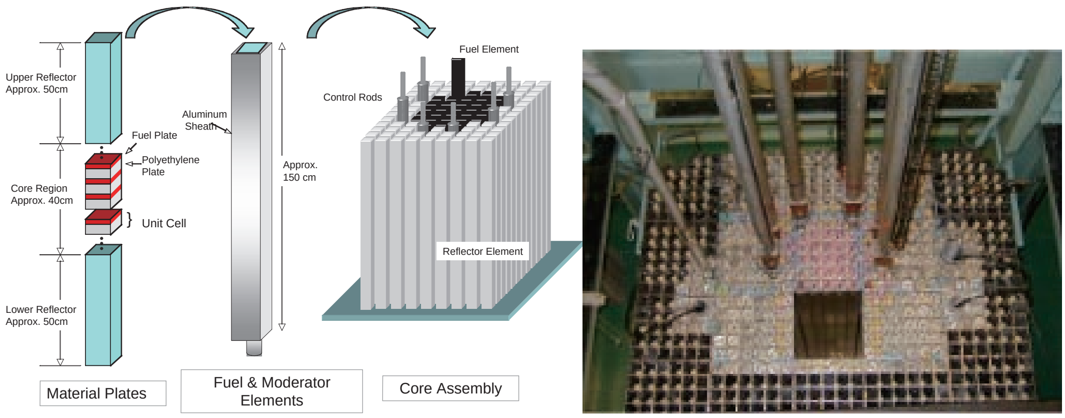

Fig. 3. A schematic view of solid moderated core

Table I Comparison of core parameters

Case	Average enrichment	Er content[*1]	$H/^{235}U$	Outline
Core-0	5.4wt%	0.3wt%	274	Homogeneously Er loaded core Very soft spectrum
Core-1	5.4wt%	0.3wt%	91	Zone type core with driver Simulate PWR spectrum
Core-2	9.6wt%	0.6wt%	48	Zone type core with driver Harder spectrum

*1: Erbia / U-total

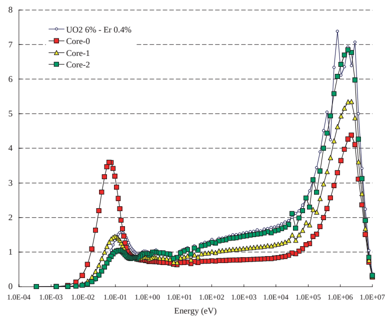

Fig. 4. Comparison of neutron spectra

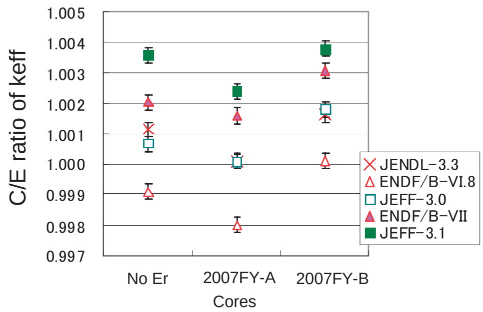

Fig. 5 Comparison of core criticality analysis

IV. Results of uncertainty Reduction Method

A new method[4] is proposed by combining the generalized bias factor method and the cross section adjustment method. The present method is applied to evaluate the prediction uncertainty of neutronics characteristics of the fuel fabrication plant loading the erbia-bearing fuel. The uncertainty of the erbia worth is reduced through the cross section adjustment using the erbia sample worth.

The prediction uncertainty of the k_{eff} in the PWR core is evaluated using the data of the erbia sample worth measured at KUCA.

The uncertainty reduction of the k_{eff} in a blending machine is shown in Table II.

The result indicated that the prediction uncertainty of the neutronics characteristics was improved by the present method.

Table II Rresults of uncertainty reduction methods

Method	Uncertainty Reduction*
GB factor (present method)	0.760
Conventional Bias method	0.593

*: Here, the uncertainty reduction is defined as 1-var(Bias methods)/ var(No bias)

V. Criticality Safety Analysis of Fabrication Plant

The Erbia content with above 5wt% enriched fuel should be determined so that the criticality safety in existing facilities equivalent to that with the conventional below 5wt% enriched fuel. In this evaluation, the KENO V.a code and the 44group library equipped in the SCALE5 code system are used.

The selected configurations used for evaluation are as follows;

-Simple shapes, such as homogeneous and heterogeneous sphere, infinite circular cylinder and infinite slab, with water reflector

-Large sphere of UO_2 powder under moderation control

-Infinite array of fuel assembly storage rack.

The evaluated results of Erbia content for those three configurations are shown in Fig. 6. As shown in Fig. 6, the area above all the three curves indicate the high enriched (>5wt%) fuel with Erbia becomes sub-critical. We refer to this figure as “Erbia COntent for Sub-criticality judgment (ECOS)” diagram[5].

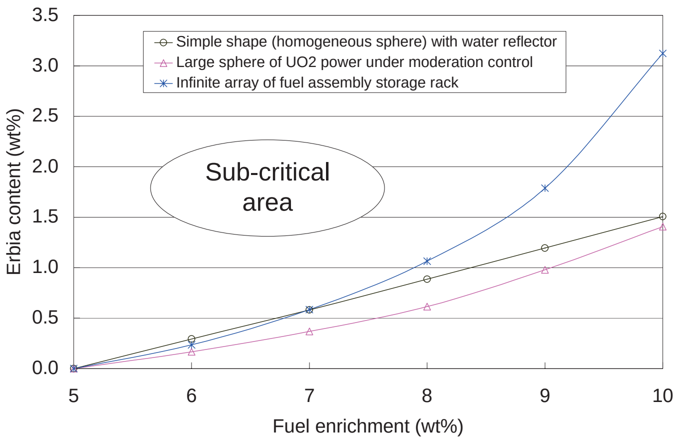

Fig. 6. ECOS diagram

VI. CONCLUSIONS

In order to reduce the number of spent fuel assemblies and to improve fuel economics, the development project on Erbia bearing super high-burnup fuel with high uranium enrichment is under going. The development program covers wide aspect of the development of LWR fuel. Inn this paper, the current status of (1)Critical experiments, (2)Results of uncertainty reduction method and (3)Criticality safety analysis is summarized. Consequently of these studies, the feasibility of Er-SHB is confirmed from the viewpoint of nuclear property prediction and criticality safety.

REFERENCES

1. W. J. Anderson, et al., "Reactor Physics and Criticality Benchmark Evaluations for Advanced Nuclear Fuel," US-DOE NERI Annual Report, 01-124 (2002).

2. A. Shimoura, M. Mori, H. Takabatake and M. Yamasaki, "Neutronics Design of an Erbia Bearing Super High-Burnup Fuel Assembly for Pressurized Water Reactors," *Trans. Am. Nucl. Soc.,* **93,** *669* (2005).

3. H. UNESAKI, T. TOSHIKAZU, A. YAMAMOTO, M. MORI and M.YAMASAKI, "Integral experiment on erbia-loaded thermal spectrum cores using Kyoto University Critical Assembly," *Proc. Int. Conf. on the Physics of Reactors "Nuclear Power: A Sustainable Resource" Casino-Kursaal Conference Center, Interlaken, Switzerland, September 14-19, (2008),* CD-ROM.

4. T. TAKEDA, T. SANO, T.KITADA, T. KUROISHI, M. YAMASAKI and H. UNESAKI, "A new uncertainty reduction method for PWR cores with erbia bearing fuel," *Proc. Int. Conf. on the Physics of Reactors "Nuclear Power: A Sustainable Resource" Casino-Kursaal Conference Center, Interlaken, Switzerland, September 14-19, (2008)*, CD-ROM.

5. T. KUROISHI, M. YAMASAKI, "Evaluation of erbia content in Er-SHB fuel for criticality safety of fabrication facilities," *Proc. Int. Conf. on the Physics of Reactors "Nuclear Power: A Sustainable Resource" Casino-Kursaal Conference Center, Interlaken, Switzerland, September 14-19, (2008),* CD-ROM.

13. Recent Activities of OECD/NEA/NSC/WPEC

Jun-ichi Katakura
Nuclear Data Center, Japan Atomic Energy Agency
Tokai-mura, Naka-gun, Ibaraki-ken 319-1195
e-mail: katakura.junichi@jaea.go.jp

The activities of Working Party on International Nuclear Data Evaluation Co-operation (WPEC), OECD/NEA Nuclear Science Committee (NSC) are presented. Up to now 32 short-term subgroups have been organized and 7 groups are actively working. The activities of the rest 25 groups were closed and the reports of the group activities were published. As for long-term subgroup, 3 subgroups were organized at first, but only one group, the group of high priority request list, is still working. The activities of the subgroups are briefly presented.

1. Introduction

Working Party on International Nuclear Data Evaluation Co-operation (WPEC) was organized in late 1980's under Nuclear Science Committee (NSC), OECD/NEA. The purpose of the working party is to promote the exchange of information on nuclear data evaluations, validation and related topics. Another specific aim is to provide a framework for co-operative activities between the members of the major nuclear data evaluation projects. The parties to the project are: ENDF (USA), JEFF/EFF (member countries of the NEA Data Bank) and JENDL (Japan). Co-operation with evaluation projects of non-OECD countries, specifically the Russian BROND and Chinese CENDL projects, is organized through the Nuclear Data Section of the International Atomic Energy Agency.

Under the working party several sub-groups have been established to discuss specific issues of nuclear data evaluation. Up to now 32 sub-groups were established. The number of presently working subgroups is 7 excepting the long-term sub-group of high priority request list.

In this paper, recent activities of the subgroups are presented.

2. Long-term subgroups

The long-term subgroups were organized in order to discuss the issues not reconciled in short term. They are A) Nuclear Model Codes, B) Formats and Processing and C) High Priority Request List. The first two subgroups, however, have already closed because of the fulfillment of the subgroups purposes. Therefore, only one subgroup of High Priority Request List is actively working. The purpose of the subgroup is to compile the most important nuclear data requirement and to provide a guide for those planning measurement, nuclear theory and evaluation programs. The requests are divided into two main categories: 1) High Priority Request, 2) General Request. The category 1) needs sensitivity analysis to justify the request. Up to now 25 high priority and 10 general requests are selected.

3. Short-term subgroups

The term of the short-term subgroups are 2 – 3 years. As of November 2008, there have been 32 subgroups organized, even though the 11th subgroup was skipped. Of these subgroups, 26 subgroups including the skipped 11th subgroup have been completed and 23 subgroups have already published their final reports. These reports are available from OECD/NEA web site (http://www.nea.fr/html/science/wpec/index.html) as pdf files. The works of two subgroups have been completed and their reports are being prepared now. The on-going subgroups are as follows:

SG24 Covariance Data in the Fast Neutron Region,
SG27 Prompt Photon Production from Fission Products,
SG29 U-235 Capture Cross Section in the keV to MeV Energy Region,
SG30 Improvement of Accessibility and Quality of the EXFOR Database
SG31 Meeting Nuclear Data Needs for Advanced Reactor Systems,
SG32 Unresolved Resonance Treatment for Cross Section and Covariance Representation.

The works of these subgroups are described below.

SG24: Covariance Data in the Fast Neutron Region

The activities of SG24 focused on the development of covariance capabilities within codes used for theoretical modeling of nuclear reactions and investigation of methods for including experimental data in Monte Carlo sensitivity method. The Monte Carlo sampling and the Basian approaches were used for providing the covariances. The results of both method showed a reasonable agreement in the model-based uncertainties as shown in Fig.1.

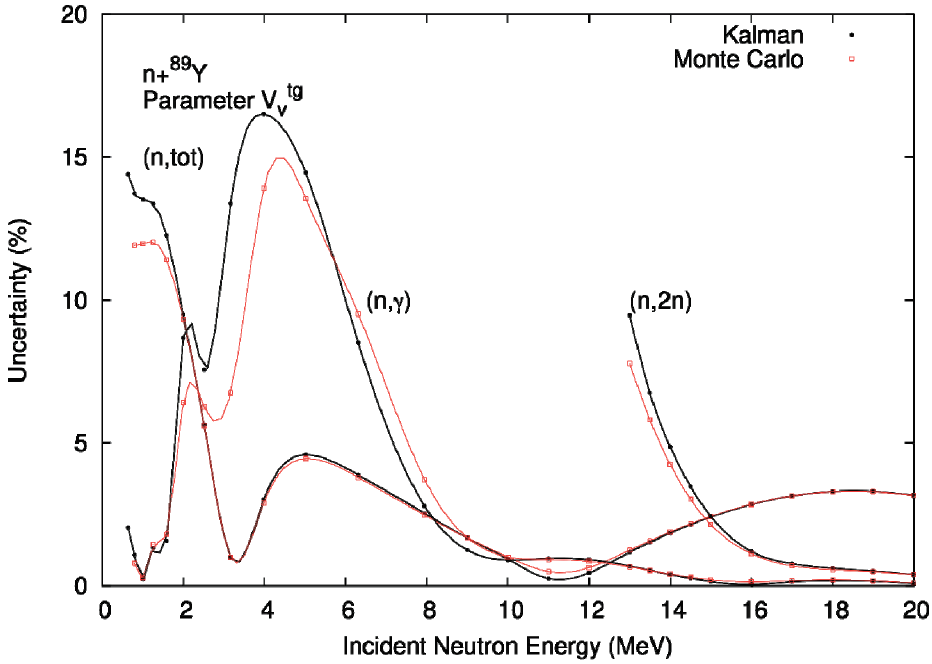

Fig. 1 Comparison of the model-based cross section uncertainties using Monte Carlo and Bayesian (Kalman) method[1]). (From the 20th WPEC Meeting.)

The subgroup also has worked on the inclusion of experimental data, the development of the Unified Monte Carlo approach, and fission spectra covariances. The activity of this subgroup is expected to continue until 2009.

<u>SG27: Prompt Photon Production from Fission Products</u>

Gamma heating is important in a nuclear reactor. The data of the gamma-ray production, however, show gaps and inconsistecies in evaluated nuclear data. The subgroup selects important FPs, identifies and reviews suitable gamma source data. For important FPs, they try to make model calculation to fulfill the gaps. The subgroup, now, has selected important FPs and makes ranking on them. The example of the ranking is shown in Table 1.

Table 1. Example of Ranking (From the 20th WPEC Meeting)

Isotopes	Rank	Contribution@60 GWd/Te over 4 Years
Xe135	1	10.842 %
Pm147	11	3.370 %
Eu155	12	3.278 %
Eu154	13	2.940 %
Pm148m	21	1.145 %
Pd107	23	0.838 %
Zr93	24	0.727 %

The subgroup is going to identify and to review other sources to plug outstanding gaps and to try to complement from model calculations.

SG29: U-235 Capture Cross Section in the keV to MeV Energy Region

The subgroup was organized in May 2007 to investigate U-235 capture cross section in the keV to MeV energy region. The subgroup was proposed by Japan based on the request from fast reactor design side[2)]. Figure 2 shows the underestimation of sodium voided reactivity using recent evaluated data.

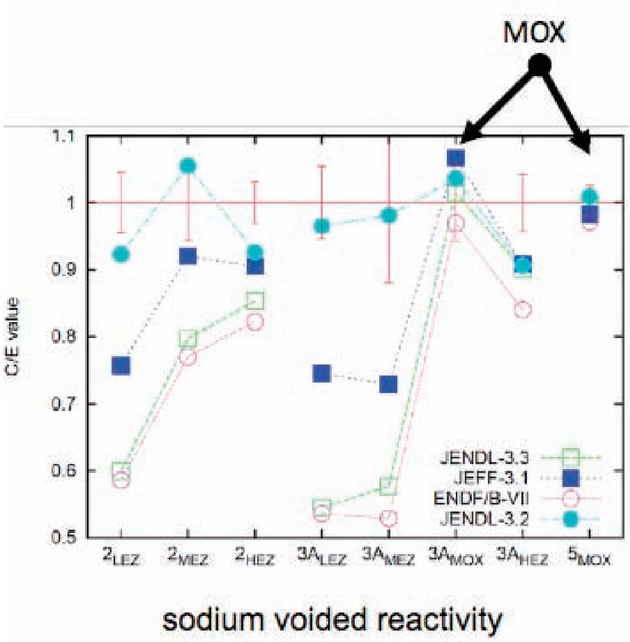

Fig. 2 Comparison of sodium voided reactivity calculation.
(From the 20th WPEC Meeting)

Some benchmark and sensitivity studies have been performed. The sensitivity studies have confirmed the possible underestimation of the U-235 cross section of keV region in JENDL-3.3, ENDF/B-VII.0 and JEFF-3.1 files. As the planned sodium void experiment in FCA is postponed because of a trouble, the subgroup will be extend 10-12 months in order to include the FCA experiment.

SG30 Improvement of Accessibility and Quality of the EXFOR Database

The objective of this group is to establish EXFOR file[3)] an easy accessible and correct database, available in computational format. The experimental data are basis of nuclear data evaluation and it is of importance to keep the high quality of the data base EXFOR. An example of the EXFOR database is shown in Fig. 3.

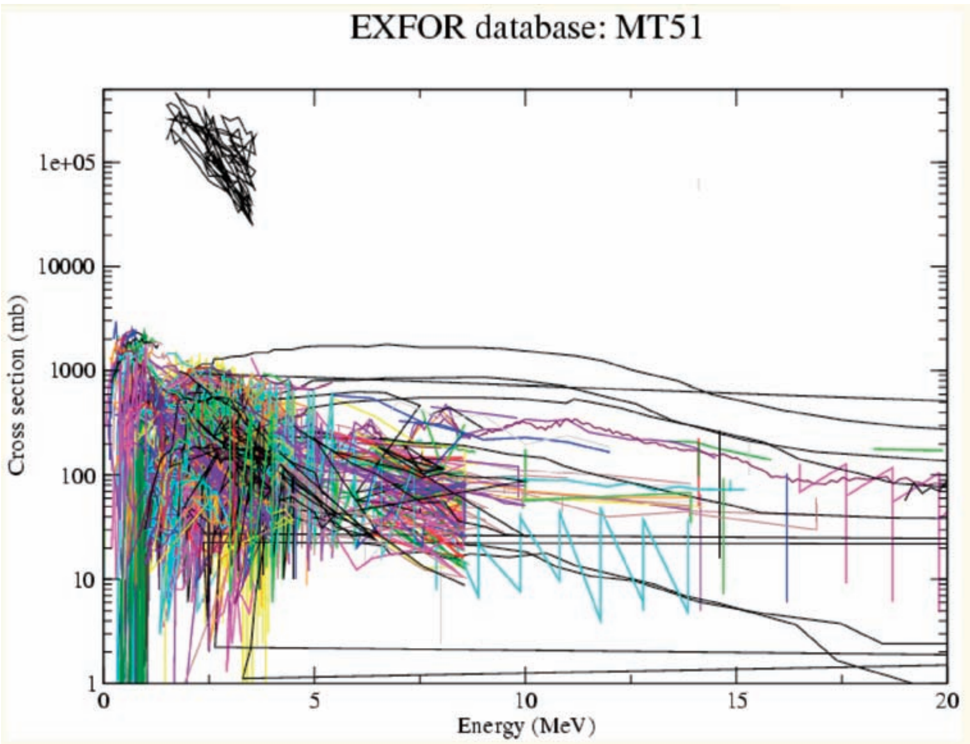

Fig.3 Example of the EXFOR database (From the 20th WPEC meeting)

The first important step was the translation of EXFOR data to the data of more convenient format XC4 by the cooperation with IAEA. The IAEA is now regularly providing updated versions of both the entire EXFOR master data base and the computational database. From the XC4 database, a directory structured database has been created. In these processes, many errors were found and corrected.

4. Newly proposed subgroups

At the 20th WPEC meeting held at Tokai, Japan on June 5-6 2008, three subgroups were proposed. The titles of these proposed subgroups are followings:

1) Meeting Nuclear Data Needs for Advanced Reactor Systems,
2) Assessment of the unresolved resonance treatment for cross section and covariance representation,
3) Methods and issues for the combined use of integral experiments and covariance data.

The first proposal is a follow-up of subgroup 26 which has identified the nuclear data needs for advanced reactor systems[4]. This group considers the practicality of meeting those data needs and identifies the correct path. This group will be comprised primarily of nuclear data measurement experts. The second proposal is to assess the present treatment of cross sections and covariancess in unresolved resonance region and to make a suggestion for the improvement. The third one comes from the recognition after the work of subgroup 26 that some of the target accuracies of design requirement very tight and not likely to be achieved with current experimental measurement techniques. The combined use of integral experiments and differential information would provide designers with improved nuclear data that would be able to meet design target accuracies.

The first and second proposals were accepted by the WPEC members as subgroups 31 and 32 respectively. The third proposal was questioned by the members whether the proposal belonged within WPEC or would be better suited for another NSC Working Party and whether the study would be qualitative or quantitative. It was decided to forward the decision to the next NSC meeting.

5. Summary

The activities of Working Party on International Nuclear Data Evaluation Co-operation (WPEC) have been briefly presented. The WPEC is an international framework to discuss common issues relating to nuclear data evaluation. Any proposal are welcome from evaluators and users.

References:

1) T. Kawano and K. Shibata, “Covariance Evaluation System”, JAERI-Data/Code 97-037, Japan Atomic Energy Research Institute (1997), [in Japanese]

2) T. Hazama, “Recent Topics of Fast Reactor Physics Relating to GEN-IV and Fast Reactor Cycle System Technology Development Project”, Nuclear Data News, No.81 p.24 (2005) [in Japanese]

3) Nuclear Data Centers Network, *EXFOR Systems Manual: Nuclear Reaction Data Exchange Format,* Report BNL-NCS-63330 (1996), compiled and edited by V. McLane, National Nuclear Data Center, Brookhaven National Laboratory, U.S.A.

4) “Uncertainty and Target Accuracy Assessment for Innovative Systems Using Recent Covariance Data Evaluations”, International Evaluation Co-operation Volume 26, OECD/NEA (2008)

This is a blank page.

14. Current status of Nuclear Reaction Data File for Astrophysics (NRDF/A)

T. Yoshida, N. Furutachi, M. Kimura, M. Asano, T. Togashi, H. Murakami and K. Kato

Nuclear Research Data Centre, Hokkaido University (JCPRG)

N. Otuka

Nuclear Data Section, International Atomic Energy Agency

Abstract

Recent activities in JCPRG for compilations of EXFOR and Nuclear Reaction Data File (NRDF) have been introduced. As an extension of such activities, a preparation of new nuclear data libraries: Nuclear Reaction Data File for Astrophysics (NRDF/A) has been planned. The framework of the data table has been almost built. As the next step, evaluations by using cluster models have been planned.

Introduction

The main activity of JCPRG is compilation of experimental nuclear reaction data. Compilation works of observed data are done in the following steps: compilers input bibliography, experimental condition and numerical data from experiment and complete the EXFOR compilations. This is usually done within few weeks after publications of the articles if they agree with JCPRG responsibility of compilations. If the numerical data are not available from authors, we make digitization of the figures of experimental data. As the next step, we transmit compiled data to IAEA Nuclear Data Section. After that, EXFOR reviewers check the compiled data and obtain author’s proof. Finally, the nuclear data in the articles will be released about six month after publication. The total number of charged particle reaction experiments for EXFOR compilation is about 3000. Our compilations contribute about 10 percent of the whole EXFOR data.

Besides EXFOR, we have been developing the original format, Nuclear Reaction Data File (NRDF). Recently, the charged-particle nuclear data become more and more important, due to the increase of astrophysical interest and medical use. By using NRDF, we can specifically treat physical quantity even if they correspond to the integrated cross section (which astrophysical and medical applications usually use) or nuclear structure data (typically differential cross section). The NRDF format has flexibility which does not much depend on characteristic data in fields of study because of its large capacity of construction of compilation codes.

Astrophysical nuclear reaction is one of the applications of NRDF where the nuclear network calculation plays an important role [1]. For such reactions, we focus on neutrons, protons, alpha, gamma, or neutrino as incident or emitted particles. To study the evolution of the early universe, the reactions concerning with light nuclei below the pf shell are important. Some of these astrophysical reactions occur at very low temperature, which are difficult to reproduce by experiments because of the very small reaction rates. The evaluations based on the theoretical calculations are indispensible to make up for the experiments. NACRE (Nuclear Astrophysics Compilation of Reaction rates) is one of the most widely used evaluated astrophysical nuclear reaction data base [2]. However, it becomes much better to take into account the most recent experimental data and use more sophisticated calculation in order to obtain more reliable evaluation.

Construction of the data table

We construct a new database for this study: we call this file as Nuclear Reaction Data File for Astrophysics (NRDF/A). In the previous version of NRDF/A (2006), we have assembled only 31 reactions for nuclei from C to Mg. In the present new version (2008), the astrophysical important light nuclei up to Si are included to achieve the coverage for NACRE. As a result, the number of reactions to be compiled is about 200.

We are planning to use cluster model calculations for evaluation. As one of such models, we use Anti symmetric Molecular Dynamics (AMD) [3]. This can be a good candidate for the models because of its wide scope of application below the pf shell nuclei. Here, we can treat two important pictures, shell model like configuration and cluster configuration by taking proper parameters for effective nuclear interactions.

Before making the evaluation, we are now preparing the data table. For each reaction, we search for the corresponding articles in order to obtain the numerical data for future works of evaluation. Here, we utilize the bibliographic information from Nuclear Science References (NSR) of National Nuclear Data Center (NNDC). The data table consists of reaction information, energy range, information of physical quantity and bibliographic information.

In the reaction information, energy ranges are given in addition to reaction equations. We also compile how the physical quantities (cross section, reaction rate, S-factor, spectrum, electro-magnetic transition strength and log(ft)) are obtained. Here, we must notice that the numerical values have not been compiled at the present stage. In compensation, we distinguish the analyzed, deduced, measured and calculated data. The bibliographic information consists of key-number, journal name, volume number, publications year and author name. For the convenience, we make the link to pdf files of articles by using digital object identifier (D.O.I.) if it is available.

In order to choose the articles which are needed to assemble the numerical data for the evaluation, we check the NRDF/A against EXFOR. This is because that we would like to directly use the numerical values which is already appears in EXFOR. For this purpose, we put the coverage information against EXFOR into each data set. After construction of the data table including numerical values, the evaluation based on cluster model will be performed.

References

[1] E. M. Burbidge et al., Rev. Mod. Phys. **29**, 547 (1957).

[2] Angulo et al., Nucl. Phys. A **656**, 3 (1999).

[3]Y. Kanada En'yo, H. Horiuchi and A. Ono, Phys. Rev. C **52**, 628 (1995).

Table 1 Example of data table in NRDF/A

reaction	energy-min	energy-max	cross-section	S-factor	key-numbe	article	volume	page	year	first author
6Li(p,g)7Be	*8E+03	*1.3E+05		ded	2004PR09	PR/C	70	55801	2004	R.M.Prior
6Li(p,g)7Be	*1E+03	*1E+07	ana		2004MUZX	INDC(JPN)/U	192	156	2004	T.Murata
6Li(p,g)7Be	*8E+05		mes		2000SK02	ref[a]	5	198	2000	E.Skreti
6Li(p,g)7Be	*8E+04	*1.1E+05			2000KEZY	ref[b]		42	2000	J.H.Kelley
6Li(p,g)7Be				cal	2000BA09	PR/C	61	25801	2000	D.Baye
6Li(p,g)7Be	Not given	*2E+06			1997NO04	PR/C	56	1144	1997	K.M.Nollett
6Li(p,g)7Be	Not given				1996RE16	APP/B	27	231	1 6	H.Rebel 99
6Li(p,g)7Be		*8E+04		ded	1996LA10	PR/C	53	1977	1996	C.M.Laymon
6Li(p,g)7Be	*3E+04	*1.8E+05	mes	mes	1993BRZQ	ref[c]		169	19 3	R.Bruss 9
6Li(p,g)7Be	*4E+04	*1.8E+05		ded	1992CE02	NP/A	539	75	1992	F.E.Cecil
6Li(p,g)7Be	*4E+04	*1.8E+05			1991CEZZ	BAP	36	No.4, 1242, B10 12	1991	F.E.Cecil
6Li(p,g)7Be			cal		1990KUZW	ref[d]		90	1990	P.D.Kunz
6Li(p,g)7Be	*5E+05	*1E+06			1987TI05	AJP	40	319	1987	C.I.W.Tingwell
6Li(p,g)7Be	Not given				1983SEZT	BAP	28	No.7,965,AB7	1983	R.G.Seyler
6Li(p,g)7Be	*4E+05	*1.1E+06	*mes *cal		1983OS04	NC/A	76	73	1983	R.Ostojic
6Li(p,g)7Be	*2E+05	*1.2E+06	*mes		1979SW02	NP/A	331	50	1979	Z.E.Switkowski
6Li(p,g)7Be	*2E+05	*1.2E+06	mes		1978SWZZ	REPT UM-P	88	23	1978	Switkowski
6Li(p,g)7Be	low		cal		1974BAXA	REPT CONF	740218	36	1974	
6Li(p,a)3He	*9E+04	*5.8E+05	mes	ded	2008CR02	JP/G	35	14004	2008	J.Cruz
6Li(p,a)3He	low		ana	ana	2003SP02	NP/A	719	9 9 c	2003	C.Spitaleri
6Li(p,a)3He	low		ana		2002BA77	NP/A	707	277	2002	F.C.Barker
6Li(p,a)3He		1E+06		ana	1998AN18	NP/A	639	733	1998	C.Angulo
6Li(p,a)3He		*2E+06			1997NO04	PR/C	56	1144	1997	K.M.Nollett
6Li(p,a)3He		5E+05			1997BO12	NP/A	617	57	1997	Y.Boudouma
6Li(p,a)3He	Not given				1997BA95	NP/A	627	324	1997	A.B.Balantekin
6Li(p,a)3He	1E+04	1.004E+06	*mes	ded	1992EN01	PL/B	279	20	1992	S.Engstler
6Li(p,a)3He	*1.8E+05	*2.8E+05			1991BU14	NIM/A	301	383	1991	L.Buchmann
6Li(p,a)3He	*1.68E+08	*2.01E+08	*mes		1987BIZY	ref[e]		E82	1987	L.Bimbot
6Li(p,a)3He	*4.78E+07	*6.25E+07	*mes		1984NE05	YF	40	43	1984	O.F.Nemets
6Li(p,a)3He	*4E+09		*mes		1979FR12	PR/C	20	2257	1979	S.Frankel
6Li(p,a)3He	*1E+06	*2.6E+06	*mes		1977LI01	NP/A	275	93	1977	C.-S.Lin
6Li(p,a)3He	*4.5E+07		*mes		1972DE01	NP/A	178	417	1972	R.M.Devries
6Li(p,a)3He	*4.5E+07		*mes		1972BU16	JCP	50	1295	1972	S.N.Bunke
6Li(p,a)3He	*1.51E+05	*3.17E+05	*mes ded		1971SP05	NP/A	164	1	1971	H.Spinka
6Li(p,a)3He	*1.51E+05	*3.17E+05	*mes ded		1971SP05	ref[f]	196	6 34	1972	H.Spinka
6Li(p,a)3He	*4.5E+07		*mes		1971BU24	NP/A	178		1983	S.N.Bunker
6Li(p,a)3He	*4.5E+07		*mes ded		1971BR12	PR/C	3	1771	1971	K.H.Bray
6Li(p,a)3He	*6.65E+08		mes		1970KO25	YF	11	711	1970	V.I.Komarov
6Li(p,a)3He	*6.65E+08		mes		1970KO25	Sov.J.Nucl.Phys	11	399	1970	V.I.Komarov
6Li(p,a)3He	*1.36E+06		mes		1969LE08	NIM	69	115	1969	G.M.Lerner
6Li(p,a)3He	*2.3E+04	*5E+04	*mes		1967FI05	NP/A	96	513	1967	O.Fiedler
6Li(a,g)10B	Resonance				2004GYZZ	ref[g]			2004	Gy.Gyurky
6Li(a,g)10B	*1.17E+06	*1.185E+06			2004GY02	EPJ/A	21	355		Gy.Gyurky
6Li(a,g)10B		*2E+06			1997NO04	PR/C	56	1144	1997	K.M.Nollett
6Li(a,g)10B	Not given				1996RE16	APP/B	27	231	1 6	H.Rebel 99
6Li(a,g)10B	*1.085E+06	*1.175E+06	*mes		1989BA24	NP/A	499	353	1989	A.K.Basak
6Li(a,g)10B	*1.276E+06		mes		1987MU13	PRL	59	1088	1987	D.E.Murnick
6Li(a,g)10B	*1E+06	*18E+06			1986MYZZ	BAP	31	No.4, 787, BI5	1986	E.G.Myers
6Li(a,g)10B		*3.7E+06	ana		1986CE05	NIM/A	245	547	1986	F.E.Cecil
6Li(a,g)10B	Resonance				1985NE05	PR/C	31	2295	1985	J.E.Nelson
6Li(a,g)10B	*1.03E+06	*1.2E+06			1984NA07	NP/A	417	289	1984	J.Napolitano
6Li(a,g)10B	Resonance				1983NAZZ	BAP	28	No.4, 650, AG4	1983	J.Napolitano
6Li(a,g)10B	*1.14E+06	*1.25+E06	*mes		1979SP01	NP/A	318	21	1979	R.H.Spea

references of article
[a] Trans.Bulg.Nucl.Soc.
[b] Triangle Univ.Nuclear Lab., Ann.Rept.
[c] Proc.2nd Intern.Symposium on Nuclear Astrophysics, Nuclei in the Cosmos, Karlsruhe, Germany 6-10 July, 1992, F.Kappeler, K.Wisshak, Eds., IOP Publishing Ltd., Bristol, England
[d] Univ.Colorado, Nucl.Phys.Lab., Tech.Prog.Rept.
[e] Univ.Paris, Inst.Phys.Nucl., 1986 Ann.Rept.
[f] Erratum Nucl.Phys/A
[g] nucl-ex/0402020,02/26/2004 (2004)

15. Evaluation of Neutron Cross Sections on Silver Isotopes for JENDL-4

Nobuyuki Iwamoto

Abstract

Neutron nuclear data on fission products have been evaluated for the development of JENDL-4. In this work I presented the evaluated results of silver isotopes (^{107,109,110m,111}Ag) in the incident neutron energy range from 1 keV to 20 MeV. The data on ^{111}Ag isotopes will be newly added in JENDL-4. In this evaluation I obtained neutron transmission coefficients of target nuclei from the optical model calculations with coupled channels method based on the rigid rotator model. Using the transmission coefficients, various reaction cross sections were calculated by a nuclear reaction code CCONE. I evaluated neutron cross sections, angular distributions, energy spectra and double differential cross sections in comparison with available measurements. The presently obtained results well reproduced the experimental data.

1 Introduction

The evaluation of neutron nuclear data on fission products has been performed for the development of JENDL-4. This work presents the nuclear data on silver isotopes.

Natural silver with atomic number $Z = 47$ consists of two stable isotopes (^{107}Ag: 51.839%, ^{109}Ag: 48.161%). The unstable ^{110}Ag isotope is not produced by fissions because it is shielded by stable ^{110}Pd isobar. However, the 6^+, 117.59 keV isomer of ^{110}Ag is relatively long-lived with half-life of 249.76 days, and is synthesized by the capture reaction of ^{109}Ag. Therefore, neutron-induced cross sections on ^{107,109,110m}Ag isotopes were compiled in JENDL-3.3[1], ENDF/B-VII.0[2], and JEFF-3.1[3]. For nuclear applications, the latter two libraries further included the cross section data on ^{111}Ag isotope because the fission yields of ^{111}Ag reach about 1 % at 14 MeV for ^{235,238}U fission. Note that ^{107}Ag is not an important fission product because ^{107}Pd is long-lived isobar with half-life of 6.5×10^6 yr, and its decay has little contribution to the production of ^{107}Ag.

The nuclear data on four Ag isotopes in ENDF/B-VII.0 and JEFF-3.1 were not evaluated by a consistent way. Some of important cross section data were not calculated in JEFF-3.1. Therefore, this evaluation was carried out by the same models and methods for all calculations of cross sections. This consideration was required to predict the reliable cross sections of isotopes, which do not have any experimental data.

2 Theoretical Models and Evaluation Methods

The neutron cross sections of silver isotopes (^{107,109,110m,111}Ag) were evaluated in the incident neutron energy range from 1 keV to 20 MeV. The neutron transmission coefficients for target nuclei were obtained by using the OPTMAN code[4] which calculates the optical model with coupled channels method based on the rigid rotator model. For the optical model calculations the potential parameters were mainly taken from Kunieda [5]. Some of the parameters were modified to obtain better fit to experimental data. The coupled levels were shown in Table 1. I took into account the ground-state band up to $9/2^-$ levels for the isotopes with odd mass number. Since the band structure has not been known for ^{110m}Ag isotope, I assumed the

Table 1: Coupled levels and deformation parameters for optical model calculations

Isotope	^{107}Ag		^{109}Ag		^{110m}Ag		^{111}Ag	
	E_x(keV)	J^π	E_x(keV)	J^π	E_x(keV)	J^π	E_x(keV)	J^π
	0.00	$1/2^-$	0.00	$1/2^-$	117.59	6^+	0.00	$1/2^-$
	324.81	$3/2^-$	311.38	$3/2^-$	395.59	7^+	289.71	$3/2^-$
	423.15	$5/2^-$	415.21	$5/2^-$			391.28	$5/2^-$
	973.30	$7/2^-$	912.10	$7/2^-$			845.88	$7/2^-$
	1146.90	$9/2^-$	1090.60	$9/2^-$			1023.98	$9/2^-$
β_2	0.1800		0.1850		0.1875		0.1900	
β_4	-0.0500		-0.0500		-0.0500		-0.0500	

7^+ level at the excitation energy $E_x = 395.59$ keV, which was inferred from the level structure of ^{106,108}Ag isotopes. It was found that the artificial level was essentially needed to obtain the total cross section consistent with those of the other isotopes. I confirmed that the small variation of excitation energy did not have a large influence on the total cross section if the presence was postulated at $E_x \sim 400$ keV.

The transmission coefficients were calculated by the global optical model potentials by Koning & Delaroche[6] for proton, Lohr & Haeberli[7] for deuteron, Becchetti & Greenlees[8] for triton and ^{3}He, and Huizenga & Igo[9] for α particle. The neutron transmission coefficients for the other nuclei were adopted from Koning & Delaroche[6].

The reaction cross sections through the compound and preequilibrium processes were calculated by the nuclear reaction model code, CCONE[10]. The compound process was calculated by the Hauser-Feshbach statistical model with width fluctuation correction[11]. The data of discrete levels and γ-branching ratios were obtained from RIPL-2[12]. The level density above the adopted discrete levels was calculated from the Gilbert and Cameron formalism. The shell effects[13] and pairing correlations were taken into account for the Fermi-gas model[14]. The asymptotic value a^* of a parameter was fixed for each nucleus which has the experimental information of average spacing of s-wave neutron resonances. For the gamma-ray strength function I adopted the (enhanced) generalized Lorentzian form for the E1 transition[15] and the Lorentzian form for the M1 and E2 transitions[16].

For the preequilibrium process two-component exciton model[10, 17] was adopted together with the parameterization[18]. The complex-particle emission was also taken into account by considering the pick-up and knock-out processes[19]. The gamma-ray emission in the preequilibrium process was also included to treat the direct and semi-direct capture reactions[10, 20].

3 Evaluated Results

The calculations were done mainly for the total, elastic and inelastic scattering, $(n, 2n)$, $(n, 3n)$, (n, γ), (n, p), $(n, n'p)$, (n, α) and $(n, n'\alpha)$ reaction cross sections, the angular distributions, and double differential cross sections of emitted particles and γ-rays. The other reaction cross sections were also calculated, if the reaction channels were open below 20 MeV. Since measurements have been done only for stable ^{107,109}Ag isotopes and natural Ag, the cross sections mentioned above were evaluated to reproduce the experimental data. The obtained results were compared with all experimental data available and three evaluated libraries[1, 2, 3].

The nonelastic scattering cross sections for natural Ag were measured in 1950s. The comparison of the calculated cross section with the experimental data is useful to check the validity of the optical model potential with the used parameters. The present result showed a marginal agreement with the measurements.

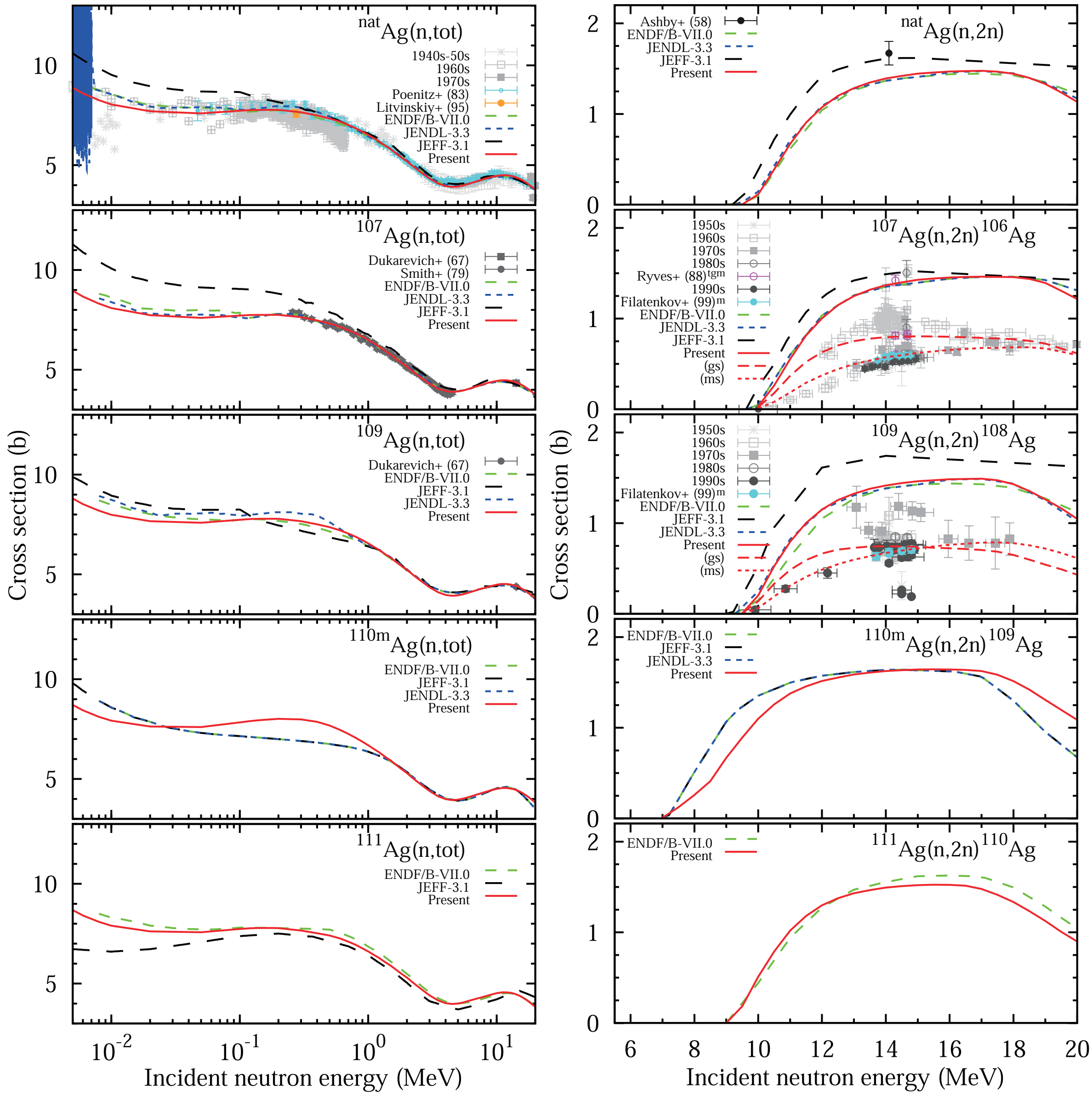

Figure 1: Comparisons of the present results with experimental data and evaluated libraries for ^{nat,107,109,110m,111}Ag. The total and $(n, 2n)$ reaction cross sections are shown in the left and right panels, respectively.

The evaluated total cross sections are represented in the left panel of Fig. 1, in which experimental data were taken from EXFOR database[21]. The total cross sections of ^{nat,107}Ag were measured and the present calculations well reproduced the experimental data. Therefore, the presently determined parameters of optical model potential were used to calculate the total cross section of the other isotopes. It was found that there were not so large differences between the present results and the evaluated libraries above 1 MeV incident energies. In contrast, some differences existed below 1 MeV. In particular, the ^{107}Ag data showed significant differences between JEFF-3.1 and the others. The calculation of ^{110m}Ag isomer was only performed in JENDL-3.3. The comparison between JENDL-3.3 and the present result revealed the different energy dependence of the cross section.

The comparisons of the calculated $(n, 2n)$ reaction cross section for ^{nat,107,109,110m,111}Ag

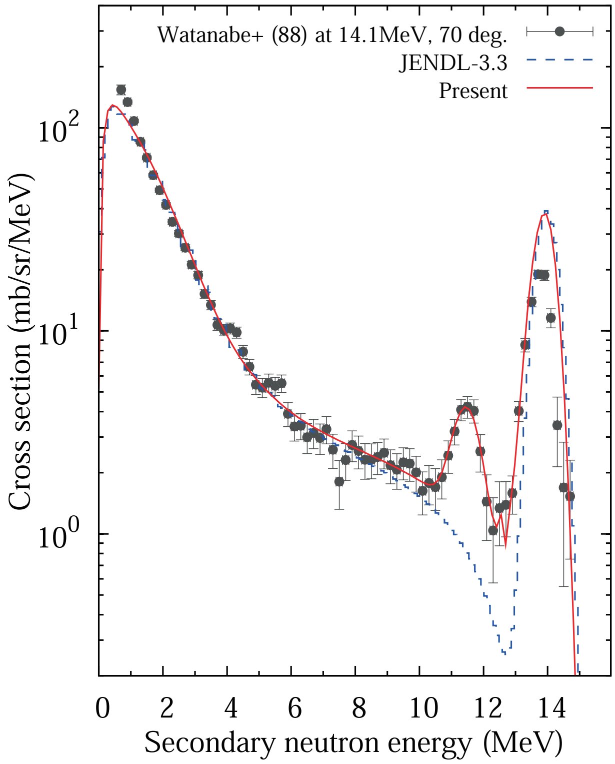

Figure 2: Comparison of the calculated double differential cross section of secondary neutrons for natural Ag with the experimental data[22] and JENDL-3.3.

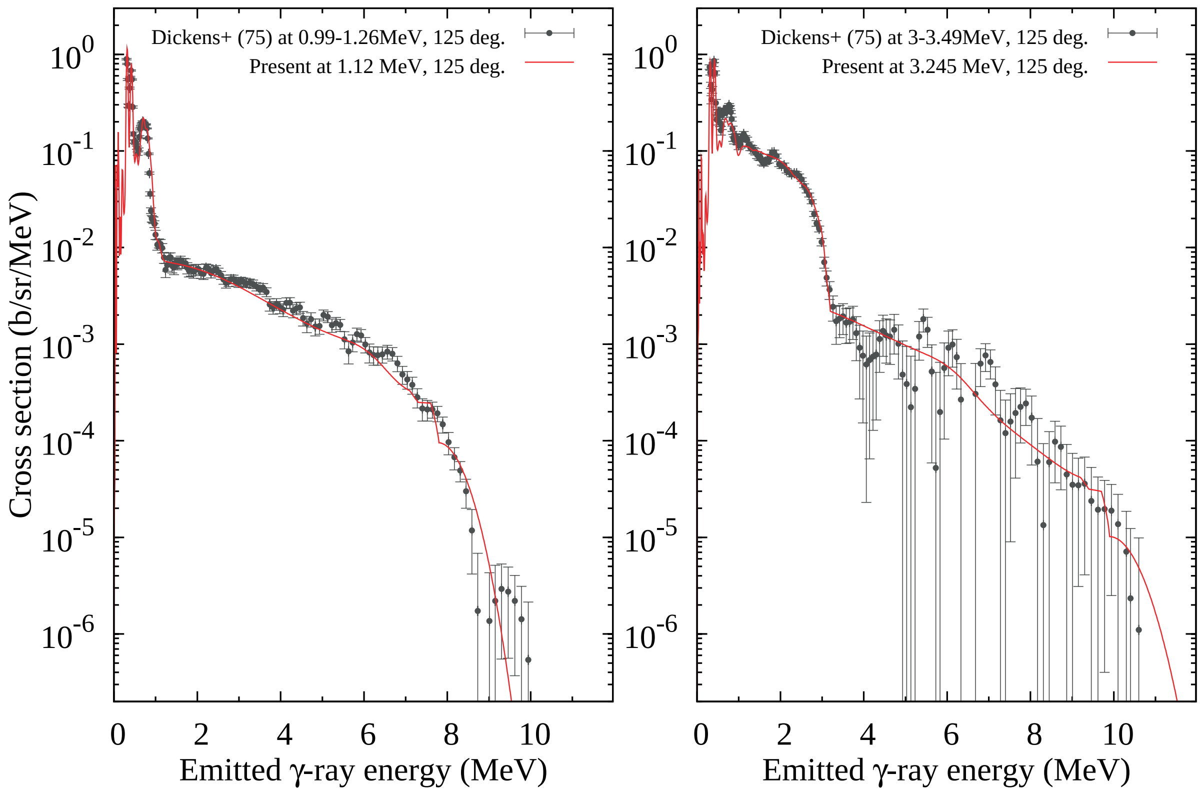

Figure 3: Comparison of the calculated double differential cross section of emitted γ-rays for natural Ag with the experimental data[23].

with available experimental data are illustrated in the right panel of Fig. 1. It was found that the excitation functions of ^{107,109,111}Ag isotopes in the present results were similar to those in JENDL-3.3 and ENDF/B-VII.0. In the present evaluation I considered to explain the production cross sections of the ground-state (gs) and meta-state (ms) for ^{107,109}Ag$(n,2n)$ reactions, and obtained good agreements with the recent measurements. The cross sections for stable Ag isotopes, especially ^{109}Ag, in JEFF-3.1 are large relative to the other libraries including the present calculations. This JEFF-3.1 evaluation might be to explain the only measured data of natural Ag. The increasing contribution of $(n,3n)$ reaction was not taken into account in JEFF-3.1. This is recognized by the decrease of the $(n,2n)$ cross sections at higher energies in the other libraries. The ^{110m}Ag$(n,2n)$ cross section in JENDL-3.3 is almost same as the present one at around 14 MeV, although the excitation functions are different.

Figure 2 compares the calculated double differential cross section of emitted neutrons for natural Ag with the experimental data[22] and JENDL-3.3. The collective excitation, which has the width of 0.4 MeV, was taken into account for the stable isotopes at $E_x = 2.5$ MeV in the present calculations. The effect on the cross section is found at around the emitted energy of 11.5 MeV. Thus, in contrast to the result of JENDL-3.3, I obtained a better agreement with the measured data. The double differential cross sections of emitted γ-rays were calculated for natural Ag, and were shown in Fig. 3, in which the present results at 1.12 and 3.245 MeV incident energies were compared with the experimental data at 0.99-1.26 and 3-3.49 MeV incident energy ranges, respectively[23]. The present results reproduced the measured data.

4 Summary

I systematically evaluated neutron nuclear data on four silver isotopes (^{107,109,110m,111}Ag) by using the updated models for nuclear reaction calculations. In JENDL, the ^{111}Ag data were evaluated for the first time. I showed that the present calculations of various reaction cross sections well explained the available experimental data. It was found that the evaluated results for ^{110m}Ag were largely different from those of JENDL-3.3 at incident energies below 1 MeV. These evaluated data will be included in JENDL-4.

References

[1] K. Shibata, T. Kawano, T. Nakagawa, *et al.*, "Japanese Evaluated Nuclear Data Library Version 3 Revision-3: JENDL-3.3," *J. Nucl. Sci. Technol.*, **39**[11], 1125–1136 (2002).

[2] M. B. Chadwick, P. Oblozinsky, M. Herman, *et al.*, "ENDF/B-VII.0: Next generation evaluated nuclear data library for nuclear science and technology," *Nucl. Data Sheets*, **107**, 2931–3060 (2006).

[3] A. Koning, R. Forrest, M. Kellett, *et al.*, "The JEFF-3.1 Nuclear Data Library," *JEFF Report 21* (2006).

[4] E. Sh. Soukhovitski, S. Chiba, O. Iwamoto, *et al.*, "Programs OPTMAN and SHEMMAN Version 8 (2004)," JAERI-Data/Code 2005-002, Japan Atomic Energy Research Institute (2005).

[5] S. Kunieda, S. Chiba, K. Shibata, *et al.*, "Systematical nucleon-induced optical model analysis for medium and heavy nuclei with coupled-channel framework," *Proceedings of International Conference on Nuclear Data for Science and Technology 2007*, 227–230 (2008).

[6] A. J. Koning, J. P. Delaroche, "Local and global nucleon optical models from 1 keV to 200 MeV," *Nucl. Phys.*, **A713**, 231–310 (2003).

[7] J. M. Lohr, W. Haeberli, "Elastic scattering of 9-13 MeV vector polarized deuterons," *Nucl. Phys.*, **A232**, 381–397 (1974).

[8] F. D. Becchetti, Jr., G. W. Greenlees, *Ann. Rept. J.H.Williams Lab., Univ. Minnesota*, (1969).

[9] J. R. Huizenga, G. Igo, "Theoretical reaction cross sections for alpha particles with an optical model," *Nucl. Phys.*, **29**, 462–473 (1962).

[10] O. Iwamoto, "Development of a Comprehensive Code for Nuclear Data Evaluation, CCONE, and Validation Using Neutron-Induced Cross Sections for Uranium Isotopes," *J. Nucl. Sci. Technol.*, **44**[5], 687–697 (2007).

[11] P. A. Moldauer, "Statistics and the average cross section," *Nucl. Phys.*, **A344**, 185–195 (1980).

[12] T. Belgya, O. Bersillon, R. Capote, *et al.*,"Handbook for calculations of nuclear reaction data, RIPL-2," *IAEA-TECDOC-1506*, available online at `http://www-nds.iaea.org/RIPL-2/` (2006).

[13] A. V. Ignatyuk, G. N. Smirenkin, A. S. Tishin, "Phenomenological description of the energy dependence of the level density parameter," *Sov. J. Nucl. Phys.*, **21**, 255 (1975).

[14] A. Mengoni, Y. Nakajima, "Fermi-gas model Parametrization of nuclear level density," *J. Nucl. Sci. Technol.*, **31**[2], 151–162 (1994).

[15] J. Kopecky, M. Uhl, R. E. Chrien, "Radiative strength in the compound nucleus ^{157}Gd," *Phys. Rev.*, **C47**, 312–322 (1993).

[16] J. Kopecky, M. Uhl, "Test of gamma-ray strength functions in nuclear reaction model calculations," *Phys. Rev.*, **C41**, 1941–1955 (1990).

[17] C. Kalbach, "Two-component exciton model: Basic formalism away from shell closures," *Phys. Rev.*, **C33**, 818–833 (1986).

[18] A. J. Koning, M. C. Duijvestijn, "A global pre-equilibrium analysis from 7 to 200 MeV based on the optical model potential," *Nucl. Phys.*, **A744**, 15–76 (2004).

[19] C. Kalbach, " The Griffin model, complex particles and direct nuclear reactions," *Z. Phys.*, **A283**, 401–411, (1977).

[20] J. M. Akkermans, H. Gruppelaar, "Analysis of continuum gamma-ray emission in precompound-decay reactions," *Phys. Lett.*, **157B**, 95–100 (1985).

[21] EXFOR/CSISRS: Experimental Nuclear Reaction Data, available online at `http://www-nds.iaea.org/exfor/`.

[22] Y. Watanabe, I. Kumabe, M. Hyakutake, *et al.*, "Preequilibrium (n, n') cross sections on nuclei around atomic number 50 at $E_n = 14.1$ MeV," *Phys. Rev.*, **C37**, 963–968 (1988).

[23] J. K. Dickens, T. A. Love, G. L. Morgan, "Gamma-ray production due to neutron interactions with silver for incident neutron energies between 0.3 and 20 MeV - Tabulated differential cross sections," *Oak Ridge National Lab. technical memo No.5081* (1975).

16. Measurement of Neutron-Production Double-Differential Cross Section for Continuous-Energy Neutron-Incidence on Al

Yasuhiro NAKAMURA[1)] Hiroyuki ARAKAWA[1)] Daisuke MORIGUCHI[1)]
Tsuyoshi KAJIMOTO[1)] Shusaku NODA[1)] Takehito WATANABE[1)]
Nobuhiro SHIGYO[1)] Kenji ISHIBASHI[1)] Robert C. Haight[2)]

1)*Kyushu University, 744, Motooka, Nishi-ku, Fukuoka 819-0395 Japan*
2)*Los Alamos National Laboratory, Los Alamos, NM 87545 USA*

Abstract. Continuous-energy neutron-incident neutron-production double-differential cross sections were measured on Al at 90 - 110 MeV. The results were compared with the evaluated values of JENDL-HE and LA150, and the PHITS code.

I Introduction

Neutron-incident cross sections of intermediate energy range are required for the designs of various accelerator-based applications. However the experimental data of neutron-incident neutron-production $(n\ xn)$ double-differential cross sections in the intermediate energy range are insufficien in comparison to the proton-incident neutron-production $(p\ xn)$ data because of a few quasi-monochromatic neutron sources and neutron measurement difficulties

In this study, we measured the double-differential cross sections $(n\ xn)$ at 90 - 110 MeV on Al with a continuous energy neutron source.

II Experiment

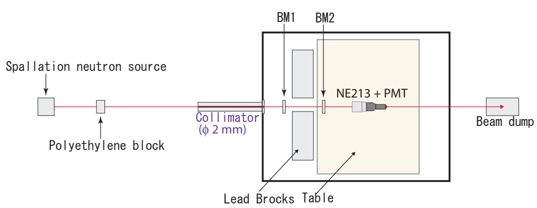

Figure 1. Experimental arrangement for response function.

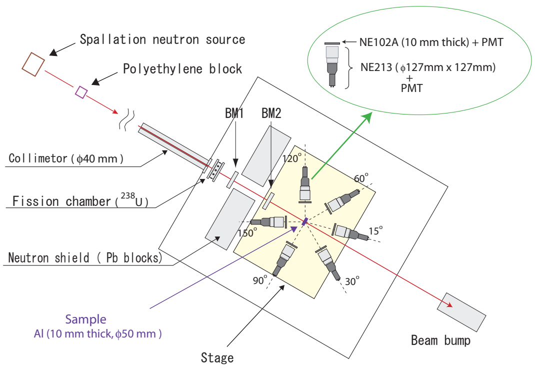

Figure 2. Experimental arrangement for DDX.

The experiment was carried out at the 4FP15L beam line of the WNR facility in Los Alamos Neutron Science Center (LANSCE). It is enable to use continuous energy neutrons up to 750 MeV produced by spallation reaction of a tungsten target (Target-4) with 800 MeV protons. These neutrons were transported on 90 m long beam line, and came into the experimental area through a collimator. A polyethylene block was placed on the beam line to reduce the number of lower energy neutrons. A fissio ionization detector,[1)] BM1 and BM2 (BM stands for Beam Monitor which is plastic scintillator) were set behind the collimator as flu monitors for incident neutrons.

The firs experiment was the measurement of response functions of the NE213 liquid organic scintillators. Because the responses of the NE213 detectors by neutrons has continuous light output spectra, the energy spectra of emitted neutrons were derived from unfolding their deposition energy spectra with them. The experimental arrangement is illustrated in Figure 1. Each detector was placed on the neutron beam line which was collimated into a diameter of 2 mm, and spallation neutrons were directly induced on a detector.

The second experiment was the main measurement for giving the double-differential cross sections (DDX). The experimental arrangement is shown in Figure 2. Emission neutrons were detected with the NE213 at 15°, 30°, 60°, 90°, 120° and 150°. An Al sample was 50 mm in diameter and 10 mm thick. The distance between the sample and each detector was about 0.7 m. In front of each NE213 detector, the NE102A plastic scintillator was mounted as a veto counter to eliminate charged particle events by anti-coincidence method. The neutron beam was collimated into a diameter of 40 mm.

III Analysis

The energy of incident neutron was determined by the TOF method between Target-4 and an emitted neutron detector. The TOF consisted of components of incident and emitted neutrons. Figure 3 shows a outline drawing of the TOF. The fligh path from Target-4 to a sample was 90 m and that between a sample and an emitted neutron detector was about 0.7 m. The total fligh time was assumed as a component of incident neutron because of the difference between their lengths. Figure 4 stands for one of TOF spectrum. The sharp peak seen in Figure 4 is flas γ-ray events from the Target-4, and was used as the time base to get TOF of incident neutron.

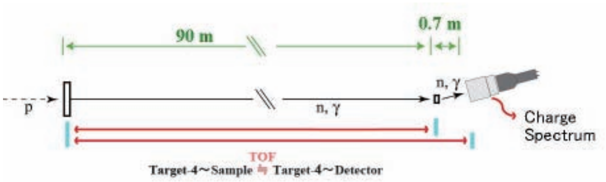

Figure 3. An outline drawing of the TOF.

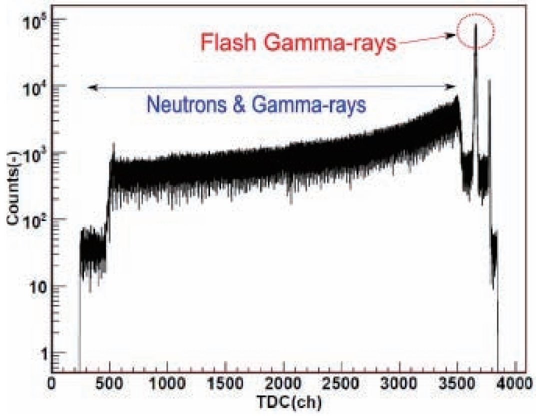

Figure 4. TOF spectrum between the spallation target and a neutron detector. (1 ch = 0.5 ns)

The number of incident neutrons was obtained by the equation (1). This equation where $F_{up}(E_n)$, n_f and $\sigma(E_n)$ are incident neutron flux counts of the fissio chamber and the fissio cross sections of ^{238}U for corresponding neutron energy E_n. $\varepsilon_{\mathrm{eff}}$ is the detection efficien y of the fissio chamber, and ρ_f is the areal density of ^{238}U deposited on the foil in the chamber. n_{bc} is the number of simultaneous counting with the accelerator, BM1 and BM2. Figure 5 shows the incident neutron flu which was obtained in this experiment.

$$F_{up}(E_n)\Delta E_n = \frac{n_f(E_n)\Delta E_n}{\sigma(E_n) \times \varepsilon_{\mathrm{eff}} \times \rho_f} \times \frac{1}{n_{bc}} \tag{1}$$

Charged particle events were eliminated by discrimination of signals from NE102A plastic scintillators because charged particles deposit higher energy in the NE102A scintillator than neutrons and γ-rays. Figure 6 stands for ADC spectrum by the NE102A.

The *gamma*-ray events were discriminated using the two gate integration method since NE213 detector were sensitive to not only neutrons but also γ-rays.[2] Figure 7 stands for a schematic view of the gate

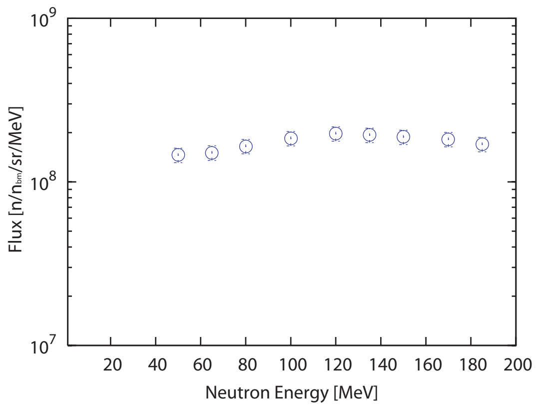

Figure 5. Incident neutron flux

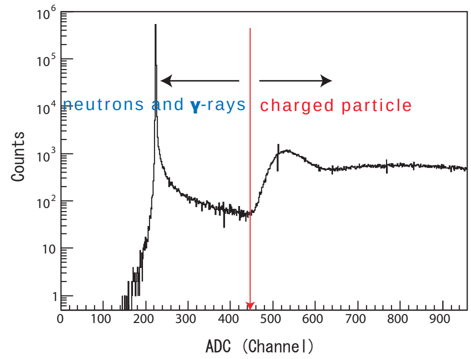

Figure 6. ADC spectrum of the NE102A.

integration method. The NE213 has different response to neutron and γ-ray, for higher LET of recoil protons from neutrons incident as opposed to the lower LET from fast electrons produced by γ-rays, the pulse shape has a longer tail in time. Comparison between charge spectrum with the total gate and that with the slow gate enables to discriminate between neutrons and γ-rays. Figure 8 illustrates an example of the two dimensional plots of the spectrum with the total gate and the slow one.

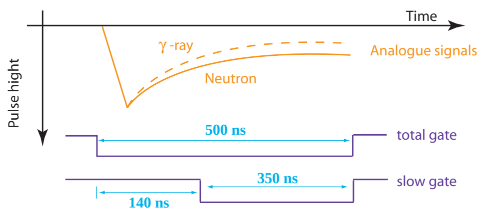

Figure 7. Schematic view of gate integration method.

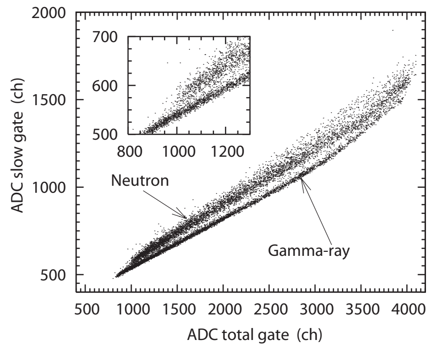

Figure 8. Discrimination of neutrons and γ-rays.

Charge-integration spectra were calibrated to get corresponding electron-equivalent light-output for all neutron detectors. The γ-ray compton-edges of ^{60}Co and Pu-Be sources were used with the semi-empirical formula of Dietze et al[3] for low energy part. For the calibrations of higher energy range, neutron energies were identifie by the TOF between the spallation target and neutron detectors and were converted into light-unit using the empirical formula by Cecil.[4]

Response functions normalized by the number of incident neutrons were shown in Figure 9. In this experiment, the SCNFUL-QMD[5] calculation results were adjusted to reproduce experimental data with light attenuation were used as response matrix elements below incident energy of 25 MeV for all neutron detectors since there were no experiment data below this energy.

Deposition energy spectrum at 90 - 110 MeV normalized by the number of incident neutron and subtracted background spectrum is shown in Figure 10.

The energy spectra of emitted neutrons were derived by unfolding their deposition energy spectra with the responses of the detectors. In this experiment, elastic scattering component was considered

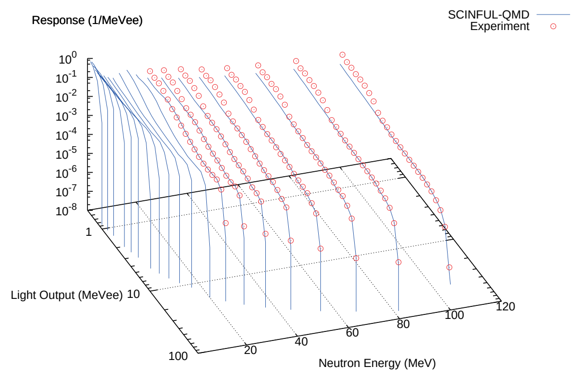

Figure 9. Response functions of the NE213 scintillator at 30°.

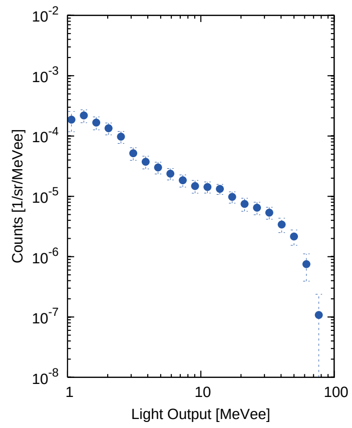

Figure 10. Deposition energy spectrum at 90 - 110 MeV neutron incident energy at 30°.

separately from the other reaction ones. The determinant of this experiment was the equation (2).

$$\begin{pmatrix} \vdots \\ y_\xi \\ \vdots \end{pmatrix} = \begin{pmatrix} \ddots & \vdots & \vdots \\ \vdots & a_{\xi\ E} & \vdots \\ \vdots & \vdots & \ddots \end{pmatrix} \cdot \begin{pmatrix} \vdots \\ x_E \\ \vdots \end{pmatrix} \cdot k + \begin{pmatrix} \vdots \\ a_{\xi\ E_{in}} \\ \vdots \end{pmatrix} \cdot x_{el} \cdot k \tag{2}$$

In this equation, y_ξ, $a_{\xi\ E}$, x_E were deposition energy spectra, response function, double-differential cross section. x_{el} was elastic scattering factor. k was matching factor for absolute value of response functions with deposition energy spectra. x_E was assumed to conform to the equation (3).[6)]

$$\left(\frac{d^2\sigma}{d\Omega dE_{kin}}\right)_{MS+G} = \sum_{i=1}^{3} pA_i exp\left\{-\left(\frac{E_{kin}+m-p\beta_i\cos\theta}{\sqrt{1-\beta_i^2}}-m\right)\Big/T_i\right\} + A_G exp\left\{-\frac{(E_{kin}-E_G)^2}{\sigma_G^2}\right\} \tag{3}$$

In this equation, E_{kin} and p is the kinetic energy (MeV) and the momentum (MeV/c) of an emitted neutron in the laboratory frame and m the neutron mass (MeV). The firs term is called the moving source model. The quantities of A_i, β_i and T_i are called amplitude, velocity and temperature parameters. Three components of i=1 to 3 correspond to individual processes of the cascade, the pre-equilibrium and the evaporation. The second term presents a gaussian-shaped from the quasi-elastic and quasi-inelastic-like scattering processes. The quantities of A_G, E_G and σ_G are adjustable parameters. In the process of unfolding these deposition energy spectra, neutron-incident neutron-production double-differential cross sections were decided the parameter with the equation (3) by SALS code[7)] as a least mean square approximation program.

IV Results

The results of neutron-incident neutron-production double-differential cross sections are shown in Figure 11. These results were compared with the evaluated value of LA150,[8)] JENDL-HE[9)] and the PHITS[10)] calculation data. The experimental data are approximately good agreement with the evaluated value expect in the evaporation processes. But the experimental data underestimate the evaluated value in the evaporation processes. On the other hand, the PHITS calculation are approximately good agreement with the forward angles of experimental data under 10 MeV, and overestimate over 10 MeV. For backward angles, the PHITS calculation underestimate the experimental data.

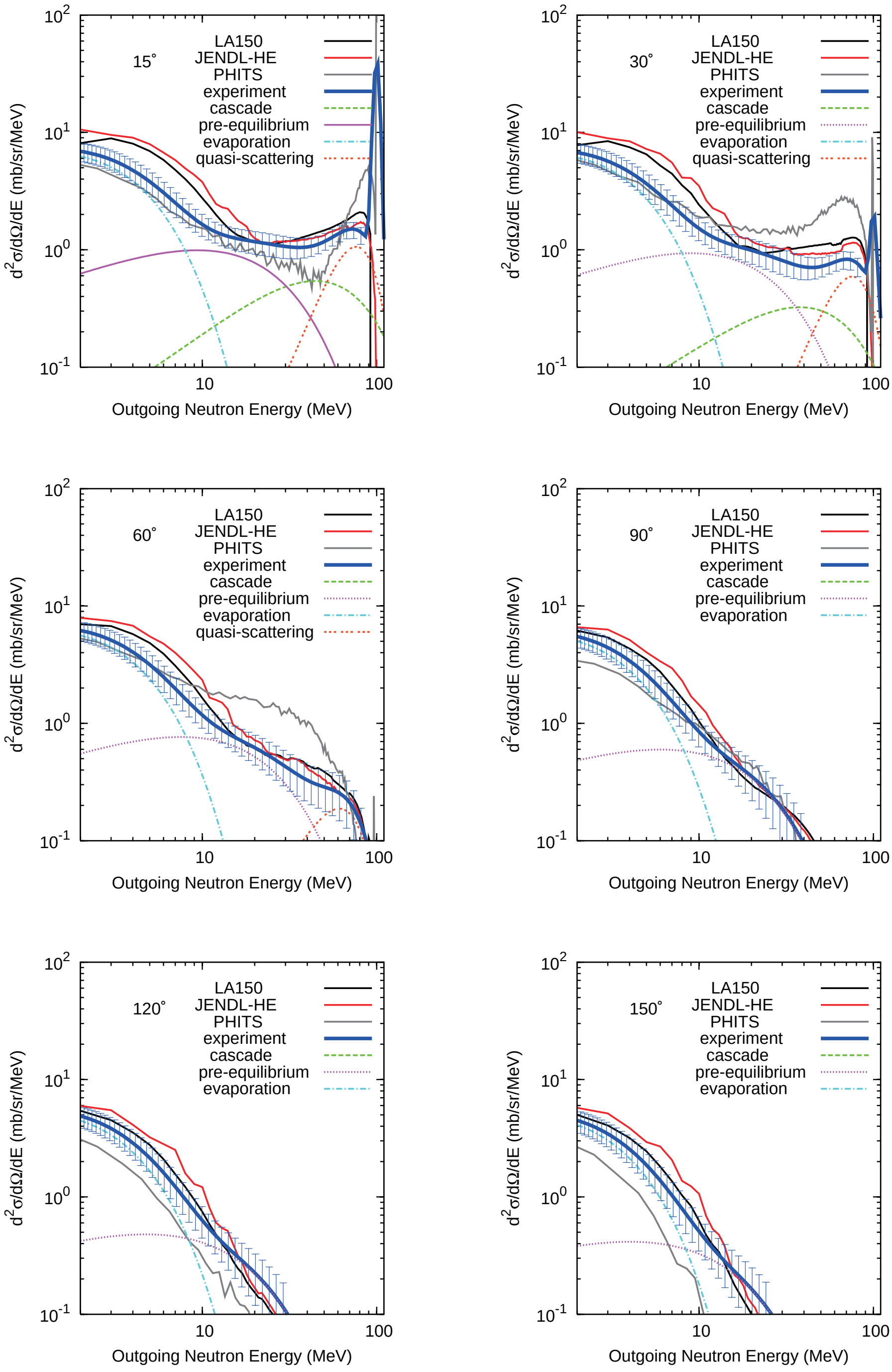

Figure 11. Double-differential cross sections at incident energies of 90 - 110 MeV on Al.

V Conclusion

The neutron incident neutron production double-differential cross sections at 90 - 110 MeV on Al were measured using the continuous energy neutron source. The response functions for the NE213 detectors were also measured. Incident neutron energy was determined by TOF between the neutron source and neutron detectors. The double-differential cross sections were obtained by unfolding method. The experimental results were compared with LA150, JENDL-HE and PHITS.

References

[1] S. A. Wender, S. Balestrini, A. Brown, R. C. Haight, C. M. Laymon, T. M. Lee, P. W. Lisowski, W. McCorkle, R. O. Nelson and W. Parker, *Nucl. Instr. and Meth. in Phys. Res.*, A**336**, 226 (1993).

[2] M. Moszynski, G. J. Costa, G. Guillaume, B. Heusch, A. Huck, S. Mouatassim, Y. Elmasri, P. Leleu, P. Lipnik, I. Tilquin, F. Hanappe, G. Bizard, D. Durand, J. Peter and B. Tamain, *Nucl. Instr. Meth.*, A**343**, 563 (1994).

[3] G. Dietze and H. Klein, *Nucl. Instr. Meth.*, **193**, 549 (1982).

[4] R. A. Cecil, B. D. Anderson, and R. Madey, *Nucl. Instr. Meth.*, **161**, 439 (1979).

[5] D.Satoh,T.Sato,N.Shigyo and K.Ishibashi, JAEA-DATA/Code 2006-023 (2006).

[6] H. Kitsuki, K. Ishibashi, N. Shigyo, S. Kunieda, "*Parameterization of proton-induced neutron production double differential cross section up to 3 GeV in terms of moving source model*", J. Nucl. Sci. Technol. 38 (1) (2001) 1-7.

[7] T. Nakagawa, Y. Oyanagi, Program system SALS for nonlinear least-squares fittin in experimental science, "*Recent Developments in Statistical Inference and Data Analysis*", (K. Matsusita, ed.), NorthHolland. Publ. Amsterdam, **221** (1980).

[8] M. B. Chadwick, P. G. Young, S. Chiba, S. C. Frankle, G. M. Hale, H. G. Hughes, A. J. Koning, R. C. Little, R. E. MacFarlane, R. E. Prael, and L. S. Walter, *Nucl. Sci. Eng.*, **131**, 293-328 (1999).

[9] T. Fukahori, Y. Watanabe, N. Yoshizawa, F. Maekawa, S. Meigo, C. Konno, N. Yamano, A. Y. Konobeyev, and S. Chiba, *J. Nucl. Sci. Technol. Suppl.*, **2**, 25 (2002).

[10] Iwase, H., et al. *J. Nucl. Sci. Techonol.*, **39**, 1142-1151 (2002).

17. Analysis on analyzing power data by a global dispersive coupled-channel optical model potential

Lijuan Hao[1], Weili Sun[2] and E Sh Soukhovitskii[3]

[1]Dept. Applied Quantum Physics and Nuclear Engineering, Kyushu University, Fukuoka 8190395, Japan

[2]Institute of Applied Physics and Computational Mathematics, Beijing 100088, China

[3]Joint Institute for Energy and Nuclear Research, Minsk-Sosny 220109, Belarus

Abstract. The global dispersive coupled-channel optical model potential is used to analyze the proton elastic/inelastic analyzing power in order to investigate the prediction power of this potential. The numerical calculations show good agreement with available experimental data for proton elastic data and overall agreement for proton inelastic data.

1. Introduction

The prediction power of a global optical potential can be proved by the prediction for both angular distributions and analyzing power data. Many calculations had demonstrated that the global spherical optical model potential, such as Koning and Delaroche[1] potential, is of such an capability. However, there is few such demonstrations of the prediction power for the analyzing power by using a global potential for deformed nuclei. In our previous work[2], we had given a global dispersive coupled-channel optical model potential for deformed even-even nuclei from A=24-122, where the experimental data of analyzing power were not used for the adjustment of potential parameters. This global potential was proved to be of good prediction power for elastic and inelastic angular distributions. However the prediction power for analyzing power is not shown well there. Therefore this work is a supplemental calculation to our previous work, aimed at showing how the the prediction power is for the analyzing power by using our global potential.

2. Dispersive Coupled-channel Optical Model Potential

2.1. The Formalization of the Dispersive Coupled-channel Optical Model Potential

The details of our global dispersive coupled-channel optical model potential had been described before[2], therefore only the outline is mentioned briefly below.

With account of the deformed nuclear shapes, the coupled-channel optical model potential followed the standard Woods-Saxon form with conventional definition for the symbols[3]:

$$V(r, R(\theta', \varphi'), E) =$$

$$
\begin{aligned}
&- [V_\mathrm{v}(E) + \mathrm{iW_v(E)} + \Delta \mathrm{V_v^{Coul}(E)}]\mathrm{f_{WS}[r, R_v}(\theta', \varphi')] \\
&- [V_\mathrm{s}(E) + \mathrm{iW_s(E)} + \Delta \mathrm{V_s^{Coul}(E)}]\mathrm{g_{WS}[r, R_s}(\theta', \varphi')] \\
&- \left(\frac{\hbar}{\mu_\pi c}\right)^2 [V_\mathrm{so}(E) + \mathrm{iW_{so}(E)}]\frac{1}{\mathrm{r}}\frac{\mathrm{d}}{\mathrm{dr}}\mathrm{f_{WS}[r, R_{so}}(\theta', \varphi')] \\
&\times \boldsymbol{\sigma} \cdot \mathbf{L} + V_\mathrm{Coul}[r, R_\mathrm{c}(\theta', \varphi')],
\end{aligned} \tag{1}
$$

with the geometrical form factors given as:

$$
\begin{aligned}
f_\mathrm{WS}\left[r, R_i\left(\theta', \varphi'\right)\right] &= \left[1 + \frac{\exp\left(r - R_i\left(\theta', \varphi'\right)\right)}{a_i}\right]^{-1}, \quad i = \mathrm{v, s, so} \\
g_\mathrm{WS}\left[r, R_\mathrm{s}\left(\theta', \varphi'\right)\right] &= -4a_\mathrm{s}\frac{\mathrm{d}}{\mathrm{dr}}f_\mathrm{WS}\left[r, R_\mathrm{s}\left(\theta', \varphi'\right)\right].
\end{aligned} \tag{2}
$$

The Coulomb potential $V_\mathrm{Coul}[r, R_\mathrm{c}(\theta', \varphi')]$ is calculated using a spherical term plus a higher multipole expansion of charged ellipsoid with a uniform charge density, as suggested by Satcher *et al.*[4]. The details had been described in Ref.[5]. For more accuracy, however, the spherical term is calculated taking into account the diffuseness of the charge distribution with a charge density form factor equal to $f_\mathrm{c} = [1 + \exp(r - R_{0\mathrm{c}})/a_\mathrm{c}]^{-1}$.

The Coulomb correction volume term $\Delta V_\mathrm{v}^\mathrm{Coul}(E)$ and surface term $\Delta V_\mathrm{s}^\mathrm{Coul}(E)$ are written as follows:

$$
\Delta V_\mathrm{v,s}^\mathrm{Coul}(E) = -C_\mathrm{Coul}\frac{ZZ'e^2}{\sqrt[3]{A}}\frac{\mathrm{d}}{\mathrm{d}E}V_\mathrm{v,s}(E) \tag{3}
$$

with Z and Z' being charges of target and projectile in electron charge units.

Based on the dispersion relation theory[6, 7], the real potentials are written as[8, 9]:

$$
V_\mathrm{v}(E) = V_\mathrm{HF}(E) + \Delta V_\mathrm{v}(E) = A_\mathrm{HF}\mathrm{e}^{-\lambda_\mathrm{HF}(E - E_\mathrm{f})} + \Delta V_\mathrm{v}(E). \tag{4}
$$

$$
V_\mathrm{s}(E) = \Delta V_\mathrm{s}(E). \tag{5}
$$

$$
V_\mathrm{so}(E) = V_\mathrm{so}\mathrm{e}^{-\lambda_\mathrm{so}(E - E_\mathrm{f})} + \Delta V_\mathrm{so}(E) \tag{6}
$$

where A_HF, λ_HF, V_so and λ_so are undetermined parameters, E_f is the Fermi energy.

The terms $\Delta V_\mathrm{v}(E)$, $\Delta V_\mathrm{s}(E)$ and $\Delta V_\mathrm{so}(E)$, so-called the dispersive correction terms, are calculated using the dispersion relation:

$$
\Delta V(E) = \frac{\mathcal{P}}{\pi}\int_{-\infty}^{+\infty}\frac{W(E')}{E' - E}\mathrm{d}E', \tag{7}
$$

where the symbol $\mathcal{P}$ denotes that the principal value of the integral should be taken.

The energy dependence for the imaginary terms are represented as [10, 11]:

$$
W_\mathrm{v}(E) = A_\mathrm{v}\frac{(E - E_\mathrm{f})^S}{(E - E_\mathrm{f})^S + B_\mathrm{v}^S} \tag{8}
$$

$$
W_\mathrm{s}(E) = A_\mathrm{s}\frac{(E - E_\mathrm{f})^S}{(E - E_\mathrm{f})^S + B_\mathrm{s}^S}\mathrm{e}^{-C_\mathrm{s}|E - E_\mathrm{f}|}, \tag{9}
$$

$$
W_\mathrm{so}(E) = A_\mathrm{so}\frac{(E - E_\mathrm{f})^S}{(E - E_\mathrm{f})^S + B_\mathrm{so}^S}, \tag{10}
$$

where A_{v}, B_{v}, A_{s}, B_{s}, C_{s}, A_{so} and B_{so} are undetermined parameters. The power S was 4 in the paper of Delaroche *et al.* [11], but we use $S = 2$.

The isospin dependence of the potential is considered in real volume $V_{\mathrm{HF}}(E)$ and imaginary surface $W_{\mathrm{s}}(E)$ potentials as follows:

$$\begin{aligned} A_{\mathrm{HF}} &= V_0 + (-1)^{Z'+1} C_{\mathrm{viso}} \frac{N-Z}{A} \\ A_{\mathrm{s}} &= W_0 + (-1)^{Z'+1} C_{\mathrm{wiso}} \frac{N-Z}{A}. \end{aligned} \tag{11}$$

It can be seen that the difference between the neutron and proton potentials is identified by the isovector term, Coulomb correction term and Fermi energy, so all the parameters are taken to be equal for neutron and proton potentials, while for Koning-Delaroche's[1] spherical potential, the parameters for neutron and proton potentials are different, especially for parameters of real part.

With the above dispersive consideration for each potential term, the potential of Eq. (1) is called as dispersive coupled-channel optical model potential.

2.2. Potential Parameters

In the previous work[2], the potential parameters for deformed even-even nuclei in the mass range of A=24-122 for incident energy up to 200 MeV had been derived. The potential parameters fitting was performed by the OPTMAN code[12]. Note that only the experimental data of neutron total cross sections, neutron/proton elastic and inelastic angular distributions are used in the fitting procedure, while the analyzing power data are not included since the OPTMAN code has not such an option. The potential parameters are given in table 1.

Table 1. Potential parameters for global dispersive coupled-channel optical model potential.

	Volume	**Surface**
Real depth (MeV)	$_0 = 56\ 73 - 1\ 00 \times 10^{-2}$	dispersive
	$_{\mathrm{HF}} = 9\ 95 \times 10^{-3} + 3\ 84 \times 10^{-10}\ \ ^3$	
	$_{\mathrm{viso}} = 15\ 9$	
Imaginary (MeV)	$_{\mathrm{v}} = 12\ 55 + 1\ 34 \times 10^{-2}$	$_0 = 10\ 73 + 1\ 44 \times 10^{-6}\ \ ^3$
	$_{\mathrm{v}} = 80\ 46$	$_{\mathrm{s}} = 10\ 35$
	$_{\mathrm{a}} = 385$	$_{\mathrm{s}} = 1\ 81 \times 10^{-2} - 7\ 40 \times 10^{-3}\ \ ^{-\frac{1}{3}}$
		$_{\mathrm{wiso}} = 23\ 5$
Geometry (fm)	$_{\mathrm{v}} = 1\ 20$	$_{\mathrm{s}} = 1\ 29 - 4\ 85 \times 10^{-1}\ \ ^{-\frac{1}{3}}$
	$_{\mathrm{v}} = 6\ 30 \times 10^{-1} + 4\ 40 \times 10^{-4}$	$_{\mathrm{s}} = 8\ 75 \times 10^{-1} - 1\ 02\ \ ^{-\frac{1}{3}}$
	Spin-orbit	**Coulomb**
Real depth (MeV)	$_{\mathrm{so}} = 5\ 922 + 3\ 00 \times 10^{-3}$	$_{\mathrm{Coul}} = 1\ 3$
	$_{\mathrm{so}} = 0\ 005$	
Imaginary (MeV)	$_{\mathrm{so}} = -3\ 1$	
	$_{\mathrm{so}} = 160\ 00$	
Geometry (fm)	$_{\mathrm{so}} = 1\ 18 - 6\ 50 \times 10^{-1}\ \ ^{-\frac{1}{3}}$	$_c = 1\ 45 - 9\ 79 \times 10^{-1}\ \ ^{-\frac{1}{3}}$
	$_{\mathrm{so}} = 0\ 59$	$_c = 5\ 87 \times 10^{-1} - 1\ 80 \times 10^{-1}\ \ ^{-\frac{1}{3}}$

3. Result and discussion

The previous work had shown the predictions of proton analyzing power for ^{56}Fe and ^{120}Sn, here we present some more calculations for other nuclei: ^{24}Mg, ^{28}Si, ^{60}Ni and ^{90}Zr, as shown in Figure 1, 2, 3, 4 respectively, in order to indicate how the predictive power of this global potential is for analyzing power data. As the OPTMAN code has no option to calculate analyzing power, the ECIS06t code[13], with three levels coupled, was used for such calculations.

Firstly, our global potential gave generally good predictions of the proton elastic A_y data for ^{24}Mg, except for low incident energy 15.00 MeV and for 49.20 MeV and 65.00 MeV at large angles. However the agreement for the proton inelastic analyzing power data with experimental data is not satisfactory.

For ^{28}Si, at energies below 20.50 MeV, the predictions for proton elastic scattering analyzing power are generally good, but there are obvious deviations at backward angles. And for 65.00 MeV and 80.00 MeV, the calculations overestimate the experimental data at angles beyond 60^0. The results for proton inelastic scattering analyzing power are smaller than the measurements.

We obtained rather perfect description for proton elastic analyzing power data of ^{60}Ni at overall incident energies and angles. And the predictions for inelastic analyzing data are also good enough. On average, the difference between the calculation and measurement is less than 10%.

Finally, the predictions of proton elastic analyzing power for ^{90}Zr described the experimental data very well below 79.60 MeV. The calculations also described the data well at higher energies, except the deeper extrema. For the inelastic analyzing power, the results are smaller than experimental data.

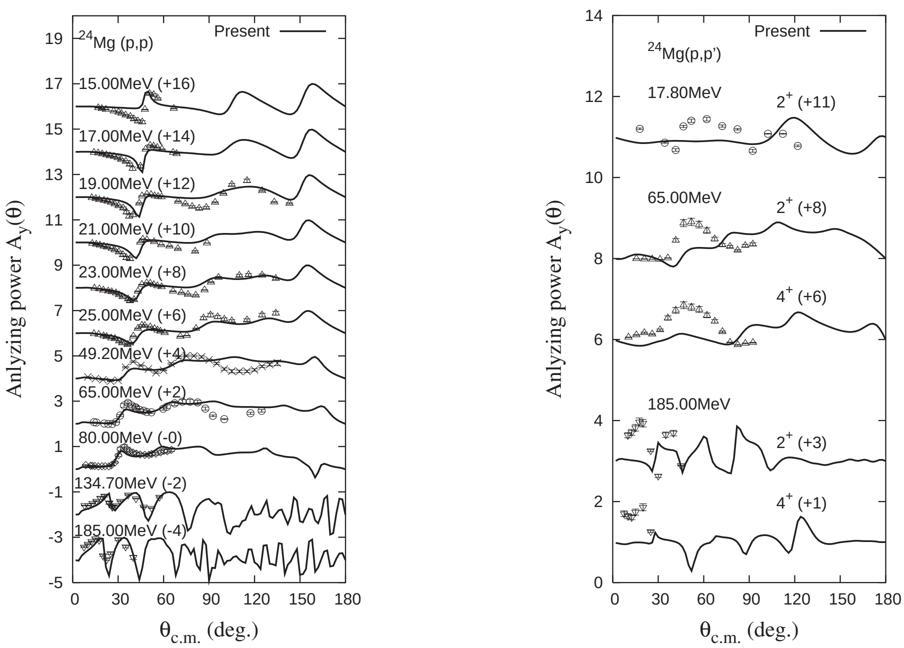

Figure 1. Comparison of the predicted and experimental analyzing power for proton elastic scattering (left) and inelastic scattering (right) from ^{24}Mg. The curves and data points are offset by adding 2,4,6 etc to their values. All the experimental data (here and in later figures) are taken from the EXFOR [14] database.

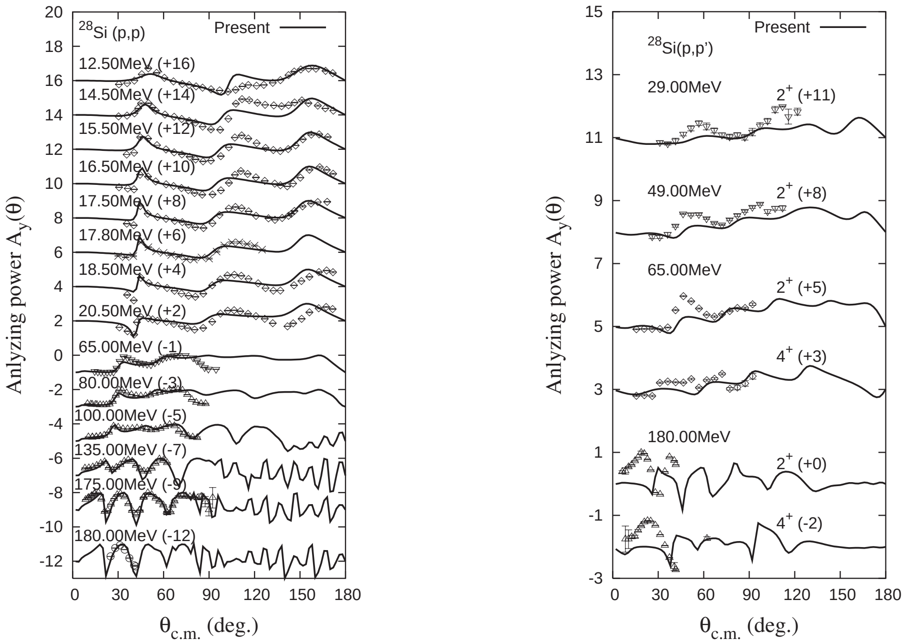

Figure 2. Same as Figure 1 but for ^{28}Si.

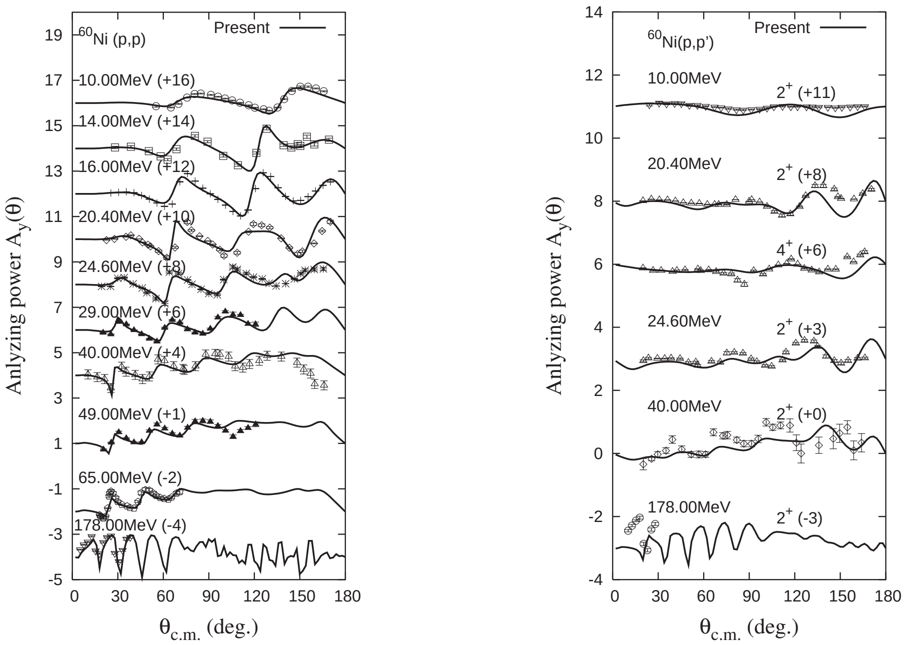

Figure 3. Same as Figure 1 but for ^{60}Ni.

It can be seen that our potential gives rather good or generally good prediction for proton elastic analyzing power for all nuclei. The proton inelastic analyzing power can be also described in overall agreement for near spherical nuclei, such as ^{60}Ni. However for those strong deformed nuclei, such as ^{24}Mg (β_2= 0.5438) and ^{28}Si($\beta_2 = -0.4203$), the predictions are a little worse. Considering the fact that the experimental data of analyzing power are not used in the fitting for our potential parameters, while being employed for Koning and Delaroches spherical potential parameters, it is satisfactory that our global potential can describe simultaneously proton elastic and inelastic scattering analyzing power to such an extent. Our future plan is to incorporate the analyzing power data into OPTMAN code to make more accurate analysis for both

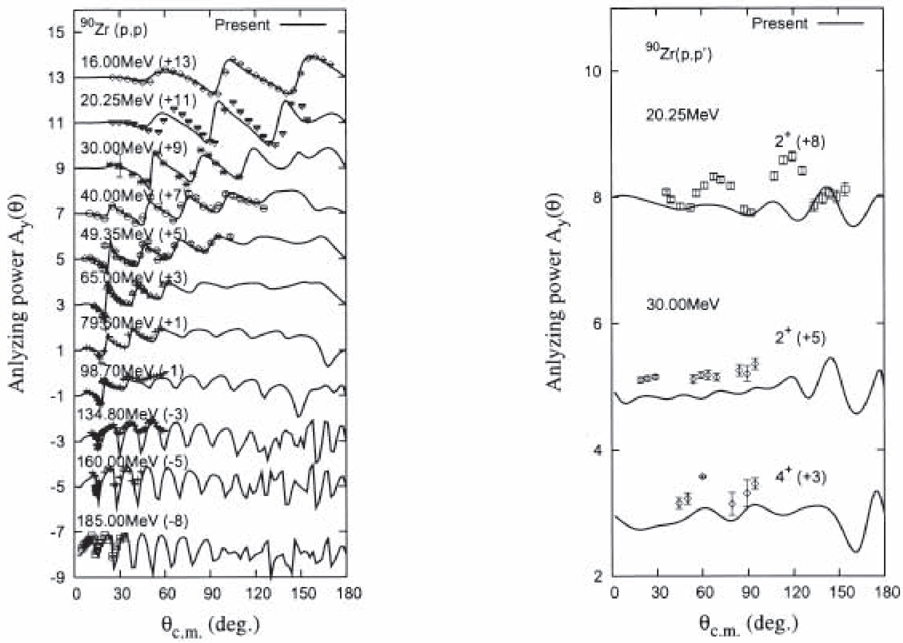

Figure 4. Same as Figure 1 but for ^{90}Zr.

angular distributions and analyzing power data simultaneously.

4. Summary and Conclusion

The global dispersive coupled-channel optical model potential obtained is used to analyze the analyzing power data for some nuclei. The numerical calculations had shown that this potential predicts the proton elastic analyzing power data with general good precision, while the predictions for proton inelastic analyzing power data are a little worse. More improvements need to be done.

References

[1] A.J. Koning and J.P. Delaroche, *Nucl. Phys.* A **713**, 231 (2003).
[2] L.J. Hao, W.L. Sun and E.S. Soukhovitskii, *J. Phys. G: Nucl. Part. Phys.* **35**, 095103 (2008).
[3] E.S. Soukhovitskii, R. Capote, J.M. Quesada and S. Chiba, *Phys. Rev.* C **72**, 024604 (2005).
[4] R.H. Bassel, R.M. Drisko and G.R. Satchler, *Oak Ridge National Laboratory Report* (1962).
[5] E.S. Soukhovitskii, S. Chiba, O. Iwamoto and Y.V. Porodzinskii, *Nucl. Phys.* A **640**, 147 (1998).
[6] C. Mahaux and H. Ngô, *Nucl. Phys.* A **431**, 486 (1984); C. Mahaux, H. Ngô and G.R. Satchler, *Nucl. Phys.* A **449**, 354 (1986); C. Mahaux and R. Sartor, *Nucl. Phys.* A **468**, 193 (1987).
[7] C. Mahaux and R. Sartor, *Nucl. Phys.* A **484**, 205 (1988); C. Mahaux and R. Sartor, *Nucl. Phys.* A **493**, 157 (1989).
[8] R. Lipperheide, *Z. Phys.* **202**, 58 (1967).
[9] R.L. Walter, *Proc. Meeting on Nuclon-Nucleus Optical Model up to 200 MeV* (France: Bruyères-le-Chatel) November 13-15, 199 (1996).
[10] G.E. Brown and M. Rho, *Nucl. Phys.* A **372**, 397 (1981).
[11] J.P. Delaroche, Y. Wang and J. Rapaport, *Phys. Rev.* C **39**, 391 (1989).
[12] E.S. Soukhovitskii, S. Chiba, O. Iwamoto, K. Shibata and G.B. Morogovskij, JAERI-Data/Code 2005-002, *Japan Atomic Energy Research Institute Report* (2005).
[13] J. Raynal, *Notes on ECIS94, CEA Sacley Report No. CEA-N-2772* (1994).
[14] Available online at http://www-nds.iaea.or.at/exfor/exfor00.htm.

18. Nuclear Data-Induced Uncertainty Calculation for Fast Reactor Eigenvalue Separation

Go CHIBA
Reactor Physics Group, Japan Atomic Energy Agency
Tokai-mura, Naka-gun, Ibaraki-ken 319-1195
e-mail: chiba.go@jaea.go.jp

In the present study, we calculated eigenvalue separations and their uncertainties induced by nuclear data for two fast reactors, PNC600 and JSFR-1500. The eigenvalue separations between the fundamental and first modes were +3.4%dk/kk' for PNC600 and +1.5%dk/kk' for JSFR-1500. The nuclear data-induced uncertainties for the eigenvalue separations up to the 5-th mode were less than 1.5% for both the cores. We conclude that the nuclear data-induced uncertainties in the eigenvalue separations are negligibly small.

1. Introduction

A size of commercial fast reactors designed recently has become larger from an economical aspect. However, such large cores sometimes become unstable from a view point of neutronics since spatial decoupling becomes stronger. It has been suggested that an eigenvalue separation be considered as an index of the spatial decoupling [1][2], and that core design studies on stability be carried out more effectively with it.

In the present study, we calculate eigenvalue separations for a large-sized fast reactor designed recently together with a medium-sized fast reactor, and grasp the nuclear data-induced uncertainties in these eigenvalue separations.

2. Eigenvalue separation as an index of core stability

The neutron transport equation can be written as

$$L\psi_n = \frac{1}{\lambda_n} M\psi_n \ , \qquad (1)$$

where L and M correspond to a neutron loss operator and a neutron generation operator, respectively. In Eq. (1), the maximum eigenvalue λ_0 and its eigenfunction ψ_0 correspond to the neutron multiplication factor k and the neutron flux ϕ.

Here, we assume that a multiplication factor k and neutron flux ϕ satisfy the following neutron transport equation at a reference state;

$$L\phi = \frac{1}{k} M\phi \ .$$

When a perturbation is given to this reference state, the operators, the multiplication factor and the neutron flux are perturbed. The perturbation in neutron flux $\delta\phi$ can be expressed with the eigenfunctions in Eq. (1) under the first order approximation as follows:

$$\delta\phi = \sum_{n=1}^{\infty} a_n \psi_n \quad , \tag{2}$$

$$a_n = \frac{\int_0^{\infty} dE \int dV \psi_n^+ \left(\frac{1}{\lambda_0} \delta M - \delta L \right) \phi}{\left(\frac{1}{\lambda_n} - \frac{1}{\lambda_0} \right) \int_0^{\infty} dE \int dV \psi_n^+ M \psi_n} \quad , \tag{3}$$

where ψ_n^+ is an adjoint eigenfunction in the reference state. This adjoint eigenfunction satisfies the following adjoint equation:

$$L^+ \psi_n^+ = \frac{1}{\lambda_n} M^+ \psi_n^+ \quad ,$$

where L^+ and M^+ are the adjoint operators corresponding to L and M, respectively.

Here, we define the n th eigenvalue separation $(IE)_n$ as

$$(IE)_n = 1/\lambda_n - 1/\lambda_0 \, .$$

From Eqs. (2) and (3), we can find that a component of ψ_n in the neutron flux perturbation becomes large when the n th eigenvalue separation is small. Since we can regard a magnitude of response in neutron flux by a perturbation as instability of core neutronics, the eigenvalue separation can be regarded as an index of core stability.

3. Calculation of higher-mode eigenfunctions

The power method is to obtain the maximum eigenvalue and its eigenfunction. In order to obtain higher-mode eigenvalues and their eigenfunctions, the deflation method has been widely used [1].

In the deflation method, an approximated solution for the n th mode at the m th iteration $\tilde{\psi}_n^m$ is calculated from a solution at the $(m-1)$ th iteration ψ_n^{m-1} as

$$L \tilde{\psi}_n^m = \frac{1}{\lambda_n^{m-1}} M \psi_n^{m-1} \, .$$

An initial value ψ_n^0 should include a component of the eigenfunction of the n th mode. After obtaining $\tilde{\psi}_n^m$, a solution at the m th iteration can be obtained by extracting components of the lower-order modes from this approximated solution as

$$\psi_n^m = \widetilde{\psi}_n^m - \sum_{l=0}^{n-1} \psi_l \cdot \frac{\int_0^\infty dE \int dV \psi_l^+, M\psi_n^m}{\int_0^\infty dE \int dV \psi_l^+, M\psi_l}.$$

With the above procedure for all the modes, we can obtain the higher-mode eigenvalues and their eigenfunctions.

4. Implementation

We implement the deflation method into a unified neutron transport simulation code system CBG. At the present, CBG has a capability to obtain the higher-mode solutions with diffusion solvers PLOS for Cartesian and cylindrical systems and DHEX for Hexagonal-Z systems. These solvers are based on the finite difference method. Sensitivities of higher-mode eigenvalues to cross sections $S_\sigma^{\lambda_n}$ can be calculated with both the solvers. An implementation of the deflation method for discrete ordinates transport solvers will be done in future.

5. Numerical results

In the present study, we calculate eigenvalue separations for two fast reactors. One is “PNC600” (600MWe) at the initial state and the other is “JSFR-1500” (1500MWe) at the end of cycle. Layouts of these cores are shown in Fig. 1.

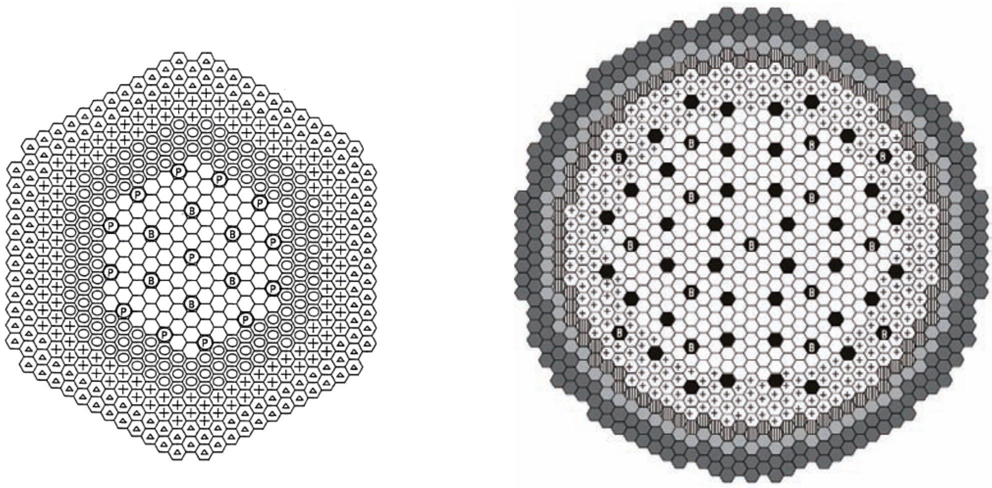

Fig.1 Core layouts of PNC600 (left) and JSFR-1500 (right)

For effective cross section calculations, we utilize the SLAROM-UF code and a 70-group library UFLIB based on JENDL-3.3. With the obtained effective cross sections, higher-mode calculations are performed with DHEX for half-core three-dimensional models and with PLOS for whole-core cylindrical models.

Figure 2 shows eigenvalues and spatial distributions of eigenfunctions on the X-Y plane for the half-core three-dimensional models. In this figure, a sign “+” or “-” indicates positive or negative values of eigenfunctions. The eigenvalue separations between the fundamental and first modes are +3.4%dk/kk’ for PNC600 and +1.5%dk/kk’ for JSFR-1500. It is found that the eigenvalue separation of JSFR-1500 is smaller than that of PNC-600.

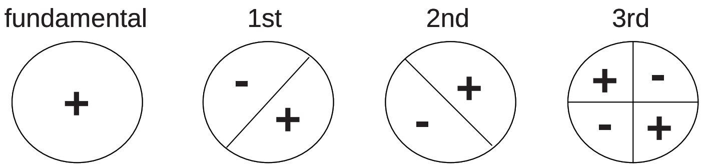

	fundamental	1st	2nd	3rd
PNC600	1.07681	1.03855	1.03562	0.97739
JSFR-1500	0.98692	0.97271	0.97248	0.95139

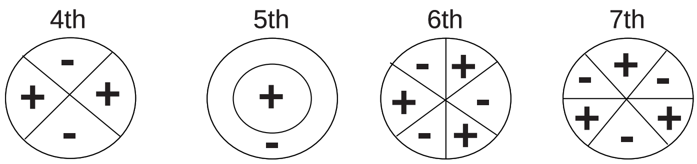

	4th	5th	6th	7th
PNC600	0.97538	0.91662	0.90977	0.89884
JSFR-1500	0.94736	0.92801	0.92087	0.91871

Fig. 2 Results for half-core three-dimensional models

With the half core models, it is impossible to see all the higher-mode eigenfunctions which have a distribution along to the Z-axis (axial mode). Figure 3 shows the higher-mode solutions obtained with the whole-core cylindrical models. We find that the eigenvalues of the axial mode are much smaller than those of the radial modes. This is because both the cores are flat in a horizontal view in order to reduce sodium void reactivity worth.

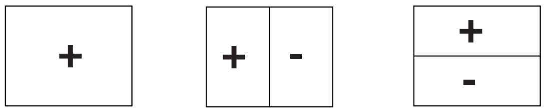

PNC600	1.06826	0.90661	0.79056
JSFR-1500	0.98604	0.92551	0.69736

Fig.3 Results for whole-core cylindrical models

Next, we evaluate the nuclear data-induced uncertainties in the eigenvalue separations. Covariance data for U-235, -238, Pu-239, -240, -241 and Na-23 given in JENDL-3.3 are processed with the ERRORJ code [3] and the 70-group covariance matrices are obtained. Sensitivities of the eigenvalue separations to cross sections $S_\sigma^{(IE)_n}$ are calculated from $S_\sigma^{\lambda_n}$ as

$$S_\sigma^{(IE)_n} = \frac{1}{(IE)_n}\left(\frac{S_\sigma^{\lambda_0}}{\lambda_0} - \frac{S_\sigma^{\lambda_n}}{\lambda_n}\right). \qquad (4)$$

Using the covariance matrices and the sensitivities $S_{\sigma}^{(IE)_n}$, we calculate the nuclear data-induced uncertainties in the eigenvalue separations. The results are shown in Table 1. The nuclear data-induced uncertainties in the eigenvalue separations up to the 5-th mode are less than 1.5% for both PNC600 and JSFR-1500.

Table 1 Eigenvalue separations (dk/kk') and their nuclear data-induced uncertainties (%)

Mode	PNC600	JSFR-1500
1	0.034 (1.01)	0.015 (1.29)
2	0.037 (1.01)	0.015 (1.28)
3	0.094 (1.04)	0.038 (1.31)
4	0.097 (1.04)	0.042 (1.32)
5	0.162 (1.30)	0.064 (1.50)

As shown in Eq. (4), the sensitivities of the eigenvalue separations to cross sections are calculated with $S_{\sigma}^{\lambda_n} / \lambda_n$. Figures 4 and 5 show these "eigenvalue-divided" sensitivities to Pu-239 fission cross section and U-238 capture cross section for JSFR-1500. The energy profiles of these sensitivities of the higher-mode eigenvalues are very similar to that of the fundamental mode eigenvalue. Hence, it is supposed that the eigenvalue separations are insensitive to cross sections. This is consistent with the numerical results of the small nuclear data-induced uncertainties in the eigenvalue separations.

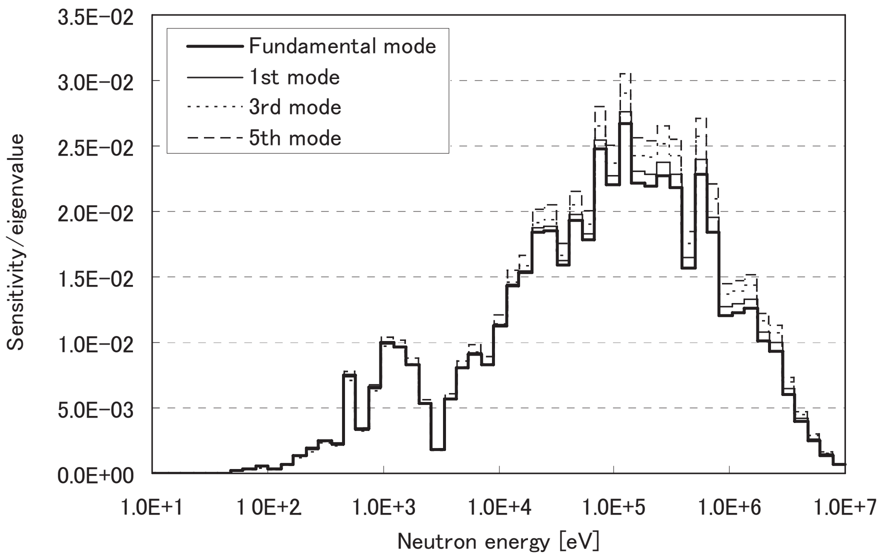

Fig.4 Sensitivities of eigenvalues to Pu-239 fission cross section for JSFR-1500

Let us consider a one-group diffusion problem. After rewriting the divergence (leakage) term with the buckling, we can obtain the following equation:

$$\lambda_n = \nu\Sigma_f \Big/ \left(DB_n^2 + \Sigma_a\right) .$$

Since a contribution of the leakage term to the eigenvalue is small in a large core, a mode dependence of sensitivities, $S_\sigma^{\lambda_n}$ or $S_\sigma^{\lambda_n} / \lambda_n$, is considered to be small.

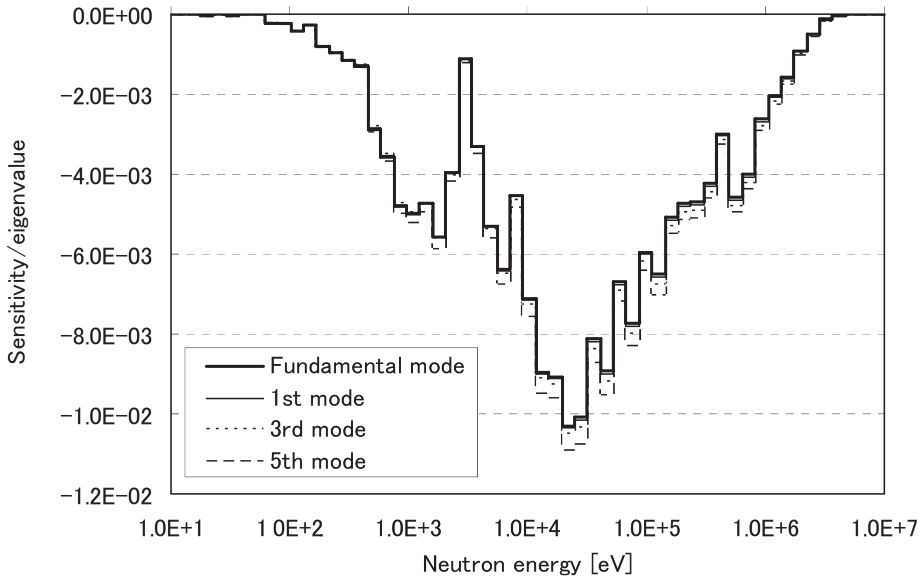

Fig.5 Sensitivities of eigenvalues to U-238 capture cross section for JSFR-1500

6. Conclusion

In the present study, we calculated the eigenvalue separations and their uncertainties induced by nuclear data for the fast reactors, PNC600 and JSFR-1500. The eigenvalue separations between the fundamental and first modes are +3.4%dk/kk' for PNC600 and +1.5%dk/kk' for JSFR-1500. The nuclear data-induced uncertainties for the eigenvalue separations up to the 5-th mode are less than 1.5% for both PNC600 and JSFR-1500. We can conclude that the nuclear data-induced uncertainties of the eigenvalue separations are negligibly small.

Acknowledgment

The author wishes to express his gratitude to Y. Kitamura and T. Kugo of Japan Atomic Energy Agency for providing useful comments on this manuscript.

References

[1] K. Hashimoto: “Analysis of spatial decoupling of large core with spatial higher-mode functions,” Doctoral thesis, Nagoya university (1985). [in Japanese]

[2] K. Shirakata, et al.: “Neutronic decoupling characteristics of large fast reactor cores,” Trans. At. Energy Soc. Jpn. 2. p.163 (2003). [in Japanese]

[3] G. Chiba: “ERRORJ: A code to process neutron-nuclide reaction cross section covariance, version 2.3,” JAEA-Data/Code 2007-007 (2007).

19. Criticality Calculations with Fission Spectrum Matrix

Go CHIBA
Reactor Physics Group, Japan Atomic Energy Agency
Tokai-mura, Naka-gun, Ibaraki-ken 319-1195
e-mail: chiba.go@jaea.go.jp

In the present study, the author implemented a procedure to treat a fission spectrum matrix into neutron transport solvers of a code system CBG, and quantified errors of usual procedures utilizing a fission spectrum vector. Numerical results showed that the errors of the usual procedures are negligible if the fission spectrum vector is generated from the fission spectrum matrix with weight functions obtained by cell calculations. On the other hand, when a library built-in function is used as a weight function for the fission spectrum vector generation, the errors become large if there is a large difference between the library built-in function and the neutron energy spectrum of the target system.

1. Introduction

A fission spectrum (an energy distribution of secondary neutrons generated by fission reactions) is given in a matrix form in the ENDF-formatted nuclear data files since the fission spectrum depends on incident energies of neutrons causing the fission reactions. On the other hand, most deterministic neutron transport codes treat the fission spectrum in a vector form. Hence, it is necessary to generate the fission spectrum vector equivalent to the fission spectrum matrix when such deterministic codes are used for criticality calculations.

In the present study, we realize criticality calculations with the fission spectrum matrix. In addition, using the solutions of such calculations as references, we quantify errors of the usual procedures with the fission spectrum vector for criticality calculations.

2. Fission source representations

Considering the incident energy dependence of the fission spectrum, we can write a fission source term in a multi-group neutron transport equation as

$$F_g = \sum_n \sum_{g'} \chi^n_{g'\to g} N^n (\nu\sigma)^n_{f,g'} \phi_{g'} = \sum_{g'} \phi_{g'} \left(\sum_n N^n (\nu\sigma)^n_{f,g'} \chi^n_{g'\to g} \right), \tag{1}$$

where n and g correspond to a nuclei and energy group, respectively. Other notations are classical. Here, we can define a macroscopic fission spectrum $\bar{\chi}_{g'\to g}$ as

$$\bar{\chi}_{g'\to g} = \sum_n \chi^n_{g'\to g} N^n (\nu\sigma)^n_{f,g'} \Big/ \sum_n N^n (\nu\sigma)^n_{f,g'} .$$

With the above macroscopic fission spectrum, we can write the fission source term in a macroscopic form as

$$F_g = \sum_{g'} \overline{\chi}_{g' \to g} (\nu\Sigma)_{f,g'} \phi_{g'} .$$

Most deterministic neutron transport codes treat the fission spectrum as a vector. In this case, the fission source term is written as

$$F_g = \overline{\chi}_g \sum_{g'} (\nu\Sigma)_{f,g'} \phi_{g'} .$$

In order to make the above fission source term equivalent to Eq. (1), the fission spectrum vector should be defined as

$$\overline{\chi}_g = \sum_{g'} \overline{\chi}_{g' \to g} (\nu\Sigma)_{f,g'} \phi_{g'} \Big/ \sum_{g'} (\nu\Sigma)_{f,g'} \phi_{g'} . \quad (2)$$

We can find from the above equation that the energy spectrum of the neutron flux is necessary to obtain the fission spectrum vector. Rigorously speaking, the fission spectrum vector should be obtained iteratively since the energy spectrum of the neutron flux depends on the fission spectrum vector. Such a procedure [1] is, however, inefficient from a view point of computation time. Hence, the following two procedures have been usually utilized. Multi-group libraries normally contain weight functions which are used in the library generation process from original ENDF files. One procedure is to use this library built-in function as a weight function in Eq. (2). The other procedure is to use an energy spectrum of a neutron flux obtained in a cell calculation (B1 spectrum calculations, collision probability calculations, etc).

In the present study, we quantify the errors of these two procedures.

3. Implementation and realization

A procedure to treat a fission spectrum matrix is implemented into neutron transport solvers of a code system CBG. The CBG system is written by the objected-oriented computer language C++ and all the neutron transport solvers inherit a power iteration procedure from a base class. Hence, we have to add a capability to perform criticality calculations with a fission spectrum matrix only into this base class. After that, all the neutron transport solvers, SNR based on the discrete ordinates method and PJI based on the collision probability method and so on, can treat a fission spectrum matrix.

4. Numerical results

In the present study, criticality calculations are performed for six spherical systems in the ICSBEP handbook [2]. Four of them are fast systems (Jezebel [PU-MET-FAST-001], Godiva [HEU-MET-FAST-001], Flattop-Pu [PU-MET-FAST-006] and Flattop-U [HEU-MET-FAST-028]) and the others are thermal solution systems reflected by water (HST010-1 [HEU-SOL-THERM-010-1] and PST004-1 [PU-SOL-THERM-004-1]).

For effective cross section calculations, we utilize the SLAROM-UF code [3] and UFLIB (175-group) for the fast systems and CBG/SelfShieldingCalculator and CBGLIB [4] (107-group) for the thermal systems. UFLIB and CBGLIB have a typical thermal reactor's one (thermal Maxwellian+1/E+fission spectrum) as library built-in functions. With the obtained effective cross sections, criticality calculations are performed with a one-dimensional discrete ordinates solver CBG/SNR. The option of this calculation is P_3DP_{24}. In addition, continuous-energy Monte Carlo calculations are performed with MVP-II and its library based on JENDL-3.3 with a fission spectrum matrix. Statistical uncertainties of the MVP-II results are less than 0.02%dk/kk' as a 1σ reliability.

Obtained effective multiplication factors are shown in Table 1.

Table 1 Effective multiplication factors for six critical systems

Core	Vector		Matrix	Matrix (MVP-II)
	Built-in flux	Cell flux		
Jezebel	0.99435	0.99686	0.99710	0 99717 .
Godiva	1.00042	1.00244	1.00254	1.00255
Flattop-Pu	0.98943	0.99240	0 99224 .	0.99241
Flattop-U	0.99571	0.99843	0.99834	0.99867
HST010-1	1.00032	1.00041	1 00033 .	1.00095
PST004-1	1.00729	1.00724	1.00728	1.00807

Results of CBG/SNR calculations with a fission spectrum matrix agree with the MVP-II results within 0.08%dk/kk'. Hence, it is verified that the procedure to treat the fission spectrum matrix has been successfully implemented into CBG.

Next, using the results obtained with the fission spectrum matrix as reference solutions, we quantify errors of the usual procedures based on the fission spectrum vector. Table 2 shows the errors of the two procedures.

Table 2 Errors of the usual procedures based on the fission spectrum vector (unit: dk)

Core	Built-in flux	Cell flux
Jezebel	−0.00275	−0.00024
Godiva	−0.00212	−0.00010
Flattop-Pu	−0.00281	0.00016
Flattop-U	−0.00263	0.00009
HST010-1	−0.00001	0.00008
PST004-1	0.00001	−0.00004

It is found that the errors of the usual procedures with the fission spectrum vector are negligible if the fission spectrum vector is generated from the fission spectrum matrix with the weight function obtained at the cell calculation. On the other hand, when the library built-in function is used as a weight function in Eq. (2), large errors are observed in the small fast systems. These large errors are caused by differences between the library built-in function and the neutron energy spectra of the target systems. The sizes of these fast systems are small and they contain no moderator material. Since the neutrons emitted by the fission reactions may cause the next fission reactions without losing energy by scattering in these small fast systems, the neutron multiplication factors are considered to be sensitive to the shapes of the fission spectra in these systems. It is expected that the errors due to the differences in weight functions in Eq. (2) are small for thermal systems or large fast systems.

5. Conclusion and perspective

In the present study, a procedure to treat the fission spectrum matrix has been implemented into neutron transport solvers of a code system CBG, and errors of the usual procedures utilizing the fission spectrum vector have been quantified. Numerical results have shown that the errors of the usual procedures are negligible if the fission spectrum vector is generated from the fission spectrum matrix with a weight function obtained by a cell calculation. On the other hand, when a library built-in function is used as a weight function, the errors become large if there is a difference between a library built-in function and a neutron energy spectrum of a target system.

In order to develop a deterministic reactor calculation code system applicable to various kinds of reactors with a wide range of neutron spectra, it is necessary to prepare the fission spectrum matrix in its library and to implement a function to generate the fission spectrum vector from the fission spectrum matrix with a neutron flux obtained at a cell calculation. We can conclude that the power iteration with the fission spectrum matrix is not needed from a view point of eigenvalue calculations. We, however, need more investigations on this necessity for others, such as effective delayed neutron fraction calculations with a “prompt k-ratio method” [5], in which treatments of fission spectrum matrices are important.

Acknowledgment

The author wishes to express his gratitude to S. Okajima, K. Okumura and T. Kugo of Japan Atomic Energy Agency for providing useful comments on this manuscript.

References

[1] C. Mounier, et al.: “Fission source calculations and its influence in criticality applications,” Proc. of Int. Conf. on the Physics of Reactors (Physor2008), Interlaken, Switzerland (2008).

[2] J. Blair Briggs (ed.): International handbook of evaluated criticality safety benchmark experiments, NEA/NSC/DOC(95)03/I, Nuclear Energy Agency, Paris(2006 Edition).

[3] T. Hazama, et al.: “Development of SLAROM-UF : a lattice calculation code with fine and ultra-fine energy group cross sections,” J. Nucl. Sci. Technol., 43, p.908 (2006).

[4] G. Chiba: “CBGLIB: A multi-group neutron library for precise neutronics simulations,” Proc. of 2007 Symposium on Nuclear Data, p.114, JAEA-Conf 2008-008 (2008).

[5] M. M. Bretscher: “Evaluation of reactor kinetic parameters without the need for perturbation code,” Proc. Int. Mtg. Reduced Enrichment for Research and Test Reactors, Jackson Hole, Wyoming (1997).

20. Recent progress of fragment measurement from tens of MeV proton induced reaction using Bragg Curve Counter

T.Sanami, M.Hagiwara, M.Takada[1] and M.Baba[2]

High Energy Accelerator Research Organization (KEK)
[1]National Institute of Radiological Science
[2]Cyclotron Radioisotope Center, Tohoku University
email: toshiya.sanami@kek.jp

The system including Bragg Curve Counter (BCC) to measure double differential cross section (DDX) of fragment production from tens of MeV proton induced reactions was updated to reduce energy threshold of measurements by reducing thicknesses of a sample and an entrance window. The DDX data were obtained for 40 and 80 MeV proton on Carbon using the system.

1. Introduction

The double differential cross section (DDX) data of fragment production from tens of MeV proton induced reactions are required to establish reaction models and parameters for energy deposition process simulation of tens MeV nuclides. We have conducted measurement of DDX data in this energy range using a Bragg Curve Counter (BCC). The DDX data of 50 and 70 MeV proton induced fragment production reaction were measured for C, Al and Si target [1,2,3]. The acceptable energy range of the BCC has improved using newly developed techniques of particle identification and off-line analysis [1,2]. The energy threshold of the whole system, however, is still not enough due to thickness of entrance window and samples for heavier fragments. The reduction of energy threshold is important to estimate amount of low energy fragments from evaporation process that accounts for large part of total production.

In this year, we replace the window and the sample to thinner one to use whole acceptable energy range of the BCC. The improvement is demonstrated through experimental data for the DDX measurement of 40 and 80 MeV proton induced fragment production reaction.

2. Apparatus

2-1. Bragg curve counter

The detail of the system employing the BCC was described in references [1,2]. Outline of this system is described. Figure 1 shows schematic view of the BCC. The BCC is a parallel plate ionization chamber with a grid, the structure of which is contained in a stainless steel cylindrical chamber. The distances between cathode and grid, and, grid and anode are 300 mm and 5 mm, respectively. High voltage is applied to the cathode and grid electrode to form electric field for electron drift. The field shaping rings maintain uniformity of the electric field. The cylindrical chamber is sealed using O-rings to keep low-pressure counting gas, typically 200 Torr Ar+10% CH_4 gas, inside. The cathode side wall of the chamber has a hole covered with a thin entrance window to introduce fragments from the sample that is placed in a scattering chamber. Figure 2 shows a picture of the apparatus that consist of BCC and scattering chamber, etc.

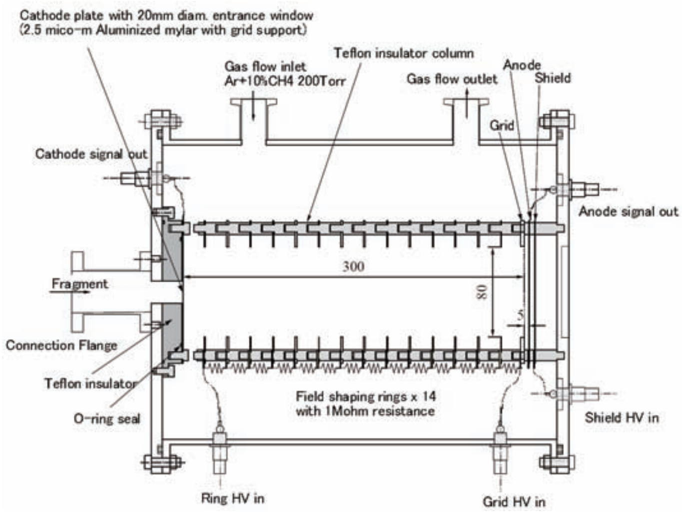

Fig. 1: Schematic drawing of the Bragg curve counter.

Figure 3 shows schematic diagram of the BCC. The fragment entered to the chamber stops and deposits its energy through ionization process. The distribution of the electrons produced in the process along their trajectory is proportional to energy loss of the fragment, i.e, Bragg curve. Since the uniform electric field between the cathode and grid, the electrons drift toward to the grid with keeping their distribution. By choosing adequate ratio of electric field strength between cathode-grid and grid-anode, all electrons reach on the anode with passing through the grid. Because of electric shielding of the grid, time distribution of the anode signal (Pa) has inverse shape of the original distribution of electrons that equal to Bragg curve. The

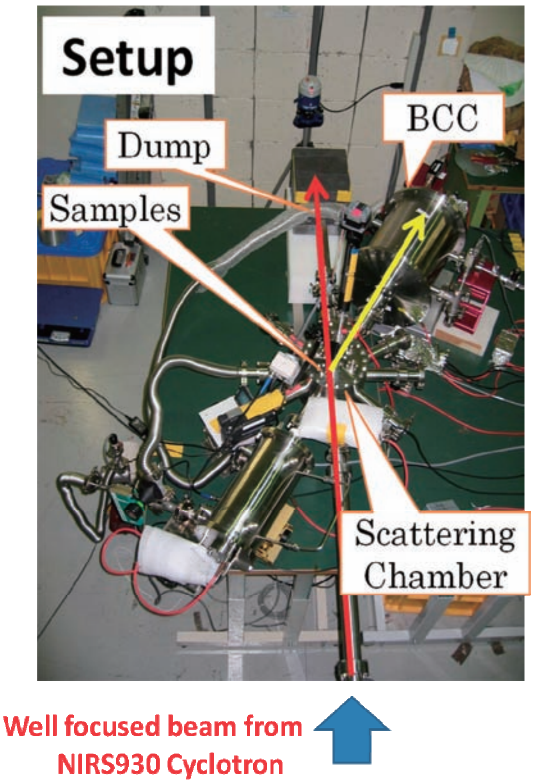

Fig. 2: Picture of the experimental setup for DDX measurement with the BCC at 30-dgree.

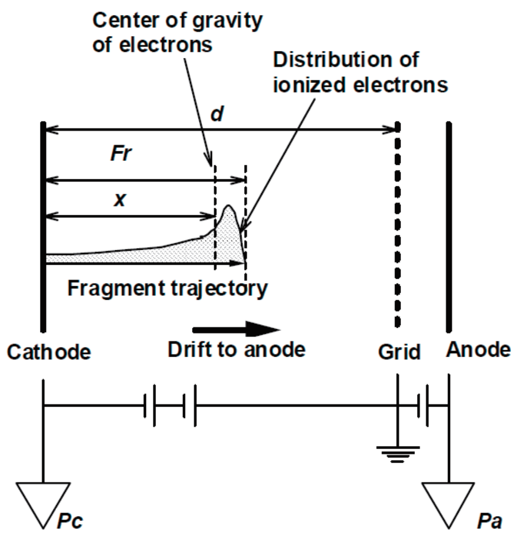

Fig.3 Schematic diagram of the BCC

integral and peak height of the Bragg curve is proportional to energy and atomic number of the fragment. As a consequence, we can determine energy and atomic number of the fragment from the anode signal.

Figure 4 shows typical two dimensional spectrum for fragment identification. The vertical axis corresponds to Bragg peak height that is obtained by processing the anode signal using an amplifier with short time constant relative to the signal duration. The horizontal axis corresponds to energy that is obtained using long time constant. Because of difference of Bragg peak height, fragments are indentified clearly. In addition to this, we have developed a method to reduce energy threshold of the fragment identification using the signal from the cathode [1]. Punch-out fragments are utilized through off-line analysis to enhance upper limit of acceptable fragment energy range [2].

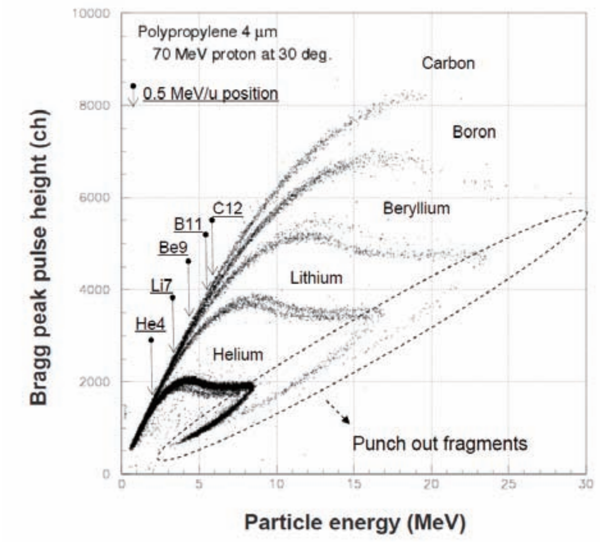

Fig.4: Typical two dimensional spectrum for fragment identification.

2-2. Improvement of the system

To utilize entire acceptable energy range of the BCC, the entrance window and the sample should be replaced to thinner one since energy threshold of data are determined by fragment energy losses before entering the BCC.

The entrance window of the BCC is replaced from 2.5 μm thick Aluminized Mylar foil to 0.2 μm thick SiN membrane. The membrane is supported by a 500 μm thick Si frame that divides four 4.7×4.7 mm^2 area[1]. The frame was mounted on the cathode plate of the BCC with 1 cm diameter hole with epoxy resin. The membrane is robust up to around 400 Torr counting gas pressure. The sample thickness is also reduced by replacing from 4 μm thick polypropylene to 200 $\mu g/cm^2$ thick graphite foil. By these changes, the energy losses before entering the BCC are reduced, especially for fragments having energy of particle identification threshold, 0.5 MeV/n. The threshold energy of the system is equal to the energy of the BCC.

3. Experimental

The measurement of fragment DDX from 40 and 80 MeV proton induced reaction were done using the NIRS 930 cyclotron in National Institute of Radiological Science (NIRS) to confirm effectiveness of this improvement. The other conditions of the system and data analysis procedure are

1 http://www.silson.com/

same as reference [1,2]. Figure 2 shows experimental setup for DDX measurement with the BCC at 30-degree.

Figure 5 shows the comparison of the experimental results of DDX at 30-degree, the $^{12}C(p,B)$ reaction for Ep=50MeV, between different window and sample thickness. The identification thresholds of the BCC are same for both cases, however, the threshold energy of the results are different due to the effect of energy loss compensation analysis. The amount of energy compensation that reaches up to 4 MeV for Boron under previous condition increases energy threshold of the system. Under the present condition, energy threshold of the system is close to the particle identification threshold of the BCC. The difference of the thresholds increases with atomic number (Z) of the fragment.

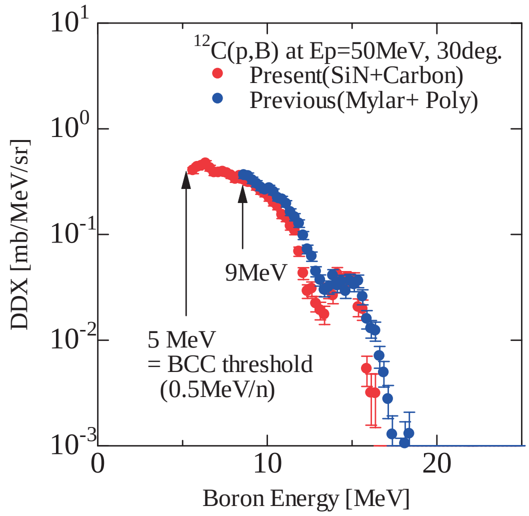

Fig. 5: Experimental results of DDX at 30-dgree, the $^{12}C(p,B)$ reaction for Ep=50 MeV

3. Results and discussion

Figures 6-9 show results of DDXs for Li, Be, B and C productions on C, respectively, at 30 degree in comparison with four different incident proton energies, 40, 50, 70 and 80 MeV. The results obtained from PHITS code [4] calculation with different models are also plotted in the figures. From these figures, the following facts can be deduced.

(1) Most of the fragments are emitted through evaporation process in this energy range. (2) The combination of ISOBAR and GEM models reproduces experimental results better than one of Bertin and GEM for all the cases. The changing INC model corresponds to changing energy for evaporation process that determines number of fragments. Thus, we have to choose (3) pre-equilibrium model and parameters that gives appropriate energy for evaporation process to simulate fragment production. For 40 and 50 MeV proton data, mono-energetic peaks of ^{6}Li and ^{7}Be can be observed at the upper end of the spectra. The peaks indicate the products are from the $^{12}C(p,^{6}Li)^{7}Be$ reaction. It is obvious that (4) two-body components are not able to be calculated owing to lack of model. (5) The data at very low energy region (less than 0.5 MeV/n) are not available by this system. E-TOF system instead of the system would be required to obtain such low energy range data.

4. Conclusion

The threshold energy of fragment measurement using the system including BCC is improved by replacing the entrance window and sample to thinner one. The threshold energy of 0.5 MeV/n were achieved by this improvement. The effects of this improvement are confirmed through DDX measurement of fragments from 40 and 80 MeV proton induced reaction on carbon. Through the comparison with PHITS results, the spectra of fragments can be reproduced using the combination of ISOBAR and GEM models well.

References

1. T.Sanami, M.Hagiwara, T.Oishi, M.Baba, M.Takada, Nucl. Instrm. Meth. **A Vol 589/2** pp 193-201 (2008)
2. M. Hagiwara, T. Sanami, T. Oishi, M. Baba, M. Takada, *Nucl. Instrm. Meth.* **A Vol 592** pp 73-79 (2008)
3. M. Hagiwara, T. Oishi, S. Kamada, M. Baba, T. Sanami, M. Takada and N. Miyahara, "Measurements of Double Differential Fragment Production Cross Sections of Silicon for 70 MeV Protons", Procedings of 2005 Symposium on Nuclear Data (JAEA-Conf 2006-009)
4. H.Iwase et al., *J.Nucl.Sci.Technol.*, **39** (2002) 1142

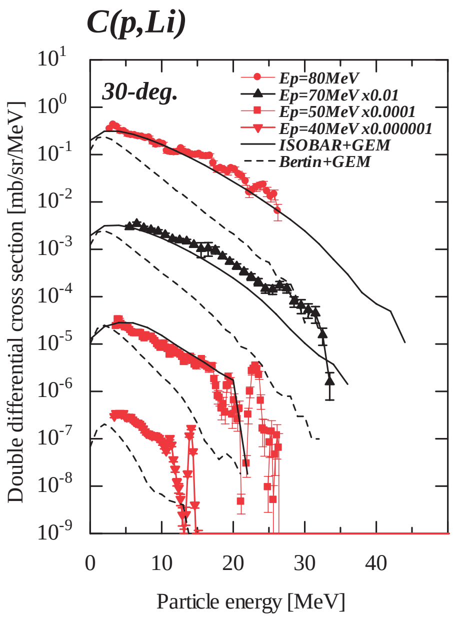

Fig.6 DDX for Li production on C at 30 degree for 40-80 MeV proton induced reaction.

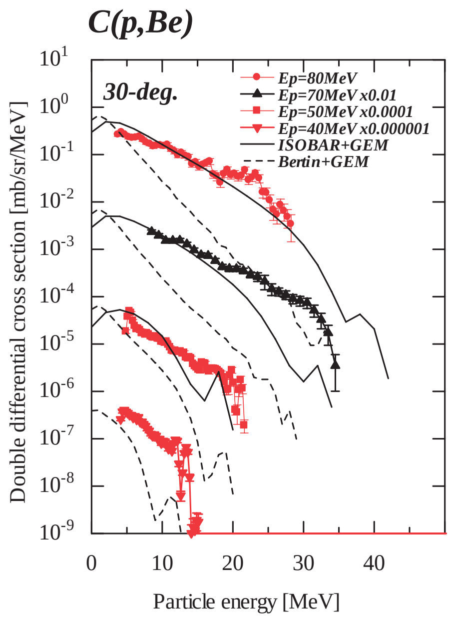

Fig.7 DDX for Be production on C at 30 degree for 40-80 MeV proton induced reaction.

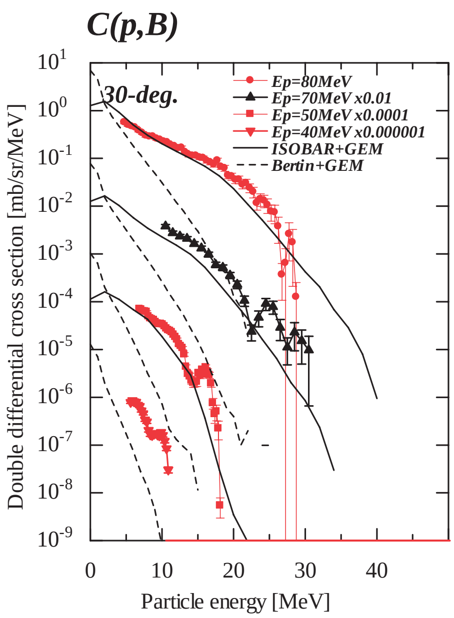

Fig.8 DDX for B production on C at 30 degree for 40-80 MeV proton induced reaction.

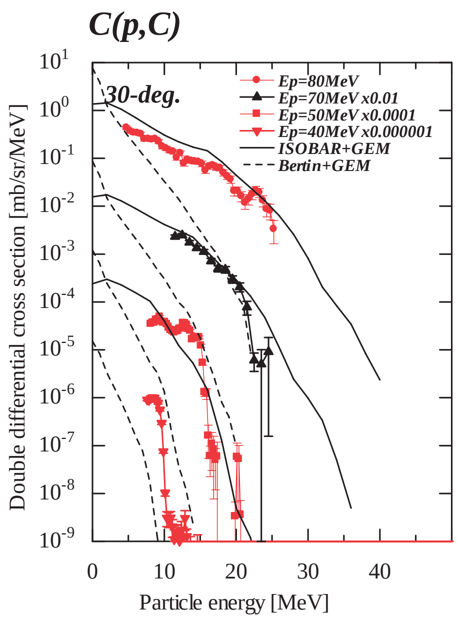

Fig.9 DDX for C production on C at 30 degree for 40-80 MeV proton induced reaction.

21. Photon scattering experiment on ^{139}La up to the neutron separation energy

A. Makinaga[1], G. Rusev[2,3], R. Schwengner[2], A. R. Junghans[2], A. Wagner[2]

[1] *Department of Physics, Konan University, Okamoto 8-9-1, Higashinada, Kobe 658-8501, Japan*
[2] *Institute fur Strahlenphysik, Forschungszentrum Dresden-Rossendorf, Postfach 510119, D-01314 Dresden, Germany*
[3] *Triangle Universities Nuclear Laboratory, Duke University, Durham, NC27708, USA*
e-mail:dn521001@center.konan-u.ac.jp

Abstract

Gamma strength function is the important input parameter to determine the photodisintegration rate and neutron capture rate for astrophysics and nuclear technologies. To test the model calculation, photon-scattering cross sections were measured for ^{139}La below neutron separation energy with bremsstrahlung at an electron kinetic energy of 11.5 MeV. The experimental data was analyzed with statistical methods (Monte Carlo simulation of nuclear γ-ray cascades) to obtain the intensities of the ground-state transitions and their branching ratios. The present ^{139}La photon scattering cross sections are combined with ^{139}La photoneutron cross sections smoothly. The present data also shows the large enhancement at gamma energy range of about 6 - 8 MeV. This may be related to a pygmy dipole resonance.

1 Introduction

There exist 35 neutron-deficient nuclides heavier than iron which can't be produced via slow and rapid neutron capture process. The nucleosynthesis of these nuclides are referred to as p-process and produced in the hot stellar environment with temperature around 2.5 $\times 10^9$ K [1]. In such condition, the thermal population of nuclear levels have a strong influence on photodisintegration rates. So the experimental studies of nuclei below particle separation energy are important parameters for the stellar model.

The origin of the rare odd-odd p-nucleus ^{138}La is generally underproduced in p-process calculations. Theoretical studies show that exploding sub-Chandrasekhar-mass CO white dwarfs and SNe-II are significant to produce ^{138}La. The problem of the ^{138}La is discussed in references [1, 2, 3, 4]. On the other hand, ν process from ^{138}Ba via the charged current reaction was suggested as the origin of ^{138}La and attempted to explain the underproduction of ^{138}La [4]. However, reaction rates are still critical for thermonuclear production of ^{139}La and ^{138}La.

^{139}La (N=82) which has a closed neutron shells is also of special importance in nuclear structure. In some nuclei around Z, N=20, 28, Z=50, N=82, and doubly magic nuclei, extra strength,

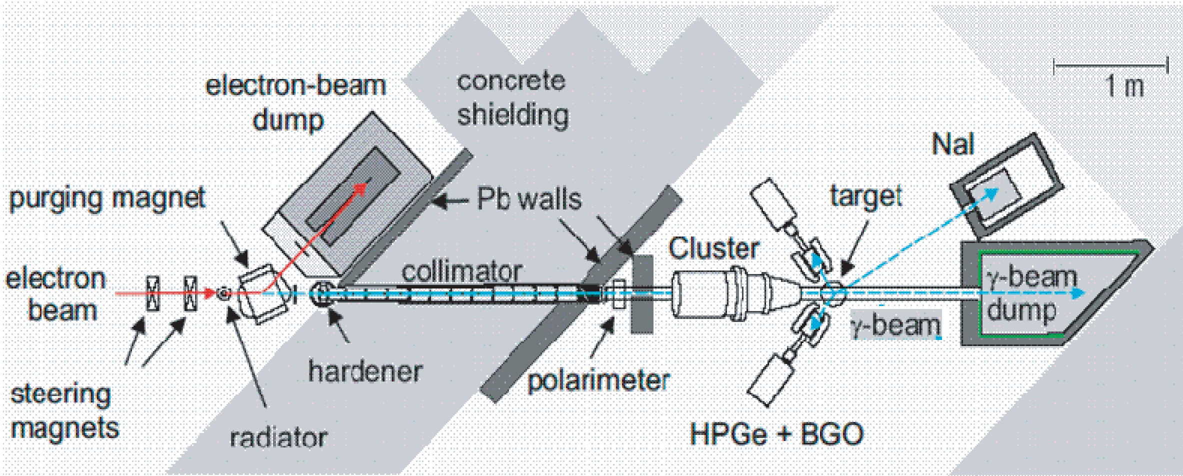

Fig. 1: Experimental set up for photon-scattering at bremsstrahlung facility ELBE of the Research Center Dresden-Rossendorf. [8, 9] The bremsstrahlung photons are produced by hitting niobium radiator with electron beam. Produced bremsstrahlung is collimated by an Al collimator and iraddiate ^{139}La.

so-called "pygmy dipole resonance" (PDR), was found at the low-energy tail of the GDR in the photon-scattering experiments [5, 6].

Recently experimental photodisintegration cross sections for ^{139}La were measured by using quasi-monochromatic gamma ray beams from laser Compton scattering (LCS γ-rays) at AIST in Japan. Although the experimental data for ^{139}La(γ,n)^{138}La strongly constrained the stellar rate on the ground-state target, uncertaity of photodisintegration rate from below neutron separation energy still remained [7].

All these reasons motivated new measurements of photon scattering cross section of ^{139}La below neutron separation energy.

2 Photon scattering

Photon scattering cross section $\sigma_{\gamma f}(E_R)$ can be measured via γ ray transition from given excitation level E_R and de-excitation to a level E_f in the target. In case of non-overlapping resonances, photon scattering is described to process via a compound-nucleus reaction with uncorrelated channels f characterized by the partial width Γ_f, so photon-scattering cross section $\sigma_{\gamma f}(E_R)$ can be described as:

$$\sigma_{\gamma f}(E_R) = \sigma_\gamma(E_R)\frac{\Gamma_f}{\Gamma} \tag{1}$$

where all partial widths contribute to the total level width $\Gamma = \sum\Gamma_f$.

$$I_s = \int_0^\infty \sigma_{\gamma f}(E)dE = \frac{2J_R+1}{2J_0+1}(\frac{\pi\hbar c}{E_R})^2\Gamma_0\frac{\Gamma_f}{\Gamma} \tag{2}$$

where I_s is the scattering cross section integral for the level R and Γ_f is the partial width for a transition from R to a level f. Measured intensity of γ-rays emitted to the ground state at $E_\gamma = E_R$ with an angle θ can be expressed as:

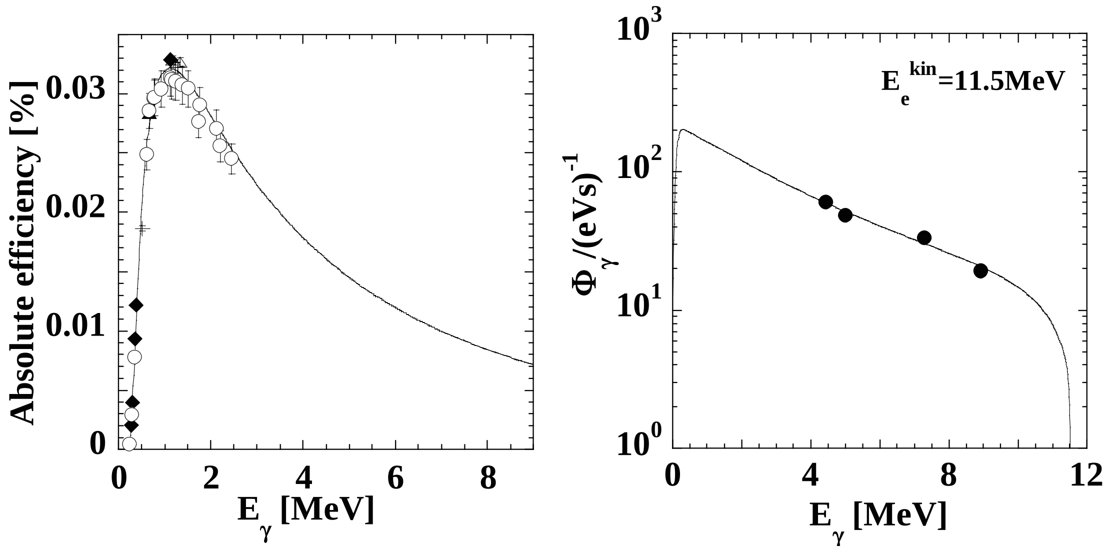

Fig. 2: The absolute efficiency of HPGe detectors at 127 degrees measured by using ^{22}Na, ^{60}Co, ^{65}Zn, ^{133}Ba, ^{137}Cs and ^{226}Ra as calibration sources, and simulated with the Geant3 code (left). Absolute photon flux at the target deduced from intensities of 4 known transitions in ^{11}B using the calculated efficiency (right).

$$I_\gamma(E_\gamma,\theta) = I_s(E_R)\Phi(E_R)\epsilon(E_\gamma)N_{at}W(\theta)\frac{\Delta\Omega}{4\pi} \tag{3}$$

where $\Phi(E_R)$ is the abslute photon flux at energy of E_R and $\epsilon(E_\gamma)$ is the absolute full-energy-peak efficiency of the detector and N_{at} is the number of atoms in the target. $W(\theta)$ is the angular distribution of this transition and $\Delta\Omega$ is the solid angle of the detector.

3 Experiment and Data analysis

Photon-scattering cross section measurement on ^{139}La was performed at the superconducting electron accelerator ELBE of the Research Center Dresden-Rossendorf. Bremsstrahlung was produced by hitting 4 μm niobium radiator with electron beams of 11.5 MeV kinetic energy and average current of 520 μA. Produced bremsstrahlung was collimated by an Al collimator with a length of 2.6 m and an opening angle of 5 mrad. A 10 cm length of cylindrical Al absorber was placed between the radiator and the collimator to reduce the low-energy part of the bremsstrahlung spectrum. The scattered photons were measured with four 100 % HPGe detectors surrounded by escape-suppression shields. Two Ge detectors were placed vertically at 90 degrees relative to the photon-beam direction at a distance of 28 cm from the target to measure azimuthal asymmetries of the γ intensities with polarized photons. The other two Ge detector placed at 127 degrees were used to deduce angular distributions of the γ rays. To deduce the low-energy part of background photon absorbers of 8mm Pb plus 3 mm Cu were placed in front of the detectors at 127 degrees and 13 mm Pb plus 3 mm Cu were used for the detectors at 90 degrees. Spectra of photons for ^{139}La was measured for 6914 minutes. Natural 3790 mg

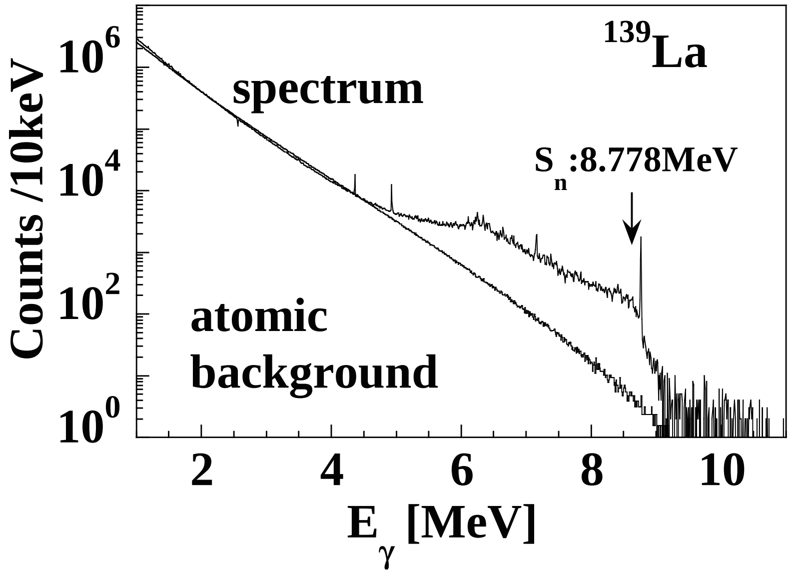

Fig. 3: Experimental spectrum of photon scattered from ^{139}La (corrected for room background and detector response) and simulated spectrum of atomic background.

^{139}La (99.9 %) target was irradiated with bremstrahlung. ^{11}B (99.5 %, 337.9 mg) was also used to determine the photon flux. Further experimental details can be found in the literature [5, 6].

In the data analysis, absolute efficiency of the HPGe detector was determined by using ^{22}Na, ^{60}Co, ^{65}Zn, ^{138}Ba, ^{137}Cs and ^{266}Ra as calibration sources as shown in Fig.2 (left). Absolute photon flux determined by using the four known integrated scattering cross section of transitions in ^{11}B (4444.9 keV, 5020.3 keV, 7285.5 keV, 8920 keV) [10] and Geant3 simulation code is shown in Fig.2 (right). Experimental spectrum of photons scattered from ^{139}La(corrected for room background and detector response) and simulated spectrum of atomic background is shown in Fig.3. In this spectrum, extra enhancement can be seen at around 6 MeV. In photon-scattering experiment, experimental spectra also included the contribution of inelastic and cascade transitions. To obtain the intensities of the ground-state transitions and their branching ratio, Monte Carlo code for the simulation of γ ray cascade has been developped at Forschungszentrum Dresden-Rossendorf [5, 6, 8]. In the simulation, BSFG (back-shifted fermi gas) model is used for level density. The level density parameter a=12.27(34) MeV^{-1} and the back-shift energy E1=-0.22(23) for ^{139}La are taken from a reference [11]. The Wigner distribution is used for the nearest-neighbor spacing. The parameters for E1 γ strength function was taken from RIPL-2 [13]. The Porter-Thomas distribution is used for the fluctuations of the partial decay widths [12].

4 Result

The measured photon scattering cross sections for ^{139}La in this work is shown in Fig.4 comparison with the photoneutron cross section data obtained with the LCS γ rays, the positron annihilation γ rays and betatron bremsstrahlung.The present data can connect smoothly to

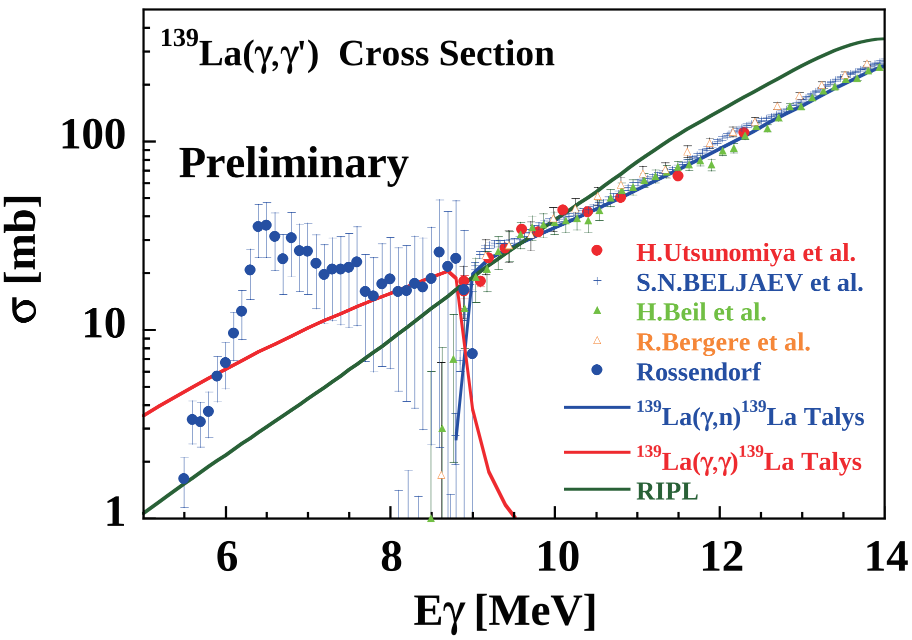

Fig. 4: Present result of photon scattering cross sections for ^{139}La. Present data can connect smoothly to photoneutron cross sections and provide an extension of the cross section data toward low energy below neutron separation energy. Photoneutron cross sections for ^{139}La obtained with photon sources of LCS-γ beam, positron annihilation in flight and bremsstrahlung are also shown for comparison. we also compare the present data with TALYS code.

photoneutron cross sections for ^{139}La and provide an extension of the cross section data toward low energy below neutron separation energy. The extra strength(PDR) is found around 6.5 MeV. In Fig.4, we compare the present experimentaldata with TALYS code. In the calculation, Ferimi-gas model for level density and Lorentz type E1 strength function are used. While photoneutron cross sections for ^{139}La calculated with TALYS is consistent with the experimental data, experimental photon scattering cross sections for ^{139}La, especially extra strength from 6 - 8 MeV region, can't be explained with currently used model.

5 Sumary

Photon-scattering cross sections for ^{139}La up to the neutron-separation energy were measured at bremsstrahlung facility ELBE of the Forschungszentrum Dresden-Rossendorf at an electron kinetic energy of 11.5 MeV. The experimental data was analyzed with statistical methods to obtain the intensities of the ground state transitions and their branching ratios. Present result shows the extra strength at γ ray energy of about 6 MeV to 8 MeV. This extra strength will strongly affect the photodisintegration rate for ^{139}La and a large thermonuclear contribution to the ^{138}La p-process solar abundance.

Acknoweledgement

We thank the staff of the ELBE accelerator for their cooperation during the experiments. We also thank to H.Utsunomiya for his teaching in the early stage of this research for photoneutron experiment. This work was supported by Forschungszentrum Dresden-Rossendorf and Japan Private School Promotion Foundation.

Reference

[1] M. Arnould, S. Goriely, Phys. Rep. **384**, 1 (2003).

[2] S. Goriely, M. Arnould, I. Borzov, and M. Rayet, Astron. Astrophys. **375**, L35 (2001).

[3] J. Audouze, Astron. Astrophys. **8**, 436 (1970).

[4] S. E. Woosley, D. H. Hartmann, R. D. Hoffman, and W. C. Haxton, Astrophys. J. **356**, 272 (1990).

[5] G. Rusev, R. Schwengner, F. Dönau, M. Erhard, E. Grosse, A. R. Junghans, K. Kosev, K. D. Schilling, A. Wagner, F. Bečvář, and M. Krtička, Phys. Rev. **C 77**, 064321 (2008).

[6] R. Schwengner, G. Rusev, B. Benouaret, R. Beyer, M. Erhard, E. Grosse, A. R. Junghans, J. Klug K. Kosev, L. Kostov, C. Nair, N. Nankov, K. D. Schilling, and A. Wagner, Phys. Rev. **C 76**, 034321 (2007).

[7] H. Utsunomiya, A. Makinaga, S. Goko, T. Kaihori, H. Akimune, T, Yamagata, M. Ohta, H. Toyokawa, S. Müller, Y.-W. Lui, and S. Goriely, Phys. Rev. **C 74**, 025806 (2006).

[8] G. Rusev, PhD dissertation,Technische Universität Dresden, 2007 (Wissenschaftlich-Technische Berichte, FZD-478, 2007); https://www.fzd.de/publications/010008/10008.pdf.

[9] R. Schwengner, R. Beyer, F. Dönau, E. Grosse, A. Hartmann, A. R. Junghans, S. Mallion, G. Rusev, K. D. Schilling, W. Schulze and A. Wagner, Nucl. Inst. Method. **A 555**, 211 (2005).

[10] F. Ajzenberg Selove, Nucl. Phys. **A 506**, 1 (1990).

[11] T. von Egidy and D. Bucurescu, Phys. Rev. **C 72**, 044311 (2005).

[12] C. E. Porter and R. G. Thomas, Phys. Rev. **104**, 483 (1956).

[13] http://www-nds.iaea/RIPL 2/.

22. Neutron Capture Cross Section Measurement on ^{243}Am with a 4π Ge spectrometer

J. Hori[1], M. Oshima[2], H. Harada[2], K. Furutaka[2], M. Koizumi[2], F. Kitatani[2], Y. Toh[2], S. Nakamura[2], A. Kimura[2], M. Igashira[3], M. Mizumoto[3], T. Ohsaki[3]†, T. Katabuchi[3], J. Goto[4]

[1] *Research Reactor Institute, Kyoto University, Kumatori-cho, Sennan-gun, Osaka 590-0494, Japan*
[2] *Nuclear Science and Engineering Directorate, Japan Atomic Energy Agency, Tokai-mura, Naka-gun, Ibaraki 319-1195, Japan*
[3] *Research Laboratory for Nuclear Reactor, Tokyo Institute of Technology, O-okayama, Meguro-ku, Tokyo 152-8550, Japan*
[4] *Radioisotope Center, Niigata University, Asahimachi-dori, Niigata, Niigata 951-8510, Japan*

e-mail: hori@rri.kyoto-u.ac.jp

The neutron capture cross section of ^{243}Am has been measured relative to the ^{10}B(n,αγ) standard cross section by the neutron time-of-flight (TOF) method in the energy range of 0.01 to 400 eV using a 46-MeV electron linear accelerator (linac) at the Research Reactor Institute, Kyoto University. For the capture γ-ray measurement, a 4π Ge spectrometer surrounded with large $Bi_4Ge_3O_{12}$ (BGO) detectors for anti-Compton suppression was employed. The relative measurement has been normalized at 0.0253 eV to the reference value of 76.6 b in JENDL-3.3. The present results have been compared with the evaluated and experimental values.

1. Introduction

Accurate nuclear data of minor actinide (MA) are required for transmutation study and design of innovative reactor system. Americium-243 is an important MA which is abundantly produced next to ^{237}Np and ^{241}Am in spent-fuels of light water reactors. Moreover, the neutron capture reaction for ^{243}Am which produces higher-mass Cm isotopes plays a significant role in the nuclear waste inventories. However, the present status of experimental data is inadequate since high-radioactivity of ^{243}Am sample makes it difficult to measure the neutron capture cross section. Especially number of the measurements is limited in the resonance or low energy region, although a few cross section data at thermal neutron energy have been reported. Wisshak and Käppeler measured the neutron capture cross section in the range from 5 to 250 keV using a Moxon-Rae

† Present address: Research and Development Division, Intellectual Property Bank Corp., 1-21-19 Toranomon, Minato-ku, Tokyo 105-0001, Japan

detector and the $^7Li(p,n)^7Be$ neutron source [1]. Weston and Todd measured the neutron cross section in the range from 0.26 to 92 keV using a NE-226 liquid scintillator and electron linac as a photo-neutron source [2].

Recently we have installed an innovative detector system with a 4π Ge spectrometer [3] and started a series of measurements for MAs such as ^{237}Np, ^{241}Am and ^{243}Am. The results of ^{237}Np have already been reported [4]. In this paper, the results of ^{243}Am are shown.

2. Experiments

2.1 Experimental set-up

The neutron capture cross section measurement has been carried out by the TOF method with the 46-MeV linac at the KURRI. The experimental arrangement is shown in **Fig. 1**. Bursts of fast neutrons were produced from the water-cooled photo-neutron target assembly, 5 cm in diameter and 6 cm long, which was composed of 12 sheets of tantalum (Ta) plates with total thickness of 29 mm. The target was surrounded with a water moderator. The flight path used in the experiment is in the direction of 90-degree to the linac electron beam. In order to reduce the γ flash generated by the electron burst from the target, a lead shadow bar, 7 cm in diameter and 10 cm long, was placed in front of the entrance of flight tube. The neutron collimation system was mainly composed of Pb and Boron-mixed polyethylene rings, and tapered from about 24 cm in diameter at the entrance of the flight tube to about 3 cm in diameter at a capture sample, which was placed at a distance of 9.97 m from the Ta target. A BF_3 proportional counter was set at the exit of the first flight tube as shown in Fig. 1 and used as a neutron intensity monitor. The linac was operated at a pulse width of 100 ns, a repetition rate of 100 Hz, an averaged current of 30 μA and an electron energy of 30 MeV.

2.2 Samples

The sample of ^{243}Am was 128 mg of americium oxide (AmO_2) powder packed in an aluminum disk container 30 mm in diameter and 0.5 mm thick walls. The thickness of sample was 8.92×10^{-5} atoms/b. A radioactivity (835 MBq) of the sample leads to very high TOF independent background. To decrease the background, a 10 mm thick lead was set on the surface of each detector. The dummy sample of identical Al case without the americium oxide powder was used for the background measurements. The identical Al case with Pb was also used for determination of background level due to neutrons scattered by the capture sample. The enriched ^{10}B sample, whose purity was 93 %, was used for the measurement of the incident neutron flux/spectrum on the sample. The ^{10}B sample was encapsulated in a cylinder thin-walled (0.2 mm) aluminum container 25 mm in diameter, with a sample material thickness 5.68×10^{-2} atoms/b.

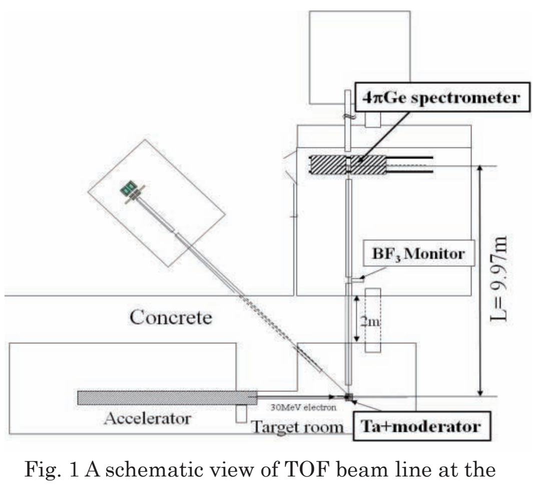

Fig. 1 A schematic view of TOF beam line at the KURRI linac

2.3 4π Ge spectrometer and data acquisition system

Prompt capture γ-rays from the sample were measured with a 4π Ge spectrometer. The characteristics of the spectrometer have been described in detail elsewhere [5], so is summarized in this paper. The spectrometer consists of two cluster and four clover Ge detectors surrounded by BGO anti-Compton shields. The thirty signals from the Ge crystals and more than hundred signals from BGO anti-Compton shields were fed into the developed data acquisition (DAQ) system [6] which consists of three modules: main ADC modules, fast timing modules, and coincidence modules. The discrimination level of γ-ray pulse height (PH) was set at about 400 keV not to detect the decayed γ rays from ^{243}Am sample. In the case of ^{10}B run, the discrimination level was set at about 100 keV to measure the 478 keV γ ray from the ^{10}B(n,αγ) reaction. The events were stored with the list mode.

3. Data processing and analysis

3.1 Capture γ-ray yield

The stored data consist of γ-ray pulse height (PH), TOF and time-interval-of-coincidence (FER). The two dimensional matrices for TOF and summed PH were produced in off-line mode. The spurious signals due to γ flash or radio-frequency noises from the accelerator were eliminated by using the FER information. The γ-ray PH for each Ge was calibrated using the well know γ rays from neutron capture of chlorine in a NaCl sample. Neutron energy calibration was made with the energies of resolved isolated resonances of ^{243}Am from the evaluated data [7]. The γ-ray PH spectra gated with the prominent 3.424-eV resonance and the off-resonance region were shown in **Fig. 2**. The difference between two spectra was observed clearly. It corresponds to the net counts from the neutron capture γ-ray events. The TOF spectrum of ^{243}Am sample was obtained by gating with the PH region between 700 keV and 5.4 MeV.

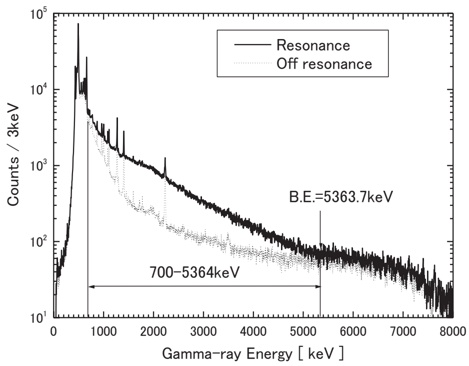

Fig. 2 γ-ray PH spectra gated with resonance and off resonance regions

3.2 Dead time correction

In order to estimate the dead time of whole detection system, external random signals made with a pulse generator and a noise pulsar were fed into a preamplifier of each Ge detector. The pulse height of the signal was set about 10 MeV, which was able to be distinguished from true capture events. The number of the input signals was also counted. The dead time was estimated by comparing the peak count of the stored signals with the number of the counted input ones. The time dependent dead time was obtained as shown in **Fig. 3**. In this experiment, the dead time correction factors were about 54%, 27% and 21% for ^{243}Am, ^{10}B and dummy sample runs, respectively.

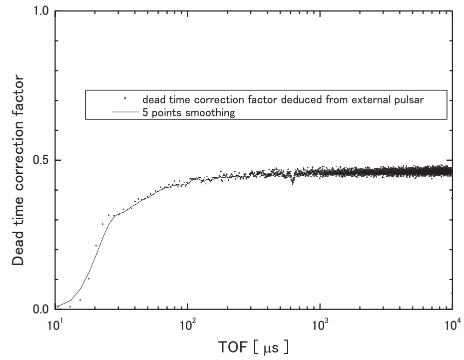

Fig. 3 Dead time correction factor for capture γ-ray yield from the ^{243}Am

3.3 Background determination and neutron flux

For the ^{10}B sample, the time dependent of the background was determined by interpolating between the values observed in the transmission minima measured with black resonances of 336 eV (Mn), 132 eV (Co), 5.19 eV (Ag), 1.457 eV (In) and the constant component around the TOF channel of 10 ms. The TOF spectra of ^{10}B with and without resonance filter are shown in **Fig. 4**. The neutron flux at the sample position was deduced from the net spectrum of ^{10}B, the detection efficiency for the 478-keV γ ray and the cross section of the $^{10}B(n,\alpha\gamma)$ reaction taken from the JENDL-3.3 as shown in **Fig. 5**.

For the ^{243}Am sample, the background determination is more complicated. The constant background level was determined from the counting rate measured with ^{243}Am sample without neutron beam. The time dependent of the background was determined by using net TOF spectrum for Al dummy. The components due to scattered neutron were estimated by normalizing the difference between the TOF spectra of Pb scatterer and Al dummy. The TOF spectra of ^{243}Am, Al dummy and Pb scatterer are shown in **Fig. 6**.

3.4 Corrections

The effects due to overlap neutrons from the previous pulse were deduced from the counts in the TOF time range from 6 ms to 10 ms by extrapolation with the exponential function.

The correction function for the neutron self-shielding and multiple scattering in the sample was calculated by the Monte Carlo code MCNP-4C [8]. **Figure 7** shows the correction function for the ^{243}Am sample, and the random history number is 10^7. It is found that the largest correction factor is about 2.1 at the 3.424-eV resonance.

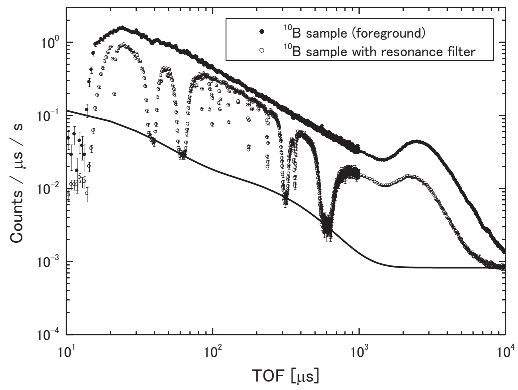

Fig. 4 TOF spectra of ^{10}B with and without resonance filter

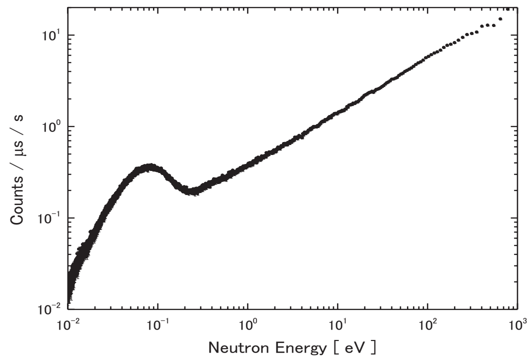

Fig. 5 Neutron flux at the sample position

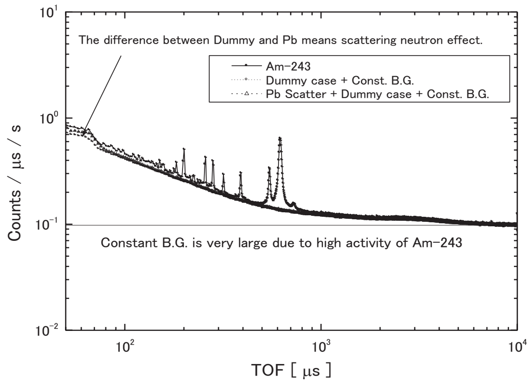

Fig. 6 TOF spectra of ^{243}Am, Al dummy and Pb scatterer

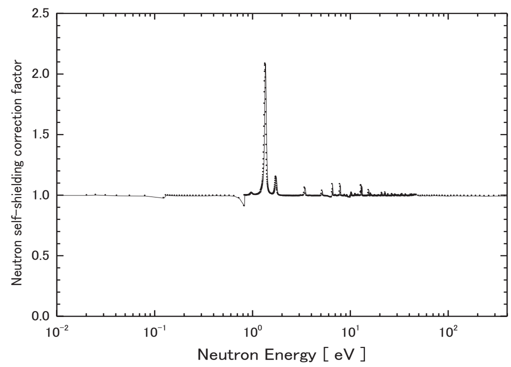

Fig. 7 Correction function for the neutron self-shielding and multiple scattering in the ^{243}Am sample

4. Results and discussion

The relative capture cross sections of ^{243}Am have been obtained from 0.01 to 400 eV as a function of neutron energy. The relative cross sections have been normalized at 0.0253 eV to the reference value of 76.6 b in JENDL-3.3 [9]. The present results are shown in **Fig. 8** with the evaluated data of JENDL-3.3. The present results are in agreement with the evaluated data in JENDL-3.3 except for the region from 0.1 to 0.8 eV where the uncertainties are large because of the correction for the effect due to overlap neutrons.

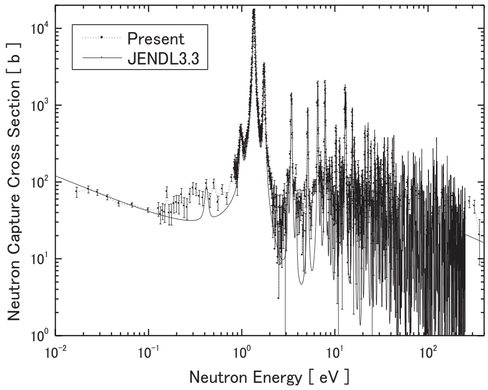

Fig. 8 Comparison of the present measurement and the evaluated data of JENDL-3.3 for the ^{243}Am(n,γ) reaction.

The partial resonance integral from 0.5 to 100 eV was derived from the present cross section weighted by a 1/E neutron spectrum. The rest part above 100 eV is found from calculation with the evaluated data in JENDL-3.3 to be 62 b. The resonance integral (I_0) values are shown in **Table 1** in comparison with other activation data and the evaluated values. The resonance integral to thermal cross section ratios (I_0/σ_0) are also listed in the same table. The I_0/σ_0 for present data is in agreement with those for the data by Garvilov *et al.*, [11] and the recommended value by Mughabghab [18] within experimental error. The evaluated data of JENDL-3.3 is smaller than the present ratio by about 10%. Recently Ohta *et al.*, have measured the effective cross section of ^{243}Am for thermal neutron [19] and their data have supported 2250 b as the resonance integral in combination with the thermal cross section reported by Marie *et al.*, [10]. The ratio derived from the results of two recent experiments [10, 19] is 27.5±1.2, which is in consistency with the present result within experimental error.

Table 1 Comparison of the resonance integral and the ratio (I_0/σ_0) obtained in present TOF experiment with the other activation data and evaluations

References	σ_0 [b]	I_0 [b]	I_0/σ_0
Present result	76.6 (assumed)	1969±111	25.7±1.5
Marie *et al.,* (2006) [10]	81.8±3.6	(2250) [19]	(27.5±1.2)
Garvilov *et al.,* (1977) [11]	83±6	2200±150	26.5±2.6
Simpson *et al.,* (1974) [12]	---	1810±70 a)	---
Schuman and Berreth (1969) [13]	---	2160±120	---
Folger *et al.,* (1968) [14]	78	2250 b)	29
Bak *et al.,* (1967) [15]	73±6	2300±200	32±4
Ice (1966) [16]	84, 66		
Butler *et al.,* (1957) [17]	73.6±1.8	2290±50	31±1
JENDL-3.3 (2002) [9]	76.7	1787	23.3
Mughabghab (1984) [18]	75.1±1.8	1820±70	24.2±1.1

a) Cut-off energy was taken as 0.625 eV.
b) Cut-off energy was taken as 0.83 eV.

5. Summary

The neutron capture cross section of ^{243}Am has been measured relative to the ^{10}B(n,αγ) standard cross section from 0.01 to 400 eV with the 4π Ge spectrometer by the TOF method. The relative measurement has been normalized to the reference value of 76.6 b at 0.0253 eV. The resonance integral was derived from the present cross section data. The ratios of resonance integral to thermal cross section were compared with previous activation data and the evaluated values.

Acknowledgments

This work was supported by the Ministry of Education, Culture, Sports, Science and Technology in Japan under the project "Fundamental R&D on Neutron Cross Sections for Innovative Reactors using Advanced Radiation Measurement Technology".

References

[1] K. Wisshak, F. Käppeler, *Nucl. Sci. Eng.*, **85**, 251 (1983).
[2] L. W. Weston, J. H. Todd, *Nucl. Sci. Eng.*, **91**, 444 (1985).
[3] M. Koizumi, *et al.*, *Nucl. Instrum. Methods*, **A562**, 767 (2006).
[4] M. Mizumoto, *et al.*, *Proc. Int. Conf. on Nucl. Data for Science and Technology (ND2007)*, Nice, France, April 22-27, 2007, pp591-594 (2008).
[5] M. Oshima, *et al.*, *Proc. Int. Conf. on Nucl. Data for Science and Technology (ND2007)*, Nice, France, April 22-27, 2007, pp603-606 (2008).
[6] A. Kimura, *et al.*, AIP Conference Proc., **769**, 792 (2005).
[7] S. I. Sukhoruchkin, Z. N. Soroko, V. V. Deriglazov, *Landolt-Börnstein, New Series I/16B, Tables of Neutron Resonance Parameters*, Springer, Berlin (1998).
[8] J. F. Briesmeister, Ed. "MCNP—A general Monte Carlo N-Particle Transport code, version 4c," LA-13709-M (2000).
[9] K. Shibata, *et al.*, *J. Nucl. Sci. Technol.*, **39**, 1125 (2002).
[10] F. Marie, *et al.*, *Nucl. Instrum.Methods*, **A556**, 547 (2006).
[11] V. D. Gavrilov, *et al.*, *Sov. At. Energy*, **41**, 808 (1977).
[12] O. D. Simpson, *et al.*, *Nucl. Sci. Eng.*, **55**, 273 (1974).
[13] R. P. Shuman, *et al.*, *Idaho Nuck. Corp. Reports*, 1296 (1969).
[14] R. L. Folger, *et al.*, *Proc. Int. Conf. on Neutron Cross Sections and Technology*, Washington D.C., USA, March 4-7, 1968, Vol. 1, p.1279 (1968).
[15] M. A. Bak, *et al.*, *Sov. At. Energy*, **23**, 1059 (1967).
[16] C. H. Ice, *Du Pont, Savannah River Reports*, **66**, 69 (1966).
[17] J. P. Butler, *et al.*, *Can. J. Phys.*, **35**, 147 (1957).
[18] S. F. Mughabghab, *Neutron Cross Sections, Vol. 1, Neutron Resonance Parameters and Thermal Cross Sections, Part B: Z=61-100*, Academic Press, New York (1984).
[19] M. Ohta, *et al.*, *J. Nucl. Sci. Technol.*, **43**, 1441 (2006).

23. Calculation of β–delayed fission and neutron emission probabilities with the use of gross theory and KTUY mass formula

T.Tachibana [1,2], H.Koura [2] and S.Chiba [2]
1 Waseda University Senior High School
Kamishakujii 3-31-1, Nerima-ku, Tokyo 177-0044, Japan
email:ttachi@waseda.jp
2 Advanced Science Research Center, Japan Atomic Energy Agency
JAEA Shirakata-shirane 2-4, Tokai, Naka-gun, Ibaraki 319-1195, Japan

We made an improvement of the calculation of β–delayed fission and neutron emission probabilities for nuclei in the region far from the experimentally known nuclides. In these calculations we need the decay widths Γ_γ and Γ_n. In order to estimate these widths, we improved the nuclear level density model by Kawano *et. al*. to take the effects of collective motion into account. The 2nd version of gross theory of β–decay was adopted in this calculation. Shell energies, paring energies, fission barriers and Q_β-values were obtained by using KTUY mass formula.

1. Introduction

Probabilities of the β–delayed neutron emission are important information for reactor-physics especially the study of decay heat calculation.[1] On the other hand, the effect of fission of heavy nuclei in the r-process nucleosynthesis is a quite interesting topic recently.[2] The β–delayed neutron emission probabilities also play an important role in the calculation of the r-process. These two probabilities are necessary information in the consideration of freeze out at the last stage of the r-process. The β–delayed fission probability and β–delayed neutron emission probability are referred to as P_f-value and P_n-value, respectively, hereafter.

In ref.[3] P_n- and P_f- values were calculated by using the nuclear level density arranged by Kawano *et al*.[4] In this paper we carry out a new calculation of these probabilities with the use of the modified nuclear level density. These calculated P_n- and P_f- values will be good database for the studies of not only reactor-physics but also nuclear astro-physics.

2. Nuclear level density

Kawano *et al*.[4] readjusted the parameter values in the Gilbert-Cameron type nuclear level density formula [5] by using the pairing and shell energies of the KTUY mass formula.[6] In order to remove the shell structure in the level density parameter, the asymptotic level density parameter is introduced in Ref.[4] At higher excitation energy E_x, this phenomenological formula is expressed as,

$$\rho_{\mathrm{G}}(E_x,\ J) = \frac{1}{12\sigma\sqrt{2}} \frac{\exp(2\sqrt{aU})}{a^{1/4}U^{5/4}} \frac{2J+1}{2\sigma^2} \exp\left\{\frac{-(J+1/2)^2}{2\sigma^2}\right\}. \tag{1}$$

At lower excitation energy E_x, it is given by,

$$\rho_{\mathrm{T}}(E_x,\ J) = \frac{1}{T}\exp\left(\frac{E_x - E_0}{T}\right)\frac{2J+1}{2\sigma^2}\exp\left\{\frac{-(J+1/2)}{2\sigma^2}\right\}. \tag{2}$$

Here, $U = E_x - \Delta$ with the pairing energy Δ which can be obtained with the use of KTUY mass formula. The nuclear spin of the level, the energy shift, and the nuclear temperature are denoted by J, E_0 and T, respectively. The level density formula ρ_{G} and ρ_{T} are referred to as the Fermi gas model and the constant temperature model, respectively, hereafter.

The level density parameter a and the spin cut-off parameter σ in Eqs.(1) and (2) are given by

$$a(U) = a^*\left\{1 + \frac{\delta W}{U}(1 - \exp(-\gamma U))\right\}, \tag{3}$$

$$\sigma^2 = cA^{5/3}\sqrt{\frac{U}{a}}. \tag{4}$$

Here a^* is the asymptotic level density parameter. The shell energy δW is obtained with the use of KTUY mass formula. In this paper we adopt the same values for the parameters in Eqs.(3) and (4) those used in Ref.[4], that is to say $\gamma = 0.31A^{-1/3}$ and $c = 0.00347$ where A is the mass number of the nucleus.

In order to consider the collective motion of the nucleus, we adopt the formula used in Ref.[7] ,

$$\rho(E_x,\ J) = K_{\text{rot}} K_{\text{vib}} \times \begin{cases} \rho_{\text{G}} & \text{for higher excitation energy,} \\ \rho_{\text{T}} & \text{for lower excitation energy.} \end{cases} \tag{5}$$

The effect of rotation is considered with the use of parameters of quadrupole and hexadecupole deformation of nucleus, β_2 and β_4. The values of these deformation parameters are also obtained from KTUY mass formula.

$$K_{\text{rot}} = \begin{cases} 1 & \text{for spherical nucleus,} \\ \theta_{\perp} T_0 & \text{for deformed nucleus,} \end{cases}$$

$$K_{\text{vib}} \approx \exp(0.0555 A^{2/3} T_0^{4/3}), \tag{6}$$

$$\theta_{\perp} = 0.4 M R^2 \left(1 + \sqrt{\frac{5}{16\pi}} \beta_2 + \frac{45}{28\pi} \beta_2^2 + \frac{15}{7\sqrt{5}\pi} \beta_2 \beta_4\right) \text{ and } T_0 = \sqrt{U/a} \quad .$$

Here, M and R are the nuclear mass and radius, respectively.

In Ref.[4] the effect of the collective motion of the nucleus was not considered, but in this paper we take it into account by using Eqs.(5) and (6). Although we adopt the same functional form of a^* that used in Ref.[4], we readjust the parameter values in a^* with the use of averaged experimental s-wave resonance spacing in Ref.[8]. The level density formulas in Eq.(5) are connected at a certain excitation energy E_{m} referred to as matching energy.

$$K_{\text{rot}} K_{\text{vib}} \rho_{\text{G}}\big|_{E_x = E_m} = K_{\text{rot}} K_{\text{vib}} \rho_{\text{T}}\big|_{E_x = E_m} \tag{7}$$

$$\frac{d}{dE_x}(K_{\text{rot}} K_{\text{vib}} \rho_{\text{G}})\big|_{E_x = E_m} = \frac{d}{dE_x}(K_{\text{rot}} K_{\text{vib}} \rho_{\text{T}})\big|_{E_x = E_m}. \tag{8}$$

Fig.1 Connection of two models

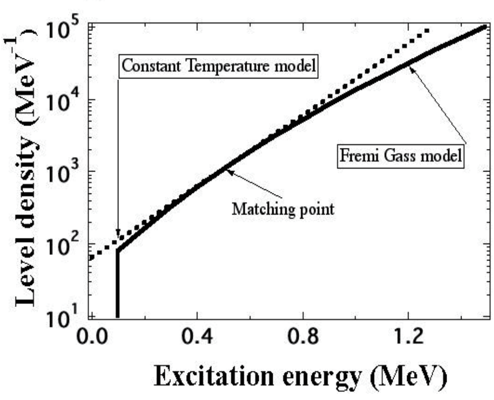

From Eq.(8) we can get a relation between E_{m} and T. The value of E_{m} can be fixed so as to get a positive value for T. After obtaining the values of E_{m} and T, the value of E_0 can be fixed by using Eq.(7). In our calculation, T_0 in Eq.(6) is fixed to $T_0 = \sqrt{(E_m - \Delta)/a}$ for the excitation energy lower than E_{m} for simplicity. A schematic illustration of the smooth connection of these two models is shown in Fig.1. Above (below) the matching energy E_m, the Fermi gas model (the constant temperature model) is used.

3. Partial decay width

According to the statistical model, the partial decay widths Γ_f and Γ_n are generally expressed by using the integral of the level density as,

$$\Gamma_f(E) = \frac{1}{2\pi}\frac{1}{\rho(E)}\int_{-\infty}^{E-S_f}\rho^*(E-S_f-\varepsilon)d\varepsilon \tag{9}$$

$$\Gamma_n(E) = \frac{1}{2\pi}\frac{1}{\rho(E)}\frac{2MR^2}{\hbar^2}g\int_{0}^{E-S_n}\rho^*(E-S_n-\varepsilon)\varepsilon d\varepsilon \quad . \tag{10}$$

Here, ρ and ρ^* are the level densities of the compound nucleus and of the residual nucleus after the fission or neutron emission, respectively. The spin factor is given by g, the fission barrier height by S_f, and the neutron separation energy by S_n. Although the partial γ-decay width $\Gamma\gamma$ may be estimated by using an integral of the level density with the dipole photoabsorption cross section, we employ, for simplicity, the empirical formula estimated by Malecky *et al.*[9] which is a modified model of Weisskopf estimation. We adopt the KTUY mass formula for obtaining Q_β-values, S_n-values and S_f-values.

The examples of the calculation are given in Figs.2 and 3. In the case of ^{260}Pa, β–delayed fission is dominant within the β–decay window. On the contrary, the β–delayed neutron emission is dominant in the case of ^{276}Np.

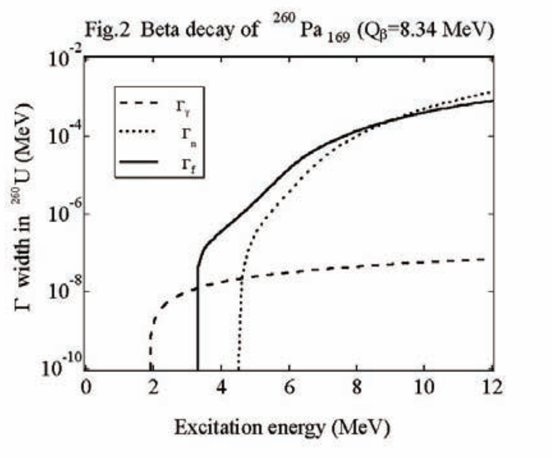

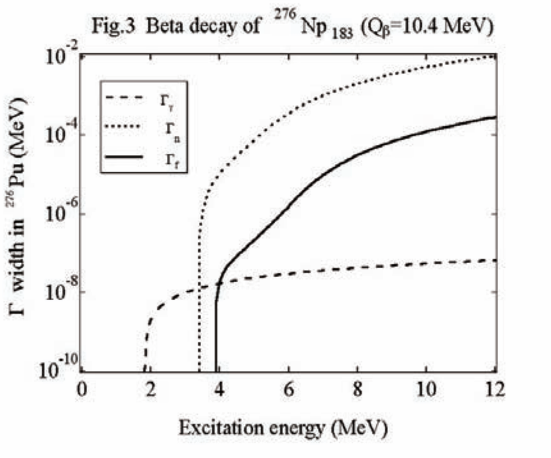

4. β–delayed fission and neutron emission probabilities

The probabilities of β–delayed fission and neutron emission are expressed with the use of the total β–decay strength function $S_\beta(E)$ and competition factor $\Gamma_k/(\Gamma_\gamma+\Gamma_n+\Gamma_f)$ as

$$P_k=\frac{C}{\lambda}\int_{-Q_\beta}^{0} S_\beta(E)\,f(-E)\frac{\Gamma_k}{\Gamma_n+\Gamma_\gamma+\Gamma_f}dE, \qquad k=\left\{\begin{matrix} \mathrm{f} & \text{delayed fission} \\ \mathrm{n} & \text{delayed neutron emission} \\ \gamma & \text{delayed } \gamma-\text{emission} \end{matrix}\right\}. \tag{11}$$

Here, the function $f(-E)$ is the integrated Fermi function and λ is the decay constant of the β–decay. We can estimate the β–strength function and the decay constant by using 2nd version of the gross theory of nuclear β–decay [10]. This theory includes the allowed (Fermi and Gamow-Teller) and first-forbidden transitions. The accuracy of β–decay half-lives calculated by this theory is fairly good in comparison with experimental data [2].

5. Results and conclusion

Examples of the calculated β–delayed fission and neutron emission probabilities are give in Table 1 for ^{260}Pa and ^{276}Np comparing with other models.[11] It is found that fluctuation among the estimated probabilities is large, especially in the case of ^{276}Np. The β–delayed γ emission probabilities of our calculation are larger than the estimations by Meyer *et al.* It may suggest that the integral of the level density with the dipole photoabsorption cross section, like Eqs.(9) and (10), should be used for the calculation of γ emission probability instead of using the empirical formula by Malecky *et al*. We should note that the integrand is dominant in the energy region of $-Q_\beta+S_k\le E\le 0$ (k=f or n) in Eq.(11) because of the competition factor $\Gamma_k/(\Gamma_\gamma+\Gamma_n+\Gamma_f)$. Although β–decay half-life reflects the β–strength function near the ground state of daughter nucleus, the P_f - and P_n -values reflect the strength in the higher excitation energy region of the daughter nucleus. We can use the calculated half-lives, P_f - and P_n -values as an examination of the reliability of the estimated strength function in the whole excitation energy region.

In our previous r-process calculations, the P_f -values in Ref.[12] were roughly estimated as $P_f\approx 50\%$ if fission is possible, and the P_f - and P_n -values in Ref.[3] were calculated by using the level density without the effect of the collective motion. As for the fission fragment mass distribution we used the fission model derived from the two-center shell model and multi-dimensional Langevin calculation. It is found that the effect of the β–delayed fission appears

100< A <160 of the r-process abundances. The universality of the r-process abundances is influenced if β–delayed fission is significant. A test calculation of r-process nucleosynthesis by using newly calculated P_f - and P_n -values including the collective motion are in progress.

Table 1. Delayed fission and neutron emission probabilities of ^{260}Pa and ^{276}Np

	^{260}Pa			^{276}Np		
	P_f	P_n	P_γ	P_f	P_n	P_γ
Thielemann et. al (complete damping)	100 %	-----	-----	25 %	-----	-----
Meyer et. al. (complete damping)	92 %	-----	-----	83 %	-----	-----
Meyer et. al. (WKB barrier penetration)	97 %	0 %	3 %	9 %	84 %	7 %
This work	63 %	2 %	35 %	0 %	66 %	34 %

Acknowledgements

This work was partly supported by Grant-in-Aid for Young Scientists (B) 19740151 of the Ministry of Education, Culture, Sports, Science and Technology (MEXT) of Japan, Grant-in Aid for Scientific Research (C) 18560805 of Japan Society for the Promotion of Science, and Waseda University Grant for Special Research Projects 2008A-121.

References

[1] J. Katakura et al., Evaluation of Delayed Neutron Data for JENDL-3.3, J. Nucl. Sci. Technol., Suppl. 2, 2002, p444.
[2] M.Arnould, S.Goriely and K.Takahashi, Physics Reports **450**, N0s 4-6, September 2007.
[3] S.Chiba *et. al*., Int. Symp. on Origin of Matter and Evolution of Galaxies (OMEG07) AIP1016, pp.162 (2008)
[4] T.Kawano, S.Chiba and H.Koura, J. Nucl. Sci. Tech., **46**, 1 (2006)
[5] A.Gilbert and A.G.Cameron, Can. J. Phys., **43**, 1446 (1965)
[6] H.Koura, T.Tachibana, M.Uno and M.Yamada, Prog. Theor. Phys., **113**, 305 (2005).
[7] A.S.Iljinov *et al*., Nucl. Phys., **A543** (1992) 517
[8] Reference Input Parameter Library, RIPL-2, Section 6, Nuclear Level Densities, Coordinators, A.Ignatyuk and R.Capote, IAEA-TECDOC, (2004)
[9] H.Malecky *et.al*., Yad. Phys., **13**, 240 (1971)
[10] T.Tachibana and M.Yamada, Proc. Int. Conf. on Exotic Nuclei and Atomic Masses, Arles 1995. p.763, and references therein.
[11] H.L.Hall *et al*., Annual Review of Nuclear and Particle Science, **42** 147 (1992)
[12] M.Ohta, et al., Int. Nucl. Phys. Conf. (INPC2007), (Tokyo 2007) Vol.2 pp .558

24. Global Properties of Nuclear Decay Modes

Hiroyuki KOURA[1)], Takahiro TACHIBANA[2,1)] and Satoshi CHIBA[1)]
[1)]Advanced Science Research Center, Japan Atomic Energy Agency
Tokai-mura, Naka-gun, Ibaraki 319-1195
[2)]Waseda University Senior High School
Kamishakujii 3-31-1, Nerima-ku, Tokyo 174-0044
e-mail: koura.hiroyuki@jaea.go.jp

A limit of existing of nuclei is discussed by using a global nuclear mass model, the KTUY mass formula. To estimate total half-lives of nuclei, alpha decay, beta decay, proton emission and spontaneous fission are considered. These calculation gives prediction for existing of approximately ten thousands nuclei including nuclei beyond so-called superheavy nuclei with half-lives of one nanosecond or longer.

1. Introduction

Nucleus is a composite system consisting of protons and neutrons, and approximately 3000 nuclides have been identified [1]. However, the existence of much more nuclides is postulated theoretically. How far the area of nuclei extends is an essential and important question in nuclear physics.

So far, the existence of "island of stability of superheavy nuclei" was considerably discussed from a viewpoint of macroscopic-microscopic models and also some microscopic calculations. Some models give a doubly-magic nucleus $^{298}[114]_{184}$ or $^{310}[126]_{184}$ heavier next to the known doubly-magic nucleus $^{208}Pb_{126}$. On the other hand, nuclei beyond the superheavy nuclei mentioned above are little discussed in previous study. In this paper we investigate theoretical nuclear decay modes and total half-lives in the superheavy and extremely superheavy nuclei and present a limit of existing of nuclear region.

We have developed an original model based on the macroscopic and mean-field models to describe the global features of nuclear masses, called the KTUY (Koura

-Tachibana-Uno-Yamada) nuclear mass model [2]. The standard deviation of this prediction from known masses is 0.67 MeV, and below 0.4 MeV from some separation energies: the former value is competitive to other recent global mass models, and the latter value is smaller than others. The calculated separation energies shows a change of magicities from N=20 (or 14) to 16, N=28 to 32 (or 34), N=50 to 58 etc. in the very neutron-rich region. The prediction of location of the light neutron-drip line from resent experiments is also well. (See in Ref. [2].)

By using the KTUY model, we calculate partial half-lives for alpha decay, beta decay, proton emission and spontaneous fission ranging from light nuclei to superheavy nuclei including unknown ones, and estimated the dominant nuclear decay modes for each of nuclei.

In section 2, we review the KTUY mass model, which gives global properties of nuclear masses in this calculation. We give a short explanation of calculation of nuclear-decay half-lives in section 3. Finally we show our result and discuss a limit of existence of nuclei in section 4.

2. Mass Model

The KTUY mass formula is composed of three parts; a macroscopic spherical part, an averaged even-odd part and a shell part. The first part is expressed as a function of proton and numbers, Z and N, and is a main amount of nuclear masses and represents a bulk property of nuclei as a liquid drop. The second part is introduced in a phenomenological way and mainly comes from an even-odd degenerate of neutron or proton as a Fermi particle. The shell part is calculated on consideration of a spherical basis explained as follows. Firstly we prepare a single-particle potential applicable to global nuclear region and calculate spherical single-particle levels for any nuclei. Then we obtain spherical shell energy from these levels for every nucleus regardless of ground-state shape of a considered nucleus. Regarding deformed nuclei, deformed shell energy is obtained as a mixture of spherical shell energies of neighboring nuclei based on consideration of configuration mixing of spherical single-particle state (In detail, see Ref. [3]). As a spherical single-particle potential, we adopt a modified Woods-Saxon-like potential with five parameters expressed as a function of Z and N developed in Ref. [4]. This potential has two additional parameters compared to the Woods-Saxon potential, which makes a dip near the surface of a nucleus and broaden the potential shape outer. Obtained single-particle levels are well agreement with the experimental data as ^{4}He, ^{16}O... ^{132}Sn and ^{208}Pb.

3. Estimation of Nuclear Decay Modes

Without approximately 250 stable nuclei, all the nuclei decay in various ways. Among these decay modes, we consider four decay modes that are supposed to be dominant: alpha decay, beta decay, proton emission and spontaneous fission. In estimation of partial half lives of the first three decay modes, we adopt experimental decay Q-values if these experimental ones are existed, in other cases we adopt decay Q-values from the KTUY mass calculation.

Alpha-decay half-lives are well reproduced if we use measured Q-values by using a phenomenological formula based on the WKB approximation for the Coulomb potential. Some formulae with parameter sets has bee provided, however, in many cases these parameter sets were adjusted in time when there were no superheavy nuclei recently measured, or adjusted in local nuclear region. We adopt a phenomenological formula and a parameter set presented in Ref. [5], which has a global parameter set and includes even-odd hindrance factor.

Beta-decay half-life is estimated from the second version of the gross theory of beta decay [6]. In this theory the beta-decay strength function to all the final nuclear levels are treated as an averaged function based on sum rules of the beta-decay strength. This theory takes account of not only the Fermi and the Gamow-Teller transitions, but also the first-forbidden transition.

Outside the proton-drip line, proton emissions are expected, but partial half-life of proton emission is quite sensitive to Q-value and also to the angular momentum of proton. We adopt the same single-proton and the Coulomb potential as in the KTUY mass formula. The angular momentum of proton is also estimated from this single-proton potential.

On contrast to these three decays, spontaneous fission is rather complicated. One problem is to estimate potential energy surface on fission, or fission barrier, another is to calculate dynamics of fission process on the potential energy surface. The KTUY mass model gives a potential energy surface against axially- and reflectionally-symmetric deformation of a nucleus. We estimate partial half-lives of spontaneous fission; we only calculate a one-dimensional penetrability of the potential by using the WKB method along a statistical path from the ground-state shape to the fission. An effective mass appeared in this calculation is adjusted to reproduce experimental partial lives of spontaneous fission for even-even nuclei mainly located in actinide region. Odd-A and odd-odd hindrance factors are introduced for non even-even nuclei. The root-mean-square deviation from experimental data is 3.33 in $\log_{10}$. [6].

Among decay modes we concerned, spontaneous fission partial half-lives would have the largest ambiguity due to the uncertainty of the potential energy surface. However, if we only focus on the location of nuclei which decay modes is dominant, the problem would be not so serious.

We calculate each partial half-life, and then obtain main decay modes as a shortest half-life among four decays. Total half-life is obtained as a sum of inverse of partial half-lives

$$\frac{1}{T_{\mathrm{total}}}=\frac{1}{T_{\alpha}}+\frac{1}{T_{\beta}}+\frac{1}{T_{\mathrm{p}}}+\frac{1}{T_{\mathrm{sf}}}. \tag{1}$$

4. Results and Discussion

Figure 1 shows a chart of estimated nuclear decay modes for all the nuclei with total half-lives of one nanosecond or longer. Unlike the light and medium-heavy nuclear region including ^{208}Pb, various decay modes coexist and a kind of a periodic structure of the closed shell with N=126, 184, 228, and also 308 near the proton-drip line in the heavy and superheavy region. Regarding neutron-deficient side in the superheavy region, a border of one-nanosecond half-life are given not by proton emission, but by fission. For the help of your understanding, a fissility line, which corresponds to a macroscopic fissioning border, is drawn in the figure. The fissility line and the neutron-drip line cross near N=320 or larger. This location is not so different from the one-nanosecond border line. Focusing on so-called "island of stability for the superheavy nuclei" including ^{298}[114], an alpha-decay-dominant nuclear region is obtained on our results, and we also find a nucleus with the longest half-life on the beta-stability line in the order of 100 years with a certain ambiguity. Figure 2 shows a chart of estimated total half-lives. The region of nuclei proved out depending on minimum half-lives concerned. Table 1 shows estimated total numbers of nuclei having given minimum half-lives. The total number of nuclei having more than 1 ns is estimated to be approximately ten thousands. In another case, if we focus on half-lives of 1 ms or longer, number of nuclei would be roughly eight thousands.

Table 1. Number of nuclides with a certain half-lives or longer.

Shorter limit of half lives	1 s	1 ms	1 μs	1 ns
Number of nuclei	~4,000	~8,000	~10,000	~11,000

Acknowledgements

This work was partly supported by Grant-in-Aid for Young Scientists (B) 19740151 of the Ministry of Education, Culture, Sports, Science and Technology (MEXT) of JAPAN, Grant-in-Aid for Scientific Research (C) 18560805 of Japan Society for the Promotion of Science, and Waseda University Grant for Special Research Projects 2008A-121.

References

[1] T. Horiguchi, T. Tachibana, H. Koura and J. Katakura: Chart of the Nuclides 2004, Japanese Nuclear Data Committee and Nuclear Data Center, Japan Atomic Energy Research Institute (2005)

[2] H. Koura, T. Tachibana, M. Uno and M. Yamada: Prog. Theor. Phys. 113, 305 (2005)

[3] H. Koura M. Uno, T. Tachibana and M. Yamada: Nucl. Phys, A674, 47 (2000)

[4] H. Koura and M. Yamada: Nucl. Phys, A671, 96 (2000)

[5] H. Koura: J. Nucl. Radiochem. Sci. 3, 201 (2002)

[6] T. Tachibana and M. Yamada: Proc. Int. Conf. on exotic nuclei and atomic masses, Arles, 1995, eds. M. de Saint Simon and O. Sorlin, p.763. (1995, Editions Frontueres, Gif-sur-Yvette), and references therein.

[7] H. Koura: "Ground-state properties of heavy and superheavy nuclei predicted by nuclear mass models," TOURS Symposium on Nuclear Physics V, Tours, 2003, eds. M. Arnould *et al.*, p.60 (2004, AIP Conference Proceedings 794)

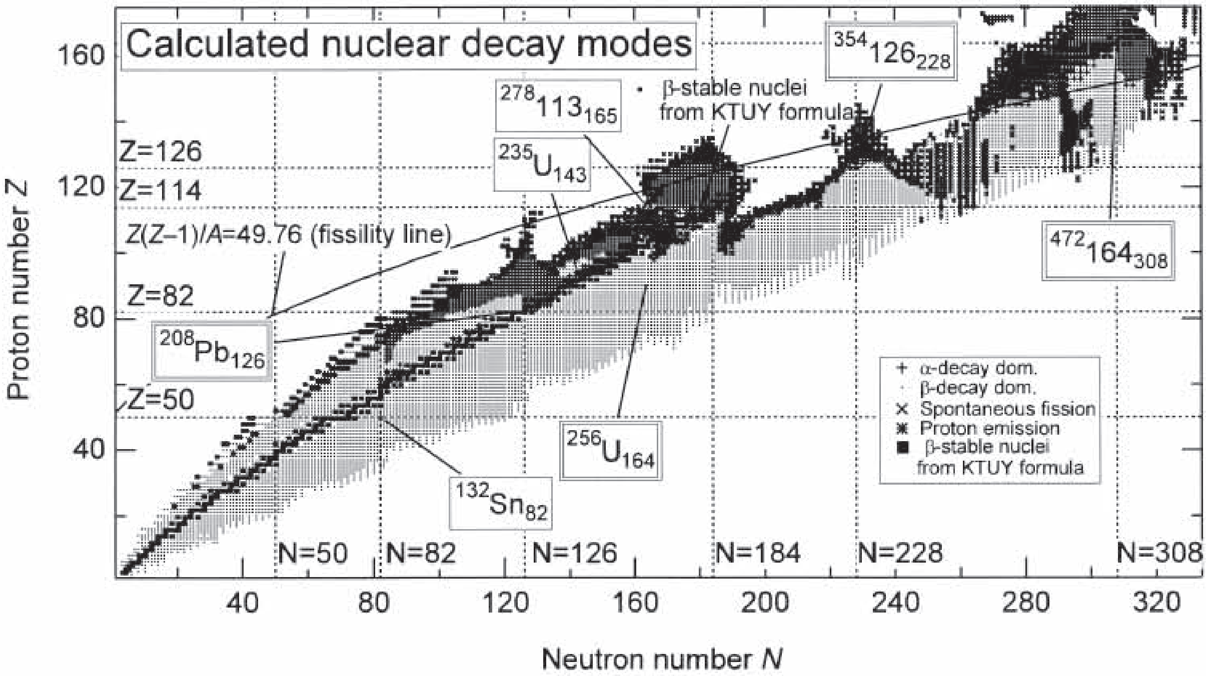

Figure 1:Chart of the nuclides for estimated dominant decay modes. Four decay modes of alpha decay, beta decay, spontaneous fission and proton emission are considered.

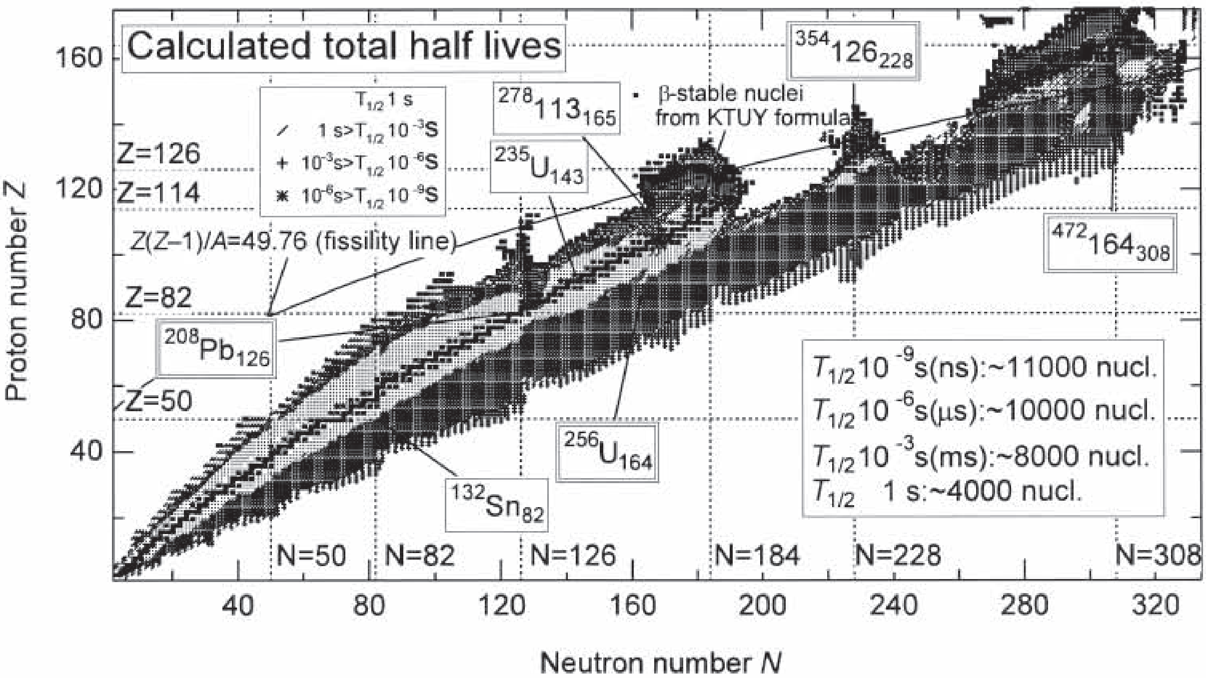

Figure 2:Chart of the nuclides for calculated total half-lives. Four decay modes of alpha decay, beta decay, spontaneous fission and proton emission are considered.

25. Re-analysis of Integral Experiment on Beryllium at JAEA/FNS

Chikara Konno[1], Kentaro Ochiai[1], Yosuke Tatebe[2], Kosuke Takakura[1], Seiki Ohnishi[1],
Keitaro Kondo[1], Masayuki Wada[3] and Satoshi Sato[1]

[1]Fusion Research and Development Directorate, Japan Atomic Energy Agency
Tokai-mura, Naka-gun, Ibaraki-ken 319-1195 Japan
e-mail : konno.chikara@jaea.go.jp

[2]Tokai University
1117 Kitakaname, Hiratsuka-shi, Kanagawa-ken 259-1292 Japan

[3]Japan Computer System
2-8-1 Chuo, Mito-shi, Ibaraki-ken 310-0805 Japan

We tried to specify a reason for the overestimation of experimental data on low energy neutrons in the beryllium benchmark experiment at JAEA/FNS. We found out that it was highly possible that the calculated thermal neutron peak was too large or the thermal neutron peak energy was too low. As one trial, we examined the case of 600 K in order to increase the thermal peak energy, though this trial was unphysical. The thermal neutron peak energy in 600 K was shifted to higher energy than that in 300 K and the calculation results for 600 K agreed with the experimental data better than those in 300 K.

1. Introduction

Beryllium is one of the most important materials as a neutron multiplier and moderator in future fusion reactors. We carried out an integral benchmark experiment on beryllium with DT neutrons at JAEA/FNS more than 15 years ago [1]. We analyzed this experiment with recent nuclear data, where calculated results agreed with experimental data on fast neutrons, while they have overestimated experimental data on low energy neutrons (the reaction rate of ^{197}Au(n,γ) and fission rate of ^{235}U) [2] as shown in Figs. 2 and 3. Here we tried to specify a reason for the overestimation.

2. Method

The Monte Carlo code MCNP4C [3] and nuclear data library FENDL-2.1 [4] were used for this analysis. The ACE files supplied from IAEA Nuclear Data Services were adopted for FENDL-2.1. If necessary, new ACE files were produced with NJOY99.259 [5].

3. Results and discussion

At first we calculated neutron spectra inside the beryllium assembly and energy profiles of the reaction rate of ^{197}Au(n,γ) and fission rate of ^{235}U. The results are shown in Figs. 4 - 6. The calculated neutron spectra have a large thermal peak. It is also found out the contributions of neurons below 1 eV are 40 – 70 % and ~ 95 % for the reaction rate of ^{197}Au(n,γ) and fission rate of ^{235}U, respectively, as shown in Fig. 7. Thus we suspected that the calculated thermal neutron peak was too large or the thermal neutron peak energy was too low.

As one trial, we calculated for the case of higher temperature because the thermal peak energy was considered to become higher in higher temperature, which changed the total cross section of ^{9}Be as shown in Fig. 8. The results are shown in Figs. 9 - 11. As expected, the thermal neutron peak energy in 600 K is shifted to higher energy than that in 300 K. It is found that the calculation results for 600 K agree with the experimental data better than those in 300 K except for the shallow part of the beryllium assembly.

4. Summary

We tried to specify a reason for the overestimation of experimental data on low energy neutrons in the beryllium benchmark experiment at JAEA/FNS. We found out that the overestimation came mainly from thermal neutrons. As one trial, we examined the case of 600 K in order to decrease calculated thermal neutrons by increasing the thermal peak energy. The calculation results for 600 K agreed with the experimental data better than those in 300 K. The temperature of 600 K is not true, but some similar drastic modification for nuclear data of ^{9}Be will be required to solve the problem for the overestimation.

References

[1] F. Maekawa, et al. : “Data Collection of Fusion Neutronics Benchmark Experiment Conducted at FNS/JAEA,” JAERI-Data/Code 98-021 (1998).

[2] C. Konno, et al. : “Analyses of fusion integral benchmark experiments at JAEA/FNS with FENDL-2.1 and other recent nuclear data libraries,” Fusion Eng. Des. **83**, 1774-1781 (2008).

[3] J.F. Briesmeister (Ed.) : “MCNP - A General Monte Carlo N-Particle Transport Code, Version 4C,” LA-13709-M (2000).

[4] D. Lopez Al-dama and A. Trokov : “FENDL-2.1 Update of an evaluated nuclear data library for fusion applications,” IAEA Report INDC(NDS)-467 (2004).

[5] R.E. MacFarlane and D.W. Muir : “The NJOY Nuclear Data Processing System, Version 91, ” LA-12740-M (1994).

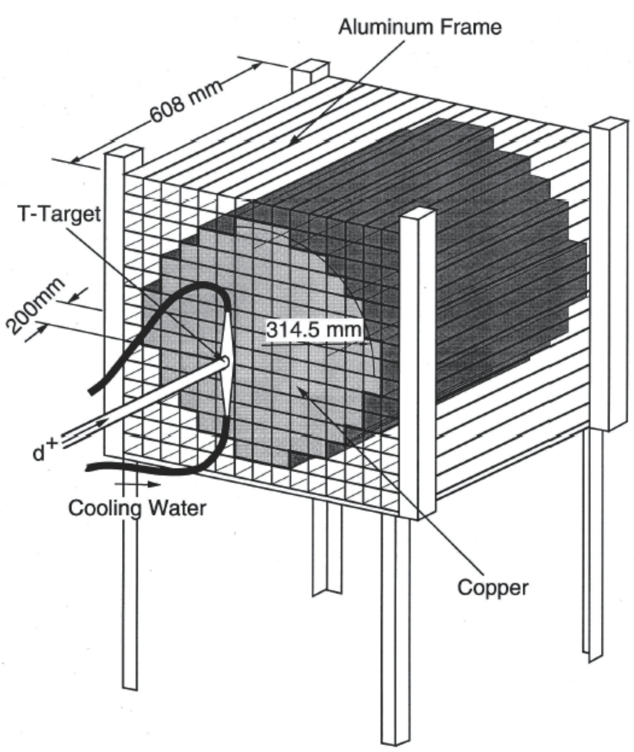

Fig. 1 Experimental configuration.

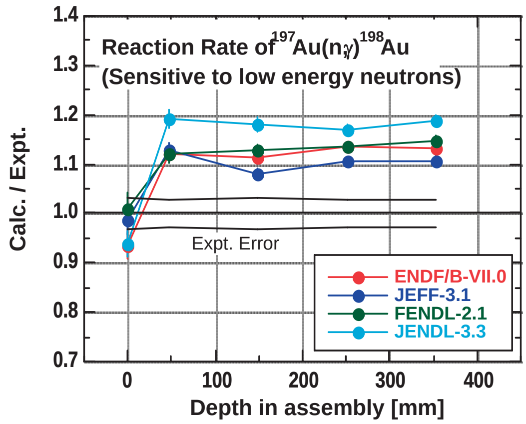

Fig. 2 C/E for reaction rate of ^{197}Au(n,γ)^{198}Au.

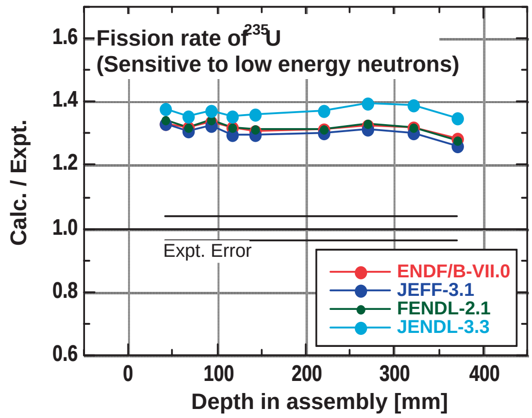

Fig. 3 C/E for fission rate of ^{235}U.

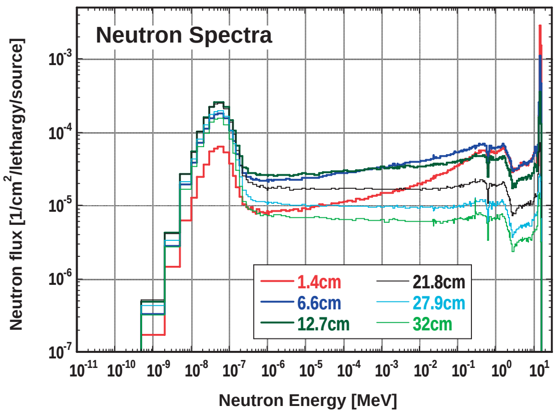

Fig. 4 Calculated neutron spectra.

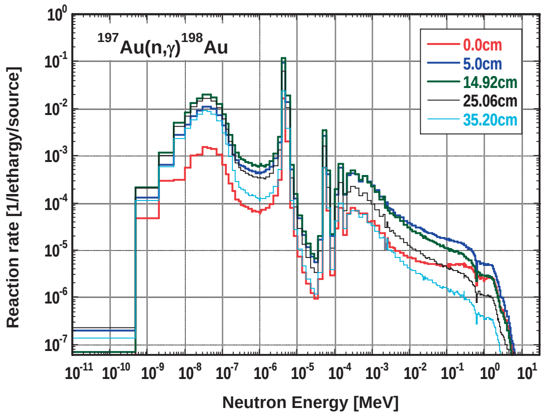

Fig. 5 Energy profiles for reaction rate of ^{197}Au(n,γ)^{198}Au.

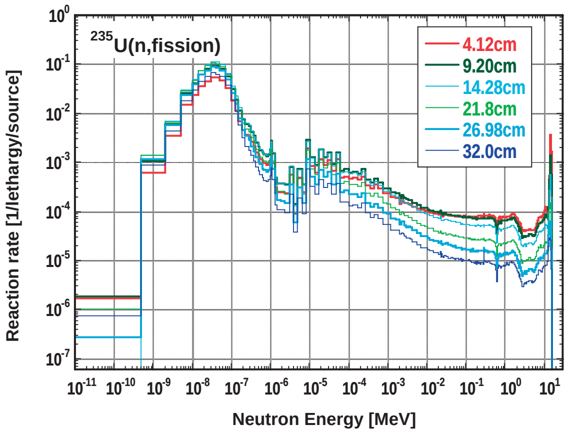

Fig. 6 Energy profiles for fission rate of ^{235}U.

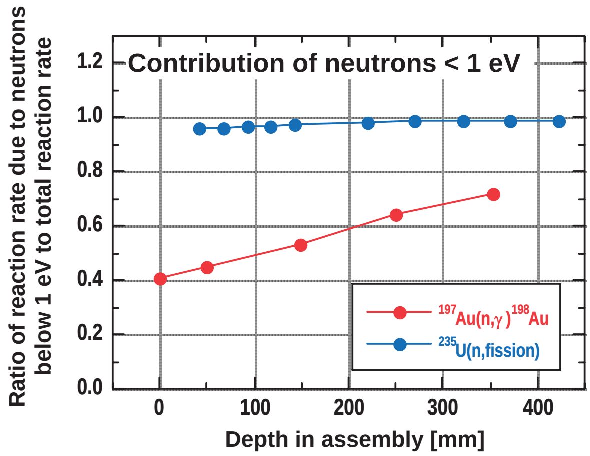

Fig. 7 Ratio of reaction rate due to neutrons below 1 eV to total reaction rate.

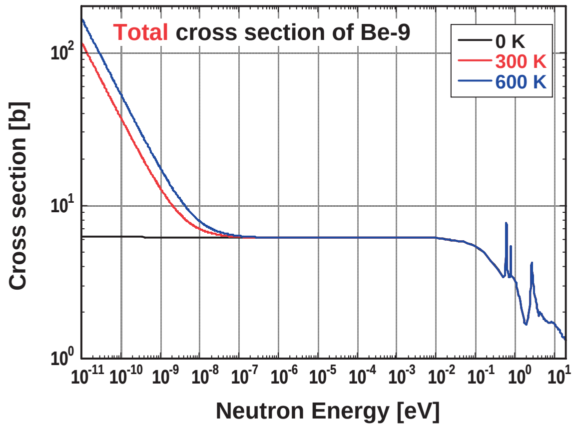

Fig. 8 Total cross section of ^{9}Be.

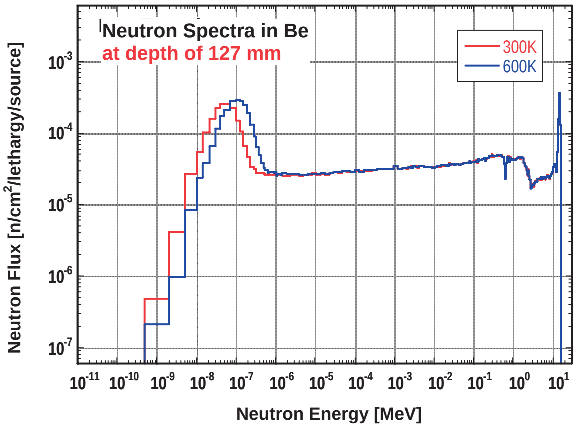

Fig. 9 Calculated neutron spectra at depth of 127 mm.

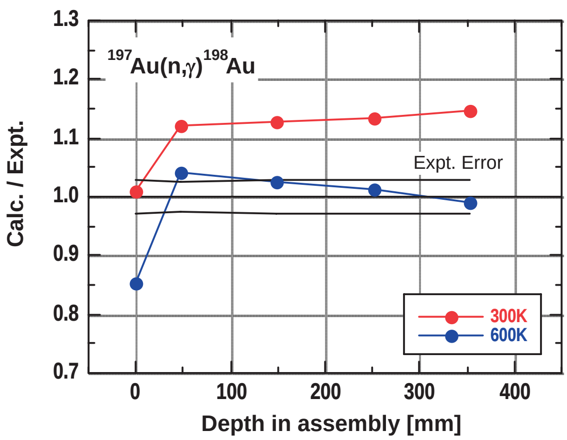

Fig. 10 C/E for reaction rate of ^{197}Au(n,γ)^{198}Au.

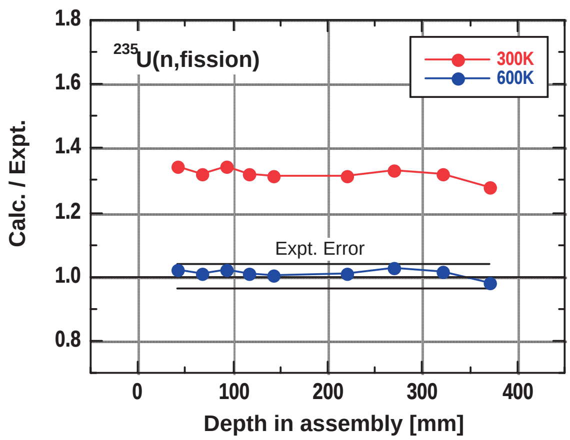

Fig. 11 C/E for fission rate of ^{235}U.

26. Measurement of keV-Neutron Capture Cross Sections and Capture Gamma-Ray Spectra of ^{88}Sr

Tatsuya Katabuchi, Nguyen Canh Hai, Masayuki Igashira, So Kamada, Michihide Tajika, and Motoharu Mizumoto

, ,
- , - , - ,

We have measured the keV-neutron capture cross sections of ^{88}Sr at incident neutron energies of $_{n}$=10 – 86.8 keV. The obtained capture cross sections were compared with previous experiment data and evaluated data of JENDL-3.3, ENDF/B-VI and ENDF/B-VII.

1. Introduction

The keV-neutron capture process by ^{88}Sr is important in nuclear astrophysics [1]–[3]. Thus, reliable data of the keV-neutron capture cross sections are desired. We have measured the neutron capture cross sections of ^{88}Sr at incident neutron energies of $_{n}$=10 – 86.8 keV.

2. Experiments

The detail of the experimental procedure has been described before [4]. Thus, it will be described briefly below.

Experiments were performed using a 3-MV Pelletron accelerator of the Research Laboratory for Nuclear Reactors at the Tokyo Institute of Technology. Pulsed neutrons were generated by the ^{7}Li(p,n)^{7}Be reaction induced by pulsed proton beam (1.5 ns width, 4 MHz repetition rate) from the accelerator bombarding a lithium target. The incident neutrons were detected with a ^{6}Li-glass scintillation detector and the neutron spectrum was determined by the time-of-flight (TOF) method. A ^{6}Li-glass detector with 5.0 mm diameter and 5.0 mm thickness was placed at a distance of 30 cm from the neutron source.

The sample of ^{88}Sr was isotopically enriched (99.9% ^{88}Sr) $SrCO_3$ powder cased in a graphite container. A disk of gold was used as a standard sample for neutron capture cross section. The characteristics of the samples are shown in Table 1. The samples were placed at a distance of 12 cm from the neutron source.

Capture -rays emitted from the sample were detected with a large anti-Compton NaI(Tl) spectrometer. The spectrometer consists of a main NaI(Tl) detector (15.2 cm diameter and 30.5 cm length) and an annular NaI(Tl) detector (33.0 cm outer diameter and 35.6 cm length) surrounding the main detector. The spectrometer was shielded with borated polyethylene, borated paraffin, potassium-free lead and cadmium. Lithium-6 hydride was also used to cut down scattered neutrons from the sample to the spectrometer. The detection angle of -rays respect to the proton beam direction was 125°.

Signals from the spectrometer were recorded in a computer as two-dimensional data of pulse height (PH) and TOF. Measurements of ^{88}Sr and ^{197}Au and without sample were repeated cyclically, thereby change of experimental conditions such as the incident neutron spectrum and the proton beam intensity averaging out. The proton beam current was around 9 A. Total measurement times of ^{88}Sr, ^{197}Au and blank runs were 109, 8 and 12 hours, respectively.

3. Data processing

The incident neutron energy spectrum was determined from TOF spectra measured with the ^{6}Li-glass scintillation detector for the blank runs. The normalized spectrum is shown in Fig. 1. The average incident neutron energy was 47.7 keV.

PH spectra of the γ-ray spectrometer were derived by setting TOF gates on the PH-TOF two-dimensional data. The TOF gates are shown in Table 2. TOF spectra measured with the γ-ray spectrometer for ^{88}Sr, ^{197}Au and blank runs are shown in Fig. 2. The six TOF gates and a background gate are shown in each figure. The broad peak below 500 ch for ^{88}Sr or ^{197}Au is induced by neutron capture events on the sample. The sharp peak around 600 ch comes from γ-rays of the $^{7}\mathrm{Li}(p,\gamma)^{8}\mathrm{Be}$ reaction in the Li target of the neutron source. As an example, foreground and background spectra of ^{88}Sr for gate 6 are shown in Fig. 3. Net PH spectra for each gate were obtained by subtracting the background PH spectrum normalized to the foreground gate channel width from the foreground PH spectrum.

Neutron capture cross sections of ^{88}Sr were obtained by applying a PH weighting technique on the net PH spectra and by determining the number of the incident neutrons from well-known ^{197}Au neutron capture cross sections [6][7]. The optimal weighting function for the PH weighting technique for ^{88}Sr or ^{197}Au was determined from response functions of the γ-ray spectrometer calculated from Monte-Carlo simulations. Then, the neutron capture yield of ^{88}Sr or ^{197}Au was obtained as the following weighted sum:

$$Y = \sum_{I} \frac{W(I)S(I)}{B_n + < E_n >}, \tag{1}$$

where Y is the capture yield, $S(I)$ is counts of the net PH spectrum at channel I, $W(I)$ is the weighting function, B_n is the neutron binding energy of ^{89}Sr or ^{198}Au and $< E_n >$ is the average neutron energy. The number of the incident neutrons on ^{197}Au was determined by the obtained capture yield of ^{197}Au and averaged capture cross section over each gate calculated from the ENDF/B-VII cross section data for ^{197}Au and normalized incident neutron energy spectrum measured in the blank runs. Then, the neutron monitor counts of the ^{6}Li-glass scintillation detector of ^{88}Sr was converted to the number of the incident neutrons from the ratio of the number of the neutrons obtained above to the ^{6}Li-glass detector counts for the ^{197}Au runs. Finally, the neutron capture cross sections of ^{88}Sr were obtained from the relation, $Y = N\phi < \sigma >$, where Y is the capture yield, N is the number of sample nuclei, ϕ is the number of the incident neutrons and $< \sigma >$ is the average neutron capture cross section for a gate. Additionally, correction for the neutron self-shielding and multiple scattering in each sample was made by Monte-Carlo simulations and impurity correction was done from capture yield calculation using JENDL-3.3 cross section data for impurity nuclei [8]. The obtained capture cross sections are summarized in Table 3 and plotted in Fig. 4.

Capture γ-ray spectra of ^{88}Sr were derived from the net PH spectra using the unfolding code, FERDOR [9]. The response matrix in unfolding was calculated from Monte-Carlo simulations. The derived capture γ-ray spectra are shown in Fig. 5.

4. Results and Discussion

In Fig. 4, the capture cross sections of ^{88}Sr measured in the present experiment are compared with experimental data of Ref. [10] and average cross sections calculated from evaluated data of JENDL-3.3, ENDF/B-VI and ENDF/B-VII [11]–[13]. Trend of energy dependence except for ENDF/B-VI is similar to the present data. The experimental data of Boldeman et al. is, however, more scattered than the present data. In JENDL-3.3 and ENDF/B-VII, the capture cross sections are calculated from resonance parameters below 300 keV and theoretical calculations above 300 keV. Discrepancy of those evaluated data with the present data increases with the incident neutron energy. At a high energy part, the evaluated data of JENDL-3.3 and ENDF/B-VII are approximately 30% or 50% lower, respectively. The large discrepancy of ENDF/B-VI comes from lack of resonance parameters.

5. Conclusion

We have measured neutron capture cross sections of ^{88}Sr at $\ _n = 10 - 86.6$ keV with an accuracy less than 9% except for small cross section region (13.6 – 19.2 keV). The obtained capture cross sections were compared with previous experiment data and evaluated data of JENDL-3.3, ENDF/B-VI and ENDF/B-VII.

References

[1] F. Käppeler, W. R. Zhao, H. Beer et al., Astrophys. J., **355**, 348 (1990).

[2] D. L. Lambert, V. V. Smith, M. Busso et al., Astrophys. J., **450**, 302 (1995).

[3] P. E. Koehler, R. R. Winters, K. H. Guber et al., Phys. Rev., **C 62**, 055803 (2000).

[4] S. Mizuno, M. Igashira, K. Masuda, J. Nucl. Sci. Technol., **36**, 493 (1999).

[5] M. Igashira, H. Kitazawa, N. Yamamuro, Nucl. Instrum. Methods, **A245**, 432 (1986).

[6] R. L. Macklin, J. H. Gibbons, Phys. Rev., **159**, 1007 (1967).

[7] ENDF/B-VII.0 data file for ^{197}Au (MAT = 7925), evaluated by P. G. Young (2006).

[8] K. Senoo, Y. Nagai, T. Shima et al., Nucl. Instrum. Methods, **A339**, 556 (1994).

[9] H. Kendrick, and S. M. Sperling, Gulf Radiation Technology, GA-9882 (1970).

[10] J. W. Boldeman, B. J. Allen, A. R. Del. Musgrove et al., Nucl. Phys., **A269**, 397 (1976).

[11] JENDL-3.3 data file for ^{88}Sr (MAT = 3837), evaluated by JNDC FP Nuclear Data W.G. (2002).

[12] ENDF/B-VI.8 data file for ^{88}Sr (MAT = 3837), evaluated by R. E. Schenter, F. Schmittroth (1990).

[13] ENDF/B-VII.0 data file for ^{88}Sr (MAT = 3837), evaluated by Y. Zhuang, C. Cai, S. F. Mughabghab (2006).

Sample	^{88}Sr	^{197}Au
Chemical form	$SrCO_3$	Au
Physical form	powder	disk
Chemical purity [%]	99.90	99.99
Weight [g]	8.392	46.17
Isotopic composition [%]		
^{84}Sr	0.01	–
^{86}Sr	0.02	–
^{87}Sr	0.08	–
^{88}Sr	99.9	–
^{197}Au	–	100
Net weight of sample [g]	4.982	46.17
Diameter [mm]	55	55
Thickness [mm]	4.2	1
$\times 10^{-3}$ [atoms/b]	1.437	5.939

Table 1: Characteristics of samples.

	Energy Range [keV]
Gate 1	10.0 – 13.6
Gate 2	13.6 – 19.2
Gate 3	19.2 – 26.0
Gate 4	26.0 – 33.9
Gate 5	33.9 – 44.5
Gate 6	44.5 – 86.8

Table 2: Setting of TOF gates.

Average neutron energy (energy range) [keV]	Capture cross section [mb]
11.6 (10.0 – 13.6)	52.7 ± 3.6 (6.9%)
16.7 (13.6 – 19.2)	2.55 ± 0.65 (25%)
23.6 (19.2 – 26.0)	10.6 ± 0.88 (8.3%)
29.7 (26.0 – 33.9)	9.4 ± 0.63 (6.7%)
38.9 (33.9 – 44.5)	4.37 ± 0.38 (8.9%)
62.7 (44.5 – 86.8)	4.83 ± 0.27 (5.6%)

Table 3: Derived neutron capture cross sections of ^{88}Sr.

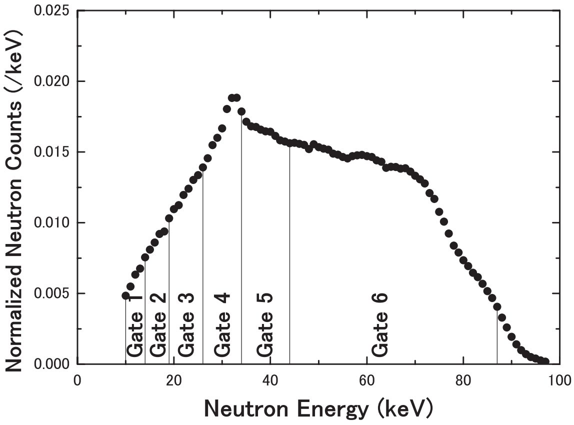

Figure 1: Incident neutron spectrum measured with the ^{6}Li-glass scintillation detector.

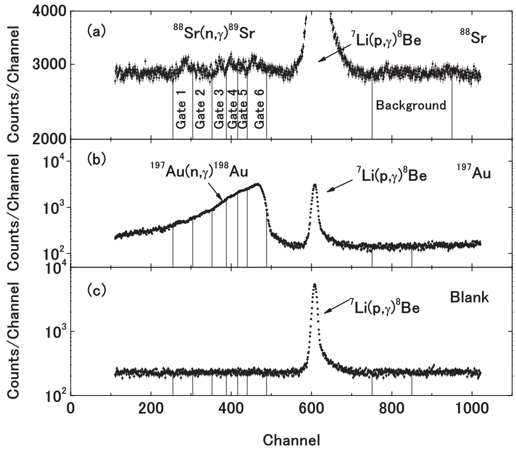

Figure 2: TOF spectra measured with the -ray spectrometer for (a) ^{88}Sr, (b) ^{197}Au and (c) blank runs.

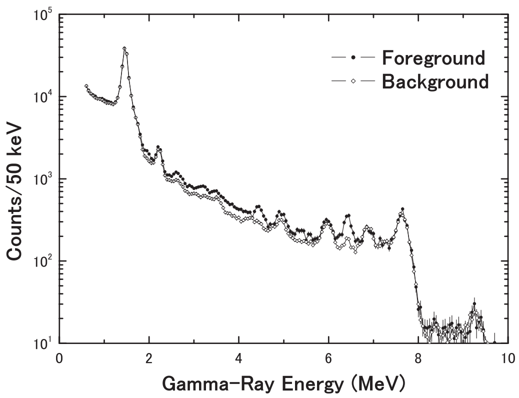

Figure 3: PH spectra measured with the -ray spectrometer for the foreground and background gates.

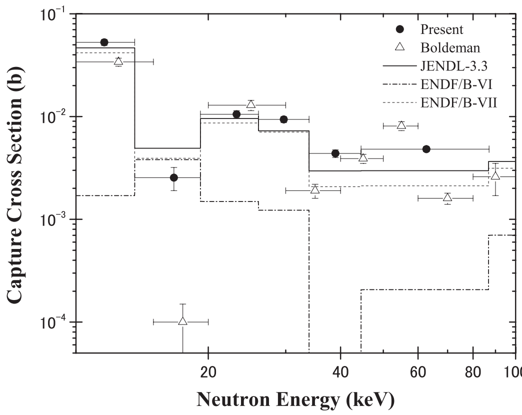

Figure 4: Derived neutron capture cross section of ^{88}Sr with experimental data of Boldeman el al. [10] and evaluated data of JENDL-3.3, ENDF/B-VI and ENDF/B-VII.

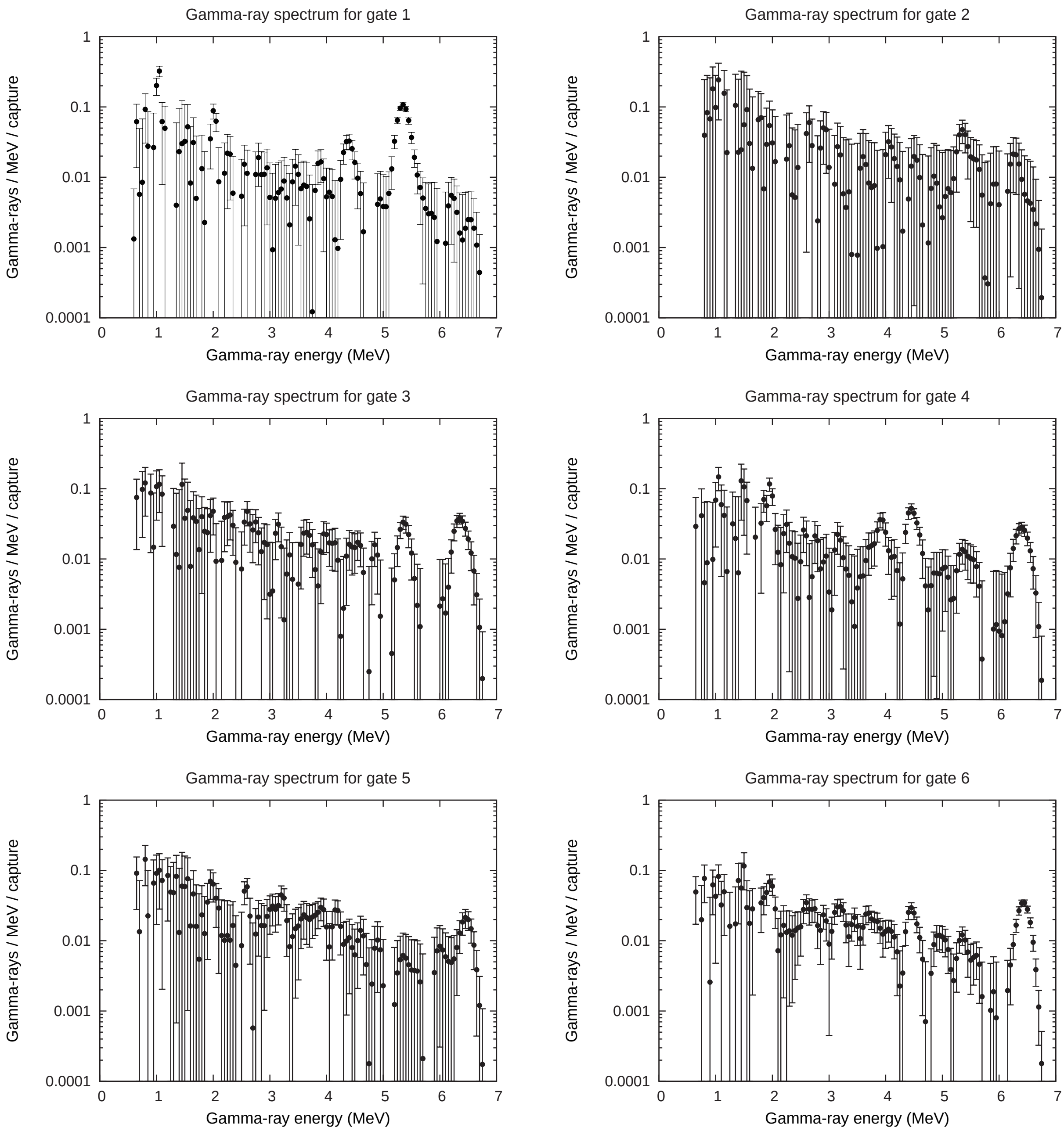

Figure 5: Derived capture -ray spectra of ^{88}Sr for all TOF gates.

27. Benchmarking of Effective Delayed Neutron Fraction With Deterministic Method

Dwi IRWANTO [a], Toru OBARA[a], Go CHIBA [b]

[a] Research Laboratory for Nuclear Reactors, Tokyo Institute of Technology

2-12-1-N1-19 Ookayama, Meguro-ku, Tokyo 152-8550, Japan

[b] Nuclear Science and Engineering Directorate, Japan Atomic Energy Agency,

e-mail : [a] irwanto.d.aa@m.titech.ac.jp, [a] tobara@nr.titech.ac.jp, [b] chiba.go@jaea.go.jp

The objective of this study is to verify nuclear data on delayed neutron through integral test with multigroup data libraries and delayed neutron data based on JENDL-3.3 and ENDF/B-VII.0. We performed calculation by mixing multigroup data libraries and delayed neutron libraries from JENDL-3.3 and ENDF/B-VII.0 in order to know effects of the differences between JENDL-3.3 and ENDF/B-VII.0 based delayed neutron data.

1. Introduction

Although only a very small fraction of the fission neutrons are delayed (less than 1%), delayed neutrons are very vital for the effective control of the fission chain reaction. In fact, it is rather difficult to measure effective delayed neutron fraction with experiments, so it is important to get precise calculation values of effective delayed neutron fraction which has been one of the concerns in nuclear field. In effective delayed neutron fraction calculations, there are two important aspects contribute to the calculation results which are nuclear data used for calculation and calculation methods.

2. Calculation Methods

Calculations are performed by mixing multigroup data libraries and delayed neutron libraries from JENDL-3.3 and ENDF/B-VII.0 in order to know effects of the differences between JENDL-3.3 and ENDF/B-VII.0 based delayed neutron data.

Table 1. Four cases calculation scheme

CASE	DELAYED NEUTRON DATA LIBRARY	MULTIGROUP DATA LIBRARY
1	ENDF/B-VII.0	ENDF/B-VII.0
2	JENDL-3.3	JENDL-3.3
3	ENDF/B-VII.0	JENDL-3.3
4	JENDL-3.3	ENDF/B-VII.0

Effective delayed neutron fraction calculations are performed by using a code system **SLAROM-UF/CBG** (Chiba.G) [1] for deterministic method for several different nuclear systems:

- ✓ GODIVA: bare core with uranium-235 fuel.
- ✓ JEZEBEL: bare core with plutonium-239 fuel.
- ✓ SKIDOO (JEZEBEL-233): bare core with uranium-233 fuel.
- ✓ JEZEBEL-240: bare core with plutonium-239 fuel and 20% plutonium-240.
- ✓ TOPSY: reflective core with uranium-235 fuel.
- ✓ POPSY: reflective core with plutonium-239 fuel.
- ✓ FLATTOP23: reflective core with uranium-233 fuel.

This deterministic procedure is then verified through a comparison with Monte Carlo solution under a consistent definition of β_{eff}. In this study we used the **MVP** code: General purpose Monte Carlo codes for neutron and photon transport calculations based on continuous energy and multigroup methods (Nagaya.Y, et al) [2].

3. Calculation Results

Calculations are performed by using the SLAROM-UF/CBG code system with delayed neutron library and multigroup data library based on JENDL-3.3 and ENDF/B-VII.0 for four cases calculation schemes described in Table 1. Table 2 shows calculation values of effective delayed neutron fraction for each case.

Table 2. Effective delayed neutron fraction values for neutron library and multigroup data library based on JENDL-3.3 and ENDF/B-VII.0

REACTOR	JENDL-3.3 (Multigroup)		ENDF/B-VII.0 (Multigroup)	
	JENDL-3.3	ENDF/B-VII.0	JENDL-3.3	ENDF/B-VII.0
GODIVA	0.00633	0.00640	0.00642	0.00650
JEZEBEL	0.00183	0.00184	0.00183	0.00185
SKIDOO	0.00291	0.00293	0.00293	0.00294
JEZEBEL-240	0.00189	0.00190	0.00191	0.00192
POPSY	0.00282	0.00278	0.00282	0.00278
TOPSY	0.00679	0.00682	0.00687	0.00690
FLATTOP-23	0.00379	0.00374	0.00380	0.00374

In order to compare nuclear data libraries used, it is important to then considering effect of difference between delayed neutron data obtained from calculations as shown in Table 3.

Table 3. Differences between effective delayed neutron values obtained based on JENDL-3.3 and ENDF/B-VII.0

REACTOR	JENDL-3.3-based	ENDF/B-VII.0-based
GODIVA	1.21%	1.22%
JEZEBEL	0.84%	0.85%
SKIDOO	0.57%	0.33%
JEZEBEL-240	0.42%	0.46%
POPSY	1.40%	1.37%
TOPSY	0.38%	0.40%
FLATTOP-23	1.31%	1.42%

The differences lies within 1.4% for Godiva, Popsy and Flattop-23, and less than 1% for others with multigroup data performed based on JENDL-3.3 and ENDF/B-VII.0. This effect of differences obtained from each delayed neutron data based were small and neglectable

Comparison between calculation values and experiment results shows that β_{eff} values for reflected cores (Popsy, Topsy, Flatop23) which are calculated based on both JENDL-3.3 and ENDF/B-VII.0 libraries take larger C/E values than for bare cores (Godiva, Jezebel, Skidoo) regardless of the fuel composition as shown in table 4.

Table 4. C/E values for β_{eff} values obtained by JENDL-3.3 and ENDF/B-VII.0

REACTOR	JENDL-3.3 (Multigroup)		ENDF/B-VII.0 (Multigroup)	
	JENDL-3.3	ENDF/B-VII.0	JENDL-3.3	ENDF/B-VII.0
GODIVA	0.960	0.972	0.974	0.986
JEZEBEL	0.943	0.951	0.945	0.953
SKIDOO	1.005	1.010	1.010	1.013
POPSY	1.022	1.007	1.022	1.008
TOPSY	1.021	1.025	1.033	1.037
FLATTOP-23	1.052	1.038	1.054	1.039

During this study we found that β_{eff} values calculated by Monte Carlo-based methods include calculation errors.

Standard definition method analytically calculates β_{eff} values, so we can consider that this method does not have error in calculation method, meanwhile Monte Carlo method (in this case is Van der Marck method) needs some approximations to obtain β_{eff} values which lead to have some errors in calculation method as shown in table 5. This calculation error could leads to misunderstanding in discussion in nuclear data accuracy, in this case is benchmark result for ENDF/B-VII.0 [3].

Table 5. Differences between values obtained by Standard Definition and Van der Marck method

REACTOR	Differences of Van der Marck Method (MVP + JENDL-3.3)
GODIVA	4.67%
JEZEBEL	6.63%
SKIDOO	5.22%
JEZEBEL-240	7.66%
POPSY	4.13%
TOPSY	4.92%
FLATTOP-23	4.34%

4. Comparison with JENDL ACTINOID FILE-2008

In JENDL Actinoid File-2008 library [5], delayed neutron data for uranium-233 was revised. Effective delayed neutron fraction calculations are performed for Skidoo and Flattop-23 which fuel contains U-233 by using delayed neutron data library based on JENDL Actinoid File-2008 and multigroup data library based on JENDL 3.3 and ENDF/B VII.0.

Table 6. C/E values for β_{eff} values obtained by JENDL ACTINOID FILE-2008

REACTOR	JENDL-3.3-based	ENDF/B-VII.0-based
SKIDOO	0.933	0.938
FLATTOP-23	0.998	1.000

Comparison between result obtained by JENDL Actinoid File-2008 and experiment data, which is shown in table 6, shows similar pattern that for reflected core (Flattop-23) C/E values takes higher value than for bare core (Skidoo), but compared with JENDL-3.3 and ENDF/B-VII.0, β_{eff} values which obtained by using JENDL Actinoid File-2008, has closer values with experiment data for Flattop-23 but not for Skidoo.

5. Comparison between CBG and MVP

β_{eff} calculation was performed by using SLAROM-UF/CBG (Chiba. G) for deterministic method and MVP for Monte Carlo method.

In the deterministic procedure, effective 70-group cross sections are generated with the SLAROM-UF code and UFLIB.J32. With the cross sections, one dimensional neutron transport calculations were performed with discrete ordinates solver CBG/SNR. Scattering anisotropy is considered up to P3 and S24 Double Gaussian level symmetric angular quadrature set it used.

In order to compare calculation results obtained by the CBG code and the MVP code, β_{eff} calculated by using Van der Marck method [4]. Klein Meulekamp and Van der Marck proposed to use number of fission reactions to calculate β_{eff} values. In this method, the expected number of fission reactions in the next generation is utilized instead of ϕ^{+} as conventional adjoint function for the weight function in the calculations of β_{eff}. And it can simply written as

$$\beta_{eff} = \frac{\langle \phi_0{}^{+}, \beta F\phi \rangle}{\langle \phi_0{}^{+}, F\phi \rangle} \quad \text{where importance function defined as} \quad A^{+}\phi_0^{+} = \Sigma_f \qquad (1)$$

with F is an operator of fission yield, $F\phi = \int_0^\infty \chi\, v\, \Sigma_f(\mathbf{r}, E, t)\, \phi(\boldsymbol{r}, E, t)\, dE$.

Table 7 shows comparison between effective delayed neutron fractions calculated with Van der Marck method by using CBG and MVP code.

Table 7. Comparison between calculation results obtained by CBG and MVP

REACTOR	CBG	MVP	DIFFERENCES
GODIVA	0.00660	0.00662	0.261%
JEZEBEL	0.00194	0.00195	0.327%
SKIDOO	0.00307	0.00307	0.265%
JEZEBEL-240	0.00201	0.00204	1.120%
POPSY	0.00274	0.00270	1.525%
TOPSY	0.00645	0.00646	0.151%
FLATTOP-23	0.00363	0.00362	0.203%

Effective delayed neutron fraction values obtained from the CBG code and the MVP code by using Van der Marck method consistently agree each other for simple sphere geometry systems and reflective sphere geometry systems. The differences are small and lies within 1.6% for all cases calculated and we could confirm that β_{eff} calculated by Van der Marck method is consistent with β_{eff} weighted by the importance function defined in equation (1).

6. Conclusions

- From our calculation results, we obtained that effect of difference between β_{eff} values calculated by using delayed neutron data based on JENDL-3.3 and ENDF/B-VII.0 were small.

- C/E values for reflected cores which calculated based on both JENDL-3.3 and an ENDF/B-VII.0 library has higher values compared with bare cores, regardless to the fuel composition.
- β_{eff} values calculated by Monte Carlo-based methods include calculation error which leads to misunderstanding in discussion in nuclear data accuracy, in this case is benchmark result for ENDF/B-VII.0
- For all cases, simple bare sphere systems and reflective sphere systems, calculation results obtained from CBG code and MVP code has good agreement, with differences lies within 1.6%.

7. References

[1] Go Chiba, private communication, (2008).

[2] Y. Nagaya, et. al, “MVP/GMVP II: General Purpose Monte Carlo Codes for Neutron and Photon Transport Calculations based on Continous Energy and Multigroup Methods”, JAERI 1348(2005).

[3] S.C. Van der Marck, “Benchmarking ENDF/B-VII.0”, Nuclear Data Sheets 107 (2006).

[4] R.K. Meulekamp and S.C. Van der Marck, “Calculating the Effective Delayed Neutron fraction with Monte Carlo”, Nuclear Science and Engineering: 152 (2006).

[5] O. Iwamoto, et al, “Development of JENDL Actinoid File”, Proc. of PHYSOR 2008 (CD-ROM) 8p, Interlaken, Switzerland (2008).

28. Effect of spectrum shifter for nuclear data benchmark in MeV energy region on $LiAlO_2$ with D-T neutrons

Masayuki OHTA[1,*], Masayuki MATSUNAKA[1], Hiroyuki MIYAMARU[1], Isao MURATA[1], Toshiyuki IIDA[1], Keitaro KONDO[2], Kentaro OCHIAI[2] and Chikara KONNO[2]

[1] *Division of Electrical, Electronic and Information Engineering, Osaka University, Yamada-oka 2-1, Suita, Osaka 565-0871, Japan*

[2] *Japan Atomic Energy Agency, Tokai-mura, Ibaraki 319-1195, Japan*

[*]e-mail: mohta@nf.eie.eng.osaka-u.ac.jp

Integral benchmark experiments with D-T neutrons were reconsidered from the viewpoint of nuclear data benchmarking in MeV energy region. In order to verify nuclear data in the MeV region with D-T neutrons efficiently, usage of a neutron spectrum shifter was proposed. To estimate the effectiveness of the shifter, the energies of neutrons before the last collision were calculated by using MCNP for the experimental system at the FNS facility of JAEA. Contributions from four neutron energy regions, i.e., more than 10 MeV, 1-10 MeV, 0.1-1 MeV, and less than 0.1 MeV, before the last collision to the calculated leakage neutron and gamma-ray spectra at the detector were calculated for a $LiAlO_2$ sample with Be, D_2O, or ^7LiD spectrum shifter. It was shown that the spectrum shifter could be important for $LiAlO_2$ especially for the leakage gamma-ray benchmark experiments.

1. Introduction

Lithium aluminate ($LiAlO_2$) and lithium titanate (Li_2TiO_3) are regarded as promising advanced breeder materials for a D-T fusion reactor. Evaluated nuclear data for these materials, which are exposed to heavy neutron irradiation in the reactor, are necessary to design the reactor. Integral benchmark experiments with D-T neutrons have been conducted so far to confirm reliability of the nuclear data on these materials at the Fusion Neutronics Source (FNS) facility of JAEA, Japan [1]. However, these experiments have not always been sufficient for nuclear data benchmarking in MeV energy region, below 10 MeV. In order to investigate the effectiveness of the experiments in the MeV region, the energies of neutrons inducing nuclear reactions at the last collision which emit neutrons or gamma-rays to be detected by the detector have been investigated for the experimental system at FNS by using the Monte Carlo code MCNP-4C [2]. In the previous analysis [3], the ratio of the amount of MeV energy neutrons to that of 14 MeV neutrons contributing to the calculated leakage neutron or gamma-ray spectra has been calculated for a Li_2TiO_3 sample. To validate nuclear data in the MeV region, it has been revealed that D-T neutrons incident to the sample have to be moderated to increase the ratio of the amount of MeV energy neutrons to that of 14 MeV neutrons. Therefore, usage of a neutron spectrum shifter has been proposed, which is placed between a sample and the D-T neutron source. We have also analyzed the effect of three shifter materials of Be, D_2O and ^7LiD for Li_2TiO_3 in the previous analysis [3]. The previous analysis

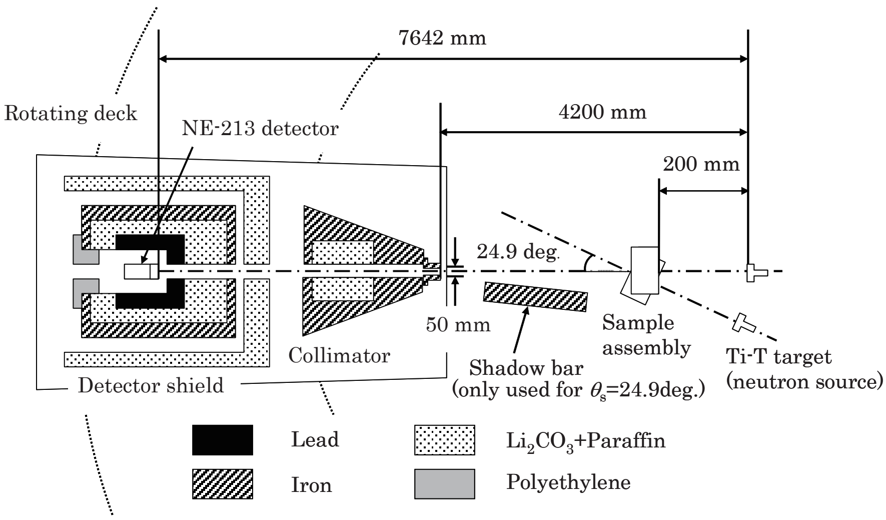

Fig. 1 Schematic drawing of the experimental configuration

suggested that the Be shifter was effective especially for the leakage gamma-ray experiments and reduced the experimental time from the standpoint of benchmark in the MeV region. However, it has not been clear how low energy neutrons at the last collision contribute to the calculated spectra, because contributions to the calculated spectra only from two neutron energy regions, more than 10 MeV and less than 10 MeV, before the last collision were investigated. In this analysis, we analyzed the contributions from four neutron energy regions, i.e., more than 10 MeV, 1-10 MeV, 0.1-1 MeV, and less than 0.1 MeV, before the last collision to the calculated spectra for a $LiAlO_2$ sample with Be, D_2O, or ^{7}LiD spectrum shifter.

2. Analysis with the Monte Carlo code MCNP

Figure 1 shows the experimental configuration for the leakage neutron spectrum measurement at FNS. The feature of the system is that a large amount of materials as a collimator or shield is placed in front of the detector to prevent direct injection of neutrons from the neutron source. Therefore, the detector views only a part of the sample. The configuration for the leakage gamma-ray spectrum measurement is similar to that for the leakage neutron, although the gamma-ray shield is a little improved. The configuration was modeled precisely, and the spectrum calculation was performed for the scattering angle of 24.9 degree by MCNP-4C [2] with the evaluated nuclear data library JENDL-3.2 [4]. The neutron source spectrum evaluated at FNS was used as the neutron source condition.

A spectrum for an energy which a neutron has before the last collision was calculated by the modified point detector tally of MCNP as described below. Figure 2 shows an example of a history for a neutron incident to a sample. In the history, a neutron collision occurs at P1 and is scattered to P2. The neutron is scattered again and escapes to the outside of the system. A photon produced at P2 is scattered at P3 and escapes to the outside. Then, the history is terminated. The spectra at the detector are calculated from many histories by the summation of contributions to the detector at every scattering point. In the case of Fig. 2, $C_n(i)$ and $C_p(i)$ (where, i = 1, 2) are counted as contributions for neutron and photon, respectively. The spectrum of neutrons before the last collision can be obtained by replacing the energy corresponding to the contribution of $C_n(1)$ with $E_n(1)$ and that of $C_n(2)$

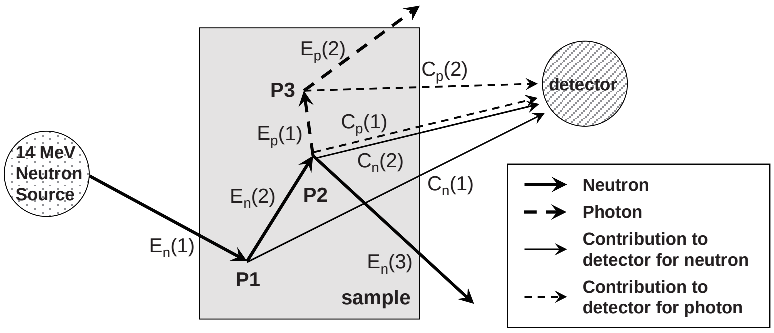

Fig. 2 History of an incident neutron

with $E_n(2)$ for neutrons, and also replacing that of $C_p(1)$ with $E_n(2)$ and that of $C_p(2)$ with $E_n(2)$ for photons in the calculation. The contributions from four regions of the neutron energy before the last collision to the calculated leakage neutron and gamma-ray spectra were calculated: more than 10 MeV, 1-10 MeV, 0.1-1 MeV, and less than 0.1 MeV. The calculations were carried out for a $LiAlO_2$ sample with Be, D_2O, or ^7LiD spectrum shifter, and the results were compared with those for Li_2TiO_3 [3].

The sizes of the sample and spectrum shifter are shown in Fig. 3 and are also listed in Table 1 with their results. In Fig. 3-(a), the spectrum shifter is placed so as to avoid direct injection of neutron or gamma-ray from the shifter to the detector. In Fig. 3-(b), the direct injection exists because the detector can view the shifter through the sample. The configuration in Fig. 3-(b) was adopted only in the calculation of the leakage gamma-ray spectrum with a Be shifter, because the production of photon is little in the shifter and the direct gamma-ray injection from the shifter is estimated to be very small. Calculations for types (a) and (a’) in Table 1 were performed without the shifter. Those of types (b)-(d) were performed with the shifter configuration shown in Fig. 3-(a), and those for types (e) and (e’) with that in Fig. 3-(b). That for type (f), which was the case that the sample area was 30.0×30.0 cm^2 instead of 40.0×40.0 cm^2 in type (a), were also performed. All calculations except for type (g) were calculated on the configuration in Fig. 1. Only calculation for type (g) was performed without the collimator, so that the direct neutron injection from the D-T neutron source could occur. Types (a)-(g) were calculated for the $LiAlO_2$ sample, and types (a’) and (e’) for Li_2TiO_3.

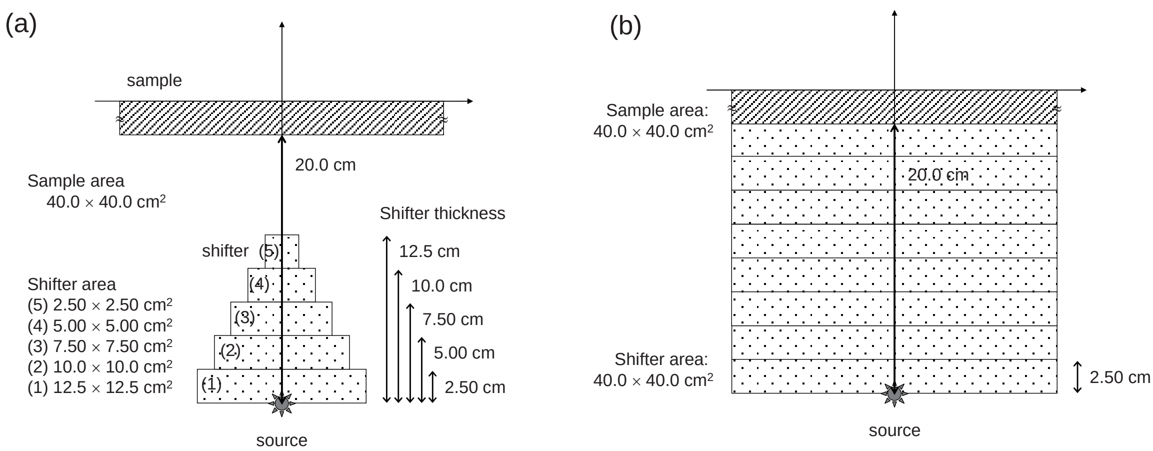

Fig. 3 Sample and shifter arrangements; (a) and (b)

3. Results and discussion

Examples of the neutron spectrum before the last collision and the calculated spectrum at the detector were shown in Fig. 4; (A) for the leakage neutron spectrum and (B) for the leakage gamma-ray spectrum. In both (A) and (B), (1) neutron spectrum before the last collision and (2) partial spectra corresponding to partial contribution of the calculated spectrum for four regions of neutron energy before the last collision, i.e., more than 10 MeV (closed circle), 1-10 MeV (open triangle), 0.1-1 MeV (closed square), less than 0.1 MeV (open diamond) were shown. The solid line is the summation, which is the calculated spectrum at the detector. For sake of simplicity, results of the ratio of contribution of 14 MeV neutrons, which were evaluated as the percentage of 14 MeV components by integrating the spectrum before the last collision for energy more than 10 MeV, for various sizes of the samples and shifters were summarized in Table 1. The ratio of estimated experimental time, which is defined as the integral count of the spectrum divided by that of the case of a 10.0 cm sample in the calculation type (a), were also listed in Table 1.

From Fig. 4 (A)-(2), it was found that neutrons in energy regions of 0.1-1 MeV and less than 0.1 MeV almost contributed to their own energy regions again. That means multiple collisions of neutrons in the energy regions could occur. Even in the energy region of 1-10 MeV, contribution from more than 10 MeV neutrons seems to be sufficiently smaller than that from 1-10 MeV neutrons. Although, in some cases in type (a), (f), (g) and (a’), contribution from more than 10 MeV neutrons exceeded that from 1-10 MeV neutrons in the energy region of 5-10 MeV in the calculated spectrum, increase in the thickness of the sample diminished sufficiently contribution from more than 10 MeV neutrons except for type (g) in which there existed direct injection from the neutron source. The effect could be seen as a decrease in the ratio of contribution of 14 MeV neutrons with the thickness in Table 1. And increase in the area of the sample would also be effective as seen in the results of types (a) and (f). However, increase in the thickness and area of the sample was not sufficient for the leakage gamma-ray benchmarking in the MeV region, because the contributions from neutrons less than 10 MeV to the gamma-ray spectrum were submerged by that from neutrons more than 10 MeV, or 14 MeV neutrons, as seen in Fig. 4 (B)-(2). To decrease the ratio of contribution from 14 MeV neutrons, the spectrum shifter was effective. The results of types (b)-(d) in Table 1 showed that the Be shifter was superior to others. Assuming that the ratio of contribution of 14 MeV neutrons was needed to be suppressed down to 50% for an effective benchmarking in the MeV region, a thick Be shifter, whose thickness was more than 20.0 cm, would be needed for the 10.0 cm thick $LiAlO_2$ sample as shown in the result of type (e). It also seems that benchmark experiments for materials having small Z-number elements needs a thicker shifter from comparison between the results of types (a) and (e) and those of (a’) and (e’). Another advantage was that the Be shifter would reduce the experimental time in both leakage neutron and gamma-ray measurements, judging from the ratio of estimated experimental time having approximately the same ratio of contribution as 14 MeV neutrons in the results of types (a) and (b). It was also important that a large amount of collimator materials decreased the ratio of contribution of 14 MeV neutrons effectively as seen in the results of types (a) and (g).

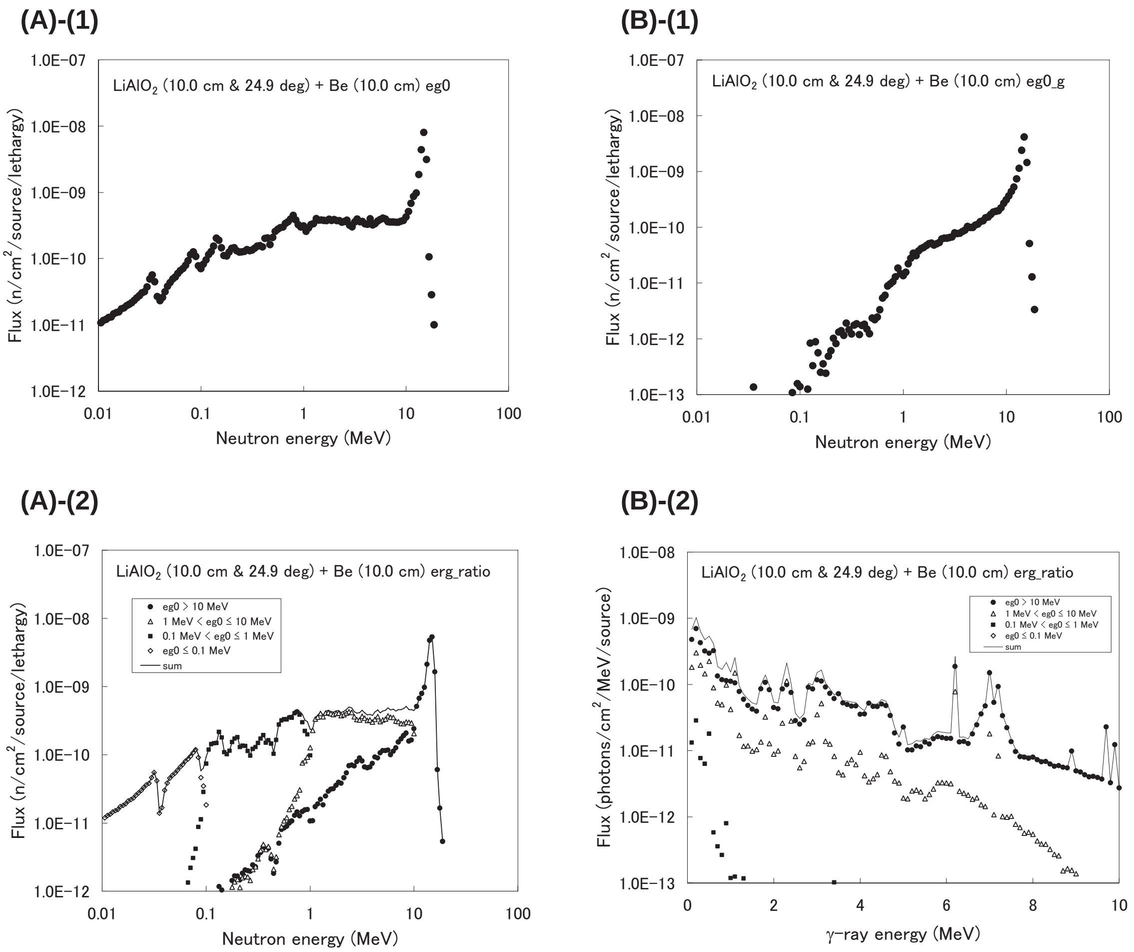

Fig. 4 Calculated spectra for $LiAlO_2$ sample (10.0 cm) with Be shifter ((4) 10.0 cm) in calculation type (b): (A) for the leakage neutron and (B) for the leakage gamma-ray. In both (A) and (B), (1) neutron spectrum before the last collision and (2) partial spectrum corresponding to partial contribution of the calculated spectrum for neutron energy before the last collision, i.e., more than 10 MeV (closed circle), 1-10 MeV (open triangle), 0.1-1 MeV (closed square), less than 10 MeV (open diamond), and the summation (solid line), which is the calculated spectrum at the detector.

4. Conclusion

The effect of the spectrum shifter was analyzed from the viewpoint of nuclear data benchmarking in the MeV region. The ratio of contribution of 14 MeV neutrons was calculated in the leakage neutron spectrum and the leakage gamma-ray spectrum for $LiAlO_2$ sample with Be, D_2O or ^7LiD spectrum shifter by using MCNP-4C code modified to obtain the neutron energy before the last collision. Increase in thickness and area of sample without shifter would suffice for neutron benchmarking in the MeV region. However, it was found that a large and thick Be shifter would be needed for the leakage gamma-ray benchmark experiment.

References

[1] I. Murata *et al.*, *Fusion Eng. Des.* **51-52**, 821-827 (2000).

[2] J.F. Briesmeister (Ed.), LA13709-M, (2000).

[3] M. Ohta *et al.*, "Preliminary spectrum shifter design for intermediate energy nuclear data benchmark experiments with DT neutrons", *Proc. 25th Symp. Fusion Technol. (SOFT-25)*, (to be published).

[4] T. Nakagawa *et al.*, *J. Nucl. Sci. Technol.* **32**, 1259-1271 (1995).

Table 1 Results of the ratio of contribution of 14 MeV neutron

calculation type	sample thickness (cm)	shifter material	shifter thickness (cm)	ratio of contribution of 14 MeV neutron (%) neutron	ratio of contribution of 14 MeV neutron (%) gamma	ratio of estimated experimental time neutron	ratio of estimated experimental time gamma
(a)	10.0	-	-	74.2	87.0	**1.00**	**1.00**
	20.0	-	-	56.8	82.9	1.70	1.07
	30.0	-	-	45.2	80.9	3.34	1.69
	40.0	-	-	37.5	79.5	7.03	3.17
(b)	10.0	Be	(1) 2.50	55.6	79.1	0.835	1.01
	10.0	Be	(2) 5.00	49.7	76.2	0.886	1.16
	10.0	Be	(3) 7.50	48.1	74.9	1.08	1.42
	10.0	Be	(4) 10.0	45.7	73.6	1.33	1.69
	10.0	Be	(5) 12.5	44.2	73.1	1.43	1.77
(c)	10.0	D_2O	(1) 2.50	63.8	82.8	0.963	0.946
	10.0	D_2O	(2) 5.00	59.8	81.1	1.05	1.01
	10.0	D_2O	(3) 7.50	58.7	80.3	1.22	1.14
	10.0	D_2O	(4) 10.0	57.1	79.9	1.43	1.27
	10.0	D_2O	(5) 12.5	56.0	79.7	1.52	1.31
(d)	10.0	^{7}LiD	(1) 2.50	62.7	80.3	0.943	1.01
	10.0	^{7}LiD	(2) 5.00	58.6	77.4	1.02	1.11
	10.0	^{7}LiD	(3) 7.50	57.5	76.3	1.20	1.31
	10.0	^{7}LiD	(4) 10.0	55.6	75.4	1.44	1.50
	10.0	^{7}LiD	(5) 12.5	54.4	75.2	1.54	1.56
(e)†	10.0	Be	15.0	-	58.6	-	1.82
	10.0	Be	17.5	-	56.7	-	2.12
	10.0	Be	20.0	-	54.4	-	2.47
(f)*	10.0	-	-	75.4	87.6	1.02	1.05
	20.0	-	-	61.1	84.3	1.84	1.19
	30.0	-	-	52.2	82.4	4.02	2.05
	40.0	-	-	46.0	80.3	9.60	4.40
(g)#	10.0	-	-	86.2	88.3	0.0387	0.0797
	20.0	-	-	76.1	84.9	0.0726	0.0785
	30.0	-	-	72.1	83.9	0.112	0.101
	40.0	-	-	73.9	84.1	0.140	0.132
(a') for Li_2TiO_3 sample	10.0	-	-	67.8	81.3	-	-
	20.0	-	-	45.8	76.2	-	-
	30.0	-	-	32.9	73.7	-	-
	40.0	-	-	25.1	72.2	-	-
(e')† for Li_2TiO_3 sample	10.0	Be	15.0	-	53.5	-	-
	10.0	Be	17.5	-	51.2	-	-
	10.0	Be	20.0	-	49.6	-	-

† is the case of shifter area 40.0×40.0 cm^2 shown in Fig. 3 (b), * is the case of sample area 30.0×30.0 cm^2, # is the case without the collimator. (a') and (e') are the results for Li_2TiO_3 sample.

29. Theoretical Model Analysis of Li(d,xn) Reactions up to 50 MeV

Tao Ye[1], Yukinobu Watanabe[1], and Kazuyuki Ogata[2]

[1]*Department of Advanced Energy Engineering Science, Kyushu University, Kasuga, Fukuoka 816-8580, Japan*
[2]*Department of Physics, Kyushu University, Fukuoka 812-8581, Japan*
Email: yetao@aees.kyushu-u.ac.jp

A theoretical model analysis is applied to deuteron breakup and stripping reactions on Li at incident energies of several tens of MeV. The continuum discretized coupled channels (CDCC) approach and Glauber model are used to describe elastic breakup and stripping processes, respectively. Both methods use the same phenomenological nucleon optical potential as input, and have no other free parameters. Our results provide an overall good description of experimental double differential (d,xn) cross sections at forward angles, and clarify that the stripping process is more important than the elastic breakup process.

1. INTRODUCTION

Deuteron induced reactions on light nuclei such as Li and Be are used as accelerator-driven neutron sources for various applications. One of the applications is the International Fusion Material Irradiation Facility (IFMIF) as the material test facility for fusion reactor designs [1]. IFMIF includes an accelerator-driven deuteron-lithium neutron source for irradiation tests. Neutrons up to about 55 MeV will be produced by two 125 mA beams of 40 MeV deuterons bombarding a thick target of flowing liquid lithium. Knowledge of the nuclear interaction of deuterons with materials is indispensable for estimating neutron yields and induced radioactivities in the engineering design of such neutron sources and accelerator shielding. From this point of view, reliable nuclear data of deuteron-induced reactions on various nuclei are currently required, and it is of great interest to investigate the reaction mechanism up to 50 MeV in detail.

In the deuteron induced reactions on Li, neutrons are produced by various reaction processes, such as deuteron breakup and proton stripping processes, sequential neutron emission from highly excited compound and residual nuclei, and so on. Neutron spectra observed at forward angles show a distinct broad peak at approximately half the incident energy [2]. This suggests the importance of deuteron breakup reaction in the direct processes, namely, deuteron elastic breakup and proton stripping, which are expected to contribute to major neutron production at higher energies. In the past works [3,4], these processes in the *d* + Li reaction were treated by using semiclassical models such as the modified INC model [3] and the Serber model [5]. Since the incident energy of interest here is relatively low, more sophisticated quantum mechanical approaches will be suitable to enhance our understanding of the Li(*d, xn*) reaction.

The purpose of this work is to analyze the Li(*d, xn*) reaction [2]. We propose to apply the CDCC method to the elastic breakup process and the Glauber model to the stripping process in the calculation of direct processes of Li(*d, xn*) reaction [2] in this paper. As one of the three-body quantum mechanical approaches, the CDCC method [6,7] can deal with the deuteron breakup processes explicitly using a three body Hamiltonian in which the nucleon-nucleus interaction is represented by the optical model potential (OMP) at half the deuteron incident energy and an effective nucleon-nucleon potential is used for the *p-n* interaction. The nucleon-OMP is only the input in the CDCC calculations. The former works show that the CDCC method describes well the deuteron induced elastic scattering [6] and the elastic breakup process [7]. Now, *d* + ^{6,7}Li elastic scattering can be described well using the CDCC method with the proper nucleon-^{6,7}Li OMP, extended Chiba OMP [8] as well. With this OMP, ^{6,7}Li(*d, np*) can also be described properly. On the other hand, no full quantum approach can describe the stripping process satisfactorily till now. Meanwhile, the Glauber model [9-13] can describe the reaction cross section and the momentum distribution of stripping process of the halo nuclei successfully. Since both the deuteron and a halo nucleus have very similar properties, low binding energy and only one bound state, we introduce the Glauber model to describe deuteron stripping process.

In the following sections, we first discuss the applicability of the Glauber model, and then the formulism is outlined. Next, the Li(*d*, *xn*) reaction at 40 MeV is analyzed using both the CDCC method and Glauber model. Finally, the conclusions are given.

2. Glauber model

The Glauber model, which is a semi-classical approach, can calculate some important variables by assuming the eikonal and adiabatic approximations. The eikonal approximation means that the projectile passes in the field of the target nucleus following a straight line trajectory. The adiabatic approximation means that the interaction between a projectile and a target does not affect the internal states in the projectile.

The eikonal approximation requires a condition where the wavelength of the projectile is short compared with the effective range of the potential between the projectile and the target. This condition can be expressed in terms of the relative wave number between the projectile and the target, *k*, and the interaction range, *a*, as shown below:

$$ka >> 1. \tag{1}$$

Then, the eikonal approximation also needs relatively high incident energy, E_{in}, compared with the potential depth, V_0, as

$$E_{\mathrm{in}} >> |V_0|. \tag{2}$$

In the case of the $d + {}^7$Li reaction at 40 MeV, the first condition is satisfied reasonably well, because of

$$ka = k(R_d + R_{\mathrm{Li}}) = 1.53 \times (1.3 \times 2^{1/3} + 1.3 \times 7^{1/3}) \approx 6.3 >> 1. \tag{3}$$

The second one is satisfied with larger relative distance between the center points of *d* and Li, *r*, as shown in Fig. 1, and fails in the interior region. However, the effect on the cross sections from the interior region is much smaller than those from the outer region, because the breakup processes take place mainly in the peripheral region. And our analysis leads to the same conclusion as shown in Fig. 2, where σ^{ℓ} is the integrated cross section with orbit momentum ℓ. The largest contribution appears at $\ell \approx ka$.

Since the eikonal approximation is satisfied and the adiabatic approximation has no special requirement, the Glauber model is applicable to the analysis of the *d* + Li reaction at 40 MeV.

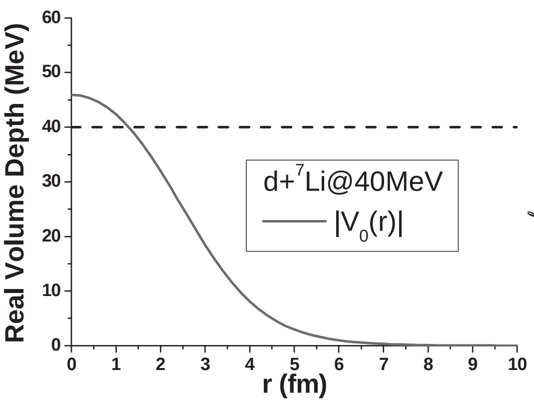

Fig. 1. Real volume depth (red solid curve) of *d*-OMP on Li

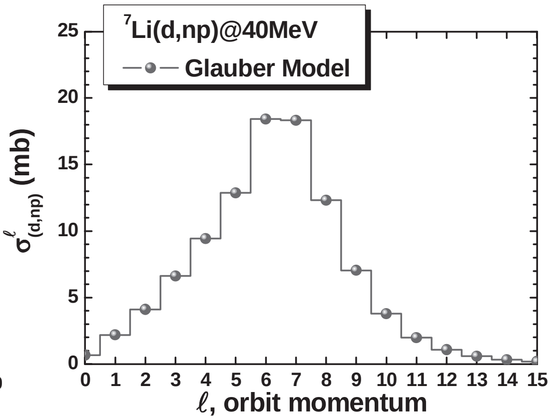

Fig. 2. Elastic breakup cross section with ℓ

In the Glauber model, the total reaction cross section of *d*-nucleus collisions, σ_R, is expressed by

$$\sigma_R = \int d\vec{b}\left[1-\left|\left\langle\psi_{00}\left|e^{i\chi(b)}\right|\psi_{00}\right\rangle\right|^2\right], \tag{4}$$

where ψ_{00} is the wavefunction of the deuteron ground state, b is the impact parameter and χ is the phase-shift function. With the eikonal approximation, the phase-shift can be connected with d-nucleus OMP by the following simple formula:

$$\chi(b) = -\frac{1}{\hbar\upsilon}\int_{-\infty}^{+\infty} dz\, V_{\mathrm{OMP}}\left(\sqrt{b^2+z^2}\right), \tag{5}$$

where z is the axis along the deuteron incident direction and υ is the relative velocity. Because the deuteron is a composite nucleus, the Few-Body Glauber (FBG) model [13] may be applied to calculate the optical phase-shift (i.e., elastic S-matrix) for d-nucleus scattering. In the FBG model, the total phase-shift is given as the sum of the phase-shifts for the scattering of all projectile constituents as shown below:

$$e^{i\chi(b)} = \exp[i\chi_{pA}(b_p) + i\chi_{nA}(b_n)], \tag{6}$$

where b_p and b_n are the coordinator projections of proton and neutron perpendicular to the z direction, respectively, and A stands for the target nucleus. According to Eqs. (2) and (3), the total phase-shift can be calculated using the nucleon OMP. There are two kinds of OMPs: the phenomenological OMP and the OMP constructed using Optical Limit (OL). In this paper, the former is chosen for the sake of simplicity and comprehensiveness. The "comprehensiveness" stands for the inclusive properties of the phenomenological OMP in which all nuclear interactions between the nucleons of deuteron and the target nucleons are included by fitting the experimental data. Meanwhile, the OL-OMP is based on the nucleon-nucleon (NN) scattering cross sections in free space.

In the FBG theory, the total reaction cross section of d-nucleus collision, σ_{R}, the proton stripping cross section, $\sigma_{\mathrm{str}}{}^{p}$, and the elastic breakup cross section, $\sigma_{\mathrm{el.BU}}$, can be formulated as follows:

$$\begin{aligned}
\sigma_R &= \int d\vec{b}\left[1-\left|\left\langle\psi_{00}\left|e^{i\chi_{pA}(b_p)+i\chi_{nA}(b_n)}\right|\psi_{00}\right\rangle\right|^2\right] \\
\sigma_{\mathrm{str}}^{p} &= \int d\vec{b}\,\left\langle\psi_{00}\left|\left|e^{i\chi_{nA}(b_n)}\right|^2\left[1-\left|e^{i\chi_{pA}(b_p)}\right|^2\right]\right|\psi_{00}\right\rangle \\
\sigma_{\mathrm{el.BU}} &= \int d\vec{b}\left\{\left\langle\psi_{00}\left|\left|e^{i\chi_{nA}(b_n)+i\chi_{pA}(b_p)}\right|^2\right|\psi_{00}\right\rangle - \right. \\
&\qquad \left.\left|\left\langle\psi_{00}\left|e^{i\chi_{nA}(b_n)+i\chi_{pA}(b_p)}\right|\psi_{00}\right\rangle\right|^2\right\}
\end{aligned}, \tag{7}$$

Following Ref. [11], the differential cross section for the proton stripping process is given by

$$\frac{d\sigma_{\mathrm{str}}^{p}(\mathrm{C.M.})}{d^3k_n^{\mathrm{C}}} = \frac{1}{(2\pi)^3}\int d^2b_p\left[1-\left|e^{i\chi_{pA}(b_p)}\right|^2\right]\left|\int d^3r\, e^{-i\vec{k}_n^{\mathrm{C}}\cdot\vec{r}}\, e^{i\chi_{nA}(b_n)}\,\psi_{00}(\vec{r})\right|^2, \tag{8}$$

in the center-of-mass (C. M.) of p-n system, where $k_n{}^{\mathrm{C}}$ is the neutron wave number and r is the relative distance between proton and neutron in the deuteron. The double differential cross section (DDX) can be given by transforming the Eq. (8) from the C.M. system to the Lab system:

$$\frac{d\sigma_{\mathrm{str}}^{p}(\mathrm{Lab})}{dE_n^{\mathrm{L}}\,d\Omega_n^{\mathrm{L}}} = \frac{m_n k_n^{\mathrm{L}}}{\hbar^2}\frac{d\sigma_{\mathrm{str}}^{p}(\mathrm{C.M.})}{d^3k_n^{C}}, \tag{9}$$

where $d\sigma_{\mathrm{str}}{}^{p}(\mathrm{Lab})$ is the differential cross section in the Lab system, and $E_n{}^{\mathrm{L}}$, $k_n{}^{\mathrm{L}}$, and $\Omega_n{}^{\mathrm{L}}$ are the energy, the wave number, and the solid angle of the neutron in the Lab system, respectively. The neutron stripping cross section can also be calculated by exchange the subscriptions (p and n) in Eqs. (8) and (9).

To include all neutrons produced by the direct processes, we have to take into account the elastic breakup process. The cross section is well described by the CDCC method [7]. If the interference term is neglected, the DDX for neutron production in the Lab system is given by the sum of two components:

$$\frac{d\sigma^{(d,xn)}}{dE_n^{\mathrm{L}} d\Omega_n^{\mathrm{L}}} = \left.\frac{d\sigma_{\mathrm{el.BU}}}{dE_n^{\mathrm{L}} d\Omega_n^{\mathrm{L}}}\right|_{\mathrm{CDCC}} + \left.\frac{d\sigma_{\mathrm{str}}^{p}(\mathrm{Lab})}{dE_n^{\mathrm{L}} d\Omega_n^{\mathrm{L}}}\right|_{\mathrm{Glauber}}, \qquad (10)$$

where the subscription, el.BU, stands for the elastic breakup process. The proton production cross section can also be calculated by replacing the subscriptions *n* (and *p*) by *p* (and *n*) in Eq. (10).

3. Results and discussions

The theoretical model discussed above is applied to the analysis of ^{7}Li(*d*, *xn*) reaction at 40 MeV. The advantage of this model is that the input is only the neutron OMP. Since Li is the target, the extended Chiba OMP [8] is used for calculations of both the CDCC method and Glauber model. The CDCC calculations are performed using the codes [7,15] developed in Kyushu University, and the Glauber calculations are given by the equations in the preceding subsection. In Fig. 3, the results are compared with experimental data [2].

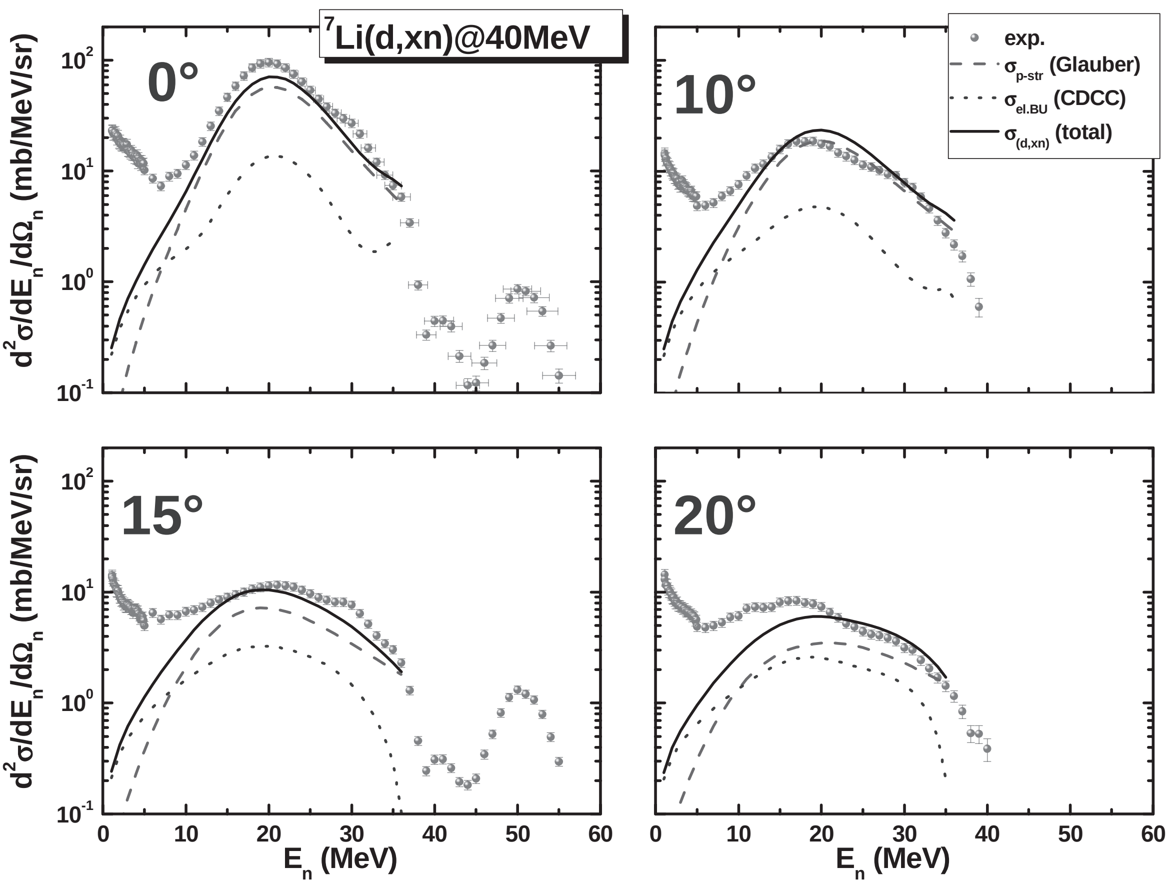

Fig. 3. Double differential cross section of ^{7}Li(*d*, *xn*) at 40 MeV

Because of limitation of the eikonal approximation, we plot those results only at forward angles up to 20 degrees. It is found that the hump structure having a peak at the neutron energy around half of the incident energy is formed by the direct processes. It is clearly shown that the proton stripping process contributes much more than elastic breakup process. Our calculations can reproduce the hump seen in the experimental data well at forward angles smaller than 15 degree.

4. Conclusions

The deuteron breakup reaction on Li at 20 MeV/nucleon was analyzed by combining two theoretical tools, the CDCC theory for elastic breakup process and the Glauber model for stripping process. The theoretical calculations include no free input parameters except the nucleon OMP. It was found that the calculations reproduce the hump structure seen in the experimental energy spectra at forward angles fairly well at relatively low incident energies. From the analyses, it was clarified that the stripping process is more dominant than the elastic breakup process in these reactions.

Since there is no experiments for (d, xn) or (d, xp) reactions on Li at deuteron energies higher than 40 MeV, the analyze will be done in the future on the experimental data of ^{9}Be(d,xp) at 100 MeV [17] with Coulomb interaction between proton and target included. Similar analyses of other targets will also be interesting.

Acknowledgements

We would like to thank M. Kawai for helpful discussions and comments on our analyses. This work was supported by a Grant-in-Aid for Scientific Research of the Japan Society for the Promotion of Science (No. 19560844).

REFERENCES

[1] H. Matsui, in *Proceedings of the 23rd Symposium on Fusion Technology*, Venice, Italy, 20–24 September 2004.
[2] M. Hagiwara, T. Itoga, N. Kawata, N. Hirabayashi, T. Oishi, T. Yamauchi, M. Baba, M. Sugimoto, and T. Muroga, *Fusion Sci. Technol.*, **48**, 1320 (2005).
[3] A. Yu. Konobeyev, Yu. A. Korovin, P. E. Pereslavtsev, U. Fischer, and U. von Mőllendorff, *Nucl. Sci. Eng.* **139**, 1 (2001).
[4] P. Pereslavtsev, U. Fischer, S. Simakov, and M. Avrigeanu, *Nucl. Instr. and Meth. in Phys. Res. B* **266,** 3501 (2008).
[5] R. Serber, *Phys. Rev.* **72**, 1008 (1947).
[6] M. Yahiro, Y. Iseri, H. Kameyama, M. Kamimura, and M. Kawai, *Prog. Theor. Phys. Suppl.* **89**, 32 (1986).
[7] Y. Iseri, M. Yahiro, and M. Kamimura, *Prog. Theor. Phys. Suppl.* **89**, 84 (1986).
[8] T. Ye, Y. Watanabe, K. Ogata, and S. Chiba, *Phys. Rev C* **78**, 024611 (2008).
[9] R. J. Glauber, *Lectures in theoretical physics*, vol. I (Interscience, New York, 1959) p.315.
[10] Y. Ogawa, K. Yabana, and Y. Suzuki, *Nucl. Phys.* ***A*543**, 722 (1992).
[11] K. Hencken, G. Bertsch, and H. Esbensen, *Phys. Rev. C* **54**, 3043 (1996).
[12] Yu. L. Parfenova, and M.V. Zhukov, *Eur. Phys. J. A* **12**, 191 (2001).
[13] J. Al-Khalili, "An Introduction to Halo Nuclei". In: *The Euroschool Lectures on Physics with Exotic Beams, Vol. I*, ed. by J. Al-Khalili, E. Roeckl, *Lect. Notes Phys.* **651** (Springer, Berlin Heidelberg, 2004) pp. 77–112.
[14] J. S. Al-Khalili, J. A. Tostevin, and I. J. Thompson, *Phys. Rev. C* **54**, 1843 (1996).
[15] Y. Iseri, M. Kamimura, M. Yahiro, Y. Sakuargi, and K. Ogata, *Bull. Res. Comput. Syst. Comput.Commun. Cent.Kyushu Univ.* **5**(3), 117 (2006) (CDCDEU); **1**(1), 16 (2007) (HICADEU); **1**(3), 88 (2008) (XPOLADEU).
[16] A. J. Koning and J. P. Delaroche, *Nucl. Phys.* ***A*713**, 231 (2003).
[17] D. Ridikas, W. Mittig, H. Savajols, P. Roussel-Chomaz, S. V. Förtsch, J. J. Lawrie, and G. F. Steyn, *Phys. Rev. C* **63**, 014610 (2000).

This is a blank page.

30. Preliminary Measurement of Neutron Emission Spectra for Beryllium at 21.65 MeV Neutrons

Chang-Lin LAN [1, *] Xi-Chao RUAN [2] Guo-Chang CHEN [2] Han-Xiong HUANG [2] Gang LIU [1]
Yang-Bo NIE [2] Qi-Ping ZHONG [2] Xia LI [2] Song-Lin WANG [1] Jie BAO [2] Zu-Ying ZHOU [2]
Hong-Qing TANG [2] Xiang-Zhong KONG [1]
1 School of Nuclear Science & Technology, Lanzhou University, Lanzhou 730000, China
2 Department of Nuclear Physics, China Institute of Atomic Energy, Beijing 102413, China
E-mail: lanchanglin2000@163.com

The neutron emission spectra were measured for the neutron induced reactions on beryllium at incident energy of 21.65 MeV using time-of-flight techniques. The measured TOF spectra were analyzed by detailed Monte-Carlo simulation and the cross sections were determined by comparing the measured TOF spectra with simulated ones. The cross sections were normalized to n-p scattering measurement. This paper gives the preliminary results of the elastic scattering angular distributions and part of the secondary neutron emission double-differential cross sections (DDXs). A theoretical model based on the Hauser-Feshbach and exciton model for light nuclei was used to describe the double-differential cross sections of n+^{9}Be. The experimental data were compared with the results of calculation and other measurements.

1. Introduction

Special attention has been paid to the neutron data above 20 MeV due to the development of ADS and other neutron application fields such as fast neutron cancer therapy in recent years. Meanwhile, DDX is one of the most important nuclear data used in nuclear engineering, particular in design of nuclear device and neutron shielding. However, the experimental and evaluation data are very sparse. Up to now, most of DDX measurements performed are at around 14 MeV, while the DDX measurements are very scarce above 20 MeV. On the other hand, the results of theoretical calculation are discrepant from each other with different light nuclei reaction models. Therefore, the DDX measurements for light nuclei are necessary for checking and improving nuclear reaction models and nuclear data evaluations.

We have a project to measure the differential and double-differential cross sections (DX and DDXs) of secondary neutron emission for some light nucleus at the neutron energy between 20 and 30 MeV at the China Institute of Atomic Energy (CIAE).

As an important material in fusion technology, beryllium has been used in various forms in a number of tritium breeding blanket designs [1]. In this work, the elastic scattering angular distributions and DDXs of n+^{9}Be have been measured at 21.65 MeV incident neutrons energy. Up to now, no measured DDX data for ^{9}Be in the energy region above 20 MeV were reported in the literature, only one published DX data at 21.6 MeV can be found. Which were measured by N.Olsson et al. [2].

---

* Present address: Department of Advanced Energy Engineering Science, Kyushu University, Kasuga, Fukuoka 816-8580, Japan. *E-mail:* lan@aees.kyushu-u.ac.jp

2. Experiment

The experiment was performed with the Multi-detector Fast Neutron TOF Spectrometer at the HI-13 Tandem Accelerator at China Institute of Atomic Energy (CIAE). Mono-energetic neutrons of 21.65 MeV were produced by the T (d, n) 4He reaction with a tritium gas target. The equipment and its application were extensively described in ref [3] [4]. And only a brief description will be given here. The diagram of the spectrometer is shown in Fig. 1.

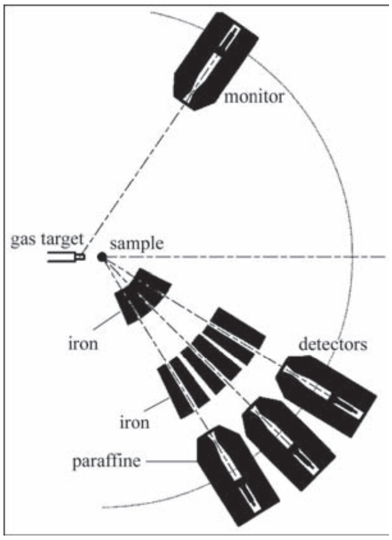

Fig. 1. Schematics view of the Multi-detector Fast Neutron TOF Spectrometer in CIAE.

A hollow cylindrical beryllium sample with the outer size of ϕ 25×40 mm and the hollow size of ϕ10 mm was used in the experiment. To normalized the measured cross sections a cylindrical polyethylene sample with diameter 30 mm and length 40 mm was used, during the experiment the samples were suspended with a thin thread in the ion-beam direction at a distance of 17.5 cm in front of the gas target and with the symmetry axis perpendicular to the scattering plane.

The spectra of the emission neutrons were measured in steps of 5^0 in the angular interval 15^0~150^0. The parameters of the projectiles, tritium gas target and detectors are listed in Table 1.

For runs of measurement with gas in (sample in and out) and gas out (sample in and out) were performed for each angle during the experiment. All events from the four detectors (three main detectors and one monitor) were recorded by list mode. For each event, there are three parameters which are PH, PSD and TOF. PH and PSD are used for the detection threshold determination and $n-\gamma$ discrimination.

3. Data reduction and theoretical calculation

The data analysis was briefly described as the following steps:

From the measured raw spectra (gas in, gas out, sample in and sample out), the net spectra were determined including the uncertainty propagation. Other relevant data such as gamma positions, neutron detection threshold, monitor count rates, channel width of time-to-amplitude converters (TAC) are also obtained.

TOF spectra were calculated by a realistic Monte-Carlo simulation with the code STREUER [5]. The code was developed in PTB Braunschweig/Germany and extensions have been made for CIAE's experimental conditions. The cross sections used in the Monte-Carlo simulation are taken from an evaluated data file (usually from ENDF/B-VI). The simulated TOF spectra would be obtained with inclusion of the differential non-linearity of the TACs, the proper detection efficiencies and the proper folding parameters. The folding function is a combination of a Gaussian function and the time response function of the neutron detectors. The time response function is calculated by Monte-Carlo method.

Table 1. Experimental parameters

Projectile		
	deuteron energy	5.8 MeV
	averaged current	≈ 0.4 μA
	pulse width (FWHM)	≈ 2.0 ns
	repetition frequency	2 MHz
Tritium gas target		
	Tritium gas chamber	
	length	30 mm
	diameter	10 mm
	gold backing	0.5 mm
	molybdenum entrance foil	10 μm
	gas pressure	2.1 atm.
	neutron energy	≈ 22 MeV
	Helium gas chamber	
	length	20 mm
	diameter	10 mm
	molybdenum entrance foil	10 μm
	gas pressure	0.3 atm.
Detectors		
	3 main detectors	BC501A
	scintillator diameter	12.7 cm
	scintillator length	5.08 cm
	flight path	≈ 6.0 m
	angle with beam axis	15.0-150.0 deg
	electron threshold	0.47 MeV
	monitor	Stilbene crystal
	scintillator diameter	3.0 cm
	scintillator length	3.0 cm
	flight path	≈ 6.0 m
	angle with beam axis	60.0 deg
	electron threshold	0.30 MeV

The measured and simulated TOF spectra were compared for the n-p scattering realized with a polyethylene sample. These ratios deduced from the comparison were used for normalization; all calculated TOF spectra were normalized to measured ones, its means that the ratios became unity. Thus, the derived cross sections are normalized with the elastic scattering on hydrogen.

Measured and calculated TOF spectra of the beryllium sample were compared with respect to specific scattering fractions, with respect to the elastic peak or to the inelastic peak or to the windows for different neutron emission energies of the continuum. These ratios of measured to calculated fractions are used to obtain differential and double-differential cross sections determined in this way is fitted by a Legendre polynomial expansion.

The results of the Legendre polynomial fitting were used to improve the input data of the Monte-Carlo simulation (it replaces the data from evaluation). In this way, the data were iteratively refined so that the measured and calculated TOF spectra were agree with each other within their experimental uncertainties. Thus, the experimental results can be obtained from the last iteration.

The uncertainties due to the statistical uncertainty, the neutron detection efficiency (3%), the scattering angle (0.5%), the normalization (1%) and the correction for multiple scattering (5%) have been taken into account, including their correlation.

To describe the neutron induced reaction behavior of n + ^{9}Be reaction, A theoretical model based on the Hauser-Feshbach and exciton model for light nuclei was used. In this model, the pre-equilibrium emission from compound nuclei to the discrete levels of the residual nuclei, the angular momentum dependent exciton model as well as the accurate kinematics was considered for all kinds of reaction processes. More detail information of this code (LUNF) were described in ref [6][7][8].

4. Preliminary results

Differential and double-differential cross sections have been obtained at 24 angles in the range between 15 degree and 150 degree. Fig. 2 shows our measured elastic differential cross sections for ^{9}Be at 21.65 MeV comparing with the LUNF calculation and other measurements [2].

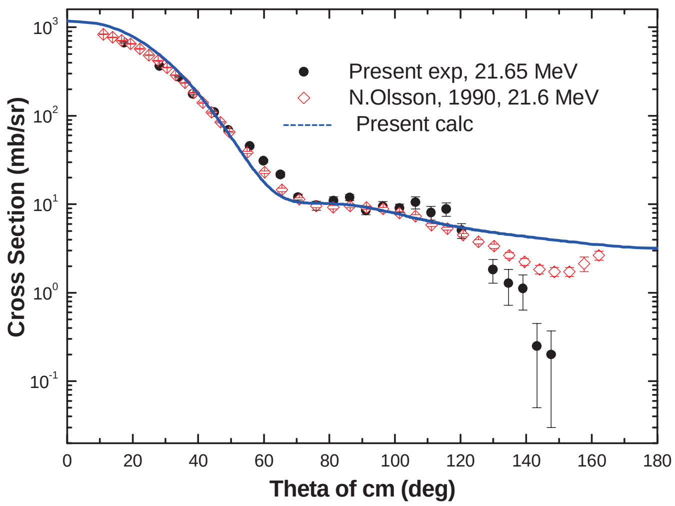

Fig. 2. Result of elastic scattering differential cross sections comparing with calculation and other measurements.

Part of the DDXs results are shown in Figure 3. In our data analysis, the elastic peak was excluded. Therefore the determined DDXs only contain the continuum part of the data. Figure 4 shows the measured secondary neutron emission spectra comparing with the calculation. It can be seen that in general the agreement between the theoretical calculation and the measurement is good, especially at the continuum part.

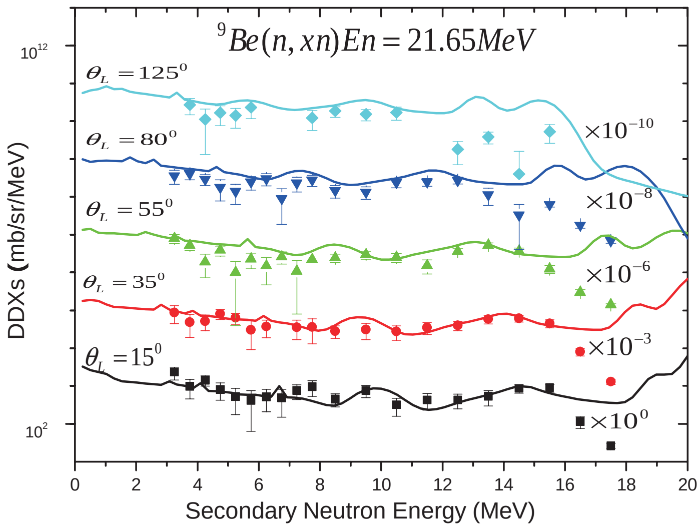

Fig. 3. DDXs results at five degrees, comparing with theoretical calculations

5. Summary

Differential and double-differential cross sections were measured for ^{9}Be at 21.65 MeV incident neutrons energy using the Multi-detector Fast Neutron TOF Spectrometer at the HI-13 Tandem Accelerator in China Institute of Atomic Energy (CIAE). The measured data were analyzed by detailed Monte-Carlo simulation. The statistical reaction model and the angular momentum dependent exciton model were applied to describe the neutron induced reaction processes. The preliminary results show that good agreement has been obtained between the experiment and the calculation.

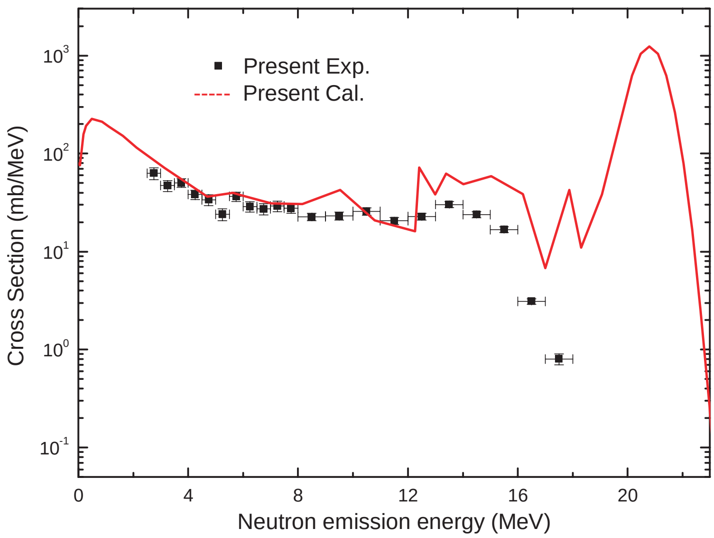

Fig. 4. Angle integral cross sections of the secondary neutron emission spectra comparing with the calculation

Acknowledges

The authors are very grateful to the staff of the HI-13 tandem accelerator at China Institute of Atomic Energy for their excellent operation of the accelerator. One of the authors (Ch. L. Lan) would like to thank the support and encouragement provided by Prof. Y. Watanabe, and also wish to thank the Nuclear Data Division, AESJ, for the financial support in attending the nuclear data symposium 2008.

References

[1] F. Scaffidi-Argentina et al. Journal of Nuclear Materials 283-287 (2000) 43-51.
[2] N. Olsson et al. Nuclear Physics A509 (1990) 161-177.
[3] Sa Jun et al. Atomic Energy Science and Technology 26(6) (1992) 1-8.
[4] Qi Bu-jia et al. Journal of Qingdao University 10(2) (1997) 86-89. (In Chinese)
[5] Dankwart Schmidt et al. Fast Neutron Spectrometry and Monte-Carlo Simulati－the Codes SINENA and STREUER. Report PTB-N-40, PTB Braunschweig, Germany (2000).
[6] CHEN Guo-Chang. Measurement and Evaluation of Neutron Emission Double Dierential Cross Section for $^{6;7}$Li Induced by Fast Neutrons. Master Thesis for Master of Science, CIAE, 2005. (In Chinese)
[7] Zhang Jing-Shang et al. Nuclear science and engineering, 133 (1999) 218-234.
[8] Zhang Jing-Shang et al., Commun. Theor. Phys. (Beijing China), 35, 579, 2001.

31. Measurement of the thermal-neutron capture cross-section and the resonance integral of the ^{112}Cd(n,γ)^{113m}Cd reaction

Shoji NAKAMURA, Hideo HARADA and Takehito HAYAKAWA
Japan Atomic Energy Agency
2-4 Shirakata-Shirane, Tokai-mura, Naka-gun, Ibaraki, 319-1195, Japan
E-mail: shoji.nakamura@jaea.go.jp

The measurement of the thermal-neutron capture cross section and the resonance integral of ^{112}Cd was performed by the activation method. The ^{112}Cd enriched samples were irradiated with and without a Gd shield for 48 hours. The neutron flux components at the irradiation positions were measured by the Westcott's convention. The γ rays from the irradiated samples were measured by a Ge detector, and the amounts of the productions were obtained. The thermal-neutron capture cross section and the resonance integral of ^{112}Cd(n,γ)^{113m}Cd were derived from the information on the amount of ^{113m}Cd and the neutron flux components.

1. Introduction

Since cadmium has the huge neutron capture cross-section, it is an effective substance as shield material. Therefore, the cross-section data are important for the nuclear field. Cadmium-112 among cadmium isotopes shown in **Figure 1** is one of the factors which generates ^{113m}Cd with the half-life of 14.1 yr**[1]** by the ^{112}Cd(n,γ)^{113m}Cd reaction, and makes cadmium shields radioactive, although the cross-section of ^{112}Cd is small. As the measured value of the thermal-neutron capture cross-section of ^{112}Cd, there was only 43±10 (mb)**[2]** for the generation of ^{113m}Cd, and 2.2±0.5 (b)**[3]** for the production of ^{113}Cd. Thus, there are only a few of data. In advance of the detailed measurements, the effective neutron capture cross-section of the ^{112}Cd(n, γ)^{113m}Cd reaction was measured in order to check the accuracy of the reported data. As the result of the comparison with the past measured data and the evaluated values, it was found that it was necessary to measure the cross section again.**[4]** Then, the experiment was planned to measure the thermal-neutron capture cross-section and the resonance integral of the ^{112}Cd(n,γ)^{113m}Cd reaction.

106	107	108	109	110	111
1.25%	6.5h	0.89%	452d	12.51%	12.81%
112	113	114	115	116	117
24.13%	14.1yr	28.72%	44.6d 54h	7.47%	2.41%

Fig.1 Nuclear abundance and half-lives of Cd isotopes

2. Experiments

The ^{112}Cd enriched (98.27±0.01 %) foil with thickness 50μm was used for the irradiation sample. Two pieces of a Cd foil (about 8×8mm in size) were prepared, and their weight were 22.46 (mg) and 25.82 (mg), respectively. A set of ^{197}Au/ aluminum, ^{59}Co/aluminum alloy wires, and Mo wire was used to monitor the neutron fluxes. One set of the monitors was attached to each Cd sample.

To measure the resonance integral, one of the Cd samples was wrapped with 0.75 mm-thick Gd shield. The thickness of the Gd foil was optimized in the neutron transmission. When the Gd foil with 0.75-mm thickness is used, its effective thickness is estimated as 1.5 mm in consideration of the geometric shape. The energy at which transmission reduced by half can be estimated as 0.5 eV. Hence, the Gd foil with 0.75-mm thickness was chosen, and the cut-off energy was set as 0.5 eV on this experiment.

The Cd samples w/o the Gd shield were irradiated for 48 hours in the middle of hydraulic irradiation equipment (HR-2) of the JRR-3. After the irradiation, the gamma rays from the monitors and Cd samples were measured by a high resolution Ge detector, of which performance was characterized by a relative efficiency of 25 % to a 7.6 cm×7.6 cmϕ NaI(Tl) detector and an energy resolution of 2.0 keV full width at half-maximum (FWHM) at the 1.33 MeV peak of ^{60}Co. The peak detection efficiencies were determined with ^{152}Eu and ^{60}Co sources. The error of the detection efficiency due to the uncertainties of the calibration γ source intensities was estimated as 2%. Radioactivities of the irradiated samples were measured at a distance of 100.-mm from the center of the detector head.

Cadmium-114 (0.52±0.01%) contained in the Cd sample generated ^{115m}Cd (half-life : 44.6 days**[1]**) and ^{115g}Cd (half-life : 53.46 hours**[1]**) via neutron capture reaction. An example of gamma-ray spectrum is shown in **Figure 2**. Many γ rays due to ^{115m}Cd and ^{115g}Cd were observed. Then, the measurements were still performed to obtain the cross sections of the ^{114}Cd(n,γ)$^{115m,\,115g}$Cd reactions. Since gamma rays from ^{115g}Cd generated a strong background around the low energy region, the Cd samples were cooled for about two weeks to attenuate ^{115g}Cd which has blocked measurement of 263-keV gamma ray from ^{113m}Cd. After the cooling, gamma-ray measurements of the Cd samples w/o Gd shield were done for 2 and 4days, respectively. Since the background was reduced when the ^{115g}Cd decayed out sufficiently, the 263-keV gamma ray was clearly observed as shown in **Figure 3**.

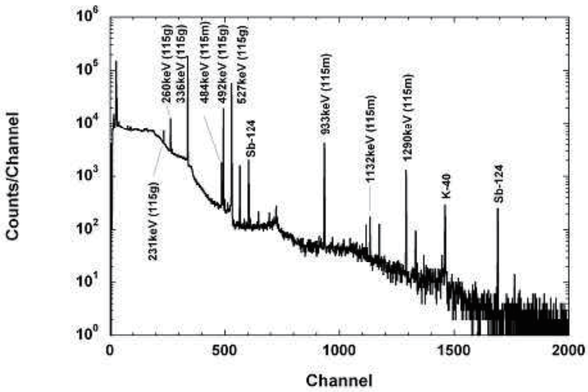

Fig.2 Gamma-ray spectrum of $^{115m,\,g}$Cd without the Gd
20 days have passed from the irradiation.
Measurement time was 3 hours.

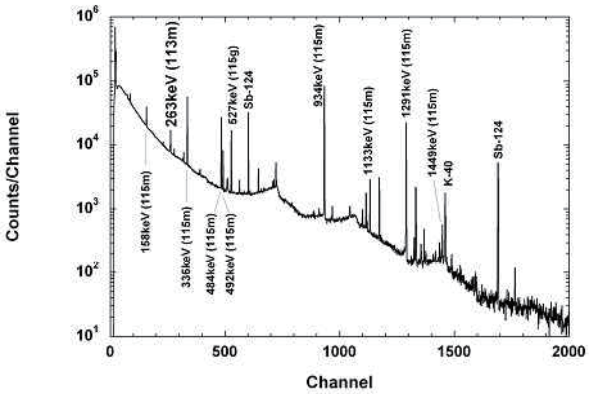

Fig.3 Gamma-ray spectrum of ^{113m}Cd without the Gd
33 days have passed from the irradiation.
Measurement time was 45 hours.

3. Analysis

The effective cross-section $\hat{\sigma}$ is defined by equating the reaction rate R to product of $\hat{\sigma}$ and $n\upsilon_0$, where $n\upsilon_0$ is the "neutron flux" in Westcott's convention **[5]** with the neutron density n, including thermal and epithermal neutrons, and with the velocity of neutron υ_0 = 2,200 m/s, so that

$$R = n\upsilon_0\hat{\sigma}\ . \tag{1}$$

When the cross-section departs from the 1/υ law, a simple relation for $\hat{\sigma}$ can be obtained as:

$$\hat{\sigma} = \sigma_0\left(gG_{th} + r(T/T_0)^{1/2}s_0G_{epi}\right), \tag{2}$$

where σ_0 is the thermal-neutron capture cross-section; g is a function of the temperature related to departure of the cross-section from the 1/υ law; r is an epithermal index in Westcott's convention.; T is neutron temperature and T_0 is 293.6 K; the quantity $r(T/T_0)^{1/2}$ gives the fraction of epithermal neutron in the neutron spectrum; the G_{th} and G_{epi} denote self-shielding coefficients for thermal and epithermal neutrons. The parameter s_0 is defined by:

$$s_0 = \frac{2I_0^{'}}{\sqrt{\pi}\sigma_0}, \tag{3}$$

where I_0' is the reduced resonance integral, i.e. the resonance integral with the 1/υ-component subtracted. Substituting Eq.(3) into Eq.(1), the reaction rates can be written in simplified forms as:

$$R/\sigma_0 = gG_{th}\phi_1 + \phi_2 \cdot s_0 G_{epi}, \tag{4}$$

for irradiation without the Gd shield, and

$$R^{'}/\sigma_0 = gG_{th}^{'}\phi_1^{'} + \phi_2^{'} \cdot s_0 G_{epi}^{'}, \tag{5}$$

for irradiation with the Gd shield. The ϕ_1 and ϕ_1'are neutron fluxes in the thermal energy region, and the ϕ_2 and $\phi_2^{'}$ are those in the epithermal energy region. The ϕ_1, ϕ_2, ϕ_1' and ϕ_2' were determined using the σ_0 data cited in Ref.6 and reaction rates R and R' of the monitor wires. Here the ϕ_1 and ϕ_1' are neutron fluxes in the low (thermal) energy region. The values of ϕ_1 and ϕ_2 at the irradiation position were obtained by using the data of s_0 and σ_0, and reaction rates R for the monitor wires. The reaction rates were calculated from peak counts of γ rays from ^{60}Co, ^{198}Au and ^{99}Mo. **Figure 4** shows the experimental relation between R/σ_0 and s_0 obtained by the flux monitor wires. The thermal-neutron flux at the irradiation position was 7.06 ±0.25 ×10^{13} (n/cm^2/s). The slope of the solid line gives the epithermal flux component, *i.e.* ϕ_2. Westcott's index **[5]** was only 0.5%; which means that the neutron flux was well-moderated.

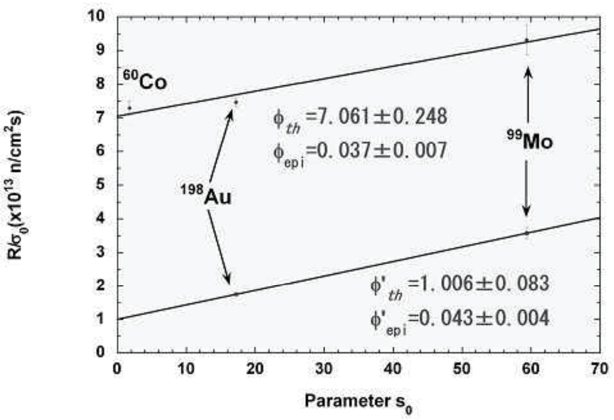

r

ig.4 Experimental relation between R/σ_0 and s_0

obtained by the flux monitors.

From Eqs.(4) and (5), the quantity s_0 is given by :

$$s_0 = -\frac{gG_{th}\phi_1 - gG_{th}^{'}\phi_1^{'}(R/R^{'})}{\phi_2 G_{epi} - \phi_2^{'}(R/R^{'})G_{epi}^{'}}. \tag{6}$$

The σ_0 is obtained by substituting s_0 into Eq.(4). The I_0' is obtained using Eq.(3). The resonance integral I_0 can be expressed as:

$$I_0 = I_0^{'} + I(1/\upsilon), \tag{7}$$

where the term I(1/υ) is the 1/υ contribution to the resonance integral above the Cadmium cut-off energy (E_{Cd}). The term I(1/υ) is given by:

$$I(1/\upsilon) = \int_{E_{Cd}}^{\infty} g\sigma_0 \sqrt{\frac{E_0}{E}} \frac{dE}{E} = 2g\sigma_0 \sqrt{\frac{E_0}{E_{Cd}}}, \tag{8}$$

where E_0 is the thermal neutron energy; *i.e.* 0.0253 eV. The E_{Cd} for isotropic incidence of neutrons on a 0.75 mm-thick Gadolinium shield is estimated as 0.5 (eV). For E_0=0.0253 eV and E_{Cd}=0.5 eV, the 1/υ contribution to the resonance integral is estimated using Eq.(8) to be:

$$I(1/\upsilon) = 0.45\sigma_0 . \tag{9}$$

Then, the resonance integral I_0 is given by

$$I_0 = I_0^{'} + 0.45\sigma_0. \tag{10}$$

4. Results and Discussions

The reaction rates were calculated from the gamma-ray yields from each Cd sample. The results of the reaction rates are listed in **Table 1**.

Table 1 Reaction rates obtained for the ^{112}Cd(n,γ)^{113m}Cd and ^{114}Cd(n,γ)^{115m,g}Cd reactions

Reaction Rate	^{114}Cd(n,γ)^{115m}Cd (×10^{-12} /s)	^{114}Cd(n,γ)^{115g}Cd (×10^{-11} /s)	^{112}Cd(n,γ)^{113m}Cd (×10^{-12} /s)
R without Gd	2.914±1.020	3.209±0.101	2.298±0.118
R' with Gd	0.609±0.045	0.786±0.025	0.649±0.035

The results of the reaction rates were analyzed with the Westcott's convention, and the thermal-neutron capture cross-sections and the resonance integrals were derived. from these reaction rates and the neutron fluxes using Eqs.(4), (6) and (10). Table 2 summarizes the present results for the thermal-neutron capture cross-sections and the resonance integrals.

The systematic errors were taken into consideration as following items: a) the detection efficiency in the g-ray measurements; b) the accuracy of the half-life data used in this analysis; c) the accuracy of the g-ray emission probabilities; d) weight measurements of the samples.

Table 2 Present results for the thermal-neutron capture cross-section and the resonance integrals

	^{114}Cd(n,γ)^{115m}Cd	^{114}Cd(n,γ)^{115g}Cd	^{112}Cd(n,γ)^{113m}Cd
σ_0	38.6±13.6 (mb)	0.41±0.02 (b)	28.1±2.1 (mb)
s_0	13.1±3.2	21.0±4.7	30.0±7.4
I_0	467±197 (mb)	7.8±1.8 (b)	760±193 (mb)

As for the ^{114}Cd(n,γ)^{115m,g}Cd reaction, the total thermal-neutron capture cross-section was found to be $\sigma_{0,m+g}$ = 0.45±0.02 (b), the resonance integral $I_{0,m+g}$ = 8.3±1.8 (b) and Isomer ratio 0.086. The effective cross-section was measured in the past was as 0.46±0.02 (b) **[4]**, which was in good agreement with the present result within the limit of error. The evaluations by Mughabghab *et al.***[6]** are σ_0 = 0.34±0.02 (b) and the resonance integral =14.1±0.7 (b). There are large discrepancies among the measured and/or evaluated resonance integrals for the ^{114}Cd(n,γ)^{115m,g}Cd reaction. It seems that the σ_0 of ^{114}Cd would be underestimated by ～30%.

As for the ^{112}Cd(n,γ)^{113m,}Cd reaction, the thermal-neutron capture cross-section was found to be $\sigma_{0,m}$ = 28.1±2.1 (mb). There is only one of data by Wahl, which is 43±10 (mb)**[2]** for the thermal-neutron capture cross-section. In comparison with the past and present values, there would be a possibility that the past one would be overestimated no less than 35%.

4. Conclusion

In terms of activation of shield material, the thermal-neutron capture cross section and the resonance integral of the ^{112}Cd(n,γ)^{113m}Cd reaction were measured by the activation method. The present result for the σ_0 of the ^{112}Cd(n,γ)^{113m}Cd reaction was 28.1±2.1(mb), which was much smaller than that by Wahl, 43±10 (mb)**[2]**. There would be an overestimation by 35%. The cross sections were also measured for the ^{114}Cd(n,γ)$^{115m,\,g}$Cd reactions. The total thermal-neutron capture cross-section to ^{115}Cd was found to be $\sigma_{0,m+g}$ = 0.45±0.02 (b), and the resonance integral was found to be $I_{0,m+g}$ = 8.3±1.8 (b). The evaluation by Mughabghab *et al.***[6]** is σ_0 = 0.34±0.02 (b). It seems that the σ_0 of ^{114}Cd would be underestimated by about 30%. These problems should be also solved in future.

Acknowledgement

The authors would like to thank the staff of the JRR-3M for their cooperation. The authors appreciate Dr. M. Oshima of Japan Atomic Energy Agency (JAEA) for his encouragement of this work.

References

[1] R. B. Firestone, V. S. Shirley, C. M. Baglin, S. Y. F. Chu, and J. Zipkin, Table of Isotopes, 8th edition, John Wiley and Sons, New York, (1995).

[2] A.Wahl: *Journal of Inorganic and Nuclear Chemistry*, 10, 1(1959).

[3] C.R.Baldock: ORNL-3994,1(1966).

[4]S.Nakamura *et al.*: 2008 *Fall Meeting of AESJ*, B25.

[5] C. H. Westcott, W. H. Walker, T. K. Alexander, "*Proc. 2nd Int. Conf. Peaceful Use of Atomic Energy, Geneva*", United Nations, New York, **16**, 70 (1958).

[6] S. F. Mughabghab, M. Divadeenam, N. E. Holden, "*Neutron Cross Section*", vol. **1**and **2**, Academic Press, New York, (1981).

This is a blank page.

32. Measurements of keV-neutron capture cross sections and capture gamma-ray spectra of $^{80, 82}$Se

S. KAMADA, M. IGASHIRA, T. KATABUCHI, M. MIZUMOTO, and M. TAJIKA
Research Laboratory for Nuclear Reactors, Tokyo Institute of Technology
2-12-1-N1-26 O-okayama, Meguro-ku, Tokyo, 152-8550, Japan
Email:kamata.s.ac@m.titech.ac.jp

The capture cross sections and capture gamma-ray spectra of $^{80, 82}$Se were measured in an incident neutron energy region from 10 to 100 keV, using a 1.5-ns pulsed neutron source by the ^{7}Li(p,n)^{7}Be reaction and a large anti-Compton NaI(Tl) gamma-ray spectrometer. A pulse-height weighting technique was applied to observed capture gamma-ray pulse-height spectra to obtain capture yields. The capture cross sections were derived with the errors of about 5% and 5-20% for ^{80}Se and ^{82}Se, respectively, by using the standard capture cross sections of ^{197}Au. The present cross section results were compared with previous experimental data and the evaluated values in JENDL-3.3, ENDF/B-VI.8 and ENDF/B-VII.0. The capture gamma-ray spectra of $^{80, 82}$Se were derived by unfolding the capture gamma-ray pulse-height spectra.

1. Introduction

Recently, a great interest has been taken in the study on the nuclear transmutation of Long-Lived Fission Products (LLFPs: ^{79}Se, ^{93}Zr, ^{99}Tc, ^{107}Pd, ^{126}Sn, ^{129}I, ^{135}Cs) generated in nuclear fission reactors. The neutron capture cross sections of LLFPs play an important role for the research and development of transmutation systems of radioactive wastes. The nuclide ^{79}Se is one of the LLFPs. However, there is no experimental data for ^{79}Se, because it is difficult to prepare the high-purity sample.

On the other hand, neutron capture cross sections of $^{77, 78, 80, 82}$Se are also important for the study on transmutation systems, because those stable isotopes are also generated in fission reactors and ^{79}Se is accompanied by them when it is loaded into a transmutation system without isotope separation. Moreover, keV-neutron capture cross sections and capture gamma-ray spectra of stable Se isotopes contain important information which is useful for the calculation of capture cross sections of ^{79}Se. Therefore, we started a systematic measurement and calculation of keV-neutron capture cross sections and capture gamma-ray spectra of all stable Se isotopes. In this contribution, the results for ^{80,82}Se are presented.

2. Experimental procedure and data processing

The capture cross sections and capture gamma-ray spectra of ^{80,82}Se were measured in an incident neutron energy region from 10 to 100 keV, using the 3-MV Pelletron accelerator of the Research Laboratory for Nuclear Reactors at the Tokyo Institute of Technology. Pulsed keV-neutrons were produced by the ^{7}Li(p,n)^{7}Be reaction with a pulsed proton beam (1.5 ns width, 4 MHz repetition rate) from the Pelletron accelerator. Both of ^{80}Se and ^{82}Se samples were made of isotopically enriched metal powder with the net weight of about 3 g and 2 g, respectively. The ^{80}Se sample was press-molded and sealed with a Mylar film of 15 μm thickness, and the ^{82}Se sample was press-molded and contained in a carbon case. A ^{197}Au sample was used as a standard capture sample. Capture gamma-rays were detected with a large anti-Compton NaI(Tl) spectrometer[1)] by means of a time-of-flight method.

A pulse-height weighting technique[2)] was applied to the observed capture gamma-ray pulse-height spectra to obtain capture yields. The capture cross sections of ^{80,82}Se were derived using the standard capture cross sections[3)] of ^{197}Au. The capture gamma-ray spectra were derived by unfolding the observed capture gamma-ray pulse-height spectra with the computer code, FERDOR[4)], and a response matrix of the spectrometer.

3. Results and discussion

The capture cross sections of ^{80,82}Se were derived with the error of about 5% and 5-20%, respectively. In Figs. 1 and 2, the present results are compared with the previous experimental data[5-8)] and the evaluated values[9-14)] in JENDL-3.3, ENDF/B-VI.8, and ENDF/B-VII.0.

The capture gamma-ray spectra of ^{80,82}Se in an incident neutron energy region from 15 to 100 keV are shown in Figs.3 and 4, respectively, where low-lying states of the residual nucleus, ^{81}Se or ^{83}Se, are also shown. The characteristic primary transitions from the capture states to low-lying states are observed.

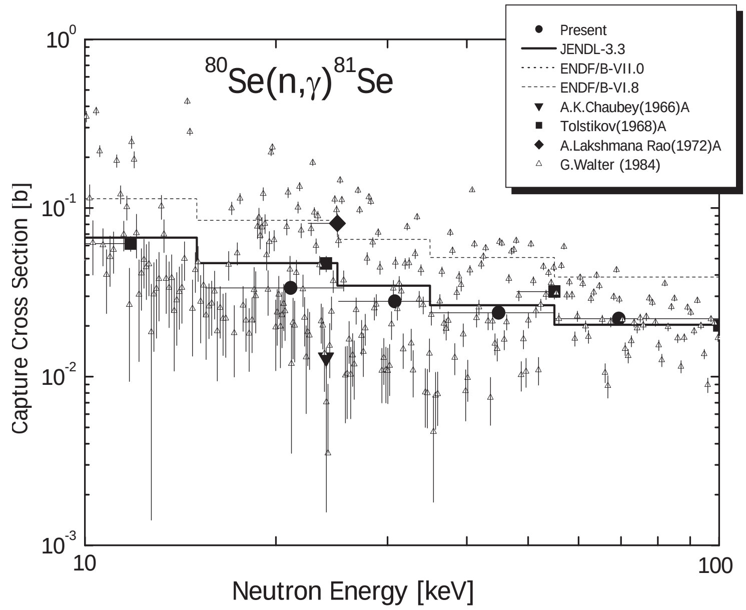

Fig.1 Neutron capture cross sections of ^{80}Se

The solid circles show the present results. Other measurements[5-8] and the evaluations of JENDL-3.3[9], ENDF/B-VI.8[10], and ENDF/B-VII.0[11] are compared with the present results. The evaluated values of ENDF/B-VII.0 are identical with those of JENDL-3.3 in this figure.

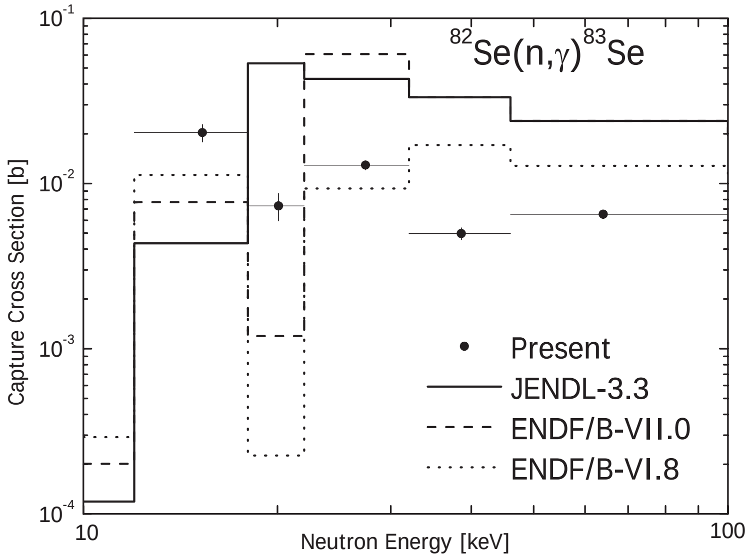

Fig.2 Neutron capture cross sections of ^{82}Se

The solid circles show the present results. The evaluations of JENDL-3.3[12], ENDF/B-VI[13], and ENDF/B-VII[14] are compared with the present results. The evaluated values of ENDF/B-VII.0 are identical with those of JENDL-3.3 above about 30 keV.

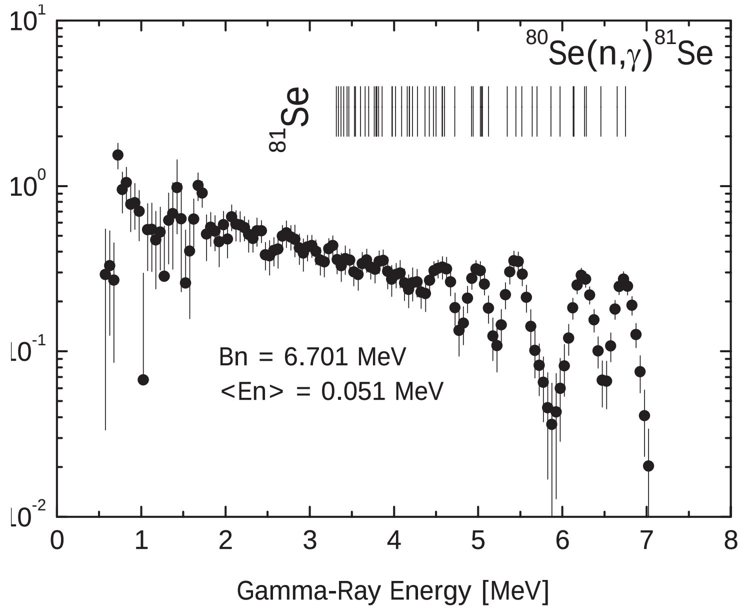

Fig.3 Neutron capture gamma-ray spectrum of ^{80}Se

The solid circles show the present spectrum. Low lying sates of ^{81}Se are shown in this figure, where the ground state is placed at 6.752 MeV (neutron binding energy of ^{81}Se, 6.701 MeV + average neutron energy, 0.051 MeV).

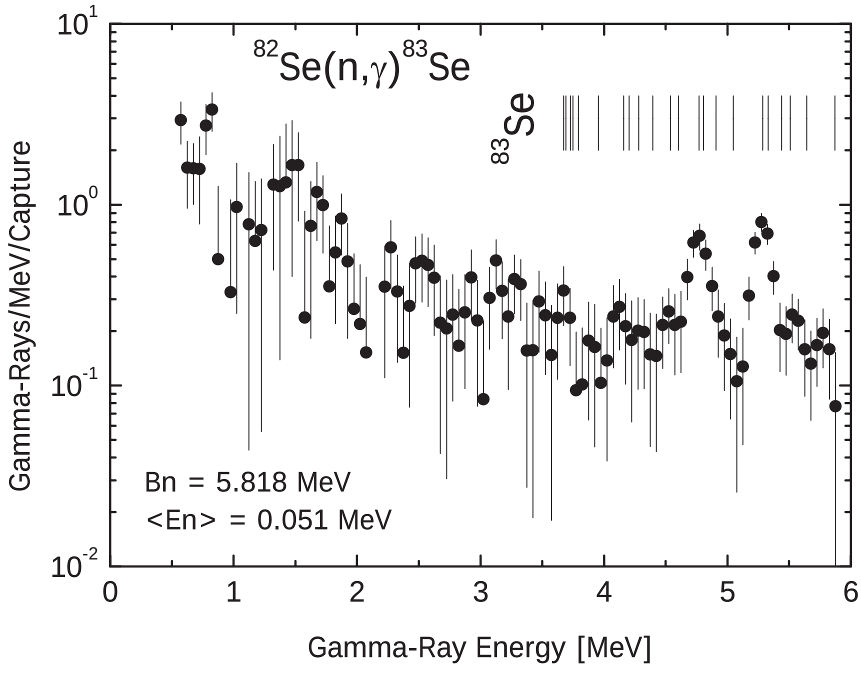

Fig.4 Neutron capture gamma-ray spectrum of ^{82}Se

The solid circles show the present spectrum. Low lying states of ^{83}Se are shown in this figure, where the ground state is placed at 5.869 MeV (neutron binding energy of ^{83}Se, 5.818 MeV + average neutron energy, 0.051 MeV).

4. Conclusion

The capture cross sections and capture gamma-ray spectra of ^{80,82}Se were measured in the incident neutron energy region from 10 to 100 keV, using a 1.5-ns pulsed neutron source by the ^{7}Li(p,n)^{7}Be reaction and the large anti-Compton NaI(Tl) gamma-ray spectrometer. A pulse-height weighting technique was applied to observed capture gamma-ray pulse-height spectra to obtain capture yields. The capture cross sections of ^{80,82}Se were derived with the error of about 5% and 5-20%, respectively, by using the standard capture cross sections of ^{197}Au. The present cross sections were compared with the previous experimental data and the evaluated values in JENDL-3.3, ENDF/B-VI.8, and ENDF/B-VII.0. The capture gamma-ray spectra of ^{80,82}Se were derived by unfolding the observed capture gamma-ray pulse-height spectra. The characteristic primary transitions from the capture states to low-lying states are observed.

Reference

1) T. Ohgama, Doctoral dissertation, Tokyo Institute of Technology, (2005).
2) R. L. Macklin and J. H. Gibbons, *Phys. Rev.*, **159**, 1007-1012 (1967).
3) ENDF/B-VII.0 data file for ^{197}Au(MAT=7925), evaluated by P.G. Young (2006).
4) H. Kendrick and S. M. Sperling, GA-9882 (1970).
5) A. K. Chaubey, Phys. Rev.,**152**, 1055-1061 (1965).
6) V. A. Tolstikov et al., Yaderno-Fizicheskie Issledovaniya Reports, **6**, 5 (1968).
7) A. Lakshamana Lao and J. Rama Rao, Phys. Rev. C6, 572-577 (1972).
8) G. Walter, Kernforschungszentrum Karlsruhe Reports No.3706, (1986).
9) JENDL-3.3 data file for ^{80}Se (MAT=3443), evaluated by JNDC FP NUCLEAR DATA W.G. (1990).
10) ENDF/B-VI data file for ^{80}Se (MAT=3443), evaluated by R.E.SCHENTER and F.SCHMITTROTH (1990).
11) ENDF/B-VII data file for ^{80}Se (MAT=3443), evaluated by JNDC FP Nuclear Data W.G. (1990).
12) JENDL-3.3 data file for ^{82}Se (MAT=3449), evaluated by JNDC FP NUCLEAR DATA W.G. (1990).
13) ENDF/B-VI data file for ^{82}Se (MAT=3449), evaluated by R.E.SCHENTER and F.SCHMITTROTH (1990).
14) ENDF/B-VII data file for ^{82}Se (MAT=3449), evaluated by JNDC FP Nuclear Data W.G. and S. F. Mughabghab (2005).

This is a blank page.

33. Analysis of the ^{7}Li (d, p) ^{8}Li reaction in the incident energy region below 10 MeV

Toru Murata
Former NAIG Nuclear Research Laboratory
e-mail : t.murata@ma.point.ne.jp

To investigate the reaction mechanism of the Li + d reaction, ^{8}Li production cross section and proton angular distributions of the $^{7}Li(d, p)^{8}Li$ reaction were analyzed with a combined model of resonance and direct reaction. Almost satisfactory agreement is obtained between analysis results and experimental data.

1. Introduction

Neutron irradiation tests are planned for the fusion materials using the Li(d, x n) reaction. Only a few experimental data are available for the Li(d, xn) reactions and to estimate the neutron production data such as cross sections, angular distributions and energy spectrum of neutrons, mechanism of the Li + d reactions should be studied. Activation cross sections of the ^{7}Li (d, p) ^{8}Li reaction were measured by many authors[1)] observing the beta-ray or delayed alpha-particles from the decay of ^{8}Li ($T_{1/2}$=838msec). The excited states above the second state of ^{8}Li are unstable by particle emissions, so the activity is mainly produced by the (d, p_0) and (d, p_1) reactions. Experimental angular distributions[2)] of the (d, p_0) reactions were also reported. Present analysis is made for these quantities using the combined model of resonance and direct reactions which was formerly adopted successfully to the analysis of the $^{24}Mg(t,p)^{26}Mg$ reaction[3)]..

2. Analysis method

The experimental ^{8}Li production cross section shows some resonance peaks below several MeV of incident deuteron energy E_d and angular distributions of emitted protons show anisotropy which seem to be predicted by direct reaction. So, these data will be analyzed with a combined model of resonance and direct reactions. Interaction time seems to be quite different between them and no interference was assumed for the reaction model.

Adopted resonance formula is obtained with the approximated R-matrix theory described formerly[3)] in the low energy region below Ed≈6 MeV. In the higher energy region, where no other resonance is assumed, extrapolated cross section with the resonance formula was corrected for the competition with other open channels besides the (d,p_0) and (d,p_1) reactions. The correction was made with the Hauser-Feshbach type statistical model using transmission coefficients.

Direct reaction cross section and angular distributions were calculated with DWBA code DWUCK4 developed by P.D.Kunz[4]. Optical model potential parameters were determined to reproduce the experimental cross sections and (d,p_0) angular distributions with the sum of the resonance and the DWBA reactions.

3. Analysis results

Obtained resonance parameters are given in Table 1. Present analysis corresponds to the excited states of ^{9}Be; Ex=17.3 ∽ 21.7 MeV. The lowest two resonance levels exactly correspond to the levels assigned in the Evaluated Nuclear Structure Data Files (ENSDF) of ^{9}Be [5]. For other resonance, listed levels in ENSDF are scarce and the correspondence is not clear. Present resonance energy and spin-party assignment for a level is only a candidate and not definite one.

Obtained optical potential parameters for DWUCK4 calculation are shown below, where E_d (in MeV) is incident deuteron energy in laboratory system.

Inc. deuteron real potential;

$V = 100\text{-}E_d$ MeV , a=0.68 fm, r_0=1.15 fm

Inc. deuteron imaginary potential;

$Ws = 13+E_d$ MeV, a=0.68 fm, r_0=1.15 fm

Using these parameters, angular distributions of elastically scattered deuterons by ^{7}Li were calculated with DWUCK4 code and compared with the experimental data by Abramovich et al.[6] in the energy range Ed=3-10 MeV. Agreement was not so good but moderately as is shown in Fig.1. For outgoing protons, optical potential given by F.G.Perey[7] was adopted.

Figure 2 shows the ^{8}Li production cross sections comparing analysis results with the experimental data[1]. Experimental data by Abramovich et al. were measured with beta–ray ($E_\beta^{max} \approx$ 13MeV) counting and multiplied by factor 1.26, which is the renormalization factor to the measurements by others with more reliable alpha particle ($E_\alpha \approx$1.5MeV) counting. The cross section by resonance reaction and that by direct reaction are also shown in the figure.

Figure 3 shows the angular distributions of emitted protons to the ground state analysis results compared with the experimental data. Angular distributions caused by the resonance reaction and those by the direct reaction are also shown. Each distribution is normalized to unity. Analysis results are weighted sum of resonance reaction distribution and direct reaction distribution. The weight of each distribution is the corresponding cross section value shown in Fig.2.

4. Conclusions

Experimental data of the ^{8}Li production cross section and angular distributions of protons emitted to ^{8}Li ground state by the ^{7}Li(d, p)^{8}Li reaction are almost satisfactory reproduced with the present combined model of resonance and direct reactions.

Neutron production by the ^{7}Li(d,xn) reactions are classified into the ^{7}Li(d,p)^{8}Li→^{7}Li+n,

^{7}Li(d,n)^{8}Be and ^{7}Li(d,α)^{5}He→^{4}He+n reactions in the present incident energy region. So, further studies should be made for the (d,n) and the (d,α) reactions, to estimate the neutron production nuclear data. For these reactions, resonance structures are clarified by the present study. For direct reaction, spectroscopic factors are key parameter for the absolute cross section calculation. Single particle width of transferred nucleon is given by DWUCK4 code, so, spectroscopic factors for the (d,p) and (d,n) reactions to the unbound states will be obtained using the resonance width of the ^{7}Li+n reaction or that of the ^{7}Li+p reactions, respectively. These resonance reactions also should be studied.

Thanks are due to Associate Professor Y. Watanabe (Kyushu.Univ.) for useful information and discussion about the present study.

References

(1) S.N.Abramovich et al. IZV.50,85(1986), A.E.Schilling et al. Nucl.Phys.A263,389 (1976), D.W.Mingay SAP.2,107(1976), L.Weissman et al. Nucl.Phys.A630,678 (1998)
(2) J.P.F.Sellschop, Phys.Rev.119,251(1960), J.P.F.Sellschop, D.W.Mingay, 62PADUA, 425(1963), A.J.Elwyn et al., Phys.Rev.C25,2168,(1982)
(3) T.Murata et al., J.Nucl.Sci.Technol.44,1484(2007).
(4) P.D.Kunz, "Distorted wave code DWUCK4", Univ. of Colorado (1974)
(5) G.H.Kelley et al., Nucl.Phys.A745,145(2004); ENSDF-Be9 (20004TI06)
(6) S.N.Abramovich et al. IZV.40,842(1976)
(7) F.G.Perey, Phys.Rev.131,745(1963)

Table 1 Resonance parameters to reproduce resonance part of ^{8}Li production cross section shown in Fig.1 (Ed: resonance energy, Ex: excitation energy of ^{9}Be, Γ_{tot}: total width, Γ_{d}: deuteron width, Γ_{p0}: proton width to the ground state, Γ_{p1}: proton width to the first excited state)

Ed(lab.MeV)	^{9}BeEx(MeV)	spin-parity	Γ_{tot} (keV)	$(\Gamma_d \cdot \Gamma_{p0})^{1/2}$ (keV)	$(\Gamma_d \cdot \Gamma_{p1})^{1/2}$ (keV)
0.780	17.301	5/2−	280	93.8	0
1.035	17.499	7/2+	80	13.4	0
1.60	17.94	7/2−	1600	347	0
1.65	17.98	9/2+	1500	371	0
1.78	18.08	11/2−	600	91.7	0
2.35	18.52	5/2+	600	38.7	140
2.89	18.94	7/2+	900	47.4	201
3.36	19.31	9/2−	800	303	77.5
4.60	20.27	11/2+	1500	687	86.7
6.50	21.74	13/2+	1500	374	8.8

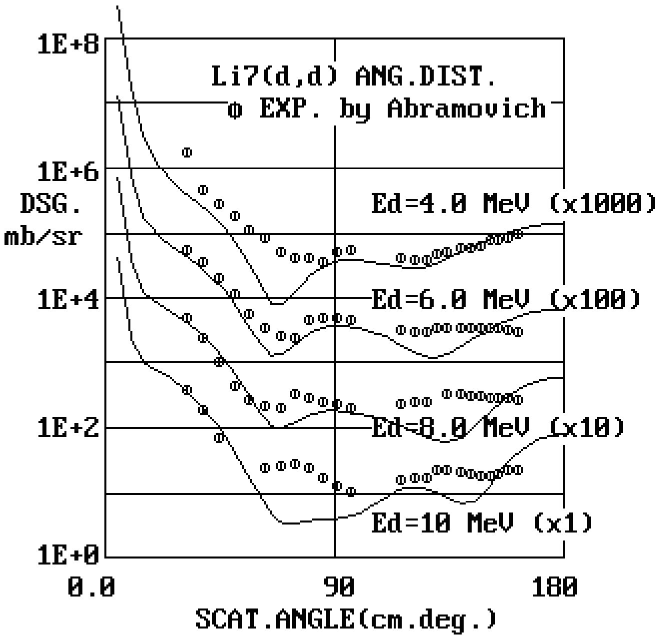

Fig.1 Comparison of experimental angular distributions[6] of deuterons elastic scattered from ^{7}Li with calculated results using the present optical potential parameters.

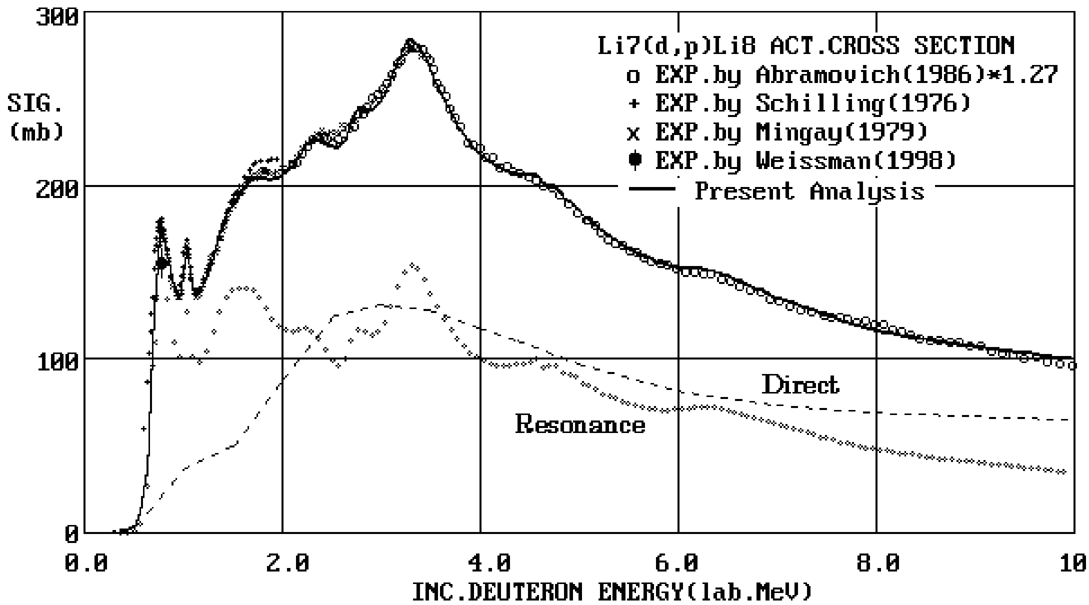

Fig.1 ^{7}Li(d,p)^{8}Li production cross section analysis results compared with the experimental cross sections[1]. Resonance reaction part and direct reaction part of the analysis are shown.

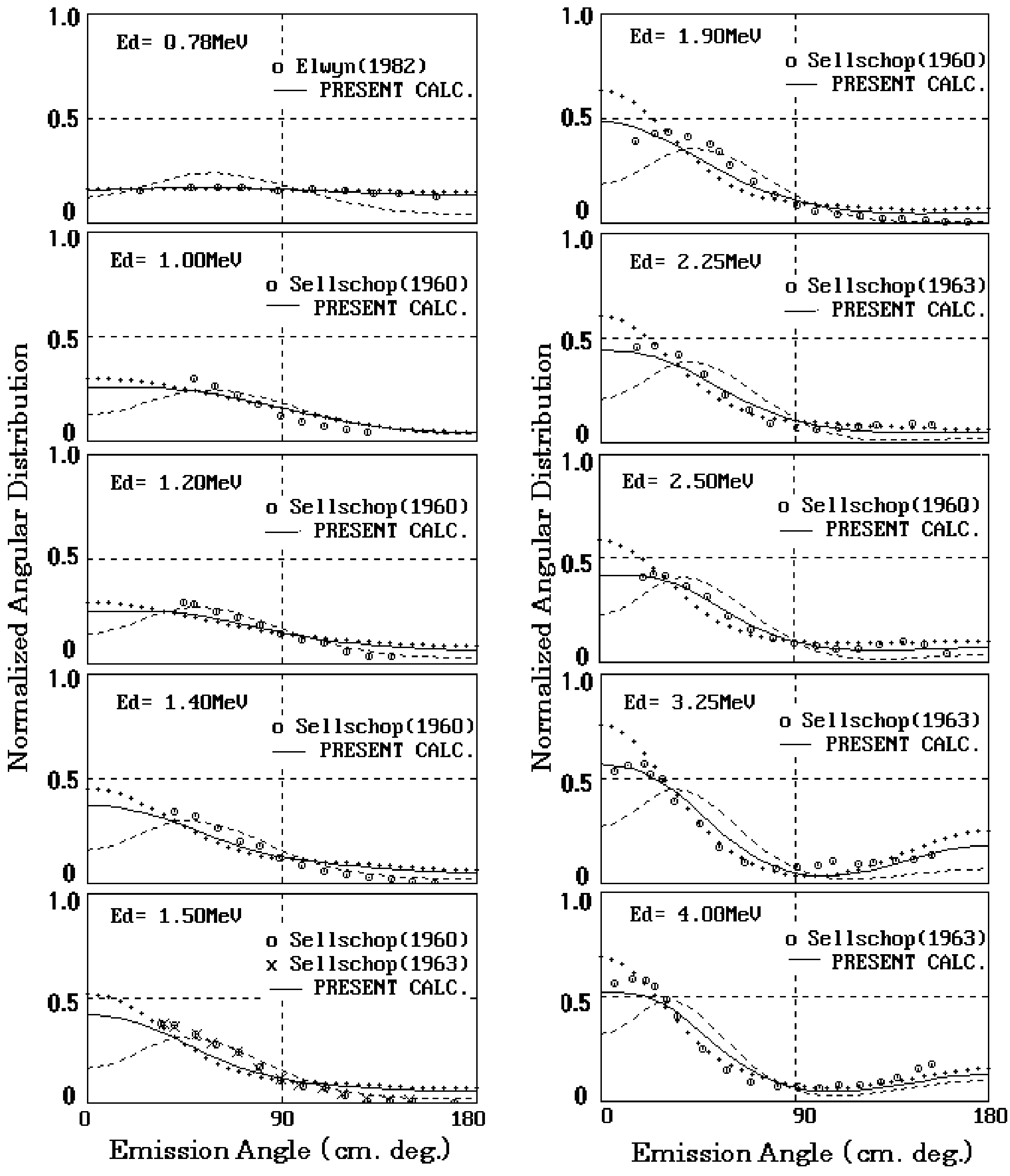

Fig.2 Angular distributions of emitted protons by the ^{7}Li(d,p$_0$)^{8}Li reaction. Experimental data[2)] (open circles), analysis results (solid lines), resonance reaction (dotted lines) and direct reaction (dashed lines) are normalized respectively.

34. Measurement of light charged particle production double-differential cross sections for 360- and 500-MeV proton induced reactions

H. IWAMOTO*, Y. KOBA, M. IMAMURA, Y. FUKUI, Y. FUKUDA, K. KIYOHARA, M. UEYAMA, G. WAKABAYASHI, and Y. UOZUMI
Department of Applied Quantum Physics and Nuclear Engineering, Kyushu University
Motooka 744, Nishi-ku, Fukuoka 819-0395, Japan
*e-mail: iwamotoh@nucl.kyushu-u.ac.jp

P. EVTOUKHOVITCH, V. KALINIKOV, N. KHOMUTOV, N. KUCHINSKIY, G. MACHARASVILI, D. MJAVIA, A. MOISEENKO, A. MOLOKANOV, A. MZAVIA, and V. SAMOILOV
Joint Institute for Nuclear Research, Dubna 141980, Russia

M. NAKANO
University of Occupational and Environmental Health, Kitakyushu 807-8555, Japan

We measured light charged particle production double-differential cross sections for 360- and 500-MeV protons on ^{232}Th. Particle energies were measured with the ΔE-E method at laboratory angles of 20°, 40°, 70°, and 105°. In the present article, detailed experimental setup, procedure of data analysis, and preliminary results are presented.

1. Introduction

The accelerator driven system (ADS) has been recognized as one of the most attractive options for the nuclear transmutation of high level nuclear waste. One may expect ADS to reduce a hazard level of the waste dramatically, and to operate as an energy generator. To realize ADS, it is necessary to conduct various areas of fundamental researches and technical developments. Double-differential cross section (DDX) data of nucleon-actinide reactions are very important for the nuclear waste transmutation facilitated by ADS. Since charged particle emission data are strongly required as well as neutron data up to several GeV, we plan to conduct light charged particle (LCP) measurements with typical actinide targets.

In the present experiment, we measured double-differential cross sections of light charged particle productions for 360- and 500-MeV proton induced reactions on thorium (^{232}Th) at the PHASOTRON facility of the Joint Institute for Nuclear Research (JINR) in Russia.

2. Experiment

The experiment was carried out at the PHASOTRON facility. The experimental setup is shown schematically in Fig. 1. Self-supporting target in a vacuum chamber of 400-mm outer diameter was bombarded with 360- and 500-MeV proton beams from PHASOTRON with a beam current of approximately 5 μA. The beam spot on the target was approximately 13 mm in diameter. Target used in this experiment was 77-μm-thick ^{232}Th. LCPs emitted from nuclear reactions were detected by ΔE-E spectrometers. For energy calibration, the elastic proton-proton scattering experiment was also carried out using a polyethylene target.

As seen in Fig. 1, we used two different types of spectrometers. They were positioned on the opposite side with respect to the beam axis in the same reaction plane. The right-side one (high-energy module) was comprised of two plastic scintilators (3 mm thick and 5 mm thick) and a BGO scintillator (60 mm in diameter and 200 mm long for 20° and 160 mm long for 40°, 70°, and 105°) connected with photomultiplier tubes (PMTs). The left-side one (low-energy module) consisted of two silicon layer (50 μm thick and either 2000 μm thick for 105° or 300 μm thick for 20°, 40°, and 70°) and two scintillation counters, a cubic CsI(Tl) (40 mm long) scintillator and a plate plastic scintillator (5 mm thick), connected with PMTs. Detailed construction of the spectrometers are illustrated in Fig. 2. The four identical detectors of each side were placed at laboratory angles of 20°, 40°, 70°, and 105° with respect to the beam axis.

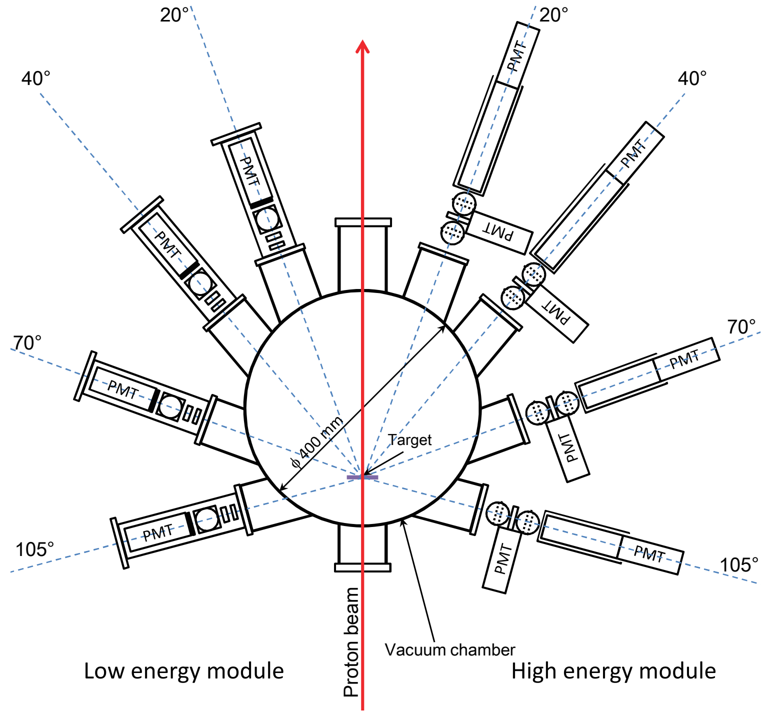

Fig. 1: Schematic view of the experimental setup.

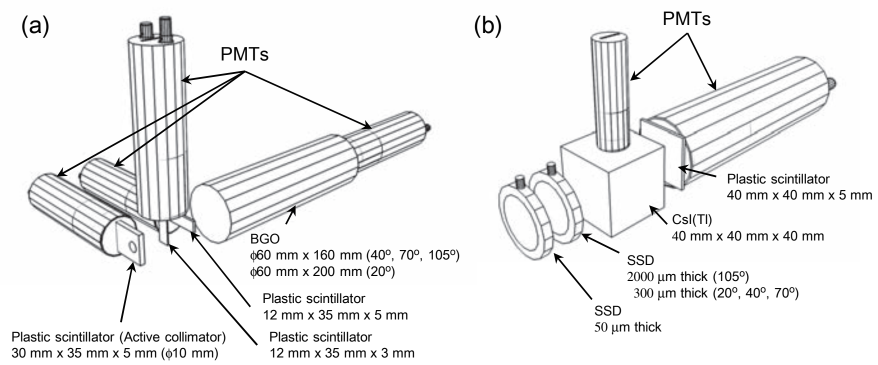

Fig. 2: Layout of the spectrometers. (a) high-energy module, (b) low-energy module.

3. Data Analysis

Data analysis procedure is basically same as Ref. [1, 2]. ADC channels of the experimental raw data were calibrated into energies deposited in the scintillators by the light response function and the elastic scattering peak of the polyethylene target. The light response of BGO is given by the following power law expression,

$$L(Z, A, E) = a_1(Z, A)E^{a_2(Z,A)}, \tag{1}$$

where $a_1(Z, A)$ and $a_2(Z, A)$ is fitting parameters. The systematics of these parameters were taken from Ref. [3]. In Ref. [3], the response function for CsI(Tl) is expressed as

$$L = \int \mathrm{d}x\, c_\alpha K \frac{\alpha K(\mathrm{d}E/\mathrm{d}x)}{1 + \alpha K(\mathrm{d}E/\mathrm{d}x) - \beta(\alpha K \mathrm{d}E/\mathrm{d}x)^2}, \tag{2}$$

where c_α, αK, and β are fitting parameters.

In order to identify different particles (protons and deuterons), the PI technique was used. The particle identification quantity, PI, is given by

$$\mathrm{PI} = E^b_{\mathrm{total}} - (E_{\mathrm{total}} - \Delta E)^b, \tag{3}$$

where E_{total} is the total energy deposited in the spectrometer, ΔE is the energy deposited in the ΔE detectors, and b denotes the parameter representing the range of each particle. In this study, $b = 1.73$ was employed. Deposit energy calculation was performed by the Bethe-Bloch equation. As an example of the particle identification, The two-dimensional plot of PI versus E_{total} at 40° for the reaction ^{232}Th(p, xp') at $E = 360$ MeV is shown in Fig. 3

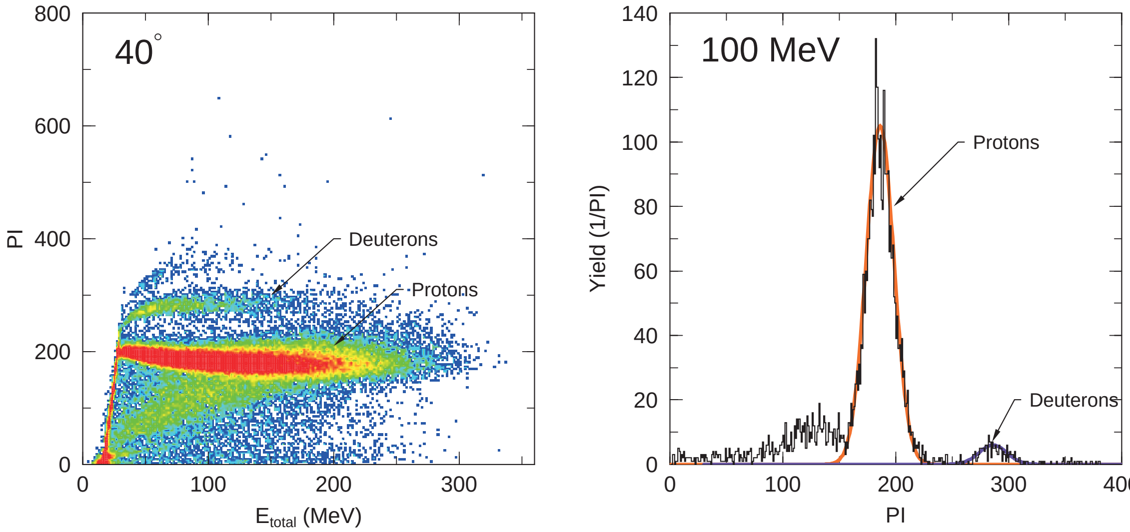

Fig. 3: Left panel: Two-dimensional plot of PI versus E_{tot} at 40° for the 360-MeV p+^{232}Th reaction. Protons and deuterons are clearly separated. Right panel: PI projection spectrum at $E_{tot} = 100$ MeV.

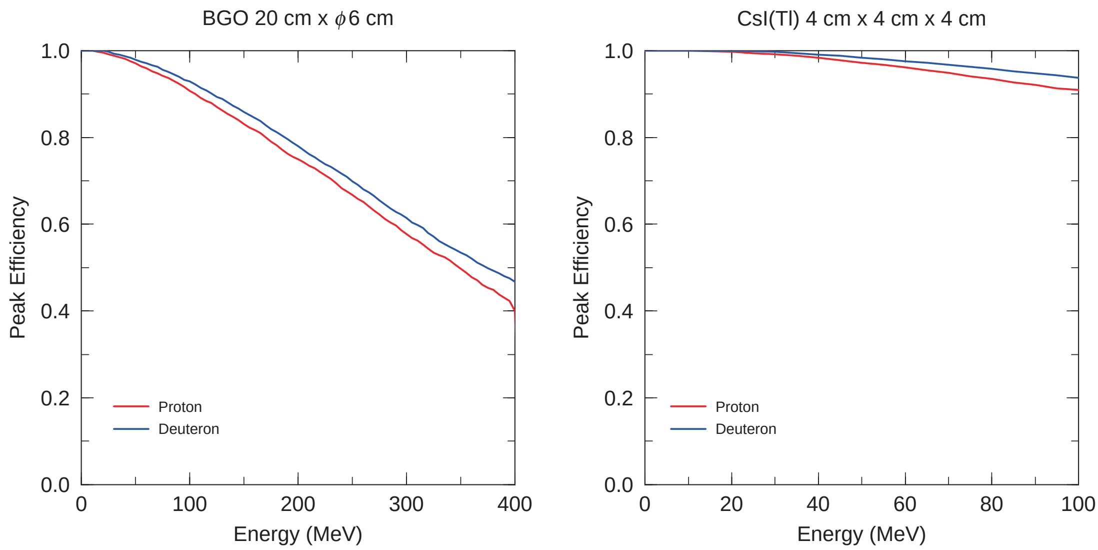

Fig. 4: Peak efficiency of the BGO (left) and CsI(Tl) (right) crystals calculated by the PHITS code

The double-differential cross sections were obtained by the following way. First, PI projection spectra were generated for each energy bin of a 10-MeV width. Next, the proton and deuteron events were counted up for each spectral peak by performing Gauss fitting (See the right panel of Fig. 3). The number of proton and deuteron events was corrected in terms of the peak efficiency. In the present analysis, proton and deuteron peak efficiencies of the BGO and CsI(Tl) scintillators were obtained from simulation results of the PHITS [4] code. In the simulation, the scintillator was included along with their precise dimensions, and monochromatic proton/deuteron beams up to 500 MeV bombarded the center of the scintillators in consideration of Coulomb diffusion. In this calculation, we set the default value for the

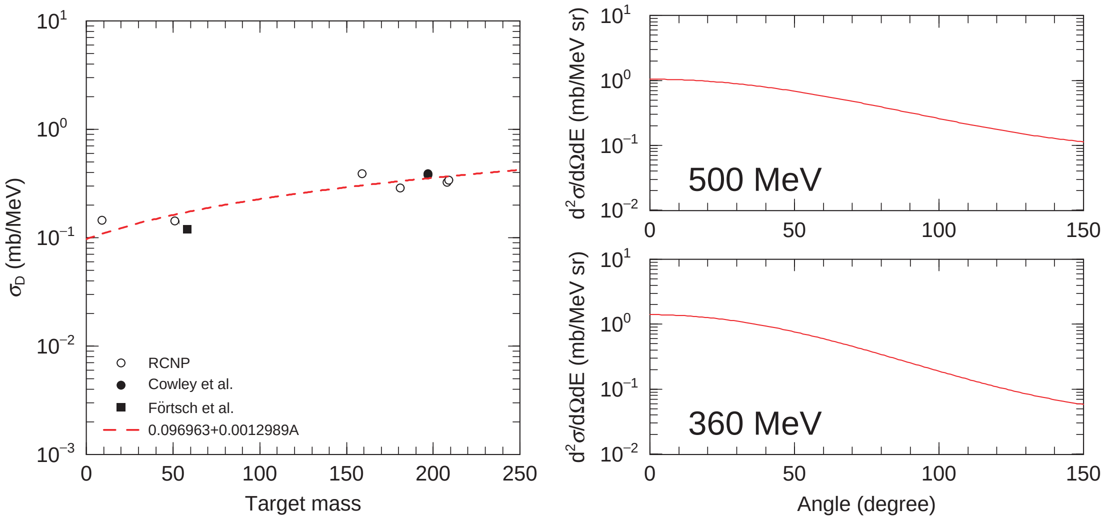

Fig. 5: Left panel: Mass dependence of the normalization factor σ_D of Eq. (5) at emission energy $E_{p'} = 105$ MeV. The data are taken from Refs [7, 8] and our previous experimental data [9]. Circles represent σ_D of ^{9}Be, ^{51}V, ^{159}Tb, ^{181}Ta, ^{197}Au, ^{208}Pb, and ^{209}Bi. Solid circle and square show that of ^{58}Nb and ^{197}Au, respectively. The dashed line is a linear fit to the experimental data. Right panel: DDXs estimated with the Kalbach systematics [Eq. (6)] with $\sigma_D = 0.398$ mb/MeV at emission energy $E_{p'} = 105$ MeV for the 500-MeV (upper) and 360-MeV (bottom) proton induced reactions on ^{232}Th.

proton-nucleus and deuteron-nucleus reactions (JQMD [5] and NASA formula for deuteron). The calculation results are shown in Fig. 4.

Finally, we determined the double-differential cross sections for each energy bin, which are given by

$$\frac{\mathrm{d}^2\sigma}{\mathrm{d}\Omega\mathrm{d}E} = \frac{Y}{PS_t\phi\Delta\Omega\Delta E}, \tag{4}$$

where ΔE and $\Delta\Omega$ are the bin size of the energy and the solid angle of the spectrometers, respectively. P is the peak efficiency mentioned above, S_t is the surface density of the target, Y is the yield per ΔE at the detection angle of interest, and ϕ is the number of incident protons.

Since we could not obtain the number of incident protons, we determined magnitude of the DDXs by use of the Kalbach systematics. The form for the MSD part of the angular distributions is given by

$$\frac{\mathrm{d}^2\sigma}{\mathrm{d}\Omega\mathrm{d}E} = \sigma_D \frac{a}{\sinh a} \exp(a\cos\theta), \tag{5}$$

where θ is the emission angle, σ_D is a normalization factor related to the angle-integrated cross sections as a function of emission energy, and a denotes the slope parameter as a function of the ratio of emission energy to incident energy, which has been parametrized by Kalbach [6]. According to Refs. [7, 8], the quantity of σ_D is independent of incident energy. We, therefore, estimated the factor σ_D of DDXs for the the 500-MeV and 360-MeV proton induced reactions on ^{232}Th by using our previous data of 392-MeV (p, xp') reactions on ^{9}Be, ^{51}V, ^{159}Tb, ^{181}Ta, ^{197}Au, ^{208}Pb, and ^{209}Bi [9]. The left part of Fig. 5 shows mass dependence of the normalization factor σ_D of Eq. (5) at emission energy $E_{p'} = 105$ MeV. A fit to the experimental data is displayed with a dashed line as a function of target mass number A. From this figure, σ_D at $A = 232$ was found to be 0.398 mb/MeV.

Magnitude of DDX for ^{232}Th target was assumed to be given by

$$\begin{aligned} &\mathrm{DDX}(E_{p'}, \theta = \theta_0) \\ &= \frac{Y(E_{p'}, \theta = \theta_0)}{Y(E_{p'} = 105\,\mathrm{MeV}, \theta = \theta_0)} \cdot \mathrm{DDX}_{\mathrm{Kalbach}}(E_{p'} = 105\,\mathrm{MeV}, \theta = \theta_0), \qquad \theta_0 = 20^\circ, 40^\circ, 70^\circ, \text{and } 105^\circ, \end{aligned} \tag{6}$$

where $E_{p'}$ denotes the proton energy and θ is the detection angles. Y is the proton yield corrected by the peak efficiency in a certain energy bin at the detection angle θ_0. $\mathrm{DDX}_{\mathrm{Kalbach}}$ shows magnitude of DDX at $E_{p'} = 105$ MeV and $\theta = \theta_0$ ($\theta_0 = 20^\circ, 40^\circ, 70^\circ$, and 105°) calculated with the Kalbach systematics with $\sigma_D = 0.398$ mb/MeV.

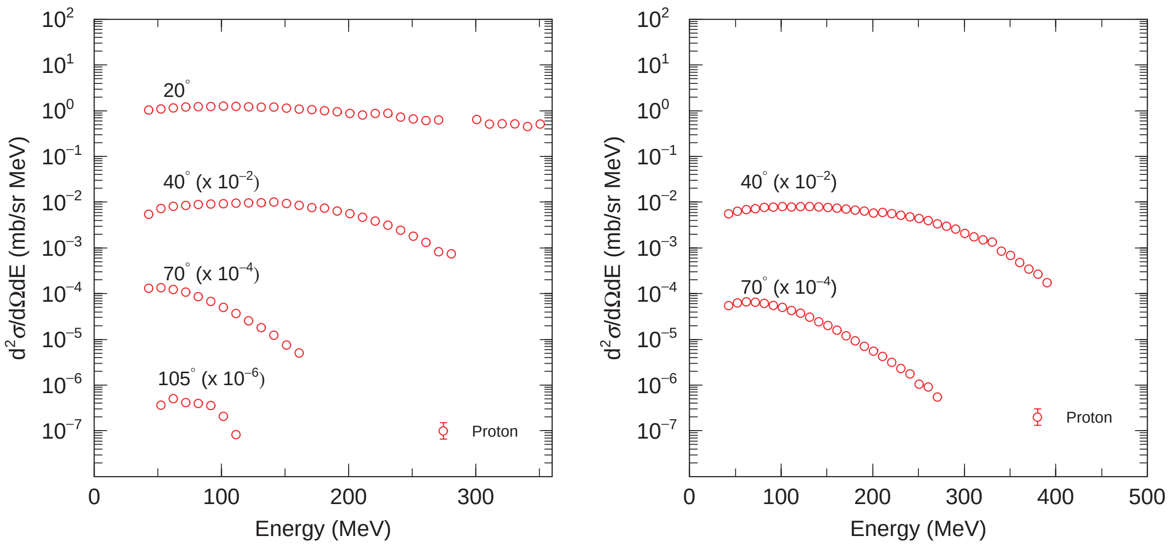

Fig. 6: Preliminary results of the measured DDXs for the 360- (left panel) and 500-MeV (right panel) proton induced reactions on ^{232}Th.

Figure 6 shows the measured DDXs for the 360- and 500-MeV p+^{232}Th reactions obtained by the high-energy module. Here the error bar shows only the statistical uncertainty. The present measured spectra have overall similar features to those of Ref. [1]. However, we should mention here that since these are preliminary experimental results, an additional experiment should be performed and the present results of DDXs should be revised.

4. Summary and conclusions

We measured light charged particle production double-differential cross sections for 360- and 500-MeV protons on the ^{232}Th target. Particle energies were measured with the ΔE-E method at laboratory angles of 20°, 40°, 70°, and 105°. In the present article, the experimental procedure and preliminary results were presented. As mentioned above, more detailed analysis and an additional experiment should be performed in order to obtain reliable data. Finally, our experimental results will be compared with the theoretical model calculations (i.e., INC and QMD).

Acknowledgements

This study was carried out under the ISTC Project #3495. The authors would like to thank the PHASOTRON crews for their assistance in the experiment. This work was supported by Grant-in-Aid for Japan Society for the Promotion of Science (JSPS) fellows.

References

[1] T. Kin, F. Saiho, S. Hohara, K. Ikeda, K. Ichikawa, Y. Yamashita, M. Imamura, G. Wakabayashi, N. Ikeda, Y. Uozumi, M. Matoba, M. Nakano, and N. Koori, *Phys. Rev*, **C72**, 014606 (2005).

[2] Y. Uozumi, P. Evtoukhovitch, H. Fukuda, M. Imamura, H. Iwamoto, V. Kalinikov, W. Kallies, N. Khumutov, T. Kin, N. Koba, Y. Koba, N. Kuchinski, A. Moisenko, D. Mzavia, M. Nakano, V. Samoilov, Z. Tsamalaidze, G. Wakabayashi, Y. Yamashita, *Nucl. Instr. and Meth. A*, **571**, 743 (2007).

[3] V. Avdeichikov, B. Jakobsson, V.A. Nikitin, P.V. Nomokonov, and A. Wagner, *Nucl. Instr. and Meth. A*, **484**, 251 (2002).

[4] H. Iwase, K. Niita, and T. Nakamura, *J. Nucl. Sci. Technol.*, **39**, 1142 (2002).

[5] K. Niita, S. Chiba, T. Maruyama, T. Maruyama, H. Takada, T. Fukahori, Y. Nakahara, and A. Iwamoto, *Phys. Rev.*, **C52**, 2620 (1995).

[6] C. Kalbach, *Phys. Rev.*, **C37**, 2350 (1988).

[7] A.A Cowley, S.V Förtsch, J.J. Lawrie, D.M. Whittal, F.D. Smit, and J.V. Pilcher *Z. Phys. A – Atomic Nuclei*, **336**, 189 (1990).

[8] S.V Förtsch, A.A. Cowley, J.J. Lawrie, D.M. Whittal, J.V. Pilcher, and F.D. Smit, *Phys. Rev.*, **C43**, 691 (1991).

[9] H. Iwamoto, M. Imamura, Y. Koba, Y. Fukui, G. Wakabayashi, Y. Uozumi, T. Kin, Y. Iwamoto, S. Hohara, and M. Nakano, in preperation.

35. Neutron flux measurement by means of multi-foil activation method in Be and Be/Li_2TiO_3 experiments with DT neutrons

Y. Tatebe[1)], K.Ochiai[2)], K. Kondo[2)], K.Takakura[2)], C.Konno[2)], S. Sato[2)], S.Ohnishi[2)], S. Yoshida[1)]

1. Tokai University, Kitakaname 1117, Hiratsuka-shi, Kanagawa, Japan
2. Japan Atomic Energy Agency, Shirakata-Shirane 2-4, Tokai-mura, Naka-gun, Ibaraki, Japan.

Abstract

In order to measure the neutron flux in ITER/TBM, we have proposed a multi-foil activation method. We examined the applicability of this method to ITER/TBM through some fundamental experiments with the DT neutron source at JAEA/FNS.

1. Background and objective

Nuclear performances of the ITER Test Blanket Module (TBM) can be calculated with a neutron transport code and nuclear data library. Neutron flux spectra in the TBM should be measured in order to validate the calculated nuclear performances of the TBM. The multi-foil activation method (MFAM) is considered to be one of the most prospective candidates for the neutron flux spectrum measurement because it is applicable in high temperature and magnetic field like TBM. In order to clarify problems on the application of MFAM to the neutron flux spectrum measurement in ITER-TBM, we have measured neutron flux spectra in TBM simulating assemblies with a DT neutron source by using MFAM.

2. Experiment

2.1 Experimental aseemblies

The experiments have been performed at the Fusion Neutronics Source (FNS) facility of Japan Atomic Energy Agency. Beryllium and Be/Li_2TiO_3 assemblies simulating ITER-TBM were used for the experiments. Reaction rates of some kinds of reactions were measured in the assemblies. Figure 1 shows the cross sectional views of experimental assemblies for the MFAM experiment. Beryllium is one of the most important materials on the TBM and characteristic nuclear performance of beryllium was reported. Therefore, we first tied to measure the neutron spectrum in the beryllium assembly. Second, we measured neutron spectrum in Be/Li_2TiO_3 assembly simulated TBM. The assemblies consisted of beryllium block, ^{6}Li(40%)-enriched Li_2TiO_3 ceramic tile and stainless steel assembly. Al, Ni, Zr, Nb, In and Au foils were selected as the multi-activation foil. ^{27}Al(n,α)^{24}Na, ^{48}Ti(n, ^{58}Ni(n,p)^{58}Co, ^{90}Zr(n,2n)^{89}Zr, ^{93}Nb(n,2n)^{92m}Nb ^{115}In(n,n')^{115m}In and ^{197}Au(n,γ)^{198}Au reactions with a germanium detector, and each reaction rates were deduced.

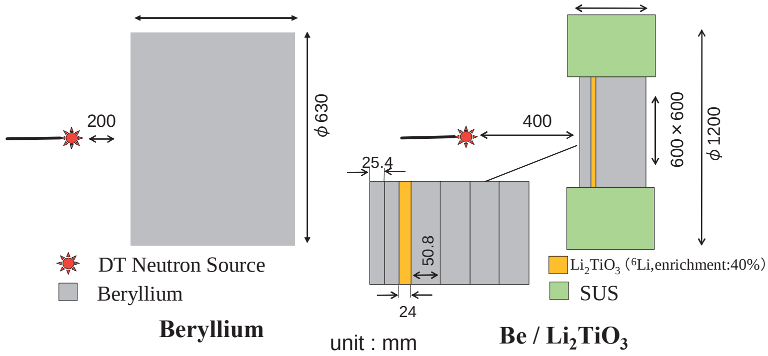

Figure 1 Cross sectional views of assemblies of MFAM experiment

2.2 Analysis

The neutron flux was estimated with the measured reaction rates and an initial guess neutron flux. The initial guess neutron flux was calculated with Monte Carlo calculation code (MCNP4C) and a nuclear data library (FENDL-2.1) [1]. JENDL Dosimetry file 99 [2] was also used as the response function of the reaction rates (see Fig.2). An unfolding code, SAND-II, [3] was used to adjust neutron flux spectra. Initial guessed neutron flux spectra were calculated with a Monte Carlo code MCNP4C and the nuclear data library FENDL-2.1. JENDL Dosimetry File 99 was adopted as response data for reaction rates. The neutron energy was segmented into 199 Groups based on VITAMIN-B6. The SAND-II unfolding code and JENDL Dosimetry File 99 (641 groups) were used for the spectrum estimation. The cross sections of 641 groups were converted to those of 199 groups with CS tape provided in SAND-II. We deduced neutron flux spectra in the simulated assemblies with the MFAM. The results indicated that the adjusted neutron flux was reasonable for fast neutrons and that measured reaction rate data of more (n,γ) reactions were necessary for more adequate adjustment for slow neutrons.

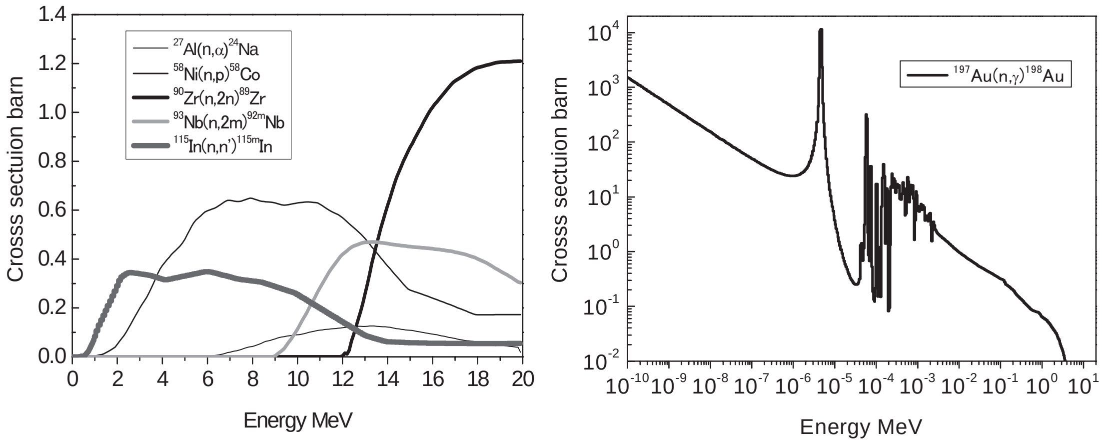

Figure 2 JENDL dosimetry 99 used for MFAM experiments.

3. Results and discussion

Figure 3 shows the initial and adjusted neutron fluxes at the point of 101.6 mm depth in the beryllium assembly and 25.4 mm depth in Be/Li_2TiO_3 assembly, respectively. The above mentioned point in beryllium fully makes the energy of DT neutron moderated and forms tailed neutron spectrum. On the other hands, in case of in Be/Li_2TiO_3 assembly, because the point of 25.4 mm is not so sufficient depth and the neutron absorber, enriched Li_2TiO_3, exists near the measuring point, the spectrum has no thermal peak. Figure 4 and Figure 5 show the ratio of calculated reaction rate and experimental one in beryllium assembly and Be/Li_2TiO_3 assembly. Moreover, in figures, we also show the ratios of calculated reaction rates and reaction rates modified with the adjusted neutron spectra. From the measurement and the spectrum adjustment in the beryllium assembly, we obtained the energy spectrum of neutron flux in the energy range between near thermal energy and about 14 MeV. Especially, the ratio between calculated reaction rate of ^{197}Au(n,γ)^{198}Au and experimental one (C/E) was near 1.2 and the estimated neutron flux below 1 eV showed to reflect the C/E.

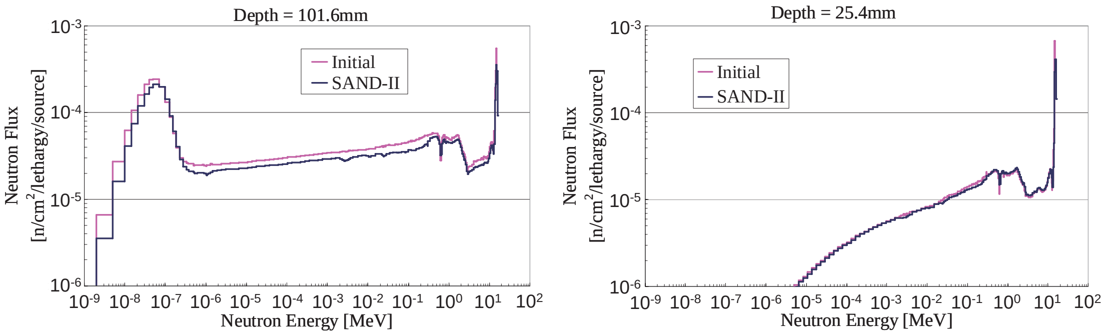

Figure 3 Initial and adjusted neutron fluxes at the point of 101.6 mm depth in the beryllium assembly and 25.4 mm depth in Be/Li_2TiO_3 assembly

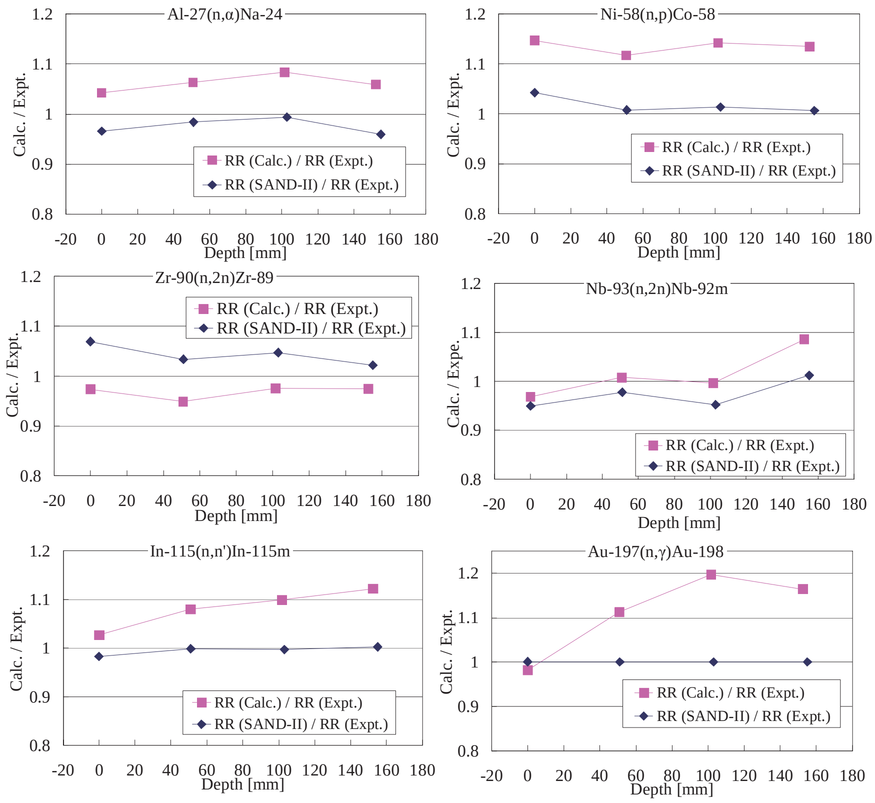

Figure 4 Ratios (Calc./Expr.) of calculated reaction rate and experimental one at measuring points in beryllium assembly and ratios of calculated reaction rates and modified with adjusted neutron spectra.

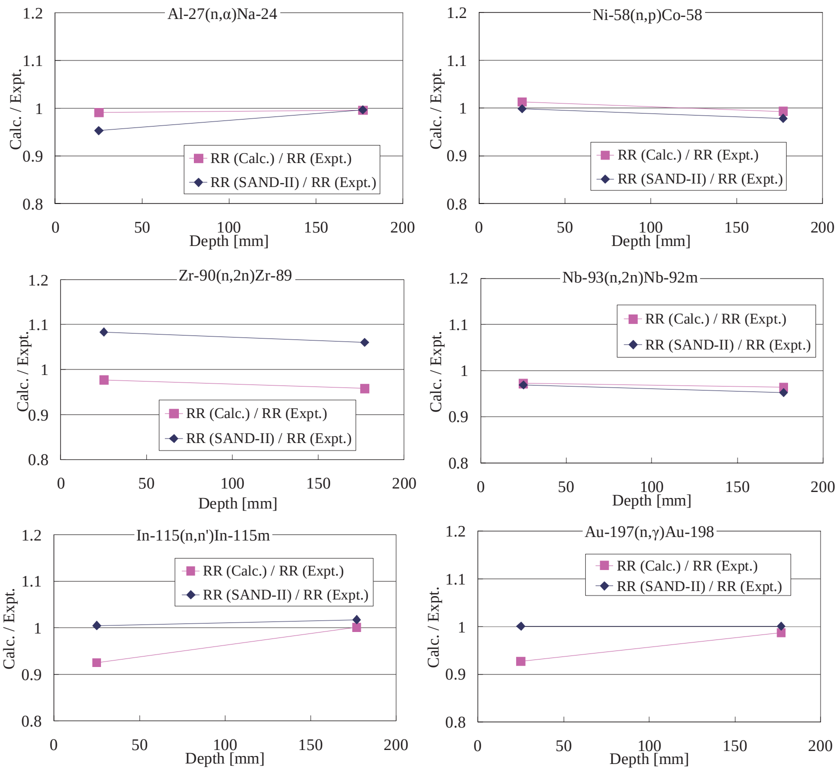

Figure 5 Ratios (Calc./Expr.) of calculated reaction rate and experimental one at measuring points in Be/Li_2TiO_3 assembly and ratios of calculated reaction rates and modified with adjusted neutron spectra.

4. Summary

We have carried out the fusion neutron flux measurement by means of multi-foil activation method in some experiments with DT neutrons and shown the characters of the method.

From the comparisons of reaction rates, it was shown that the method was effective to evaluate neutron spectrum. However, the spectrum at the energy range around 14 MeV has somewhat inadequacies.

References

[1] FENDL-2.1 （ http://www-nds.iaea.org/fendl21/）

[2] K.Kobayashi , et al. “JENDL Dosimetry File 99 (JENDL/D-99)”,JAERI 1344 （2002）

[3] McElroy, W.N. et al.; "A computer automated iterative method forneutron flux spectra determination by foil activation"Vol I - IV. Report AFWL-TR-67-41 (1967).

This is a blank page.

36. Pandemonium Problem in FP Decay Heat Calculations and its Solution

Naoto HAGURA, Tadashi YOSHIDA
Musashi Institute of Technology, Tamazutsumi 1-28-1, Setagaya-ku, Tokyo 158-8557, Japan
E-mail: g0791802@sc.musashi-tech.ac.jp

In calculating the fission product decay heat, we have to pay attention to the so-called pandemonium problem. Total Absorption Gamma-ray Spectrometer method (TAGS) is expected to be free from this problem at least ideally. A new series of TAGS measurements is being performed by a European group and their first results for Tc-104 and -105 became available quite recently. Introducing the old and new TAGS data, we calculated and analyzed the FP decay heat for Pu-239 in the cooling time range from 1 to 10,000 s. Our result showed the significance of TAGS data to improve the FP decay heat only with experimentally obtained decay data without introducing any nuclear theory.

1. Introduction

In calculating the fission product (FP) decay heat, we have to pay attention to the so-called pandemonium problem[1], which is the missing of the β-strengths in the high-energy region of the daughter nucleus in the published decay schemes of high Q-valued short-lived isotopes. In the case of JENDL (more exactly JENDL FP Decay Data File 2000) and ENDF/B-VI, the gross theory of beta decay was applied to circumvent this problem and lead to a good agreement between calculation and measurement[2]. On the other hand, JEFF-3.1 does not introduce any theoretical correction, and it is composed only of the experimental data.

In 1990's, TAGS (Total Absorption Gamma-ray Spectrometer) method, which is, at least ideally, free from the missing of high-level β-feeding, was applied to measure the β-strength of dozens of FP nuclides by a Idaho group[3]. For introducing TAGS data into the summation calculations, the average beta- and gamma-ray energies par decay (E_β, E_γ), which are prepared in existing libraries, are replaced by the TAGS-origin values. As a result, JEFF-3.1 becomes more consistent with sample-irradiation measurements, though the result based on JENDL are suffering from a deviation from these measurements.

2. TAGS measurements activity

One of the most important properties of the TAGS measurement is expected to be pandemonium-problem free. In this respect, the TAGS measurement is anticipated to provide a solid basis of the summation calculations for us.

In the early 1990's, a series of TAGS measurements was performed at INEL (Idaho National Engineering Laboratory) for 48 FP nuclides that is including 3 meta-stable state nuclides (hereafter US-TAGS)[3]. The INEL group, however, terminated their TAGS activity in the end of 1990's, then, we can no longer expect the relevant new data from the U.S. nowadays. Fortunately enough, however, a European group started a new collaboration effort, in which the TAGS technique is fully employed in measuring the *β*-strength functions of FP region nuclides. Their first results for Tc-104 and -105 were released[4] in 2008. The raw experimental data of Tc-102 is now under analysis, and the measurement of other important nuclides is expected to be carried out in due course.

3. Results and Consideration

3.1 New TAGS data from the European group

The first results by the European group became available quite recently[4] and they are summarized in Table

1 and 2. In Table 2, the row (a) stands for a case where the feeding of 9% to the ground state of the daughter nucleus Ru-105 is supposed, and for (b) the feeding to the ground state was fixed to zero. The difference between these sets of energy values is not so large. It is easy to see that the new TAGS data gives smaller E_β and larger E_γ in comparison with the existing library values. This fact suggests explicitly that the library values are suffering from the effect of pandemonium problem.

Table 1 Average beta- and gamma-ray energy for Tc-104

(all in keV)	E_β	E_γ
New Data	931	3229
JENDL	1403	2240
JEFF-3.1	1560	1890

Table 2 Average beta- and gamma-ray energy for Tc-105

(all in keV)	E_β	E_γ
New Data (a)	764	1825
New Data (b)	684	1999
JENDL	1310	790
JEFF-3.1	1310	668

3.2 Introduction of New data into Summation Calculation

Figure 1 shows the γ-ray component of the FP decay heat after a fission burst in Pu-239 calculated with JENDL (solid curve) and with JEFF-3.1 (dotted curve), respectively. Here (a) shows the calculated results based on the original data in the libraries without any modification, and (b) shows the calculations in which the E_β and E_γ values are replaced by the TAGS values reduced[5] from the measured data by the Idaho group[3]. Case (c) shows the curves in which the library values are replaced by the new TAGS data measured by the European group[4]. Case (d) provides the results after introducing all the TAGS data up to now, namely the Idaho and the European data.

As we have seen in Fig. 1 (a), the curve of JENDL is in good agreement with experimental data except around 1,000 s (indicated by broken circle). On this disagreement it was argued that the E_γ values of technetium isotopes would be responsible for it.[5,6] On the other hand, JEFF-3.1 seriously underestimates the integral experiments at Tokyo University[7] and Oak Ridge[8] from 5 to 5,000 s. This discrepancy is presumably caused by the effect of pandemonium problem. Introduction of US-TAGS into each library improves the behavior of JEFF-3.1, because the TAGS method provides the decay data free from the pandemonium problem. The US-TAGS data, however, do not include technetium isotopes mentioned above. The persistent disagreement between the experimental and the calculated values around 1,000 s is resolved only by introducing the E_γ values from the latest European measurement[4] (dotted circle in (C)). This fact confirms the result reported[6] on the basis of the preliminary results for Tc-104 and -105 by Algora et al.[9,10] and strongly indicates again that the TAGS measurement is essentially the only way to overcome the pandemonium problem experimentally.[11] In this point of view, appropriateness of the priority list[12] of nuclides that should be measured by the TAGS was clearly confirmed.

The curve of JEFF-3.1 changes for the better from Fig. 1 (a) to (d). On the contrary, the curve of JENDL is pushed out up from the area of experimental plots. The reason why JENDL become worse in its agreement with the integral experiments may not be explained theoretically. This is the reason why we expect much on the further TAGS experiments. Moreover the discrepancy still remains between JEFF-3.1 and the experiments around 20 s as seen in Fig. 1 (d) with dotted circle. For the improvement of JEFF-3.1, the next targets should be chosen from around this time region. A part of the priority lists proposed in ref.12 is shown in Table 3. This table indicates that the highest priority nuclides are Nb-98 and -101 in this cooling time region. Therefore these nuclides are the candidates of the highest priority for the next TAGS measurements.

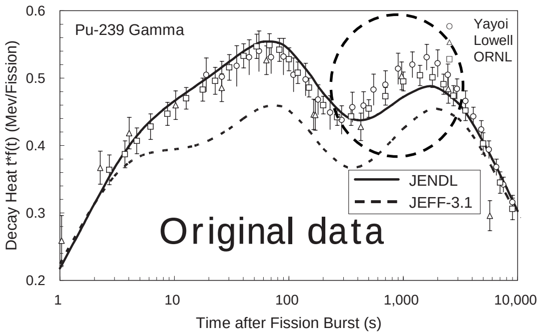

(a) Calculation results by original data in the existing libraries

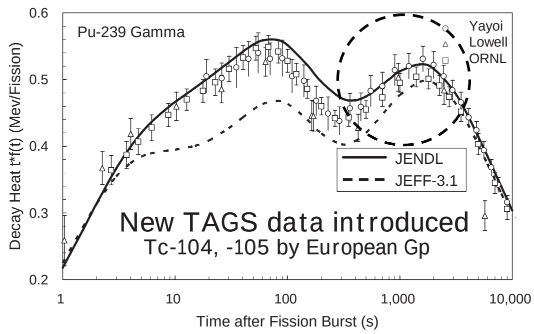

(c) Calculation results by replacing with new TAGS data measured by the European group

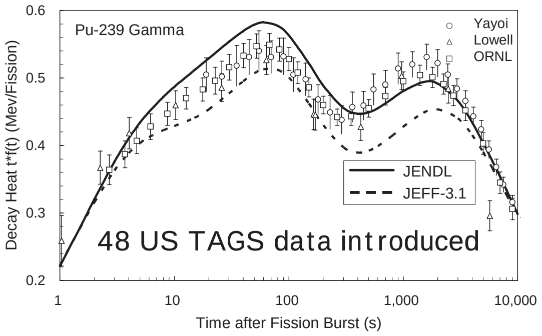

(b) Calculation results by replacing with TAGS data measured by the Idaho group

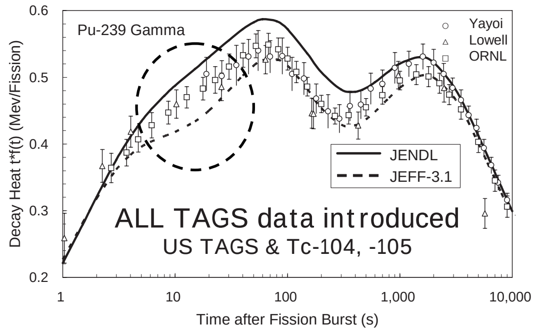

(d) The results by introduction of all TAGS data up to now

Figure 1 The γ-ray component of the Pu-239 decay heat after a fission burst calculated with JENDL (solid curve) and with JEFF-3.1 (dotted curve)

Table 3 The list of important nuclides for the cooling time on Pu-239 gamma component

time(s)	nuclide Z		A	m	Q-value (A) [keV]	last level (B) [keV]	(B) / (A) *1	JENDL (C) [MeV/s/fis.]	JEFF-3.1 (D) [MeV/s/fis.]	$\frac{(C)-(D)}{JENDL\ \ total}$ *2	Bersillon List*3	priority
20	41	Nb	98	0	4,586	2,608	56.9%	7.66E-04	2.91E-04	1.82%	○	AAA
	41	Nb	101	0	4,569	811	17.7%	6.62E-04	2.31E-04	1.65%	○	AAA
	43	Tc	106	0	6,547	3,930	60.0%	1.39E-03	1.07E-03	1.20%		AA
	42	Mo	105	0	4,950	2,766	55.9%	7.89E-04	2.97E-04	1.88%		AA
	43	Tc	107	0	4,820	2,680	55.6%	6.59E-04	2.21E-04	1.68%		AA
	42	Mo	103	0	3,750	1,621	43.2%	6.52E-04	3.61E-04	1.12%		AA
	40	Zr	100	0	3,335	704	21.1%	4.80E-04	1.65E-04	1.21%		AA
	41	Nb	99	0	3,639	236	6.5%	5.36E-04	1.51E-04	1.47%		AA
	39	Y	96	0	7,087	6,232	87.9%	3.39E-04	2.63E-05	1.20%	○	AA
	39	Y	96	1	7,087	5,899	83.2%	1.56E-03	1.13E-03	1.65%	○	AA
	52	Te	135	0	5,960	4,773	80.1%	6.34E-04	1.45E-04	1.88%	○	AA
	44	Ru	109	0	4,160	2,270	54.6%	1.46E-04	3.22E-04	-0.67%		A
	40	Zr	98	0	2,261	0	0.0%	1.36E-04	0.00E+00	0.52%		A
	54	Xe	139	0	5,057	4,228	83.6%	3.80E-04	7.11E-04	-1.27%		A
	37	Rb	92	0	8,105	7,363	90.8%	7.94E-05	2.85E-04	-0.79%	○	A
	53	I	136	1	7,570	6,624	87.5%	4.83E-04	6.54E-04	-0.66%		

The emphasized parts indicate following conditions; the ratio of the known last level to Q-value is smaller than 70% (*1), the difference between JENDL and JEFF-3.1 is over 1.0% (*2), and the nuclide appears on the Bersillon's list[13] (*3).

4. Conclusion

In the present study, we calculated the FP decay heat introducing the TAGS data from the US-TAGS and the very recent results for Tc-104 and -105 from Europe which was made available in 2008. These results suggest that the TAGS data are essential to reproduce the integral experiments of the FP decay heat at cooling range from 3 to 5,000 s. It was also confirmed that technetium isotopes are the origin of the long-standing disagreement seen in the cooling time range around 1,000 s. These results strongly indicated that the TAGS measurement is essentially the only way now available to overcome the pandemonium problem experimentally. We further suggested that the highest priority nuclides to be measured are Nb-98 and -101 among others to solve the discrepancy which still remains between JEFF-3.1 and the experiments around 20 s if we try to be independent from nuclear-theoretical supplementation.

Reference

1. J.C.Hardy, L.C.Carrez, B.Jonson, P.G.Hansen: Phys. Lett., **71B**, 307, 1977.
2. T.Yoshida, R.Nakasima: J. Nucl. Sci. Technol., Vol.18, No.6, pp.393, 1971.
3. R.C.Greenwood, R.G.Helmer, M.A. Lee, *et al*.: Nucl. Instr. and Meth., **A314,** 514, 1992.
4. A.Algora, D.Jordan, J.L.Tain, B.Rubio, *et. al.*: The 13th Int. Symposium on Capture Gamma-Ray Spectroscopy and Related Topics, August, 2008, Cologne, Germany.
5. T.Yoshida, T.Tachibana, F.Storrer, K.Oyamatsu, J.Katakura: J. Nucl. Sci. Technol., Vol.36, No.2, pp.135, 1999.
6. T.Yoshida, Y.Wakasugi, N.Hagura: J. Nucl. Sci. Technol., Vol.45, No.8, pp.713, 2008.
7. M.Akiyama, S.An: *Proc. Int. Conf. on Nuclear Data for Science and Technology*, Antwerp, 237, 1982.
8. J.K.Dickens, T.A.Love, J.W.McConnell: Nucl. Sci. Eng., **78**, 126, 1981.
9. A.Algora, J.L.Tain, B.Rubio, *et. al*.: *Proc. Int. Conf. on Nuclear Data for Science and Technology*, Nice, April 2007.
10. J.L.Tain: *Proc. Int. Conf. on Nuclear Data for Science and Technology*, Nice, April, 2007.
11. N.Hagura, T.Yoshida and T.Tachibana: J. Nucl. Sci. Technol., Vol.43, No.5, pp.497, 2006.
12. N.Hagura, T.Yoshida, M.Katsuma: JAEA-Conf 2006-009, pp.157, 2006.
13. O.Bersillon, private communication, 2005.

国際単位系（SI）

表１．SI 基本単位

基本量	SI 基本単位	
	名称	記号
長さ	メートル	m
質量	キログラム	kg
時間	秒	s
電流	アンペア	A
熱力学温度	ケルビン	K
物質量	モル	mol
光度	カンデラ	cd

表２．基本単位を用いて表されるSI組立単位の例

組立量	SI 基本単位	
	名称	記号
面積	平方メートル	m^2
体積	立法メートル	m^3
速さ，速度	メートル毎秒	m/s
加速度	メートル毎秒毎秒	m/s^2
波数	毎メートル	m^{-1}
密度，質量密度	キログラム毎立方メートル	kg/m^3
面積密度	キログラム毎平方メートル	kg/m^2
比体積	立方メートル毎キログラム	m^3/kg
電流密度	アンペア毎平方メートル	A/m^2
磁界の強さ	アンペア毎メートル	A/m
量濃度[(a)]，濃度	モル毎立方メートル	mol/m^3
質量濃度	キログラム毎立法メートル	kg/m^3
輝度	カンデラ毎平方メートル	cd/m^2
屈折率[(b)]	（数字の） 1	1
比透磁率[(b)]	（数字の） 1	1

(a) 量濃度（amount concentration）は臨床化学の分野では物質濃度（substance concentration）ともよばれる。
(b) これらは無次元量あるいは次元１をもつ量であるが、そのことを表す単位記号である数字の１は通常は表記しない。

表３．固有の名称と記号で表されるSI組立単位

組立量	SI 組立単位			
	名称	記号	他のSI単位による表し方	SI基本単位による表し方
平面角	ラジアン[(b)]	rad	1 [(b)]	m/m
立体角	ステラジアン[(b)]	sr[(c)]	1 [(b)]	m^{2}/m^2
周波数	ヘルツ[(d)]	Hz		s^{-1}
力	ニュートン	N		$m\ kg\ s^{-2}$
圧力，応力	パスカル	Pa	N/m^2	$m^{-1}\ kg\ s^{-2}$
エネルギー，仕事，熱量	ジュール	J	N m	$m^2\ kg\ s^{-2}$
仕事率，工率，放射束	ワット	W	J/s	$m^2\ kg\ s^{-3}$
電荷，電気量	クーロン	C		s A
電位差（電圧），起電力	ボルト	V	W/A	$m^2\ kg\ s^{-3}\ A^{-1}$
静電容量	ファラド	F	C/V	$m^{-2}\ kg^{-1}\ s^4\ A^2$
電気抵抗	オーム	Ω	V/A	$m^2\ kg\ s^{-3}\ A^{-2}$
コンダクタンス	ジーメンス	S	A/V	$m^{-2}\ kg^{-1}\ s^3\ A^2$
磁束	ウエーバ	Wb	Vs	$m^2\ kg\ s^{-2}\ A^{-1}$
磁束密度	テスラ	T	Wb/m^2	$kg\ s^{-2}\ A^{-1}$
インダクタンス	ヘンリー	H	Wb/A	$m^2\ kg\ s^{-2}\ A^{-2}$
セルシウス温度	セルシウス度[(e)]	℃		K
光束	ルーメン	lm	cd sr[(c)]	cd
照度	ルクス	lx	lm/m^2	$m^{-2}\ cd$
放射性核種の放射能[(f)]	ベクレル[(d)]	Bq		s^{-1}
吸収線量, 比エネルギー分与, カーマ	グレイ	Gy	J/kg	$m^2\ s^{-2}$
線量当量, 周辺線量当量, 方向性線量当量, 個人線量当量	シーベルト[(g)]	Sv	J/kg	$m^2\ s^{-2}$
酸素活性	カタール	kat		$s^{-1}\ mol$

(a)SI接頭語は固有の名称と記号を持つ組立単位と組み合わせても使用できる。しかし接頭語を付した単位はもはやコヒーレントではない。
(b)ラジアンとステラジアンは数字の１に対する単位の特別な名称で、量についての情報をつたえるために使われる。実際には、使用する時には記号rad及びsrが用いられるが、習慣として組立単位としての記号である数字の１は明示されない。
(c)測光学ではステラジアンという名称と記号srを単位の表し方の中に、そのまま維持している。
(d)ヘルツは周期現象についてのみ、ベクレルは放射性核種の統計的過程についてのみ使用される。
(e)セルシウス度はケルビンの特別な名称で、セルシウス温度を表すために使用される。セルシウス度とケルビンの単位の大きさは同一である。したがって、温度差や温度間隔を表す数値はどちらの単位で表しても同じである。
(f)放射性核種の放射能（activity referred to a radionuclide）は、しばしば誤った用語で”radioactivity”と記される。
(g)単位シーベルト（PV,2002,70,205）についてはCIPM勧告2（CI-2002）を参照。

表４．単位の中に固有の名称と記号を含むSI組立単位の例

組立量	SI 組立単位		
	名称	記号	SI 基本単位による表し方
粘度	パスカル秒	Pa s	$m^{-1}\ kg\ s^{-1}$
力のモーメント	ニュートンメートル	N m	$m^2\ kg\ s^{-2}$
表面張力	ニュートン毎メートル	N/m	$kg\ s^{-2}$
角速度	ラジアン毎秒	rad/s	$m\ m^{-1}\ s^{-1}=s^{-1}$
角加速度	ラジアン毎秒毎秒	rad/s^2	$m\ m^{-1}\ s^{-2}=s^{-2}$
熱流密度，放射照度	ワット毎平方メートル	W/m^2	$kg\ s^{-3}$
熱容量，エントロピー	ジュール毎ケルビン	J/K	$m^2\ kg\ s^{-2}\ K^{-1}$
比熱容量，比エントロピー	ジュール毎キログラム毎ケルビン	J/(kg K)	$m^2\ s^{-2}\ K^{-1}$
比エネルギー	ジュール毎キログラム	J/kg	$m^2\ s^{-2}$
熱伝導率	ワット毎メートル毎ケルビン	W/(m K)	$m\ kg\ s^{-3}\ K^{-1}$
体積エネルギー	ジュール毎立方メートル	J/m^3	$m^{-1}\ kg\ s^{-2}$
電界の強さ	ボルト毎メートル	V/m	$m\ kg\ s^{-3}\ A^{-1}$
電荷密度	クーロン毎立方メートル	C/m^3	$m^{-3}\ sA$
表面電荷	クーロン毎平方メートル	C/m^2	$m^{-2}\ sA$
電束密度，電気変位	クーロン毎平方メートル	C/m^2	$m^{-2}\ sA$
誘電率	ファラド毎メートル	F/m	$m^{-3}\ kg^{-1}\ s^4\ A^2$
透磁率	ヘンリー毎メートル	H/m	$m\ kg\ s^{-2}\ A^{-2}$
モルエネルギー	ジュール毎モル	J/mol	$m^2\ kg\ s^{-2}\ mol^{-1}$
モルエントロピー, モル熱容量	ジュール毎モル毎ケルビン	J/(mol K)	$m^2\ kg\ s^{-2}\ K^{-1}\ mol^{-1}$
照射線量（Ｘ線及びγ線）	クーロン毎キログラム	C/kg	$kg^{-1}\ sA$
吸収線量率	グレイ毎秒	Gy/s	$m^2\ s^{-3}$
放射強度	ワット毎ステラジアン	W/sr	$m^4\ m^{-2}\ kg\ s^{-3}=m^2\ kg\ s^{-3}$
放射輝度	ワット毎平方メートル毎ステラジアン	$W/(m^2\ sr)$	$m^2\ m^{-2}\ kg\ s^{-3}=kg\ s^{-3}$
酵素活性濃度	カタール毎立方メートル	kat/m^3	$m^{-3}\ s^{-1}\ mol$

表５．SI 接頭語

乗数	接頭語	記号	乗数	接頭語	記号
10^{24}	ヨタ	Y	10^{-1}	デシ	d
10^{21}	ゼタ	Z	10^{-2}	センチ	c
10^{18}	エクサ	E	10^{-3}	ミリ	m
10^{15}	ペタ	P	10^{-6}	マイクロ	µ
10^{12}	テラ	T	10^{-9}	ナノ	n
10^{9}	ギガ	G	10^{-12}	ピコ	p
10^{6}	メガ	M	10^{-15}	フェムト	f
10^{3}	キロ	k	10^{-18}	アト	a
10^{2}	ヘクト	h	10^{-21}	ゼプト	z
10^{1}	デカ	da	10^{-24}	ヨクト	y

表６．SIに属さないが、SIと併用される単位

名称	記号	SI 単位による値
分	min	1 min=60s
時	h	1h =60 min=3600 s
日	d	1 d=24 h=86 400 s
度	°	1°=(π/180) rad
分	’	1’=(1/60)°=(π/10800) rad
秒	”	1”=(1/60)’=(π/648000) rad
ヘクタール	ha	$1ha=1hm^2=10^4m^2$
リットル	L，l	$1L=1l=1dm^3=10^3cm^3=10^{-3}m^3$
トン	t	$1t=10^3$ kg

表７．SIに属さないが、SIと併用される単位で、SI単位で表される数値が実験的に得られるもの

名称	記号	SI 単位で表される数値
電子ボルト	eV	$1eV=1.602\ 176\ 53(14)\times10^{-19}J$
ダルトン	Da	$1Da=1.660\ 538\ 86(28)\times10^{-27}kg$
統一原子質量単位	u	1u=1 Da
天文単位	ua	$1ua=1.495\ 978\ 706\ 91(6)\times10^{11}m$

表８．SIに属さないが、SIと併用されるその他の単位

名称	記号	SI 単位で表される数値
バール	bar	$1\ bar=0.1MPa=100kPa=10^5Pa$
水銀柱ミリメートル	mmHg	1mmHg=133.322Pa
オングストローム	Å	$1\ Å=0.1nm=100pm=10^{-10}m$
海里	M	1 M=1852m
バーン	b	$1\ b=100fm^2=(10^{-12}cm)2=10^{-28}m^2$
ノット	kn	1 kn=(1852/3600)m/s
ネーパ	Np	SI単位との数値的な関係は、対数量の定義に依存。
ベル	B	
デジベル	dB	

表９．固有の名称をもつCGS組立単位

名称	記号	SI 単位で表される数値
エルグ	erg	$1\ erg=10^{-7}\ J$
ダイン	dyn	$1\ dyn=10^{-5}N$
ポアズ	P	$1\ P=1\ dyn\ s\ cm^{-2}=0.1Pa\ s$
ストークス	St	$1\ St\ =1cm^2\ s^{-1}=10^{-4}m^2\ s^{-1}$
スチルブ	sb	$1\ sb\ =1cd\ cm^{-2}=10^4cd\ m^{-2}$
フォト	ph	$1\ ph=1cd\ sr\ cm^{-2}\ 10^4lx$
ガル	Gal	$1\ Gal\ =1cm\ s^{-2}=10^{-2}ms^{-2}$
マクスウェル	Mx	$1\ Mx = 1G\ cm^2=10^{-8}Wb$
ガウス	G	$1\ G\ =1Mx\ cm^{-2}\ =10^{-4}T$
エルステッド[(c)]	Oe	1 Oe ≙ $(10^3/4π)A\ m^{-1}$

（c） ３元系のCGS単位系とSIでは直接比較できないため、等号「 ≙ 」は対応関係を示すものである。

表10．SIに属さないその他の単位の例

名称	記号	SI 単位で表される数値
キュリー	Ci	$1\ Ci=3.7\times10^{10}Bq$
レントゲン	R	$1\ R = 2.58\times10^{-4}C/kg$
ラド	rad	$1\ rad=1cGy=10^{-2}Gy$
レム	rem	$1\ rem=1\ cSv=10^{-2}Sv$
ガンマ	γ	1 γ =1 nT=10-9T
フェルミ		1フェルミ=1 fm=10-15m
メートル系カラット		1メートル系カラット = 200 mg = 2×10-4kg
トル	Torr	1 Torr = (101 325/760) Pa
標準大気圧	atm	1 atm = 101 325 Pa
カロリー	cal	1cal=4.1858J（「15℃」カロリー），4.1868J（「IT」カロリー）4.184J（「熱化学」カロリー）
ミクロン	µ	$1\ µ\ =1µm=10^{-6}m$

（第8版，2006年改訂）